

ABSTRACT

Title of Dissertation: SEARCH FOR SOFT UNCLUSTERED ENERGY PATTERNS AT THE LARGE HADRON COLLIDER AND STUDIES OF RADIATION DAMAGE IN PLASTIC SCINTILLATORS

Christos Papageorgakis
Doctor of Philosophy, 2025

Dissertation Directed by: Professor Sarah Eno
Department of Physics

Data collected by the Compact Muon Solenoid experiment at the Large Hadron Collider, which collides protons at a center-of-mass energy of approximately 14 TeV, enable tests of the Standard Model of Particle Physics and searches for physics beyond the Standard Model. This thesis presents studies of radiation damage to plastic scintillators, used to produce signals in the CMS calorimeter system, and a search for a beyond-the-Standard-Model particle, the Soft Unclustered Energy Pattern (SUEP).

The effects of ionizing radiation on the light output and the optical properties of plastic scintillators are assessed for a variety of materials, dopant concentrations, fluors, antioxidant concentrations, sample thicknesses, doses, and dose rates. Depending on the dose rate, the samples exhibit internal regions with different refractive indices separated by a visible boundary. Measurements of the boundary depth indicate compatibility with the expected oxygen penetration depth during irradiation. The refractive indices of the

internal regions are higher than those of the outer regions, which match the indices of unirradiated samples.

Dark sectors with a large t'Hooft coupling can give rise to SUEP, which are final states characterized by large charged particle multiplicities. A search for SUEP producing muons in the final state is also presented. The expected 95% CL upper limits for the cross sections indicate that, once unblinded, the search will be able to set upper limits about 3-4 orders of magnitude lower than the theory predictions, meaning that it is capable of either excluding the theory or discovering new physics.

SEARCH FOR SOFT UNCLUSTERED ENERGY PATTERNS AT THE
LARGE HADRON COLLIDER
AND STUDIES OF RADIATION DAMAGE IN PLASTIC
SCINTILLATORS

by

Christos Papageorgakis

Dissertation submitted to the Faculty of the Graduate School of the
University of Maryland, College Park in partial fulfillment
of the requirements for the degree of
Doctor of Philosophy
2025

Advisory Committee:

Professor Sarah Eno, Chair/Advisor

Professor Alberto Belloni

Professor Christopher Palmer

Professor Kaustubh Agashe

Professor Michael C. Laskowski, Dean's Representative

© Copyright by
Christos Papageorgakis
2025

Acknowledgments

First and foremost, I would like to express my deepest gratitude to my advisor, Prof. Sarah Eno, for her unwavering support and guidance throughout my PhD journey. Her mentorship has been invaluable to me, both scientifically and personally.

I am also very grateful to Prof. Alberto Belloni and Prof. Christopher Palmer for their thoughtful comments and guidance over the years. I am thankful to Dr. Timothy Edberg for the excellent collaboration on the plastic scintillator projects. I would also like to thank the CMS SUEP group, and in particular Prof. Karri Folan DiPetrillo, Dr. Kevin Pedro, Dr. Chad Wells Freer, and Dr. Carlos Erice Cid. Our insightful discussions and their feedback were important for the development of the search for SUEP with muons.

On a more personal note, I am always grateful for my family, my parents and my brother, who are always there for me. This PhD would not have been possible without the support of all my friends. First, all my friends from the Physics Department: Martin, Nick, Jake, Selu, Adam, Zack, Alex, just to name a few. But especially Stefano, for all the wonderful space observation and astrophotography nights, and Yihui, for all the exciting ski trips. Second, all my Greek friends: Leo, Chris, Panos, Eleftheria, Yoho, Leo, Danae, Angelos, and Panagiotis. Finally, all my friends back in Greece: Giannis, Lefteris, Vangelis, Artemis, Eirilena. Without your support, I wouldn't have made it. Thank you!

Table of Contents

Acknowledgements	ii
Table of Contents	iii
List of Tables	vii
List of Figures	ix
List of Abbreviations	xviii
Chapter 1: Introduction	1
I Introduction to the Standard Model and CMS	4
Chapter 2: The Standard Model of particle physics	5
2.1 Introduction	5
2.2 The Standard Model of Particle Physics	6
2.2.1 Quantum Electrodynamics	7
2.2.2 Electroweak Theory	8
2.2.3 The Brout-Englert-Higgs mechanism	11
2.2.4 Quantum Chromodynamics	15
2.2.5 Shortcomings of the Standard Model	17
Chapter 3: The Compact Muon Solenoid experiment	19
3.1 The Large Hadron Collider	19
3.1.1 The CERN accelerator complex	20
3.1.2 The Large Hadron Collider	20
3.1.3 Luminosity	24
3.2 The Compact Muon Solenoid experiment	25
3.2.1 Pixel tracker	27
3.2.2 Silicon strip tracker	28
3.2.3 Electromagnetic calorimeter	30
3.2.4 Hadron calorimeter	30
3.2.5 Superconducting solenoid magnet	32
3.2.6 Muon detectors	33
3.2.7 The triggering and data acquisition system	37

3.2.8	Luminosity and beam conditions	40
3.3	Offline software and computing	41
3.4	Monte Carlo simulations	41
3.5	Reconstruction	42
3.5.1	Track fitting and reconstruction	43
3.5.2	Muon reconstruction	43
3.5.3	The particle flow algorithm	44
II	Radiation damage in plastic scintillators	45
Chapter 4:	Introduction to plastic scintillators	46
4.1	Plastic scintillators in high-energy physics	46
4.2	Working principles of plastic scintillators	47
4.3	Radiation damage in plastic scintillators	48
Chapter 5:	The effect of dose rate on radiation damage	50
5.1	Introduction	50
5.2	Mechanisms and effects of radiation-induced changes to phenyl-based polymeric scintillators	52
5.2.1	The reactions of the C-centered radicals in the absence of oxygen	55
5.2.2	The reactions of the C-centered radicals in the presence of oxygen	55
5.3	Sample and irradiation details	58
5.4	Measurement technique	60
5.5	Results	63
5.6	Thickness, fluor concentration, and antioxidant concentrations	68
5.7	Conclusions	73
Chapter 6:	Effects of radiation damage on optical properties of scintillators and the role of oxygen.	77
6.1	Oxygen diffusion theory	77
6.1.1	Oxygen diffusion in polymers	78
6.1.2	JAERI model for oxidation during irradiation	81
6.1.3	Photo-oxidation model	90
6.2	Refractive index theory	95
6.3	Experimental setup and procedures	99
6.3.1	Samples and irradiations	99
6.3.2	After irradiation	100
6.3.3	Refractive index boundary depth	101
6.3.4	Refractive index measurement	102
6.4	Results	106
6.5	Conclusions	112

III Search for Soft Unclustered Energy Patterns with muons	114
Chapter 7: Introduction to SUEP	116
Chapter 8: Signal models for SUEP	119
Chapter 9: Data and Monte Carlo samples	126
9.1 Datasets	126
9.2 Monte Carlo samples	127
9.2.1 Background samples	127
9.2.2 Signal samples	130
9.3 Corrections	133
9.3.1 Pileup reweighting	133
9.3.2 L1 prefiring	133
Chapter 10: Object selection	137
10.1 Muons	137
10.1.1 General muon selection	137
10.1.2 Selections for the analysis subregions	138
10.1.3 Muon corrections	138
10.2 Tracks	139
Chapter 11: Analysis strategy	141
Chapter 12: Event selection	143
12.1 Triggers	143
12.2 Pre-selection	145
12.3 Muon sources	146
12.4 Selection regions	147
12.4.1 Control regions (CR)	147
12.4.2 Signal regions (SR)	153
12.4.3 Validation region (VR)	160
12.5 Selection summary	162
Chapter 13: Background Estimation	166
13.1 Expected backgrounds	166
13.2 Extrapolation method	169
13.3 Validation of the extrapolation method	176
Chapter 14: Systematic Uncertainties	181
14.1 Experimental uncertainties	181
14.1.1 Pileup	181
14.1.2 L1 prefiring	181
14.1.3 Muon scale factors	182
14.1.4 Luminosity	182
14.1.5 Track efficiency	183

14.2 Theoretical uncertainties	184
14.2.1 Matrix element renormalization and factorization scales	184
14.2.2 Matrix element parton distribution function	185
14.2.3 Parton shower	186
14.3 Summary of systematic uncertainties	186
Chapter 15: Results	189
15.1 Prefit plots	189
15.2 Signal model assignment for the SRs	190
15.3 Combine fit and postfit plots	191
15.4 Impact plots	193
15.4.1 Expected limits	195
 IV Final remarks	 201
 Chapter 16: Summary and conclusions	 202
 V Appendices	 206
 Appendix A: List of scintillator samples	 207
 Appendix B: $N - 1$ plots	 210
B.1 $N - 1$ plots for CR_{QCD}	210
B.2 $N - 1$ plots for CR_{DY}	211
B.3 $N - 1$ plots for $SR_{low\ T}$	217
B.4 $N - 1$ plots for $SR_{high\ T}$	222
 Appendix C: SR signal yields	 227
 Appendix D: Limits	 235
 Bibliography	 246

List of Tables

6.1	Brühl's weights. The sum of these weights gives the molecular refractivity for a compound.	97
6.2	Brühl theory predictions and experimental values for three common organic substrate materials.	98
9.1	Data taking years for Run 2 (13 TeV) used in the analysis, with the corresponding MiniAOD reprocessing used for each one, the eras that compose them, and the run range and luminosity corresponding to each of these eras. All numbers are for the DoubleMuon primary dataset.	127
9.2	The full names of the datasets in use for Run 2.	128
9.3	Background samples used for Run 2 years in the analysis, their associated cross section times branching fraction, the plotting group in which each one is included in stack plots, and the overall QCD order used in the gen-level simulation (normalization cross section).	135
9.4	Signal samples used in the analysis for the Run 2 years. The scan values for m_ϕ and $m_{A'}$ that are contained in each sample are listed in separate columns. For all samples, the scanned values for m_S are 125, 200, 300, 400, 500, 600, 800, and 1000 GeV.	136
9.5	Cross sections for all values of m_S for center-of-mass energy 13 TeV.	136
12.1	Summary of the HLT selection used in the pre-selection of events for the analysis for each associated data-taking period.	144
12.2	Summary of the trigger paths used in the pre-selection of events for the analysis and their associated data-taking periods for Run 2 years.	144
12.3	Summary of the L1 seeds for each HLT path separated by the data-taking years.	145
12.4	The values of <code>Muon_genPartFlav</code> and <code>muon</code> sources.	147
12.5	Summary of the selections.	164
12.6	Purpose of each region.	165
13.1	MC statistics table for $SR_{\text{low } T}$ for 2018. The yields for all MC processes in the discovery bin ($n_{\text{muon}} = 7$) are 0. The columns show the highest n_{muon} that is populated with MC events, its event yields, the effective total weight for that bin, the effective raw number of MC events for that bin, and the Poisson (Garwood) intervals for a bin with the same effective weight and 0 yield.	168

13.2	MC statistics table for $SR_{\text{high } T}$ for 2018. The yields for all MC processes in the discovery bin ($n_{\text{muon}} = 7$) are 0. The columns show the highest n_{muon} that is populated with MC events, its event yields, the effective total weight for that bin, the effective raw number of MC events for that bin, and the Poisson (Garwood) intervals for a bin with the same effective weight and 0 yield.	169
13.3	The final event yields for the QCD and DY MC background processes in the discovery bins of the two signal regions. These numbers are produced using the extrapolation method outlined in Section 13.2.	178
14.1	Mapping between systematics and MC processes.	187
14.2	Impacts of systematic uncertainties on the yields of the discovery bin of $SR_{\text{high } T}$ for 2018. The maximum up/down shift is displayed as a percentage of the nominal value.	187
14.3	Impacts of systematic uncertainties on the yields of the discovery bin of $SR_{\text{low } T}$ for 2018. The maximum up/down shift is displayed as a percentage of the nominal value.	188
15.1	Result for b-only fit for Run 2 with data in the CRs and blinded $SR_{\text{high } T}$ with yields set to 0. The initial value for all nuisance parameters is 0. The k-factors have initial value 1.	200
A.1	List of EJ200PS samples.	208
A.2	List of EJ200PVT samples.	208
A.3	List of EJ260PS and EJ260PVT samples.	209
A.4	List of varying antioxidant samples.	209
C.1	SR signal yields for all years in Run 2 (2016, 2017, and 2018)	227

List of Figures

2.1	The Standard Model of Particle Physics. Taken from [1].	6
2.2	The Mexican hat Higgs potential. Code was fetched from [2].	13
2.3	Rotational curves of galaxies. The solid lines are three-parameter fits, dashed curves are for visible components, dotted curves are for gas components, and the dash-dot curves are for the dark halo. Figure taken from [3].	18
3.1	Layout of the CERN accelerator complex. The LINAC 4, the Booster, and the PS are shown in shades of purple, while the SPS and the LHC are shown in shades of blue. The four interaction points of the LHC are shown with filled yellow circles. Figure taken from [4].	21
3.2	Cross-sectional view of the LHC dipole magnets. Taken from [5].	23
3.3	Cutaway diagram of CMS [6,7].	26
3.4	Layout of the pixel tracker displaying one quadrant of the r - z cross-section. The bottom of the picture shows the layout of the pixel until the end of 2016. The pixel tracker after the Phase 1 upgrade is depicted at the top [8].	28
3.5	Layout of the CMS tracker displaying one quadrant of the r - z cross-section. The pixel tracker is shown in green. Single-sided strips are shown in red, while double-sided strips are shown in blue [9].	29
3.6	Layout of one quadrant of the r - z cross-section for the HCAL. The layout depicts the HCAL after the upgrades for Run 3. The colors in the HB and HE indicate the depths, which are the layers that are connected to the same SiPM. The letters FEE show the location of the frontend electronics [10].	31
3.7	Layout of one quadrant of the r - z cross-section of CMS at the beginning of Run 3. The four muon subdetectors are shown in color. The RPC is shown in blue, the CSC in green, the DT in beige, and the GEM in red. The iron yoke is shown in dark gray [11].	34
3.8	Left: schematic of a CSC chamber. Taken from [12]. Right: installation of CSC chambers. Taken from [13].	35
3.9	Left: schematic of a DT cell including the drift lines and the isochrones. Taken from [14] Right: schematic of a DT chamber, taken from [15].	35
3.10	Left: schematic of a resistive plate chamber, taken from [16]. Right: 3D schematic of the RPC showing its working principles, taken from [17].	36
3.11	Left: layout of the GEM chambers on the CMS endcap, taken from [18]. Right: schematic of a GEM chamber showing its internal components, taken from [19].	37

5.1	Emission spectra from the Eljen Technology website for EJ-200 (blue solid) and EJ-260 (green dot). The arrows represent the emission maxima for the primary for EJ-200 (blue solid) and EJ-260 (green dot).	59
5.2	[top] A photograph of selected rods, all with nominal doping. From left to right: unirradiated EJ-200, EJ-200 irradiated to 500 kGy at 11 kGy/hr, unirradiated EJ-260, EJ-260 irradiated to 500 kGy at 11 kGy/hr. [bottom] Apparatus for measurements with an alpha source. In use, the apparatus is enclosed in a light-tight box.	62
5.3	[top] Measured energy spectrum from a rod irradiated at 3640 Gy/hr to a dose of 70 kGy when excited using an alpha source at various times since irradiation, showing the annealing process. [bottom] Typical transmission spectra for rods with nominal fluors and antioxidant concentrations and with a PVT matrix, with no fluors (black, medium dashes), EJ-260 fluors (green, short dashes), and for EJ-200 fluors (blue, long dashes).	64
5.4	[left] Ratio of the light output of rods after receiving a dose d to their unirradiated light output, versus d . The rods' matrix is PVT, and the irradiation dose rate was 0.46 kGy/hr. The different colors correspond to different irradiation dates and facilities. Rods irradiated at Sandia National Laboratories and NIST are represented with black and yellow markers, respectively. The lines are fits of the Sandia data to exponentials, one using only the lower dose data and the other using all data. Uncertainties are dominated by systematic uncertainties. [right] Same, comparing PS and PVT. All rods included in this plot have been irradiated at Sandia National Laboratories.	65
5.5	The value of D versus \mathcal{R} for scintillator rods with the EJ-200 fluors at the manufacturer's nominal concentration and with nominal antioxidant concentration, for PVT (blue markers) and PS (black markers).	66
5.6	The value of D versus \mathcal{R} for scintillator rods with the EJ-260 fluors at the manufacturer's nominal concentration and with nominal antioxidant concentration, for PS and PVT matrices.	67
5.7	[top] The value of \mathcal{D}^{-1} for scintillator with the EJ-200 fluors, for both PS and PVT, at \mathcal{R} s of 3.1 Gy/hr to a total dose of 12.6 kGy and 3900 Gy/hr to a total dose of 70 kGy. [bottom] The value of \mathcal{D}^{-1} for scintillator with the EJ-260 fluors, for both PS and PVT, at \mathcal{R} s of 3.1 Gy/hr to a total dose of 12.6 kGy and 3900 Gy/hr to a total dose of 70 kGy. In both plots, the emission range for the secondary fluor is indicated by a double arrow. Negative values of \mathcal{D}^{-1} correspond to increases in the transmission after irradiation.	69

5.8	Ratios $\mathcal{D}_1^{-1}/\mathcal{D}_2^{-1}$ are plotted versus wavelength, where \mathcal{D}_1^{-1} and \mathcal{D}_2^{-1} are values of \mathcal{D}^{-1} corresponding to different cases of irradiations or irradiated materials. The precise cases are defined separately for each ratio. Two different irradiations are included, a high \mathcal{R} one at 3900 Gy/hr (total dose: 70 kGy) and a low \mathcal{R} one at 3.1 Gy/hr (total dose: 12.6 kGy). [top] EJ-200 for PVT at low \mathcal{R} divided by high \mathcal{R} (green dash), PS at low \mathcal{R} divided by high \mathcal{R} (red dot-dash), PVT divided by PS both at low \mathcal{R} (purple dot), PVT divided by PS both at high \mathcal{R} (red dot-dash) [bottom] EJ-260 for PVT at low \mathcal{R} over high \mathcal{R} (green dash), PS at low \mathcal{R} over high \mathcal{R} (red dot-dash), PVT over PS both at low \mathcal{R} (purple dot), PVT over PS both at high \mathcal{R} (red dot-dash) In both plots, the emission range for the secondary fluor is indicated by a double arrow. The solid black line indicates a value of 1.0.	70
5.9	For rods with EJ-200 fluors made of PS: [top] value of D versus day since end of irradiation for a \mathcal{R} of 3640 Gy/hr, for rod thicknesses of 0.4 cm, 0.6 cm, 0.8 cm, and 1.0 cm; [bottom] value of D after annealing versus \mathcal{R} for rod thicknesses of 0.4 cm, 0.6 cm, 0.8 cm, and 1.0 cm.	72
5.10	[top] The value of D versus \mathcal{R} for PS scintillator rods with the EJ-200 fluors at the manufacturer's nominal concentration for antioxidants for the nominal concentration of fluors (1X1P), for double the concentration of the primary fluor (1X2P), and double the concentration of the secondary fluor (2X1P). [bottom] The value of D versus \mathcal{R} for PVT scintillator rods with the EJ-200 fluors at the manufacturer's nominal concentration for antioxidants for the nominal concentration of fluors (1X1P), for double the concentration of the primary fluor (1X2P), and double the concentration of the secondary fluor (2X1P).	74
5.11	The value of D versus \mathcal{R} for scintillator rods with the EJ-200 fluors in PVT at the manufacturer's nominal concentration for fluors without antioxidant additives (AO-0), with the nominal concentration (AO-1), and with twice the nominal (AO-2).	75
6.1	A 1-dimensional description of oxygen diffusion in the polymer. The thickness is l , C_0 , and $C(x, t)$ are the oxygen concentrations at the surface and the interior of the polymer, and x is the distance from the center.	80
6.2	The normalized oxygen concentration y at the stationary state under irradiation is plotted for the limiting case $\frac{4k_1Y\mathcal{R}}{(k_2C)^2} \ll 1$ and for a range of values of β .	85
6.3	Numerical solutions to Eq. 6.22 for various combinations of values for the parameters $A \equiv \frac{C_0k_2^2}{2Dk_1}$ and $B \equiv \frac{2Y\mathcal{R}}{DC_0}$. The parameter A is expressed through its ratio to B . The normalized reaction rate R/R_0 is shown for the entire normalized length λ . For the code used see Ref. [20].	86

6.4	Distributions of the normalized O_2 concentration and the oxidation rate for different points in time during the annealing process for the 3D finite differences simulation of the JAERI model. The input parameters are $k_1 = 5 \cdot 10^{-11} \text{ cm}^3\text{s}^{-1}$, $k_2 = 2 \cdot 10^{-10} \text{ cm}^3\text{s}^{-1}$, and $Y\mathcal{R} = 0.6 \text{ cm}^{-3}\text{s}^{-1}$. At $t = 0$, the irradiation stops and the annealing period begins.	88
6.5	The 3D finite differences simulation of the JAERI model for various combinations of the input parameters $Y\mathcal{R}$, k_1 , and k_2 . In each plot, two of the parameters are kept constant, and the third is varied over some range. The diffusion coefficient is $D = 10^{-8} \text{ cm}^2\text{s}^{-1}$ in all cases.	89
6.6	Numerical solutions to Eq. 6.26 for various combinations of values for the parameters $E \equiv \frac{c_1 l^2}{D}$ and $F \equiv c_2 C_0$. The parameter E is expressed through its ratio to F . The normalized reaction rate R/R_0 is shown for the entire normalized length λ . For the code used see Ref. [20].	94
6.7	The solution to the 2D PDE for the normalized concentration and reaction rate at steady state for a scintillator that is $1 \text{ cm} \times 1 \text{ cm} \times 5 \text{ cm}$. For the code used see Ref. [20].	96
6.8	[Left] One of the irradiated scintillator samples with a visible refractive index change boundary 15 days after the irradiation end. Irradiation was performed using ^{60}Co at NIST to a total dose of 70 kGy at a dose rate of 460 Gy/h. [Right] The processed lightness channel of a scintillator sample. The gradient of the profile is shown in yellow color, the range used for the profile is defined by red dashed horizontal lines, and the peaks are identified with red circles.	101
6.9	The setup for measurements of the index of refraction using a Nikon D7000 digital camera, an MPositioning precision stage with a sample adjacent to a Boli Optics $10 \times 10 \text{ mm}/100 \times 100$ reticle, a Thorlabs 20° circle pattern diffuser, and a 470 nm LED source.	103
6.10	A schematic showing the configurations for measuring the refractive indices in samples with two regions. The index of the inner region n_{in} is measured using the configuration shown at the top, in which the light passing through the middle of the sample is used. The index of the outer region n_{out} is measured according to the configuration shown at the bottom, which uses light passing through the periphery of the sample, thus avoiding the inner region. The fact that light traversing the inner region also traverses some of the material in the outer region requires a correction term to the inner region's measured index, as described in the text.	105
6.11	A validation of the refractive index measurement method performed against the Sellmeier equation for two BGO crystal samples. The plots show measurements of the index of refraction versus light wavelength. The red curve is the Sellmeier equation using the first-order Sellmeier coefficients that can be found in the literature. A fit of the data to the first-order Sellmeier equation is shown in black. The 1σ band is shown in gray color around the fit line.	106

6.12	The measured depths of the refractive index change boundaries for irradiated PS and PVT scintillator samples as a function of dose rate. Irradiations at 2.2 Gy/h were done using a ^{137}Cs source, the rest using ^{60}Co . The samples that were irradiated with dose rates lower than 80 Gy/h do not have a visible boundary, indicating the depth is larger than half the sample thickness. For that reason, these samples are represented by lower-pointing arrows at 5 mm whose length indicates the uncertainty of having a boundary so close to the surface that it is impossible to measure or observe. The data above 80 Gy/h are fitted with a function of the form $z = \frac{A}{\sqrt{R}}$. The 1σ bands are also shown around the fit lines.	107
6.13	Measurements of the annealing process of an irradiated scintillator. The data points represent the depth of the colored region. The finite differences simulation of the colored region depth is shown with an orange line. The depth of the refractive index boundary is shown with a dashed black line. A fit of Eq. 6.42 to the annealing data is shown as a gray line. The Eq. 6.42 doesn't explain the data fully since it is derived for thin films.	109
6.14	The refractive indices for unirradiated EJ-200 PS and PVT. The lines represent fits to the first-order Sellmeier equation. The 1σ bands are shown around the fit lines.	110
6.15	Measurements of the refractive index at $\lambda = 470$ nm after irradiation and annealing for EJ-200 PS (left plot) and PVT (right plot) for both the inner (blue) and outer (yellow) regions that are defined by the internal boundary. The average value for each region is shown with a dashed line and the standard deviation with a band around that line. The average of the measurements of the unirradiated samples is shown with a solid black line accompanied by a black-shaded area that represents the uncertainty. . . .	111
7.1	Hidden valley conceptual diagram. For the original version of this diagram, see Ref. [21]. The hidden sector is accessible only through the portal created by the LHC. The states created by the dark shower may decay back to the visible sector.	117
8.1	Feynman diagram for the SUEP process adapted from Ref. [22]. The scalar mediator is produced via gluon-gluon fusion, and then it decays back to standard model particles after creating a dark shower, hadronizing to ϕ dark mesons, and decaying to A' dark photons.	119
8.2	The branching fractions of A' to e^+e^- , $\mu^+\mu^-$, and hadrons as a function of the mass of the dark photon $m_{A'}$. [23]	122
8.3	The SUEP parameter landscape. Figure taken from Ref. [24]. Sensible ranges for m_ϕ and the ratio $\frac{T}{m_\phi}$ can be set using kinematic restrictions and desired behavior arguments.	124
9.1	The scan points chosen for T and m_ϕ . The bounds of the parametrically sensible region are denoted with black lines	132

12.1	Distribution of d_{xy}^μ for 2018 MC simulation. The left plot shows this split by the MC process, and the right plot shows the grouped contributions of each muon source.	148
12.2	CR_{QCD} for Run 2. The ratio between data and MC is also shown. A k -factor has been applied to QCD to normalize the total MC yield to data.	149
12.3	$N - 1$ distribution of d_{xy}^μ of prompt muons for 2018 MC simulation. The left plot shows this split by the MC process, and the right plot shows the grouped contributions of each muon source.	151
12.4	$N - 1$ distribution of the muon isolation for 2018 MC simulation. The left plot shows this split by the MC process, and the right plot shows the grouped contributions of each muon source.	152
12.5	CR_{DY} for Run 2. The ratio between data and MC is also shown. A k -factor has been applied to QCD to normalize the total MC yield to data.	153
12.6	$N - 1$ distributions of S_1 (left) and $m_{\mu^+\mu^-}$ (right) in $SR_{low\ T}^{tight}$ for 2018 MC simulation. The chosen cuts are indicated with black lines and red arrows on the plots.	157
12.7	$SR_{low\ T}$ regions for Run 2 MC. Left is $SR_{low\ T}^{loose}$ and right is $SR_{low\ T}^{tight}$. The discovery bin is annotated with a separate red line and a pointing arrow.	158
12.8	$N - 1$ distributions of muon isolation (left) and IP_{3D}^μ (right) in $SR_{high\ T}^{tight}$ for 2018 MC simulation. The chosen cuts are indicated with black lines and red arrows on the plots.	159
12.9	$SR_{high\ T}$ regions for Run 2 MC. Left is $SR_{high\ T}^{loose}$ and right is $SR_{high\ T}^{tight}$. The discovery bin is annotated with a separate red line and a pointing arrow.	160
12.10	$N - 1$ plots for the IP_{3D}^μ distributions grouped by the muon sources for 2018 MC simulation. The left plot is for $SR_{low\ T}^{tight}$ and the right plot is for $SR_{high\ T}^{tight}$	161
12.11	VR regions for Run 2. The left plot is VR_{loose} and the right plot is VR_{tight} . The ratio between data and MC, along with the pull plot, is also shown below each plot.	163
13.1	The normalized to unity densities for the n_{muon} distributions for $SR_{high\ T}^{loose}$ and $SR_{high\ T}^{tight}$ for QCD MC (left) and DY MC (right). The tight over loose ratios are also plotted below each histogram.	170
13.2	The normalized to unity densities for the n_{muon} distributions for $SR_{low\ T}^{loose}$ and $SR_{low\ T}^{tight}$ for QCD MC (left) and DY MC (right). The tight over loose ratios are also plotted below each histogram.	171
13.3	Extrapolation fit for QCD MC in $SR_{high\ T}$. Left is $SR_{high\ T}^{loose}$ and right is $SR_{high\ T}^{tight}$. The MC/fit ratio and the pull plots are also shown below.	173
13.4	Extrapolation fit for DY MC in $SR_{high\ T}$. Left is $SR_{high\ T}^{loose}$ and right is $SR_{high\ T}^{tight}$. The MC/fit ratio and the pull plots are also shown below.	173

13.5	Extrapolation fit for QCD MC in $SR_{low\ T}$. Left is $SR_{low\ T}^{loose}$ and right is $SR_{low\ T}^{tight}$. The MC/fit ratio and the pull plots are also shown below.	174
13.6	Extrapolation fit for DY MC in $SR_{low\ T}$. Left is $SR_{low\ T}^{loose}$ and right is $SR_{low\ T}^{tight}$. The MC/fit ratio and the pull plots are also shown below.	174
13.7	Overlays of the distributions of the loose, tight, and extrapolated tight regions for QCD MC. Left is $SR_{low\ T}$ and right is $SR_{high\ T}$	175
13.8	Overlays of the distributions of the loose, tight, and extrapolated tight regions for DY MC. Left is $SR_{low\ T}$ and right is $SR_{high\ T}$	175
13.9	$SR_{low\ T}$ regions for Run 2, including the extrapolated distributions for QCD and DY MC. Left is $SR_{low\ T}^{loose}$ and right is $SR_{low\ T}^{tight}$. The discovery bin is annotated with a separate red line and a pointing arrow.	176
13.10	$SR_{high\ T}$ regions for Run 2, including the extrapolated distributions for QCD and DY MC. Left is $SR_{high\ T}^{loose}$ and right is $SR_{high\ T}^{tight}$. The discovery bin is annotated with a separate red line and a pointing arrow.	177
13.11	Extrapolation fit for QCD MC in VR. Left is VR_{loose} and right is VR_{tight} . The MC/fit ratio and the pull plots are also shown below. There is closure between the fit and the MC.	177
13.12	Extrapolation fit for data in VR. Left is VR_{loose} and right is VR_{tight} . The data/fit ratio and the pull plots are also shown below. There is closure between the fit and the data.	178
13.13	Overlays of the distributions of the loose, tight, and extrapolated tight regions of the VR. Left is QCD MC and right is data.	179
13.14	VR regions for Run 2 with extrapolated QCD MC. The left plot is VR_{loose} and the right plot is VR_{tight} . The ratio between data and MC, along with the pull plot, is also shown below each plot. There is good closure between the fitted MC and the data.	180
15.1	The prefit n_{muon} distributions for all regions for Run 2.	190
15.2	The postfit n_{muon} distributions for the CRs and blinded $SR_{high\ T}$ for the Run 2-only fit. The MC matches very well the data in the bins with many entries, because they have the statistical power to constrain the fit.	193
15.3	Impact plot with top 30 nuisances for Run 2 fit with Asimov dataset and signal strength set to $r = 0$	195
15.4	Impact plot with top 30 nuisances for Run 2 fit with Asimov dataset and signal strength set to $r = 1$	196
15.5	Impact plot for fit with data and blinded SRs. Fit is only for Run 2. The data yields have been set to 0 in the SRs.	197
15.6	Expected 95% upper limits for the SUEP production cross section at $\sqrt{s} = 13$ TeV using the asymptotic approximation method as a function of the scalar mediator's mass, m_S , with $m_\phi = 4$ GeV and $T = 4$ GeV (left) and $m_\phi = 8$ GeV and $T = 32$ GeV (right) both for hadronically(red) and leptonically(blue) dominated decay scenarios.	198

15.7	Expected 95% upper limits for the signal strength parameter, r , using the asymptotic approximation method as a function of the scalar mediator's mass, m_S , with $m_\phi = 4$ GeV and $T = 4$ GeV (left) and $m_\phi = 8$ GeV and $T = 32$ GeV (right) both for hadronically(red) and leptonically(blue) dominated decay scenarios.	199
B.1	$N - 1$ plot for CR_{QCD} muon dxy.	210
B.2	$N - 1$ plot for CR_{DY} dimuon mass.	211
B.3	$N - 1$ plot for CR_{DY} cand muon pt.	212
B.4	$N - 1$ plot for CR_{DY} cand muon iso.	212
B.5	$N - 1$ plot for CR_{DY} cand muon ip3d.	213
B.6	$N - 1$ plot for CR_{DY} cand muon dxy.	213
B.7	$N - 1$ plot for CR_{DY} cand muon dz.	214
B.8	$N - 1$ plot for CR_{DY} muon iso.	214
B.9	$N - 1$ plot for CR_{DY} muon ip3d.	215
B.10	$N - 1$ plot for CR_{DY} muon dxy.	215
B.11	$N - 1$ plot for CR_{DY} muon dz.	216
B.12	$N - 1$ plot for $SR_{low T}^{tight}$ muon pt.	217
B.13	$N - 1$ plot for $SR_{low T}^{loose}$ muon pt.	218
B.14	$N - 1$ plot for $SR_{low T}^{tight}$ muon ip3d.	218
B.15	$N - 1$ plot for $SR_{low T}^{loose}$ muon ip3d.	219
B.16	$N - 1$ plot for $SR_{low T}^{tight}$ dimuon mass.	219
B.17	$N - 1$ plot for $SR_{low T}^{loose}$ dimuon mass.	220
B.18	$N - 1$ plot for $SR_{low T}^{tight}$ sph1.	220
B.19	$N - 1$ plot for $SR_{low T}^{loose}$ sph1.	221
B.20	$N - 1$ plot for $SR_{high T}^{tight}$ muon ip3d.	222
B.21	$N - 1$ plot for $SR_{high T}^{loose}$ muon ip3d.	223
B.22	$N - 1$ plot for $SR_{high T}^{tight}$ muon iso.	223
B.23	$N - 1$ plot for $SR_{high T}^{loose}$ muon iso.	224
B.24	$N - 1$ plot for $SR_{high T}^{tight}$ muon neutral iso.	224
B.25	$N - 1$ plot for $SR_{high T}^{loose}$ muon neutral iso.	225
B.26	$N - 1$ plot for $SR_{high T}^{tight}$ dimuon mass.	225
B.27	$N - 1$ plot for $SR_{high T}^{loose}$ dimuon mass.	226
D.1	1D limit for $m_\phi = 1$ GeV, $T = 0.25$ GeV (both decay modes) as a function of m_S	235
D.2	1D limit for $m_\phi = 1.4$ GeV, $T = 0.35$ GeV (both decay modes) as a function of m_S	236
D.3	1D limit for $m_\phi = 4$ GeV, $T = 1$ GeV (both decay modes) as a function of m_S	236
D.4	1D limit for $m_\phi = 1.4$ GeV, $T = 1.4$ GeV (both decay modes) as a function of m_S	237

D.5	1D limit for $m_\phi = 2 \text{ GeV}$, $T = 2 \text{ GeV}$ (both decay modes) as a function of m_S .	237
D.6	1D limit for $m_\phi = 8 \text{ GeV}$, $T = 2 \text{ GeV}$ (both decay modes) as a function of m_S .	238
D.7	1D limit for $m_\phi = 1.4 \text{ GeV}$, $T = 2.8 \text{ GeV}$ (both decay modes) as a function of m_S .	238
D.8	1D limit for $m_\phi = 6 \text{ GeV}$, $T = 3 \text{ GeV}$ (both decay modes) as a function of m_S .	239
D.9	1D limit for $m_\phi = 2 \text{ GeV}$, $T = 4 \text{ GeV}$ (both decay modes) as a function of m_S .	239
D.10	1D limit for $m_\phi = 4 \text{ GeV}$, $T = 4 \text{ GeV}$ (both decay modes) as a function of m_S .	240
D.11	1D limit for $m_\phi = 8 \text{ GeV}$, $T = 4 \text{ GeV}$ (both decay modes) as a function of m_S .	240
D.12	1D limit for $m_\phi = 1.4 \text{ GeV}$, $T = 5.6 \text{ GeV}$ (both decay modes) as a function of m_S .	241
D.13	1D limit for $m_\phi = 6 \text{ GeV}$, $T = 6 \text{ GeV}$ (both decay modes) as a function of m_S .	241
D.14	1D limit for $m_\phi = 2 \text{ GeV}$, $T = 8 \text{ GeV}$ (both decay modes) as a function of m_S .	242
D.15	1D limit for $m_\phi = 4 \text{ GeV}$, $T = 8 \text{ GeV}$ (both decay modes) as a function of m_S .	242
D.16	1D limit for $m_\phi = 8 \text{ GeV}$, $T = 8 \text{ GeV}$ (both decay modes) as a function of m_S .	243
D.17	1D limit for $m_\phi = 6 \text{ GeV}$, $T = 12 \text{ GeV}$ (both decay modes) as a function of m_S .	243
D.18	1D limit for $m_\phi = 4 \text{ GeV}$, $T = 16 \text{ GeV}$ (both decay modes) as a function of m_S .	244
D.19	1D limit for $m_\phi = 8 \text{ GeV}$, $T = 16 \text{ GeV}$ (both decay modes) as a function of m_S .	244
D.20	1D limit for $m_\phi = 6 \text{ GeV}$, $T = 24 \text{ GeV}$ (both decay modes) as a function of m_S .	245
D.21	1D limit for $m_\phi = 8 \text{ GeV}$, $T = 32 \text{ GeV}$ (both decay modes) as a function of m_S .	245

List of Abbreviations

ADC	Analog-to-digital converter
AK	anti- k_t
APD	Avalanche photodiode
BCM1F	Beam conditions monitor
BIB	Beam-induced backgrounds
BMTF	Barrel muon track finder
BPIX	Barrel Pixel
BRIL	Beam radiation instrumentation and luminosity system
BRILDAQ	BRIL data acquisition system
BX	Bunch crossing
CERN	European Organization for Nuclear Research
CMS	Compact Muon Solenoid
CMSSW	CMS software
CR	Control Region
CSC	Cathode strip chamber
CTF	Combinatorial track finder
DAC	Digital-to-analog converter
DT	Drift tube
EB	ECAL barrel
EE	ECAL endcap
EMTF	Endcap muon track finder
EW	Electroweak
FPIX	Forward Pixel
HB	HCAL barrel
HE	HCAL endcap
HF	HCAL forward
HO	HCAL outer
HL-LHC	High Luminosity LHC
HLT	High Level Trigger
HPL	High-pressure laminate

GEM	Gas electron multiplier
L1	Level 1
LEP	Large Electron Positron (collider)
LHC	Large Hadron Collider
LINAC	Linear Accelerator
LS	Luminosity section
NB	Luminosity nibbles
OMTF	Overlap muon track finder
OOT	out-of-time (pileup)
PF	Particle flow
PLT	Pixel luminosity telescope
PMT	Photomultiplier tube
PS	Proton Synchrotron
PSB	Proton Synchrotron Booster
PU	Pileup
QCD	Quantum Chromodynamics
QFT	Quantum Field Theory
ROC	Readout chip
RPC	Resistive plate chamber
TCDS	Time and clock distribution system
TEC	Tracker endcaps
TIB	Tracker inner barrel
TID	Tracker inner disks
TOB	Tracker outer barrel
TOD	Tracker outer disks
TP	Trigger primitive
TriDAS	Trigger and data acquisition system
TTS	Trigger throttling system
SM	Standard Model
SPS	Super Proton Synchrotron
SR	Signal Region
SST	Silicon Strip Tracker
SUEP	Soft Unclustered Energy Patterns
VEV	Vacuum expectation value

VPT Vacuum phototriode

USC Underground service cavern

UXC Underground experimental cavern

Chapter 1: Introduction

Emerging in the 1920s with the quantum revolution and expanding rapidly during the second half of the 20th century, the study of elementary particles has transformed our understanding of the most fundamental building blocks of nature. A sustained stream of discoveries has revealed a wealth of subatomic particles and is shedding light on their behavior and interactions.

The field of particle physics was effectively inaugurated by the discovery of the electron in the late 19th century by Thomson et al. and the discovery of the nucleus by Rutherford in 1918. The pioneering work of Bohr, Heisenberg, Schrödinger, and others led to the development of quantum mechanics by the early 1930s, followed by the introduction of quantum field theory (QFT) after the seminal work of Dirac. Modern particle physics owes much of its existence to Feynman, who democratized QFT calculations by inventing the Feynman rules and diagrams. Additionally, particle acceleration technology has evolved significantly since its infancy in the 1950s, contributing a long list of discoveries during the last 50 years, which culminated in the discovery of the Higgs boson in 2012 [25, 26] and the completion of the cornerstone of particle physics, the Standard Model (SM).

Despite the resounding success of the SM in incorporating all known particles, there

is overwhelming evidence that it is not the ultimate description of reality. A series of observations and discoveries, with the most notable being the discovery of neutrino oscillations [27] and the need for dark matter to explain astronomical and cosmological observations, have highlighted the need for Beyond the Standard Model (BSM) physics. In this frontier, a large number of novel theories have been proposed, aspiring to supersede the SM, including but not limited to Grand Unified Theories (GUTs), supersymmetry (SUSY), extra dimensions, sterile neutrinos, and axions, to name a few.

Of special interest to this thesis are the hidden valley or dark sector models, which attempt to extend the SM by adding a new confining gauge group [28]. This family of BSM models is capable of producing some very unique signatures at the LHC collisions, one of which is the Soft Unclustered Energy Patterns (SUEP). These are states with very large multiplicities of low-energy particles that are distributed uniformly in the detector. A search for SUEP final states with muons using data from LHC collisions collected with the CMS experiment is presented in this thesis.

Searches for new physics require large amounts of high-quality collision data. Ensuring the smooth and continuous operation of particle detectors is therefore deemed critical. One challenge in keeping particle detectors operational is the ionizing radiation that is created by the particle collisions. In fact, the quest for higher luminosities leads inevitably to larger exposures to radiation. Developing our understanding of the underlying mechanisms that cause diminished particle detection efficiency after radiation exposure is a stepping stone to realizing more resilient experiments. A significant part of this thesis is dedicated to studies of radiation damage in plastic scintillator, which is one of the most ubiquitous materials used for particle detection.

This dissertation is divided into three parts. Part I contains two chapters that introduce fundamental concepts of particle physics. Chapter 2 provides a short introduction to the Standard Model of particle physics, and Chapter 3 describes the Large Hadron Collider (LHC) and the Compact Muon Solenoid (CMS) experiment in detail. Part II consists of three chapters and examines radiation damage in plastic scintillators. Chapter 4 introduces plastic scintillators and their susceptibility to radiation. Chapter 5 presents studies of the effect of dose rate on radiation damage in plastic scintillators. Chapter 6 investigates the effects of radiation and the role of oxygen on the optical properties of plastic scintillators, with emphasis on the refractive index.

Part III includes nine chapters that describe a search for Soft Unclustered Energy Patterns (SUEP) with data collected at the LHC with the CMS experiment. Chapter 7 motivates searches for dark sector models for Beyond Standard Model physics, and briefly introduces the concept of the SUEP. Chapter 8 describes in detail the SUEP and the benchmark model that is used to generate SUEP Monte Carlo (MC) events. Chapter 9 specifies the data and MC samples used. Chapter 10 presents the objects used in the analysis and their cleaning selections. Chapter 11 explains the analysis strategy and argues for the chosen background estimation method. Chapter 12 shows the event selection criteria and presents the analysis regions. Chapter 13 builds and validates the background estimation method. Chapter 14 offers an overview of the systematic uncertainties considered in the analysis. Chapter 15 presents the final results, including the expected 95% CL upper limits for the cross section of the SUEP benchmark model. Finally, Chapter 16 summarizes the results for Parts II and III, discusses the impact of this work, and explores potential relevant improvements and new directions.

Part I

Introduction to the Standard Model and CMS

Chapter 2: The Standard Model of particle physics

2.1 Introduction

The fundamental subatomic particles are categorized into two families based on their spin values. Particles with half-integer spin values follow the Fermi-Dirac statistics and are named fermions. All fundamental fermions have spin $\frac{1}{2}$. The fermions are further divided into leptons and quarks based on their interactions. The family of leptons includes the electron (e), the muon (μ), the tau (τ), and their corresponding neutrinos (ν_e , ν_μ , and ν_τ). There are six quarks: up, down, strange, charm, bottom, and top. Ordinary matter is composed of fermions. For example, atomic nuclei are composed of hadrons, which are bound quark states, and atoms are formed by combining atomic nuclei with electrons.

Particles with integer spin values follow the Bose-Einstein statistics and are named bosons. These include the photon, γ , the W^\pm and Z bosons, and the gluon, g . All these bosons, which are also called vector bosons, have spin 1. Fermions interact by exchanging bosons, which act as force carriers, allowing quantum matter to "feel" forces. There are three fundamental forces at the quantum level: the electromagnetic force, mediated by photons; the weak force, mediated by the W^\pm and Z bosons; and the strong force, mediated by the gluons.

There is one last special particle, named the Higgs boson, which is a scalar boson, meaning it has spin 0. It is the only known fundamental particle with spin 0, and it plays a vital role in explaining the masses of the vector bosons by introducing the concept of spontaneous symmetry breaking. All fundamental particles are depicted in Figure 2.1.

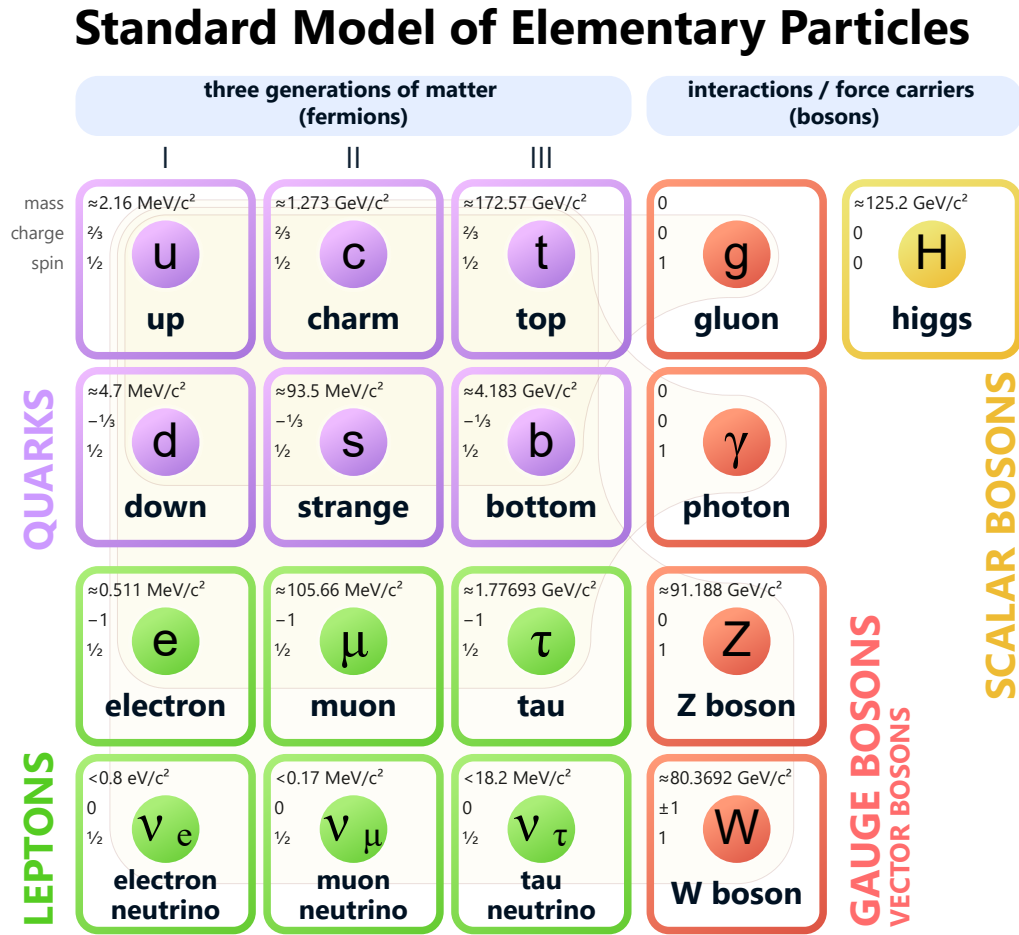


Figure 2.1: The Standard Model of Particle Physics. Taken from [1].

2.2 The Standard Model of Particle Physics

The Standard Model (SM) of particle physics, one of the greatest scientific successes of the 20th century, provides a widely accepted and mathematically consistent description

of all elementary particles and their interactions.

Mathematically, the Standard Model is a renormalizable gauge quantum field theory that describes all fundamental particles as excited states of their underlying quantum fields. It is built around the fundamental concept of local gauge invariance

$$\psi \rightarrow e^{i\alpha(x)}\psi, \quad (2.1)$$

where ψ is a quantum field and $\alpha(x)$ is a function of spacetime. Local gauge invariance implies that the physics (i.e., the Lagrangian) is invariant under such transformations. These invariances are called symmetries of the model.

The SM follows a local $SU(3)_c \times SU(2)_L \times U(1)_Y$ gauge symmetry, where Y represents the weak hypercharge, L denotes left-handedness, and c denotes color charge. The electromagnetic and weak forces, in particular, can be described in a unified manner by the $SU(2)_L \times U(1)_Y$ symmetry group, known as the electroweak (EW) symmetry.

2.2.1 Quantum Electrodynamics

Considering a fermion field, it is described by the Dirac Lagrangian

$$\mathcal{L} = \bar{\psi}(i\gamma^\mu\partial_\mu - m)\psi, \quad (2.2)$$

where ψ is a four-component bispinor field, γ^μ are the Dirac matrices that are the generators of the Dirac algebra, $\bar{\psi}$ is the adjoint bispinor $\psi^\dagger\gamma^0$, and m is the mass of the fermion. If we consider the spacetime field of the electromagnetic (EM) force, $A_\mu(x)$, then we can

easily see using the covariant derivative

$$D_\mu \psi = (\partial_\mu + ieA_\mu(x))\psi \quad (2.3)$$

that ψ is invariant under the transformation

$$D_\mu \psi \rightarrow e^{i\alpha(x)} D_\mu \psi. \quad (2.4)$$

The quantity

$$F_{\mu\nu} = \partial_\mu A_\nu - \partial_\nu A_\mu \quad (2.5)$$

is also invariant. This quantity can be used to defined the kinetic term $-\frac{1}{4}F_{\mu\nu}F^{\mu\nu}$ of the EM field. The Lagrangian that describes fermions in the presence of an EM field is

$$\mathcal{L} = -\frac{1}{4}F_{\mu\nu}F^{\mu\nu} + \bar{\psi}(i\gamma^\mu D_\mu - m)\psi. \quad (2.6)$$

This Lagrangian is called the Quantum Electrodynamics (QED) Lagrangian and is invariant under local $U(1)_{EM}$ gauge transformations. It describes well the interactions between electrons, positrons, and photons, and it involves only one quantum number, the electric charge, Q .

2.2.2 Electroweak Theory

Adding the weak interaction to the description involves the introduction of some new concepts.

First, the chirality projection operators are defined as

$$P_{L,R} = \frac{1 \mp \gamma^5}{2}, \quad (2.7)$$

where $\gamma^5 \equiv i\gamma^0\gamma^1\gamma^2\gamma^3$. The P_L and P_R operators can be used to decompose spinors into their left and right-handed components.

According to the electroweak (EW) theory, two quantum numbers are required to describe the EW symmetry, $SU(2)_L \times U(1)_Y$. The first quantum number, which is associated with the $SU(2)$ subgroup, is the weak isospin, T , and takes half-integer values for particles that interact with the W^\pm bosons. This quantum number is accompanied by its component, T_3 , along the 3-axis.

In EW theory, the three generations of left-handed leptons are grouped in doublets

$$\begin{pmatrix} \nu_e \\ e^- \end{pmatrix}_L, \quad \begin{pmatrix} \nu_\mu \\ \mu^- \end{pmatrix}_L, \quad \begin{pmatrix} \nu_\tau \\ \tau^- \end{pmatrix}_L, \quad (2.8)$$

where all the left-handed neutrinos (top rows) have $T_3 = \frac{1}{2}$, while the left-handed e, μ, τ have $T_3 = -\frac{1}{2}$

Similarly, the three generations of left-handed quarks are also grouped in doublets

$$\begin{pmatrix} u \\ d \end{pmatrix}_L, \quad \begin{pmatrix} c \\ s \end{pmatrix}_L, \quad \begin{pmatrix} t \\ b \end{pmatrix}_L, \quad (2.9)$$

All right-handed fermions have zero weak isospin and, therefore, are represented

by singlet states. For the right-handed leptons:

$$e_R^-, \quad \nu_{e,R}, \quad \mu_R^-, \quad \nu_{\mu,R}, \quad \tau_R^-, \quad \nu_{\tau,R}, \quad (2.10)$$

and for the right-handed quarks:

$$u_R, \quad d_R, \quad c_R, \quad s_R, \quad t_R, \quad b_R. \quad (2.11)$$

The second quantum number is called weak hypercharge, Y , and it is defined by the Gell-Mann–Nishijima relation

$$Q = \left(T_3 + \frac{Y}{2} \right). \quad (2.12)$$

This quantum number is associated with the $U(1)$ subgroup.

There are two covariant derivatives defined, separately for the doublets and the singlets:

$$\text{doublet states:} \quad D_\mu = \partial_\mu + ig\sigma_\alpha W_\mu^\alpha + ig'\frac{Y}{2}B_\mu, \quad (2.13)$$

$$\text{singlet states:} \quad D_\mu = \partial_\mu + ig'\frac{Y}{2}B_\mu, \quad (2.14)$$

where the gauge field B_μ is associated with the $U(1)$ symmetry, the W_μ^α are the components of the gauge field associated with the $SU(2)$ symmetry, σ_α are the group generators, and g and g' are coupling constants.

The Lagrangian for the fermion terms can be constructed like the one in Eq. 2.6. The

field kinetic term of the Lagrangian is

$$\mathcal{L}_{\text{field kin.}} = -\frac{1}{4}B^{\mu\nu}B_{\mu\nu} - \frac{1}{4}W^{\alpha,\mu\nu}W_{\mu\nu}^{\alpha} \quad (2.15)$$

Therefore, the EW theory involves four massless boson fields: W_1 , W_2 , W_3 , and B . The only missing component is a way to generate the massive W^{\pm} , Z bosons, and the massless photon.

2.2.3 The Brout-Englert-Higgs mechanism

A SU(2) doublet of complex scalar fields is introduced

$$\Phi = \begin{pmatrix} \phi^+ \\ \phi^0 \end{pmatrix}, \quad \phi^+, \phi^0 \in \mathbb{C}. \quad (2.16)$$

The Higgs doublet has weak isospin $T = \frac{1}{2}$. The 3-axis component, T_3 , is $\frac{1}{2}$ for ϕ^+ and $-\frac{1}{2}$ for ϕ^0 . Also, ϕ^+ has $Q = +1$ and ϕ^0 has $Q = 0$. Therefore, the Higgs doublet has weak hypercharge $Y = 1$.

The Lagrangian for the scalar field is

$$\mathcal{L}_{\text{scalar}} = (D^{\mu}\Phi)^{\dagger}(D_{\mu}\Phi) - V(\Phi), \quad (2.17)$$

where D_{μ} is the covariant derivative for the doublet from Eq. 2.14 and $V(\Phi)$ is the

potential of the scalar field. It turns out that the Higgs potential is a good choice

$$V(\Phi) = -\mu^2 \Phi^\dagger \Phi + \lambda (\Phi^\dagger \Phi)^2, \quad (2.18)$$

where λ and μ are arbitrary parameters, with $\lambda > 0$ to have a potential minimum.

The minimum potential energy is called vacuum expectation value (VEV) and it is given by

$$\langle VEV \rangle = |\phi|^2 = \frac{\mu^2}{2\lambda}. \quad (2.19)$$

This minimum is not unique but exists along a circle in the (ϕ, ϕ^*) plane. This implies that, to obtain the vacuum state, we are forced to pick a place along the ring, which amounts to breaking a symmetry. This is commonly referred to as spontaneous symmetry breaking [29, 30], and according to Goldstone's theorem, it gives rise to massless scalar fields that are named Goldstone bosons [31]. The shape of the potential along with the minimum can be seen in Figure 2.2. The symmetry breaking is demonstrated by points A and B. Point B breaks the symmetry of the circle of minimum values.

Eventually, the Higgs doublet at the vacuum is

$$\Phi(x) = \frac{1}{\sqrt{2}} \begin{pmatrix} 0 \\ v + h(x) \end{pmatrix}, \quad (2.20)$$

where $v = \sqrt{2}\langle VEV \rangle$, and $h(x)$ a perturbation around the minimum. Substituting this into the Higgs Lagrangian, in Eq. 2.17, yields mixing terms. These can be removed by

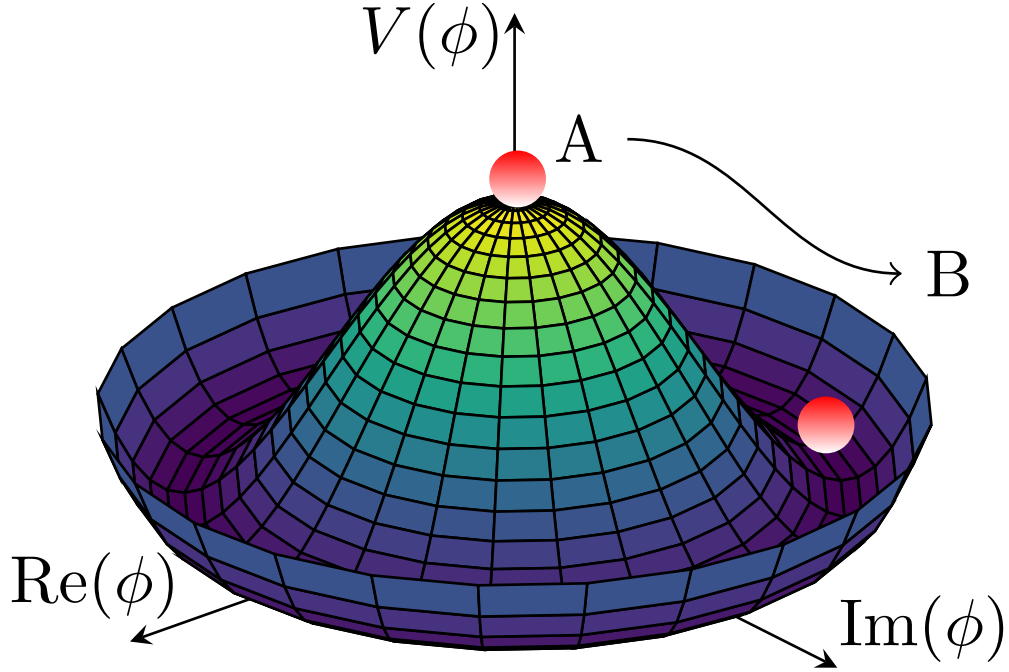


Figure 2.2: The Mexican hat Higgs potential. Code was fetched from [2].

introducing the rotation

$$\begin{pmatrix} W_\mu^3 \\ B_\mu \end{pmatrix} = \begin{pmatrix} \cos \theta_W & \sin \theta_W \\ -\sin \theta_W & \cos \theta_W \end{pmatrix} \begin{pmatrix} Z_\mu \\ A_\mu \end{pmatrix}, \quad (2.21)$$

where θ_W is called the weak mixing angle with

$$\tan \theta_W = \frac{g'}{g}. \quad (2.22)$$

Eventually, the fields for W^\pm , Z , and the photon are given by the following combi-

nations

$$W_\mu^\pm = \frac{1}{\sqrt{2}}(W_\mu^1 \mp iW_\mu^2), \quad (2.23)$$

$$Z_\mu = \frac{1}{\sqrt{g^2 + g'^2}}(gW_\mu^3 - g'B_\mu), \quad (2.24)$$

$$A_\mu = \frac{1}{\sqrt{g^2 + g'^2}}(gW_\mu^3 + g'B_\mu), \quad (2.25)$$

with the masses of the W^\pm , Z , and the photon defined using

$$m_W = \frac{1}{2}vg, \quad (2.26)$$

$$m_Z = \frac{1}{2}v\sqrt{g^2 + g'^2} = \frac{m_W}{\cos \theta_W}, \quad (2.27)$$

$$m_\gamma = 0. \quad (2.28)$$

The lepton masses can be explained by adding Yukawa couplings, y_i , between them and the Higgs field. Since only e , μ , τ have mass, the terms in the Lagrangian look like $-y_i \bar{L}_i \Phi e_R^i$, and the lepton masses are given by $m_i = \frac{y_i v}{\sqrt{2}}$.

For the quarks, both up and down families (here, up also includes the charm and top, and down includes the strange and bottom) have mass. However, up and down have opposite T_3 values. Therefore, the Yukawa terms are

$$\mathcal{L}_{q, \text{Yuk.}} = -Y_{ij}^d \bar{Q}^i \Phi D_R^j - Y_{ij}^u \bar{Q}^i \tilde{\Phi} U_R^j + h.c., \quad (2.29)$$

where Y_{ij}^d and Y_{ij}^u are the Yukawa couplings for down and up, Q is the quark doublet, $\tilde{\Phi} = i\tau_2 \Phi^*$ is the conjugate Higgs doublet, and D_R and U_R are the down and up right-

handed singlets. Eventually, the terms for the couplings between up and down quarks and the W bosons in the Lagrangian involve mixing parameters V_{ij} . These parameters form a 3×3 matrix called the Cabibbo-Kobayashi-Maskawa (CKM) matrix. The diagonal terms give the couplings between up and down quarks of the same generation. The off-diagonal terms are quark flavor-violating terms, and their values have been measured experimentally to be non-zero [32].

2.2.4 Quantum Chromodynamics

The strong force is an interaction that takes place between quarks, and it is mediated by gluons. The quarks carry a color charge that is independent of their electric charge. The color charge has three types: red (r), green(g), and blue(b). Like QED and EW, the strong interaction is described by local gauge symmetry, which in this case follows the SU(3) group. This group has 8 generators, given by matrices T^a . The QCD Lagrangian is

$$\mathcal{L}_{\text{QCD}} = \bar{\psi}_i (i\gamma^\mu (D_\mu)_{ij} - m\delta_{ij}) \psi_j - \frac{1}{4} G_{\mu\nu}^a G_a^{\mu\nu}, \quad (2.30)$$

where ψ_i are the quark fields, and $G_{\mu\nu}^a$ is the gluon field strength tensor. The $G_{\mu\nu}^a$ is defined as

$$G_{\mu\nu}^a = \partial_\mu \mathcal{A}_\nu^a - \partial_\nu \mathcal{A}_\mu^a + g_s f^{abc} \mathcal{A}_\mu^b \mathcal{A}_\nu^c, \quad (2.31)$$

where \mathcal{A}_μ^a are the gluon fields, g_s is the strong force coupling constant, and f^{abc} are the structure constants of SU(3). The last term is the kinetic term for the glue field. The

covariant derivative of QCD is

$$(D_\mu)_{ij} = \partial_\mu \delta_{ij} - ig_s (T_a)_{ij} A_\mu^a, \quad (2.32)$$

where T_a are the 8 generators of the SU(3) group.

According to QCD, there is asymptotic freedom, which means that the interaction strength diminishes with increased energy scales. Another QCD property is confinement, according to which isolating colored states, like quarks, is impossible. Attempting to separate two quarks will give them sufficient energy to create a quark-antiquark pair and keep them confined. Therefore, quarks are typically bound inside hadrons, like protons, which have a uud structure. In fact, the three structural quarks are called the valence quarks. These are embedded in a soup of gluons and other quarks, called sea quarks. All these particles are collectively called partons. For the scattering between hadrons A and B , the QCD factorization theorem gives the cross section [33]

$$\sigma(AB \rightarrow FX) = \Sigma_{a,b} \int dx_1 dx_2 f(a, x_1, Q^2) f(b, x_2, Q^2) \hat{\sigma}(ab \rightarrow F), \quad (2.33)$$

where F is the produced final state, X is the remnant of the scattering, a and b are the partons, x_1 and x_2 are the momentum fractions of the partons, and Q^2 is the energy scale of the process. The functions $f(\text{parton}, x, Q^2)$ are the parton distribution functions, and they are described by the DGLAP equations [34].

2.2.5 Shortcomings of the Standard Model

Despite its great success, the Standard Model is not a theory of everything since a number of open problems and questions exist.

From the theoretical standpoint, the absence of a description for gravity at the quantum level, the Yang-Mills mass gap problem affecting the mathematical consistency of the theory, the matter-antimatter asymmetry, the hierarchy problem, the reliance on parameter fine-tuning through experiments, and the strong CP problem all point to a lack of understanding of the underlying physics.

However, the most striking problems for the SM originate from experimental results. According to the SM, neutrinos are not supposed to oscillate between the different lepton flavors. Neutrino oscillations have been observed experimentally [27], and the most reasonable explanation is that neutrinos are massive. Accommodating masses for the neutrinos most likely involves extensions of the SM and new physics.

Cosmological observations appear to agree with the Λ CDM model [35], which predicts that about 26% of the universe should be cold dark matter and about 69% should be dark energy, leaving only 5% to ordinary matter. The vacuum energy predicted by the SM is many orders of magnitude smaller than the observed density of dark energy. Additionally, there is significant evidence that dark matter is composed of particles that do not interact with light and are not included in the SM [36].

The first evidence for dark matter originated from observations of gravitational anomalies in the Coma Cluster of galaxies [37]. The observation of anomalous galaxy rotation curves [38] established the idea that there are galaxy halos composed of dark

matter. Such curves are shown in Figure 2.3 along with a fit and curves for the components, including the dark halo [3]. Additional evidence has piled up since then, including gravitational lensing results, such as that of the Bullet Cluster [39], and the Cosmic Microwave Background anisotropies [40], which are explained well by the existence of cold dark matter of particle nature.

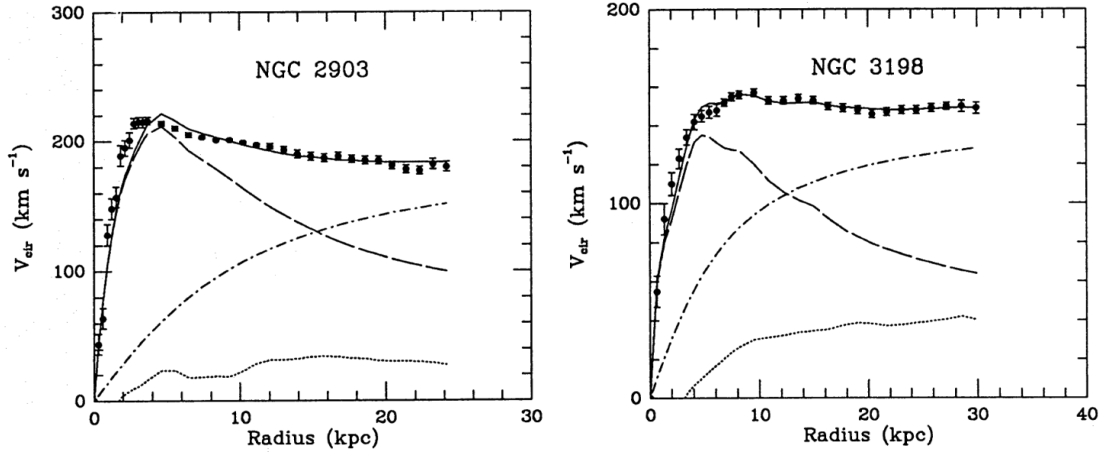


Figure 2.3: Rotational curves of galaxies. The solid lines are three-parameter fits, dashed curves are for visible components, dotted curves are for gas components, and the dash-dot curves are for the dark halo. Figure taken from [3].

All these open questions corroborate the hypothesis that there is physics beyond the Standard Model (BSM). A large number of BSM theories have been proposed to date, including supersymmetry, extra dimensions, leptoquarks, sterile neutrinos, axions, and grand unified theories. No evidence supports any BSM theories over the SM as of the time of writing this thesis. A new proposed extension of the SM, based on a class of BSM theories, called dark sectors, is introduced in Chapters 7 and 8. Part III of this dissertation is dedicated to searching for this BSM extension through a newly predicted signature named Soft Unclustered Energy Patterns (SUEP) using collision data from the Large Hadron Collider at CERN.

Chapter 3: The Compact Muon Solenoid experiment

Since beginning its operation in 2010, the Large Hadron Collider (LHC) has repeatedly proven to be an invaluable tool in the quest to explore the fundamental blocks of nature. By offering access to center-of-mass energies of 13 TeV (and more recently 13.6 TeV) and producing many orders of magnitude more collision data compared to all previous endeavors, it has significantly contributed to our understanding of the laws that govern particle physics. At the epicenters of the particle collisions, the interaction points, four particle physics experiments are housed, out of which two, ATLAS and CMS, are general-purpose particle physics experiments managed by major international collaborations. A significant part of the work that is presented in this dissertation was performed as part of the CMS experiment using data from collisions provided by the LHC. Section 3.1 gives a brief introduction to the LHC and Section 3.2.

3.1 The Large Hadron Collider

The LHC is the world's largest and most powerful particle accelerator and collider. Located at the Franco-Swiss border near Geneva, it can accelerate and collide protons at a design energy of 14 TeV with a luminosity of $10^{34} \text{ cm}^{-2}\text{s}^{-1}$ [41].

3.1.1 The CERN accelerator complex

The LHC comprises only the final stage of a chain of particle accelerators that form the CERN accelerator complex. The protons are initially stored in a bottle as hydrogen gas. Until 2020, the hydrogen atoms were fed to an ionization chamber to strip the electrons. Then the remaining protons were inserted into the linear accelerator LINAC2 to be brought to an energy of 50 MeV. Since 2020, the hydrogen atoms have been inserted into a negative hydrogen ion, H^- , source, which adds electrons to the hydrogen atoms to convert them to negative ions with energy 95 keV. The resulting negative ions are fed into the linear accelerator LINAC4 [\[42\]](#) to be accelerated to an initial energy of 150 MeV, and then they are directed to the Proton Booster Synchrotron (PBS), which strips the electrons to convert the H^- to protons using a foil at the injection point, accelerates them to 2 GeV, and places them into bunches of 10^{11} protons. The proton bunches are then transferred to the Proton Synchrotron (PS), which brings their energy to 25 GeV, and then to the Super Proton Synchrotron (SPS) to attain a final energy of 450 GeV. Finally, the SPS injects sequences of proton bunches, named trains, into the LHC. An in-depth description of the LHC injector chain can be found in [\[43\]](#). A detailed layout of the CERN accelerator complex can be seen in [Figure 3.1](#) [\[4\]](#).

3.1.2 The Large Hadron Collider

The LHC is a long double-ring particle accelerator and collider with a perimeter of 26.7 km. It is located in an underground tunnel, which was repurposed from the older large electron-positron collider (LEP), at depths ranging from 50 to 175 m below

The CERN accelerator complex *Complexe des accélérateurs du CERN*

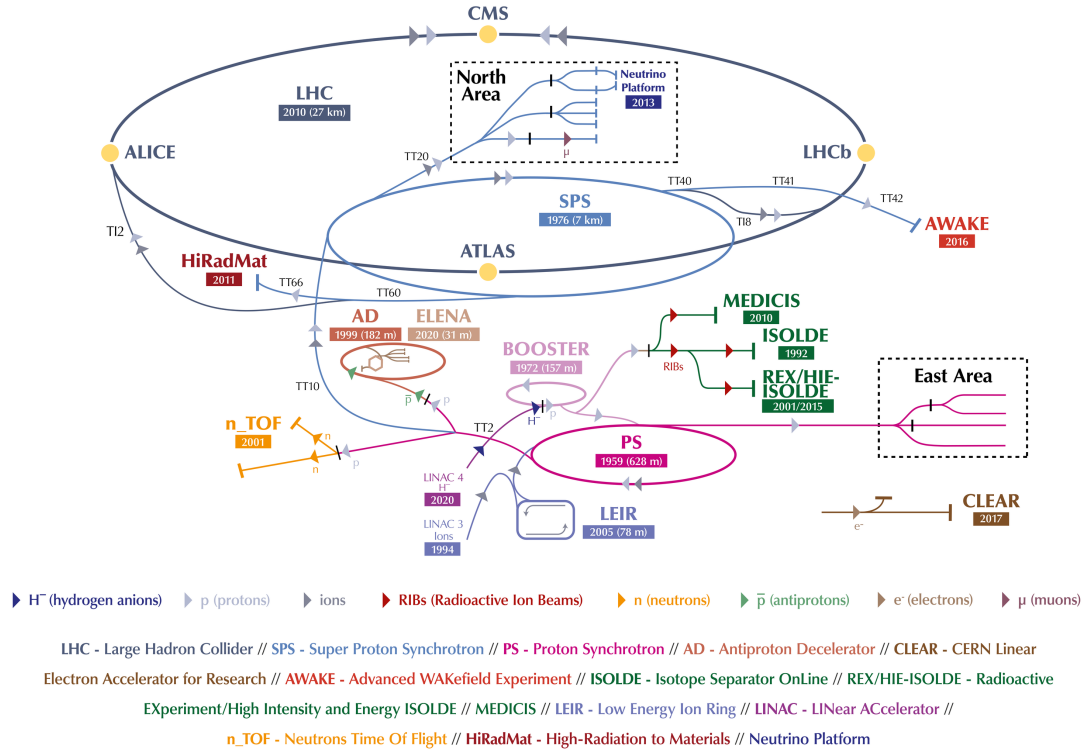


Figure 3.1: Layout of the CERN accelerator complex. The LINAC 4, the Booster, and the PS are shown in shades of purple, while the SPS and the LHC are shown in shades of blue. The four interaction points of the LHC are shown with filled yellow circles. Figure taken from [4].

the Earth's surface. The collider is divided into eight equal-length sections (octants), corresponding to the access points from the surface. Each octant serves a different purpose for the machine. Major physics experiments are located at points 1, 2, 5, and 8. The large, general-purpose experiments ATLAS and CMS are at the antipodal points 1 and 5, respectively, while the more specialized experiments ALICE and LHCb are at points 2 and 8, respectively. The interaction points are displayed with yellow circles in Figure 3.1.

The protons are injected by the SPS in opposite directions into the two parallel rings

of the machine at two injection points at octants 2 and 8. The proton beams are kept in circular orbit by 1232 15-meter-long dipole magnets that are able to generate magnetic fields close to 8 T. The dipoles are using superconducting Nb–Ti Rutherford cables that are kept in the superconductivity state by a cooling system that supplies the magnets with superfluid ^4He . The superfluid state enables more efficient transfer of heat through convection instead of conduction, thus allowing the magnets to reach temperatures close to 2 K. The cross-section of the LHC dipole magnets is displayed in Figure 3.2 [5].

Furthermore, approximately 850 quadrupole magnets are responsible for squeezing and focusing the beams, and higher-order magnets (sextupoles, octupoles, decapoles, etc.) are utilized to control various beam parameters and correct anomalies (e.g., chromaticity). In total, the LHC operates approximately 10,000 magnets. Finally, the proton beams are kept clean using collimators at points 3 and 7, which are made of graphite, carbon-carbon, and beryllium. The collimators at point 3 clean the particle momentum, while those at point 7 clean the beam's betatron amplitude.

The proton beams are accelerated by superconducting radiofrequency (RF) cavities located at access point 4. A total of 8 RF cavities are used per beam direction, delivering 2 MV at 400 MHz. The cavities are organized in 4 cryomodules per direction (2 RF cavities per cryomodule) that cool the cavities at 4.5 K to keep them superconducting. In total, the protons gain 16 MeV of energy per orbit, yielding a ramp-up rate of 0.18 TeV/s.

Extensive in-depth descriptions of all LHC parts can be found in [41, 44].

The LHC operations begin with the injection of bunches at SPS energy (450 GeV), called "INJECTION PHYSICS BEAM". The LHC supports up to 2808 proton bunches in each ring, with approximately 2500 of them colliding at points 1 and 5. The minimum

CERN AC/DI/MM - HE107 - 30 04 1999

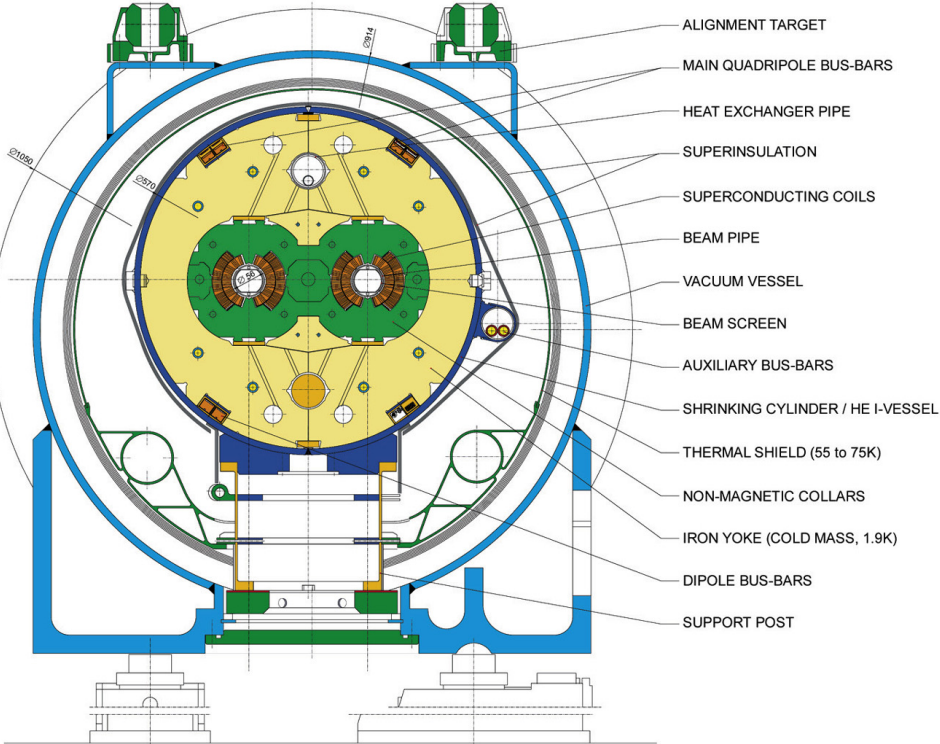


Figure 3.2: Cross-sectional view of the LHC dipole magnets. Taken from [5].

bunch spacing is 25 ns that yields a very approximate collision frequency of 40 MHz. Once all the bunches have been injected, the machine enters the "RAMP" status, and the energy is gradually brought to the final level, called "FLAT TOP" (13 TeV for years 2016-2018 and 13.6 TeV after 2022). Then, the complicated sequence of magnets and collimators takes over to squeeze and adjust the beams to obtain the desired beam parameters. Finally, the machine reaches the "STABLE BEAM" status, which indicates that the beams are colliding in the desired manner for physics data-taking.

3.1.3 Luminosity

The expected number of events for a physics process is given by

$$N = \int \sigma \mathcal{L}(t) dt, \quad (3.1)$$

where σ is the cross section of the process and \mathcal{L} is the instantaneous luminosity, which depends on the LHC beam parameters [45].

Two important beam parameters are the transverse emittance, ϵ_n , and the amplitude function at the interaction point, β^* . The emittance is defined as the surface of the x - p phase space for the beam. Beams with small spreads in momentum and position have low emittance. The emittance generally depends on the initial steps of the acceleration and then worsens after each beam operation (emittance decay). The amplitude modulation function expresses the shape change of the beam ellipse in the x - p phase space as a function of the focusing strength from the quadrupole magnets. More focusing (meaning lower β) reduces the spread in x and increases the spread in p but keeps the surface (emittance) the same [46]. The LHC can control the β^* using the inner triplet quadrupole magnets that sit next to the interaction points.

The instantaneous luminosity can be expressed in terms of the beam parameters as

$$\mathcal{L} = \frac{N_1 N_2 f_{rev} n_b}{4\pi\sigma_x\sigma_y}, \quad (3.2)$$

where N_1, N_2 are the numbers of protons in each bunch, n_b is the number of bunches, f_{rev}

is the revolution frequency, and σ_x and σ_y are the average beam cross sections along the two transverse axes, x and y . These equations are approximations, as they assume that two Gaussian beams are colliding head-on. Other effects, such as the crossing angle, the hourglass effect, and the non-Gaussian profiles, can be included to increase its accuracy. A better description of the instantaneous luminosity uses the formula

$$\mathcal{L} = \frac{N_b^2 f_{rev} n_b \gamma_r}{4\pi\epsilon_n \beta^*} F, \quad (3.3)$$

where N_b is the number of protons per bunch (assumed to be the same), γ_r is the Lorentz relativistic factor, and F is a geometric luminosity reduction factor because of the crossing angle at the interaction point [41].

The LHC attains maximum instantaneous luminosities equivalent to $2 \cdot 10^{34} \text{ cm}^{-2}\text{s}^{-1}$. For CMS and ATLAS, data taking begins at $\beta^* = 60 \text{ cm}$. During collisions, the beam intensities decrease slowly over time as the beams interact. To counteract the decrease in instantaneous luminosity, the LHC applies the so-called β^* leveling technique [47]. The inner triplet magnets gradually squeeze the beam more as needed to maintain the luminosity at the desired value. The lowest β^* value possible is 30 cm.

3.2 The Compact Muon Solenoid experiment

The Compact Muon Solenoid (CMS) experiment [14] is located at point 5 of the LHC in an underground cavern approximately 100 m below the surface. At this point, the beam pipes of the two rings are interconnected, allowing the proton beams to cross at a specific point, known as the interaction point. CMS consists of multiple particle

detection subsystems arranged in the form of a barrel that encloses the interaction point hermetically, leaving only small gaps in the two flat opposite parts of the barrel to allow access to the interaction point for the beam pipes. The detector has a length of 21.6 m and a diameter of 14.6 m, and weighs approximately 12,500 tons. A cutaway diagram of CMS is presented in Figure 3.3 [6].

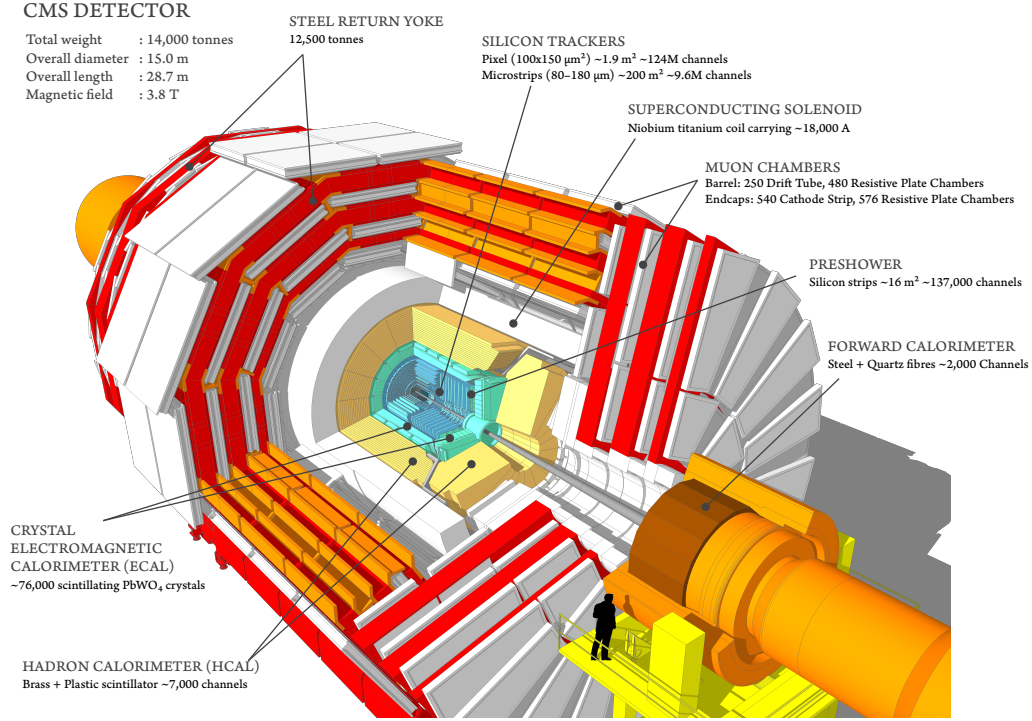


Figure 3.3: Cutaway diagram of CMS [6,7].

CMS utilizes a right-handed Cartesian coordinate system with point $(0, 0, 0)$ being the center of the detector. The x -axis points to the center of the ring, the y -axis points upward, vertically to the ground, and the z -axis points to the west, tangentially to the beam line. Two commonly used coordinates are the radial coordinates ϕ and θ . The azimuthal angle, ϕ , is defined as the angle between the transverse component of a vector, which is the projection on the x - y plane, and the unit vector of the x -axis, \hat{x} . The polar

angle, θ , is defined as the angle between a vector and the z-axis. It is even more common to express the polar angle through the pseudorapidity, η , which is defined as

$$\eta = -\ln \left(\tan \left(\frac{\theta}{2} \right) \right). \quad (3.4)$$

The Sections from [3.2.1](#) through [3.2.8](#) describe the CMS components individually. For more detailed information, an excellent resource is [\[48\]](#), which presents the CMS upgrades for Run 3. The sections below borrow heavily from the material in this publication.

3.2.1 Pixel tracker

The pixel tracker is the innermost detector of CMS, providing 3D tracking points as close to the interaction point as possible, enabling high-precision tracking and vertexing.

Until the end of 2016, the pixel detector consisted of three silicon pixel barrels at radii 44, 73, and 103 mm, and two silicon pixel endcap disks at 345 and 465 mm from the center of the detector. At the beginning of 2017, the pixel detector was replaced with an improved version, also referred to as the Phase 1 pixel detector [\[8\]](#). The new pixel detector consists of four barrel layers at radii 29, 68, 109, and 160 mm, and three endcap disks at distances 291, 396, and 516 mm from the center of the detector. The improved version increases the number of hits from three to four and broadens the pseudorapidity range of the detector up to 3.0 [\[48\]](#). [Figure 3.4](#) shows the layout of the pixel tracker both before and after the Phase-1 upgrade [\[8\]](#).

The barrel pixel (BPIX) and the forward (endcap) pixel (FPIX) parts are two mechan-

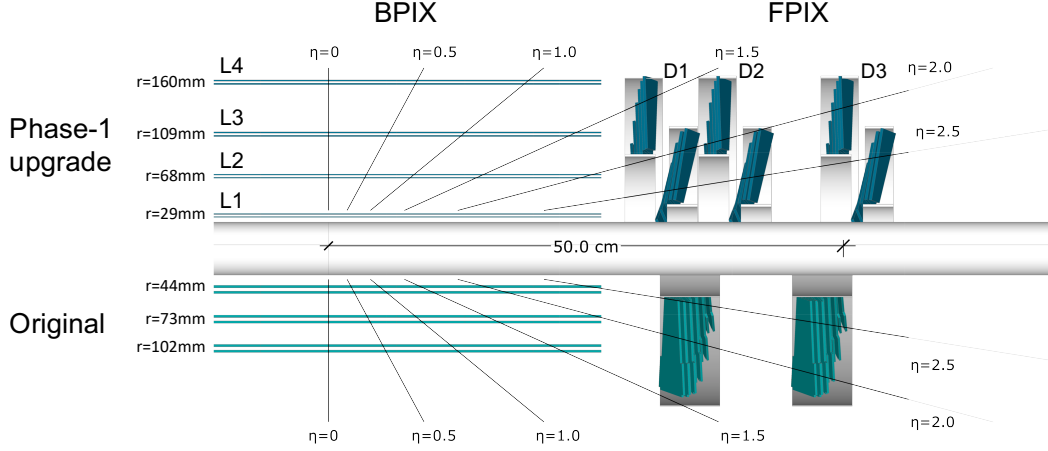


Figure 3.4: Layout of the pixel tracker displaying one quadrant of the r - z cross-section. The bottom of the picture shows the layout of the pixel until the end of 2016. The pixel tracker after the Phase 1 upgrade is depicted at the top [8].

ically and electrically independent detectors. All barrel layers and endcap disks carry silicon sensor modules that are kept at -22°C using evaporative CO_2 cooling [49], with the BPIX and FPIX having 1184 and 672 modules, respectively. Each module contains a $18.6 \times 66.6\text{ mm}^2$ silicon sensor and 2×8 readout chips (ROCs). Each ROC has 80×52 pixels of surface $100 \times 150\text{ }\mu\text{m}^2$. In total, the entire Phase 1 pixel detector includes 124 million readout channels.

The pixel tracker can accomplish high hit efficiencies and excellent position resolutions. After the Phase 1 upgrade, the hit efficiency is higher than 97% in the innermost barrel layer and higher than 99% in most other parts of the detector. The position resolution is $11\text{ }\mu\text{m}$ in the r - ϕ direction and $24.3\text{ }\mu\text{m}$ in the z direction [8].

3.2.2 Silicon strip tracker

The silicon strip tracker (SST) is situated outside of the pixel tracker, and it is responsible for tracking the trajectories of charged particles.

Like most CMS subdetectors, it has a barrel plus endcap layout with a total length of 2.5 m and a diameter of 5 m. The barrel region consists of four layers in the tracker inner region (TIB), six layers in the tracker outer layer (TOB), and three tracker inner disks (TID) placed in the inner forward region. The tracker endcaps (TEC) consist of seven disks, each with 4 to 7 rings, allowing coverage up to pseudorapidities equal to 2.5 [48]. Figure 3.5 presents the layout of both the SST and the pixel tracker [9]. In total, the SST comprises 9.8 million silicon strips, distributed over 15,148 modules. The total active silicon sensor area is approximately 198 mm^2 . During operations, the tracker is maintained at -20° C using C_6F_{14} monophasic coolant that is cooled by two cooling plants.

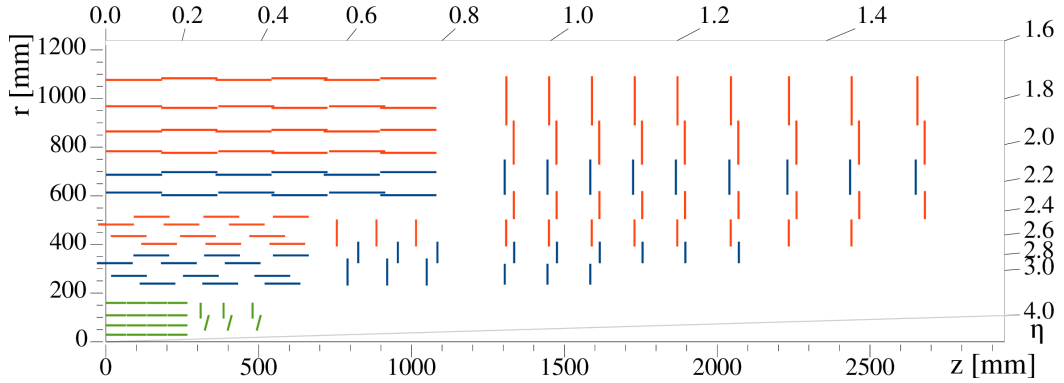


Figure 3.5: Layout of the CMS tracker displaying one quadrant of the r - z cross-section. The pixel tracker is shown in green. Single-sided strips are shown in red, while double-sided strips are shown in blue [9].

Overall, the SST is a very efficient detector that supplies high-quality data for track fitting and reconstruction, achieving an average hit efficiency of about 99.5% [50].

3.2.3 Electromagnetic calorimeter

The electromagnetic calorimeter (ECAL) [51] is a homogeneous scintillating calorimeter used to measure the energy, position, and timing of electrons and photons.

The ECAL is divided into the ECAL barrel (EB) and the ECAL endcap (EE), offering coverage up to pseudorapidities equal to 3.0. The calorimeter consists of inorganic lead-tungstate (PbWO_4) scintillating crystals whose scintillation light is detected by avalanche photodiodes (APDs) in the EB and vacuum phototriodes (VPTs) in the EE. In addition, a preshower detector (ES) is placed in front of the EE to enhance the discrimination between π^0 and photons in the forward region. The ES consists of two alternating layers of lead absorber and silicon sensor planes [48].

Regarding physics performance, the ECAL accomplishes energy resolutions of 2-4% in the barrel and 4-5% in the endcap for inclusive electron samples with time stability close to 0.1%. The timing resolution as measured in $Z \rightarrow ee$ is a few hundred ps [48].

3.2.4 Hadron calorimeter

The hadron calorimeter (HCAL) [52] of CMS is a sampling calorimeter that consists of the hadron barrel (HB) [53], the hadron endcap (HE), the hadron outer (HO) [54], and the hadron forward calorimeter (HF) [55]. The HB and HE are located right outside of the ECAL, and they provide coverage for $|\eta| < 3.0$. The very forward region is covered by the HF, which is placed around the beam line, further away from the center of the detector, to cover pseudorapidities from 3.0 to 5.2. Finally, the HO is situated outside the solenoid magnet to detect shower tails in the region $|\eta| < 1.26$. The full layout of the

HCAL is shown in Figure 3.6 [10].

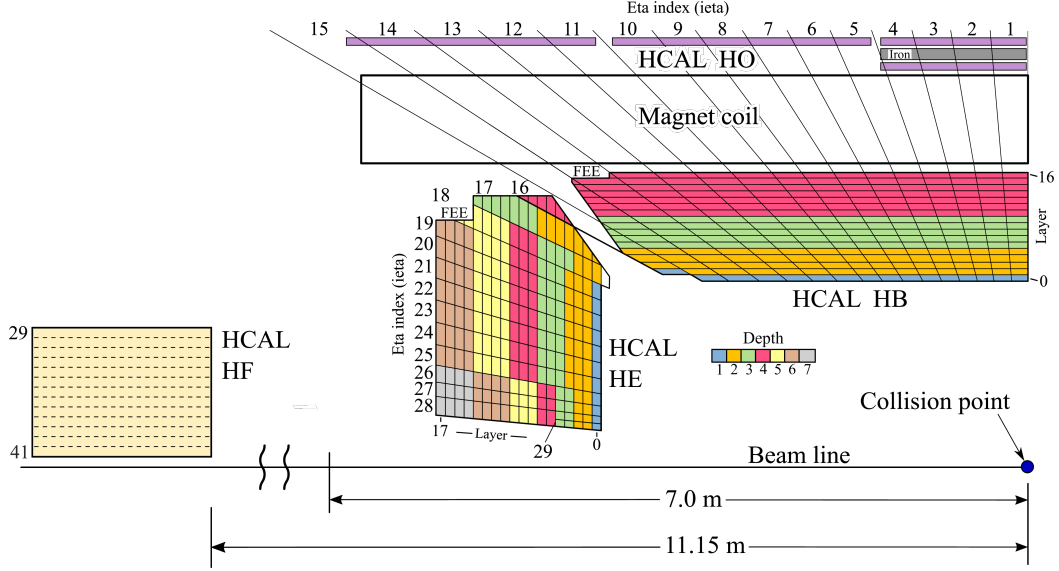


Figure 3.6: Layout of one quadrant of the r - z cross-section for the HCAL. The layout depicts the HCAL after the upgrades for Run 3. The colors in the HB and HE indicate the depths, which are the layers that are connected to the same SiPM. The letters FEE show the location of the frontend electronics [10].

The HB and HE consist of up to 17 and 18 alternating layers of brass absorber and plastic scintillator, with the exception of the inner and outer layers of HB, which use steel absorber. In the original design, plastic wavelength-shifting fibers transmit the scintillation light to hybrid photodetectors (HPDs). Since the end of Run 1, all HPDs have been gradually replaced by silicon photomultipliers (SiPMs). This upgrade has resulted in improved photon detection efficiency, higher radiation tolerance, magnetic field insensitivity, and increased depth readout segmentation, among others.

The HF is made of 0.6 mm-thick quartz fibers embedded in a steel absorber parallel to the beam line. Both short and long fibers are used to allow discrimination of electrons and photons from hadrons. The fibers are connected to photomultiplier tubes (PMTs) for signal detection.

The combined ECAL and HCAL energy resolution for charged pions, according to test beam data, is [56]

$$\frac{\sigma}{E} = \frac{84.7\%}{\sqrt{E}} \oplus 7.6\%. \quad (3.5)$$

The energy resolution for HF, according to test beam data, is [55]

$$\frac{\sigma}{E} = \frac{280\%}{\sqrt{E}} \oplus 11\%. \quad (3.6)$$

3.2.5 Superconducting solenoid magnet

One of the central design aspects of CMS, as manifested also by its name, is the superconducting solenoid magnet [57] that generates a uniform 3.8 T magnetic field in the inner barrel of the detector.

The solenoid is 6 m wide and 12.5 m long, and it is made of Type-I superconducting Niobium-Titanium Rutherford cables, similar to those used for the LHC magnets, that conduct 18,164 A when operational. The cables are embedded in a pure aluminum conductor to stabilize them. Aluminum alloy was welded on top of the pure aluminum to increase the mechanical stability of the structure further, up to the presence of 4 T magnetic fields. The coil is indirectly cooled by helium at 4.5 K, circulating in thermosiphon mode through a network of pipes welded externally [58]. The required cooling for the solenoid is supplied by a cryo plant located in the underground service cavern (USC), right next to the underground experimental cavern (UXC) where the experiment is located.

The vacuum tank, which contains the solenoid magnet, HCAL, ECAL, and the tracker, is encapsulated by a 10,000-ton saturated iron return yoke. The return yoke is

21 m-long and 15 m in diameter, and it consists of 1.5 m-thick iron segments that enclose chambers that are used as stations for the muon tracking detectors. The yoke serves two purposes. First, it returns the magnetic field lines into the muon chambers, and, second, it increases the material budget in front of the muons.

3.2.6 Muon detectors

Excellent muon tracking and triggering performance has been a priority for CMS, evidenced by the size and complexity of the CMS muon detection system. CMS includes four different muon subdetectors: the cathode strip chambers (CSC), the resistive plate chambers (RPC), the drift tubes (DT), and the gas electron multiplier chambers (GEM). The layout of the muon subdetectors is presented in Figure 3.7 [11]. The existence of these four subsystems offers complementarity and increased reliability.

3.2.6.1 Cathode strip chambers

The cathode strip chambers are part of the endcap of the CMS muon detector, spanning a pseudorapidity range of $0.9 < |\eta| < 2.4$. They are multiwire proportional chambers that consist of 7 trapezoidal panels separated by 6 gas layers. Each trapezoidal panel has cathode strips that run radially on the plane perpendicular to the beam axis and anode wires that run along the azimuth. The left picture in Figure 3.8 shows the layout of a CSC chamber with the top partially removed to demonstrate the wires [12]. The right picture in Figure 3.8 is a photograph from the installation of one CSC chamber during Long Shutdown 1 [13].

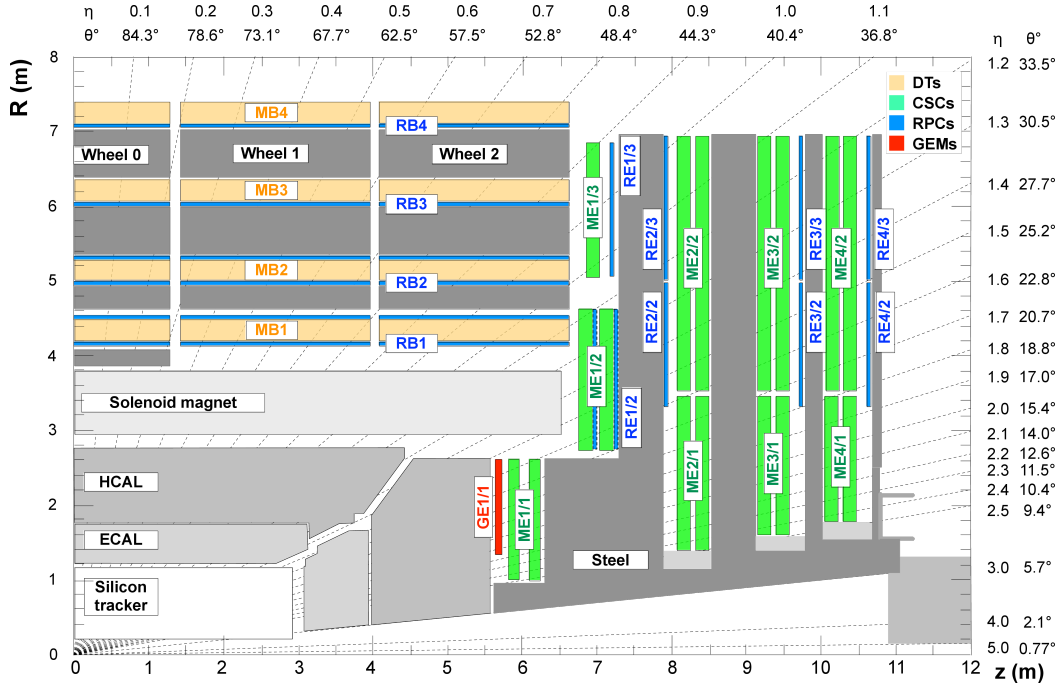


Figure 3.7: Layout of one quadrant of the r - z cross-section of CMS at the beginning of Run 3. The four muon subdetectors are shown in color. The RPC is shown in blue, the CSC in green, the DT in beige, and the GEM in red. The iron yoke is shown in dark gray [11].

The gas is a mixture of 40% Ar, 50% CO₂, and 10% CF₄. The argon gas is ionized by the traversing muons to eventually produce an electrical signal for readout. They provide spatial resolutions in the range 50 – 140 μ m and time resolution of 3 ns [48].

3.2.6.2 Drift tubes

The drift tubes (DT) are located at the barrel of the CMS muon detector. The drift cells are rectangular with transverse size $4.2 \times 1.3 \text{ cm}^2$, and they contain a gold-plated stainless steel wire set at 3600 V, electrode strips at the cell top and bottom set at 1800 V, and cathode strips at the cell side walls set at -1200 V. The DT cells are filled with a gas mixture of 85% Ar and 15% CO₂. There is a total of 250 DT chambers that cover the region for $|\eta| < 1.2$, arranged in five wheels. The drift tubes achieve excellent spatial and

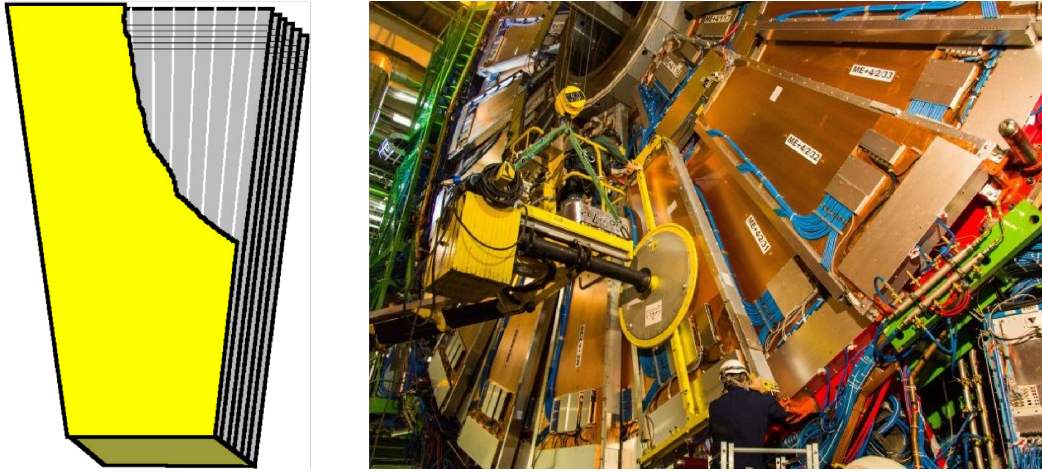


Figure 3.8: Left: schematic of a CSC chamber. Taken from [12]. Right: installation of CSC chambers. Taken from [13].

time resolutions at $100\ \mu\text{m}$ and $2\ \text{ns}$, respectively [48]. A schematic of a DT cell including the drift lines and the isochrones is shown in the left picture of Figure 3.9 [14]. The layout of a DT chamber is presented in the right picture of Figure 3.9 [15].

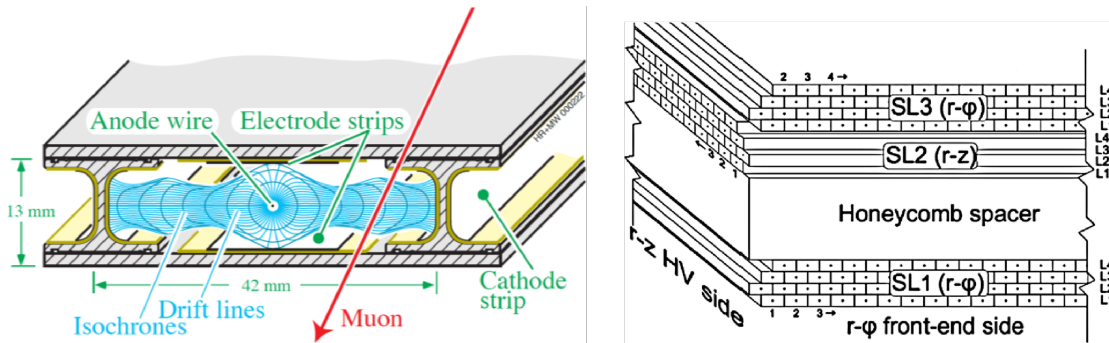


Figure 3.9: Left: schematic of a DT cell including the drift lines and the isochrones. Taken from [14] Right: schematic of a DT chamber, taken from [15].

3.2.6.3 Resistive plate chambers

The resistive plate chambers (RPCs) are muon detectors that are an essential part of both the barrel and the endcap muon detection systems of CMS. The RPCs consist of two 2 mm gas gaps separated by a copper readout plane. The gas gaps are enclosed by

high-pressure laminate (HPL) plates with bulk resistivity $\sim 10^{10} \Omega \cdot \text{cm}$ that are coated with graphite electrodes. A schematic of a resistive plate chamber can be found in the left Figure 3.10 [16]. High voltage is applied between the two graphite electrodes that enclose each gas gap. The chambers are filled with a gas mixture of 95.2% $\text{C}_2\text{H}_2\text{F}_4$, 4.5% $i\text{-C}_4\text{H}_{10}$, and 0.3% SF_6 . The working principles of RPC are shown in the 3D schematic in the right Figure 3.10 [17]. There is a total of 1056 chambers placed strategically in the barrel and the endcaps of CMS. The RPC is capable of excellent time resolutions even in the presence of high rates of background, greatly improving the muon triggering efficiency of CMS.

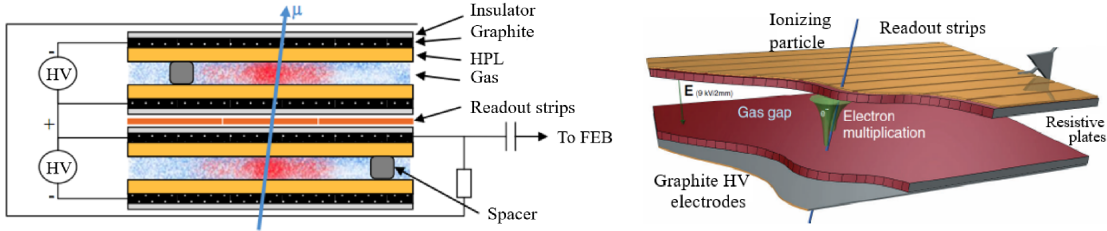


Figure 3.10: Left: schematic of a resistive plate chamber, taken from [16]. Right: 3D schematic of the RPC showing its working principles, taken from [17].

3.2.6.4 Gas electron multiplier chambers

The gas electron multiplier (GEM) [59] chambers are muon detectors in the $1.55 < |\eta| < 2.18$ region of the CMS endcap that were installed before the start of Run 3 in 2022. The addition of a new highly granular muon detector was deemed necessary to support muon tracking and triggering in the endcaps, given the expected increase in muon rates following the High-Luminosity (HL-LHC) upgrade of the LHC.

The GEM detectors are micro-pattern gas detectors that consist of a drift cathode panel at the top, followed by four gas gaps separated by three GEM foils, and a readout

board with radially-oriented readout strips at the bottom. The GEM foils are thin polyimide foil clads with thin copper layers that contain micro-pattern holes in a periodic grid layout [60]. The right picture of Figure 3.11 shows a blown-up schematic of a GEM chamber [19]. A voltage of 400 V is applied to the copper layers to create strong electric fields. The muons ionize the gas, which is a mixture of 70% Ar and 30% CO₂, and then the three GEM foils amplify the charge by a factor of $\mathcal{O}(10^5)$ to produce a signal on the readout strips.

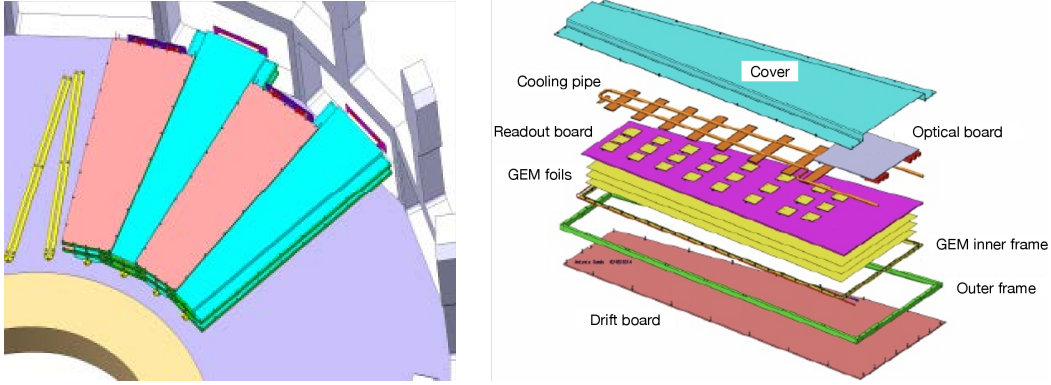


Figure 3.11: Left: layout of the GEM chambers on the CMS endcap, taken from [18]. Right: schematic of a GEM chamber showing its internal components, taken from [19].

Each CMS endcap features 36 two-layer triple GEM chambers positioned in front of the first CSC stations. The layout of the GEM chambers on the CMS endcap is illustrated in the left picture of Figure 3.11 [18]. The GEM muon chambers achieve a combined spatial resolution of $100\ \mu\text{m}$ and a timing resolution $< 10\ \text{ns}$ [48].

3.2.7 The triggering and data acquisition system

The LHC bombards CMS with a 40 MHz collision rate. Assuming an overly optimistic storage need of a few hundred kilobytes per event yields data rates over 10 Tbps,

which are impossible to process and store with current technology. Fortunately, the vast majority of the collisions provided by the LHC are just pp inelastic scatterings that are not useful for most physics analyses.

The CMS trigger system is a two-stage filtering system responsible for reducing data rates to manageable levels. Together with the CMS Data Acquisition System (DAS), it comprises the CMS Trigger and Data Acquisition system (TriDAS). The system consists of a hardware-based Level-1 (L1) triggering layer and a software-based High-Level Trigger (HLT).

3.2.7.1 Level-1 trigger

The level-1 (L1) trigger [61, 62] is based on custom hardware processors (FPGAs). The calorimeters (ECAL & HCAL) and the muon systems produce trigger primitives (TP) that represent coarser readouts of the detectors and whose size is optimized for low-latency and limited bandwidth applications. The L1 receives the TPs and performs a rudimentary reconstruction of the event, creating particle candidates for e/γ , τ , jets, and muons.

For the muons specifically [63], the L1 receives TPs from all four muon detectors, and it performs muon track reconstruction in three distinct regions. These are

- the **barrel muon track finder (BMTF)**, which covers $|\eta| < 0.83$, and uses TPs from the DT and the RPC,
- the **overlap muon track finder (OMTF)**, which covers $0.83 < |\eta| < 1.2$, and uses TPs from the DT, the CSC, and the RPC,

- and the **endcap muon track finder (EMTF)**, which covers $1.2 < |\eta| < 2.4$, and uses TPs from the CSC, the RPC, and the GEM.

A maximum of 36 muons per bunch crossing are then transmitted to the global muon trigger (μ GMT) to resolve any duplicates. Finally, up to 8 muons are transmitted to the global trigger (GT).

The GT issues a decision whether to keep or reject the event based on its compatibility with at least one of the L1 trigger bits that comprise the L1 menu. Events that have at least one L1 trigger bit on are kept and transmitted to the surface for further processing. Overall, the L1 trigger manages to reduce the event rate to approximately 100 kHz.

3.2.7.2 High-level trigger

The high-level trigger (HLT) is a software-based filter that runs on a CPU and GPU farm located at the surface level of the CMS site. Events that pass the L1 trigger are transferred to the HLT farm to undergo sequential reconstruction and filtering, using the L1 bits as input seeds. Several HLT paths exist, corresponding to interesting event cases. Events that meet the requirements for at least one HLT path are retained and transferred to permanent storage.

Certain event classes are of interest, but their rate surpasses the allocated rate budget. For these cases, CMS utilizes the concept of prescaling, which involves retaining only 1 out of N such events. The prescales exist in the form of prescale tables, which contain columns corresponding to reference instantaneous luminosities. Each column contains a list of integer numbers that are the prescale values for each HLT path. The shifters in

the CMS control room are responsible for monitoring the prescales and switching the columns as needed. A similar concept exists for the L1 bits. The data can carry prescales from both the L1 and HLT simultaneously.

Eventually, the event rate exiting the HLT is reduced to a few kHz for storage.

3.2.7.3 Data acquisition system

The CMS data acquisition system (DAQ) [64,65] is responsible for a range of tasks that begin with aggregating the data from the detector readout electronics and end with sending the events selected by the HLT to the Tier-0 for storage. More specifically, the DAQ has links that receive data from the detector backend boards, also called front-end drivers (FEDs). The readout is coordinated using the trigger throttling system (TTS) [66], which can throttle the trigger to avoid buffer overflows, causing deadtime, and the trigger control and distribution system (TCDS) [67]. Readout unit builder unit (RUBU) servers aggregate the data into superfragments, buffer, and build events out of the superfragments [68]. Filter unit (FU) servers run the HLT, and eventually, the storage and transfer system (STS) transfers the selected events to the Tier-0 for storage [48].

3.2.8 Luminosity and beam conditions

The system responsible for measuring the luminosity and monitoring the beam conditions is the beam radiation instrumentation and luminosity (BRIL) system. It measures the luminosity (both online and offline), the beam-induced background, and the beam losses. It consists of two fully dedicated luminometers, which are the pixel luminosity

telescope (PLT) [69–71] and the fast beam conditions monitor (BCM1F) [72, 73], the forward hadron calorimeter (HF) [74], and a dedicated data acquisition system (BRILDAQ). The three luminometers enhance the reliability of the luminosity measurements, and they are combined to obtain the best estimate for the offline luminosity values.

3.3 Offline software and computing

The offline computing needs of CMS are handled by the CMS offline software (CMSSW). This modular system is capable of reconstructing data, processing conditions and calibration data, and producing Monte Carlo simulations.

3.4 Monte Carlo simulations

CMSSW integrates the most popular software for generating high-energy physics MC simulations, such as PYTHIA [75], MADGRAPH [76], aMC@NLO, and POWHEG. Additionally, it includes a detailed and highly optimized simulation of the detector, based on GEANT4, which can be used to simulate the passage of particles through all components.

The simulation of pileup (PU) is handled by using minimum bias events in conjunction with the pre-mixing technique. Essentially, the additional events are added on top of the simulated MC event at a later stage.

The simulation process produces data in the following intermediate data tiers

- **LHE:** Optional step that happens when external matrix element calculators, like MADGRAPH or POWHEG, are used.

- **GEN:** At this step, the full event is generated. This includes the hard process, if not already generated at a previous step, the parton shower, consisting of initial state radiation and final state radiation, multiple parton interactions, color reconnection, fragmentation, and hadronization. This step is almost always performed using PYTHIA 8 in CMS.
- **SIM:** The result of the full GEANT4 simulation of CMS. It consists of simulated detector hits, corresponding to the energy deposits made by the passage of particles through the active material.
- **DIGI:** Digitized detector hits. They correspond to the signals that are handled by the detector backends.
- **RAW:** Detector raw readout data. This is the same format that the DAQ produces for real collision data.

3.5 Reconstruction

The event reconstruction in CMSSW begins with local reconstruction for each detector component, and concludes with a global particle-flow reconstruction that combines the information to achieve optimal reconstruction and identification for all particles. Local reconstruction includes track reconstruction, clustering of calorimeter deposits in ECAL and HCAL, and tracks in muon detectors. The reconstruction processes for the physics objects that are used in Part III are presented below in more detail.

The data tier for reconstructed data and MC is named RECO, and it contains all

the reconstructed data and objects. Keeping all this information is impractical and unnecessary for most physics analyses. Therefore, CMS prepares slimmed versions that contain less information per event. These are, in order of decreasing size per event, the AOD, the MINIAOD, and the NANO AOD.

3.5.1 Track fitting and reconstruction

Track reconstruction in CMS utilizes the combinatorial track finder (CTF) algorithm with multiple passes, in a process called iterative tracking [77]. This is an extension of the Kalman filter that allows simultaneous pattern recognition and track fitting. The core idea is to begin with reconstructing the easiest tracks in iteration 0. The reconstructed hits are then removed, reducing the combinatorial complexity for the next iteration, and this sequence is repeated multiple times. In each iteration, seeds are generated to provide track candidates. These candidates are then propagated using the Kalman filter to predict the expected trajectories. Tracks are finally selected using a set of quality criteria. Ten iterations are performed in total, with the last two iterations being dedicated to muons by including hits from the muon detectors [78].

3.5.2 Muon reconstruction

Muon reconstruction happens both using the muon detectors independently and combining them with the rest of the CMS detector. Hits within the muon detectors are clustered and fitted to form *standalone muons*. The standalone muons that are matched to tracks in the inner tracker are called *global muons*. All tracks with $p_T > 0.5 \text{ GeV}$ and

$p > 2.5 \text{ GeV}$ are extrapolated to the muon system. If they match at least one muon segment, then they become *tracker muons* [78].

The tracker generally contributes the most to the muon resolution at low momenta ($< 10 \text{ GeV}$). The muon system improves the momentum resolution of muons with $> 200 \text{ GeV}$.

3.5.3 The particle flow algorithm

Eventually, the CMS software combines all the local reconstructions into one final combined reconstruction that utilizes the Particle Flow (PF) algorithm [78]. A link algorithm is used to pair and merge the locally reconstructed objects. The PF candidates pass through identification and PU removal. A global event description is provided, leading to excellent physics performance.

Part II

Radiation damage in plastic scintillators

Chapter 4: Introduction to plastic scintillators

This Chapter gives an introduction to the use of plastic scintillators in high-energy physics experiments. The text in this section relies heavily on our publication in Ref. [79]. I contributed the majority of the text and the work for this publication, and I am the first author.

4.1 Plastic scintillators in high-energy physics

The use of plastic scintillators in high-energy physics experiments has been widespread both in past and present experiments. Their low cost, ease of production, and versatility make them attractive as the active element for a broad range of particle detectors, with calorimeters being the main beneficiaries.

Looking at past experiments, the Collider Detector at Fermilab (CDF) used a hadron calorimeter made out of alternating sheets of plastic scintillator and steel [80], and the DØ experiment had its preshower detector [81] and outer tracker made out of plastic scintillator panels and fibers [82], respectively. Moving to the present, both the ATLAS LHC Apparatus (ATLAS) and the Compact Muon Solenoid (CMS) experiments, located at the Large Hadron Collider (LHC) at CERN, make use of plastic scintillator. For ATLAS, the Tile Calorimeter (TileCal) consists of steel modules with slots for plastic

scintillating tiles equipped with wavelength-shifting fibers (WLS) [83]. For CMS, the Hadron Calorimeter (HCAL) uses alternating layers of brass and plastic scintillating tiles with WLS fibers embedded for readout [84]. The Phase 2 upgrades of CMS, which are scheduled to be installed in 2026, include the new High Granularity Calorimeter (HGCAL) that is going to use plastic scintillator tiles instrumented with Silicon Photomultipliers (SiPMs) for the low radiation regions of its hadronic part [85]. Finally, future experiments are considering the use of plastic scintillators. E.g., the IDEA detector at the Future Circular Collider for electrons and positrons (FCC-ee) is contemplating the use of plastic scintillating fibers in its dual readout calorimeter [86].

4.2 Working principles of plastic scintillators

Plastic scintillators consist of a substrate material that is typically doped with a primary fluor at a concentration of a few percent and a secondary fluor at a concentration about ten times smaller than the primary. The substrate, which is usually either polystyrene (PS) or polyvinyltoluene (PVT), acts as the main receptacle for the ionizing particle's energy. This energy is then transferred to the primary dopant either through the non-radiative Förster mechanism [87] for higher dopant concentrations ($\gtrsim 1\%$) [88] or through radiative transfer for lower concentrations. The primary dopant emits light of wavelengths that overlap with the secondary dopant's absorption spectrum. The secondary dopant receives the energy from the primary through radiative transfer and then emits light in the visible part of the spectrum.

4.3 Radiation damage in plastic scintillators

One crucial aspect of detector design for HEP experiments is radiation tolerance. Ionizing radiation is capable of breaking the polymer molecules and creating radicals, which are molecules with one or more unpaired valence electrons. The radicals are known to strongly absorb light of shorter wavelengths, and they tend to react easily with other radicals, in a group of processes called radical recombination that includes radical crosslinking, or with the oxygen dissolved in the material, thus getting oxidized. Therefore, radiation damage can be defined as the collective effect of all those chemical processes on the scintillation mechanism and the attenuation length of the material under study.

The collisions facilitated by particle accelerators are capable of creating high particle fluxes, with the regions closer to the interaction point and the endcaps being disproportionately affected. Modern experiments routinely experience total absorbed doses ~ 1 MGy for vertex detectors [89] close to the interaction point, and > 1 kGy at the calorimeter endcaps, where plastic scintillator is often found. Endcap doses are accumulated at very low dose rates ranging between 10^{-3} and 1 Gy/h. Specifically, at CMS, during the 50 fb^{-1} of integrated luminosity gathered at 13 TeV in 2017, the Hadron Endcap (HE) tiles of HCAL received doses up to a few kGy [90]. The High Luminosity (HL) era at the LHC is going to bring new challenges with respect to radiation tolerance. The anticipated high number of simultaneous collisions, also known as pileup, is expected to further increase the expected total absorbed doses up to ~ 3 kGy for the plastic scintillator that is going to be installed in the CMS HGCal [91].

Numerous studies of radiation-induced damage in scintillators exist in literature [92–104]. However, most studies use data associated with higher dose rate irradiations or are focused on scintillators read out with WLS fibers, in which the results describe the combined damage. In more recent works, lower dose rates have been studied in more detail, and the importance of the dose rate in the assessment of radiation damage has been further established [105]. In addition, the presence (or absence) of oxygen during irradiation and recovery of the scintillators affects radiation damage significantly [106–109].

Chapter 5: The effect of dose rate on radiation damage

This Chapter presents studies of the effects of dose rate on radiation damage. These studies are published in Ref. [105], and the text here relies heavily on the content of this publication. My contributions include measuring the light yields, cleaning, calibrating, analyzing, and plotting the data, as well as parts of the written text. I am the first author of this publication. A significant part of the text was written by S. Eno. The measurements and plotting for the transmission data were performed entirely by T. Edberg.

5.1 Introduction

When particle detectors based on plastic scintillator are exposed to ionizing radiation, their light output decreases with absorbed dose. For reasonably low doses, the dependence of the signal strength on the dose d can be approximated by an exponential

$$L(d) = L_0 \exp(-d/D), \quad (5.1)$$

where $L(d)$ is the signal after irradiation, L_0 is the signal before irradiation, and D is the “dose constant”, a numeric parameter whose value depends on the scintillator geometry, the specific scintillator used, environmental factors, and on the dose rate $\frac{d}{dt}(d) \equiv \mathcal{R}$.

Larger values of D correspond to greater radiation tolerance.

Because their exposures are at low \mathcal{R} (typically a few $\times 10^{-3} - 10^0$ Gy/hr), the value of D for plastic scintillators in calorimeters at current and future collider experiments at CERN's Large Hadron Collider is challenging to measure, as low \mathcal{R} exposures necessitate long irradiations and therefore can be expensive. The CMS collaboration has recently [90] reported measurements at \mathcal{R} s between a few $\times 10^{-3}$ and a few $\times 10^4$ Gy/h for plastic scintillator tiles (either SCSN-81 from the Kuraray Corporation¹ or BC-408 from the Bicron division of the Saint-Gobain Corporation²), with an embedded Y-11 wavelength-shifting fiber (Kuraray). The wavelength-shifting fiber is connected to a clear plastic fiber that leads to a photodetector. Their results show a power law dependence of D on \mathcal{R} for \mathcal{R} less than a few 10's of Gy/hr. At higher \mathcal{R} s, due to systematic uncertainties, the behavior is consistent either with a continued power law dependence or a constant D . Other recent measurements of radiation damage to plastic scintillator for particle detectors are reported in Refs. [92, 93]. Two recent reviews of radiation damage in plastic scintillator are Refs. [94, 95]. For a comprehensive review of plastic scintillators, see Ref. [110]

Several studies of the \mathcal{R} dependence of radiation damage in plastic scintillators have been published [96–104]. However, previous measurements of \mathcal{R} effects in scintillators without wavelength-shifting fibers were limited to high \mathcal{R} s and were unable to differentiate different potential causes. In this chapter, we present results for D for plastic scintillating rods manufactured by the Eljen Technology company³ using polystyrene

¹Kuraray, Ote Center Building, 1-1-3, Otemachi, Chiyoda-ku, Tokyo 100-8115, Japan

²Saint Gobain Corp, Les Miroirs, 18, Avenue d'Alsace, 92400 Courbevoie, France

³Eljen Technology, 1300 W. Broadway, Sweetwater, Texas 79556, United States

(PS) or polyvinyltoluene (PVT) as the matrix, several dopant concentrations, two different fluors (EJ-200 and EJ-260), various scintillator thicknesses, and three antioxidant concentrations for \mathcal{R} s from 2.2 Gy/hr to 3900 Gy/hr. These variations allow exploration of potential causes. In addition, our results separate the contributions to the CMS results from the plastic scintillator and the other components in the tiles and their readout.

5.2 Mechanisms and effects of radiation-induced changes to phenyl-based polymeric scintillators

Common plastic scintillator consists of a matrix (often PS or PVT) containing primary and secondary fluors. Ionizing radiation excites the matrix. This excitation can be transferred to the primary fluor via the Förster mechanism [87], which dominates at primary concentrations above approximately 1% [88], or radiatively in the UV, which dominates at low concentrations. The excitation is transferred radiatively from the primary to the secondary, which de-excites via the emission of visible light.

Radiation affects the light output of scintillators mainly through damage to the polymer substrate. The effects depend on the chemical structure, the degree of crystallinity of the irradiated polymers, and the total dose and dose rate. Dissolved oxygen in the amorphous part can also play an important role in the radiation chemistry of the polymers [106–108] both during and after irradiation.

The polymers used in our work are atactic and amorphous, meaning that their constituents are placed randomly along the chain and they lack long-range order. As a result, there is no expected effect due to the degree of crystallinity. Furthermore, the

monomers that make up PS and PVT carry a benzene ring, also called a phenyl group. For amorphous PS and PVT, the phenyl group on their backbone chains strongly decreases radiation effects [111], as its π structure provides excellent protection to the polymer chains. The photoelectric and Compton electrons, resulting from gamma radiolysis of PS and PVT, react very rapidly with the π structure of these phenyl groups, producing anion radicals. It is expected that the phenyl anions convert rapidly to C-centered radicals through a protonation reaction to produce benzyl-type radicals [112]. In amorphous materials, such as atactic PS and PVT, these benzyl-type and toluenyl C-centered radicals undergo various competing reactions depending on the presence of oxygen and the \mathcal{R} .

A decrease in light output can come from two sources: either through the formation of so-called “color centers” that absorb light emitted from the secondary fluor in transit from its creation point to the photodetector, or through a decrease in the initial production of light. The decrease of the initial light production can occur through fluor destruction or alteration, and through absorption of light in transmission between the primary and the secondary fluors. Additionally, radiation damage can enhance the de-excitation of the matrix via mechanisms that do not lead to light production (“quenching”). For example, oxygen can quench the initial light, as the excitation can transfer to it instead of to the primary fluor [94, 109]. In addition, the value of the Birk’s constant, important for highly ionizing particles, could change because it depends on the density of the primary dopant and interactions between excited substrate molecules [113].

Radicals can absorb visible light, and generally absorb more strongly at shorter wavelengths [94]. Radicals are the source of the so-called temporary damage, which decreases with time after the radiation exposure as they recombine with each other to pro-

duce stable molecules. After irradiation, $R-C^{\bullet}$ radicals in the amorphous region continue to react with oxygen and undergo crosslinking reactions. However, the $R-C^{\bullet}$ radicals have a much longer lifetime. Free radicals centered on the backbone of the polymer chain in the crystalline region transfer to the amorphous region via the hydrogen-hopping mechanism. This process is called annealing. After annealing, the remaining color centers are referred to as permanent damage. Radicals can also undergo recombination reactions (including crosslinking reactions) during irradiation. The non-standard bonds to the matrix material can form permanent bonds that can absorb in the visible, acting as color centers.

The rate of radical production during irradiation goes as [114]

$$\frac{d[Y]}{dt} = gQR - k[Y]^2, \quad (5.2)$$

where $[Y]$ is the density of radicals, g is the radiation-chemical yield, Q is the scintillator density, and k is the reaction constant for the decay of the radical. The first term represents the creation of radicals, while the second term represents two unterminated radicals recombining to neutralize (“second-order” termination). At short times, when the second term is small compared to the first, integration yields a radical density that is proportional to dose: $Y = gQd$. If the radical is not neutralized by, e.g., oxidation, then the second term grows with time, and eventually, a steady state is reached, when the two terms are equal. In this case, the radical density becomes constant with time, is no longer proportional to dose, and deviations from the expected exponential behavior described by equation 5.1

occur. When the first term dominates, Eq. 5.1 becomes:

$$L(d) = L_0 \exp(-gQd\sigma l), \quad (5.3)$$

where σ is the cross section for absorption of light by the color centers, and l is the light's path length through the scintillator to the photodetector. This would indicate $D^{-1} = gQ\sigma l$, and so D would scale with l^{-1} .

5.2.1 The reactions of the C-centered radicals in the absence of oxygen

Radiolytically produced C-centered radicals of PS and PVT undergo crosslinking reactions in the absence of oxygen. However, the steric effect of the phenyl group on the backbone of the PS and PVT chains impedes crosslinking reactions, leading to lower crosslinking radiation yield. For example, the absorption of 2000 eV gamma energy produces only one crosslink [111]. The polystyrene free radicals can also react with H-atoms, which are produced during the radiolysis, leading to their disappearance on a longer timescale.

5.2.2 The reactions of the C-centered radicals in the presence of oxygen

While high \mathcal{R} enhances the crosslinking reactions, low \mathcal{R} and the presence of oxygen promote the oxidation processes.

The depth z_0 for oxygen diffusion into a rectangular slab of plastic is [115]

$$z_0^2 = \frac{2 M C_0}{Y \mathcal{R}} = \frac{2 M S P}{Y \mathcal{R}}, \quad (5.4)$$

where M is the diffusion coefficient for oxygen, C_0 is the oxygen concentration at the matrix's surface on the matrix side, $Y (= gQ)$ is the specific rate constant of active site formation, S is the oxygen solubility, and P is the external oxygen pressure. In general, these parameters depend on temperature [116]. There is an abrupt transition between areas with and without oxygen. The oxygen concentration in the oxidized regions is almost uniform [117]. For PS rods with a thickness of 1 cm, oxygen permeates the entire sample for \mathcal{R} s below (roughly, depending on the plastic preparation and environment) 1.6 Gy/h [98, 117]. For thicknesses of 0.4 cm, 0.6 cm, and 0.8 cm, the corresponding permeation \mathcal{R} s are below 10 Gy/h, 4.4 Gy/h, and 2.5 Gy/h respectively. For \mathcal{R} s above this value, polymer oxidation will occur only in the region permeated by oxygen, contributing to an \mathcal{R} dependence of the damage to the scintillator.

The rate of polymer oxidation is [106–108, 118, 119]

$$K(C(x, t)) = -\frac{C_1 C(x, t)}{1 + C_2 C(x, t)}, \quad (5.5)$$

where $-K(C(x, t))$ is the rate at which oxygen diffuses through the polymer bulk, x is the position relative to the surface of the material where the rate is being measured, and $C(x, t)$ is the position-dependent concentration of oxygen within the matrix. The constants C_1 and C_2 depend on the kinematics of the chemical reactions. The constant C_1 is proportional to the square root of \mathcal{R} for bimolecular reactions (leading to a dose-rate effect) and to \mathcal{R} for unimolecular reactions (no dose-rate effect because integration yields a proportionality to dose).

The decay kinetics of the PS benzyl and PVT toluenyl C-centered radicals can be

summarized as follows:

$$-\frac{d[\text{R-C}^\bullet]}{dt} = k_1[\text{O}_2][[\text{R-C}^\bullet] + 2k_2[\text{R-C}^\bullet]^2] \quad (5.6)$$

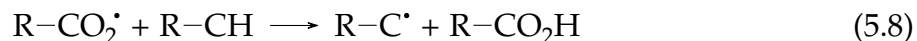
where k_1 and k_2 represent the reaction rate constants of the C-centered radicals with oxygen and the bimolecular second-order crosslinking reactions, respectively. At a sufficiently high \mathcal{R} , the rate of free radical production $\frac{d[\text{R-C}^\bullet]}{dt}$ is high enough to lead to an enhancement of the crosslinking reaction. Therefore, at very high \mathcal{R} , crosslinking competes with the diffusion rate of oxygen into the bulk of the irradiated atactic PS and PVT. Also note that, at room temperature, atactic PS and PVT are regarded as oxygen barriers, and oxygen diffusion is very low. At high \mathcal{R} , the crosslinking reactions are therefore dominant in the bulk. However, at the surfaces of the irradiated samples, PS and PVT samples where the O_2 is available, their radiolytically produced carbon-centered radical R-C^\bullet react very rapidly with oxygen to give rise to the formation of corresponding peroxy radicals [106–108, 120].

The peroxy radicals undergo bimolecular reactions to produce unstable tetraoxide intermediates



The ROOOOR intermediates undergo various decomposition reactions, producing relatively stable oxides such as organic and hydroperoxides (ROH and ROOH). These oxides can absorb strongly in the ultraviolet, leading to reduced transfer of light to the secondary fluor. Their absorption cross section decreases with increasing wavelength. Note

that $\text{R-CO}_2\cdot$ can abstract an H atom from the backbone of the neighboring molecules, producing more $\text{R-C}\cdot$, and initiating a short-chain reaction.



where R-CH is either PS or PVT. In this study, we used glassy atactic (100% amorphous) PS and PVT. Hence, the permeability of O_2 through PS and PVT is very small [121]. So, the traces of oxygen in the bulk are consumed by irradiation at a much faster rate than replenished by its permeability from outside. Hence, it is expected that the crosslinking reactions are predominant in the bulk of the PS and PVT irradiated samples, and the oxidation reactions take place mainly on the surfaces of these samples at high dose rates. Our results show the presence of oxidation products in the bulk, too. This is because our samples are relatively thin. In addition, our very low dose rates impede the crosslinking reactions and enhance the reaction of polystyrene radicals with oxygen.

5.3 Sample and irradiation details

Our scintillator samples are in the form of rectangular rods, 5 cm long and 1 cm wide, with thicknesses of 0.4 cm, 0.6 cm, 0.8 cm, and 1.0 cm. All faces are diamond-milled. The rods, supplied by Eljen Technology, contain either the primary and secondary fluors used in EJ-200 (a blue scintillator with p-Terphenyl as the primary and a POPOP-type dopant as the secondary) or EJ-260 (a green scintillator whose fluors are proprietary to Eljen Technology), with either PS or PVT as the plastic matrix. The secondary fluor emission spectra from the Eljen website for EJ-200 and EJ-260 are shown in Fig. 5.1. For

the EJ-200 fluors, the wavelength of maximum emission for the primary fluor in PS or PVT is around 320–350 nm, and the region most important for secondary emission is 410–480 nm. The primary fluor emission maximum for EJ-260 is 372 nm [122], and the secondary fluor emits primarily between 475 and 550 nm. Some of the rods had double the normal concentration of the primary dopant, and some had double the concentration of the secondary dopant. Some had no antioxidant included, and some had twice the nominal antioxidant concentration. Fig. 5.2 [top] shows a photograph of some of the rods. Rods were acquired in several purchases or gifts over several years. Lists of used samples are given in the Tables that can be found in A.

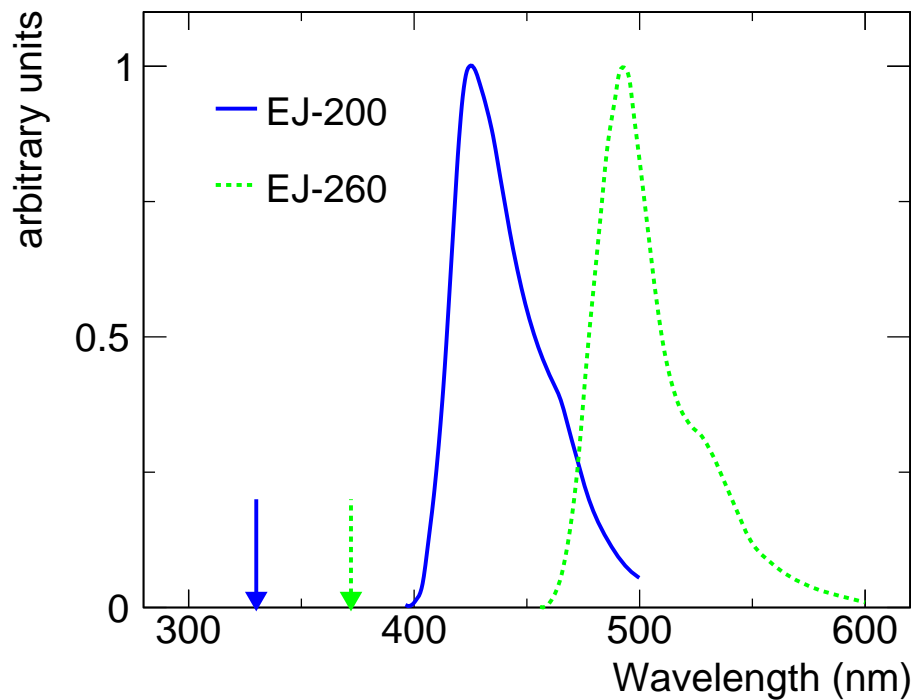


Figure 5.1: Emission spectra from the Eljen Technology website for EJ-200 (blue solid) and EJ-260 (green dot). The arrows represent the emission maxima for the primary for EJ-200 (blue solid) and EJ-260 (green dot).

Irradiations were performed at four facilities with gamma-ray sources. High \mathcal{R} irra-

diations, with \mathcal{R} s between 80.6 and 3900 Gy/hr, were performed at the National Institute of Standards and Technology, Gaithersburg, MD, and Sandia National Laboratories using ^{60}Co sources. Low \mathcal{R} irradiations, at 3.0, 3.1, and 9.8 Gy/hr, were performed at Goddard Space Flight Center using a ^{60}Co source, and at 2.2 Gy/hr at the GIF++ facility [123] at CERN using a ^{137}Cs source. The irradiations were done at room temperature. The humidity and oxygen pressure were not measured or controlled.

The irradiations at Sandia National Laboratories were subject to long, multi-hour pauses. The longest pauses lasted 1-3 days, while the full annealing time for this material is approximately 1 month. Scintillator chemistry is expected to be affected by annealing due to radical recombination and deeper oxygen penetration when irradiation is paused. For this reason, data from these irradiations are not used for dose constant calculations and they are included only in a comparison between light output and dose (Fig. 5.4).

The uncertainties on the accumulated dose and \mathcal{R} were $\pm 10\%$ for irradiations performed at Goddard Space Flight Center and GIF++, and $\pm 1.3\%$ (95% confidence level) for irradiations performed at the National Institute of Standards and Technology. Accumulated doses (in water equivalent) ranged from 12.6 kGy to 70 kGy. Irradiations were performed at various times over a period of several years. The doses were chosen to approximately halve the light yield.

5.4 Measurement technique

The light output from the rods is measured before and after irradiation using an alpha source (^{239}Pu , 80 nCi) and a Hamamatsu R6091 photomultiplier tube, as shown in

Fig. 5.2 [bottom]. The penetration depth of its 5.156 MeV alpha in PS is 0.037 mm [124]. Each rod was placed on the photomultiplier tube, operated at +1,700 V, and the source was placed on the rod. An alignment fixture ensured the reproducibility of the alignment of the three pieces. The measurements were made using a Tektronix oscilloscope model TDS7104, with a charge integration window of 100 ns. The measurements used in subsequent plots, except where explicitly noted, occurred after annealing was complete. Our measurements are therefore of the permanent damage. Figure 5.3 [top] shows alpha spectra at various times after irradiation for a rod, illustrating the annealing process.

After pedestal subtraction, the distribution is fit to a Gaussian around the peak, and its mean is used as a measure of the light yield. Before and after a series of rod measurements, we measure a standard reference rod to calibrate any photomultiplier gain drift and to validate the performance of the equipment. Each rod is measured multiple times. The systematic uncertainty in the light output is dominated by the imperfect registration of the photomultiplier, rod, and alpha source. This systematic uncertainty was estimated from the variation in repeated light yield measurements of a given rod and is $\pm 0.5\%$. Other sources of systematic uncertainty in the precision of the signal measurement for an individual rod are negligible. Systematic uncertainties due to effects of environmental factors and manufacturing tolerance on variations between rods are on the order of a few percent.

Transmission measurements as a function of wavelength were taken using a Varian Cary 300 spectrophotometer. Fig. 5.3 [bottom] shows some results of typical transmission measurements. The position of the edge in transmission for the scintillating rods corresponds to the end of the absorption spectrum for the secondary fluor.

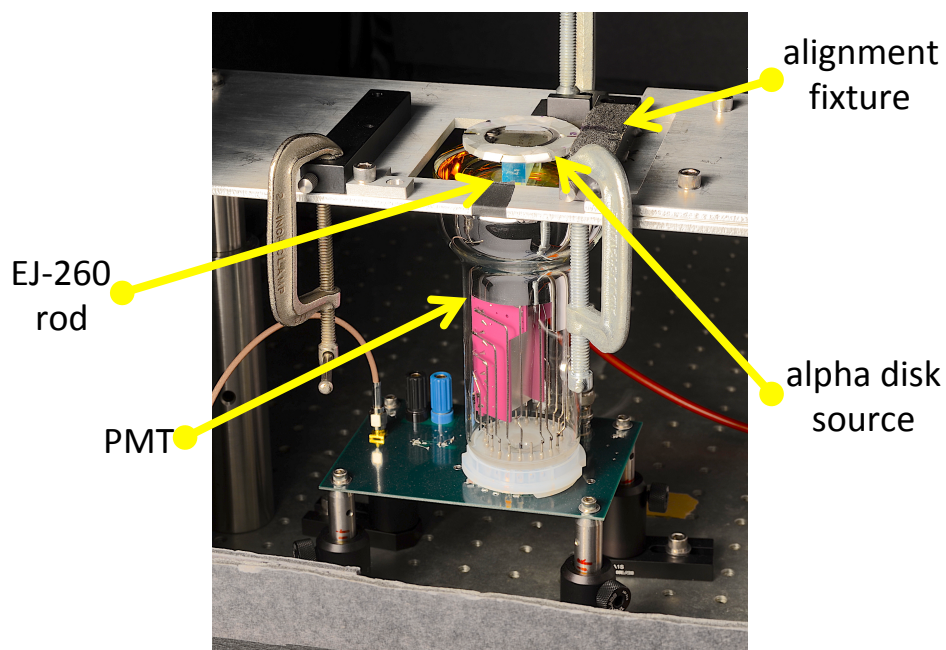
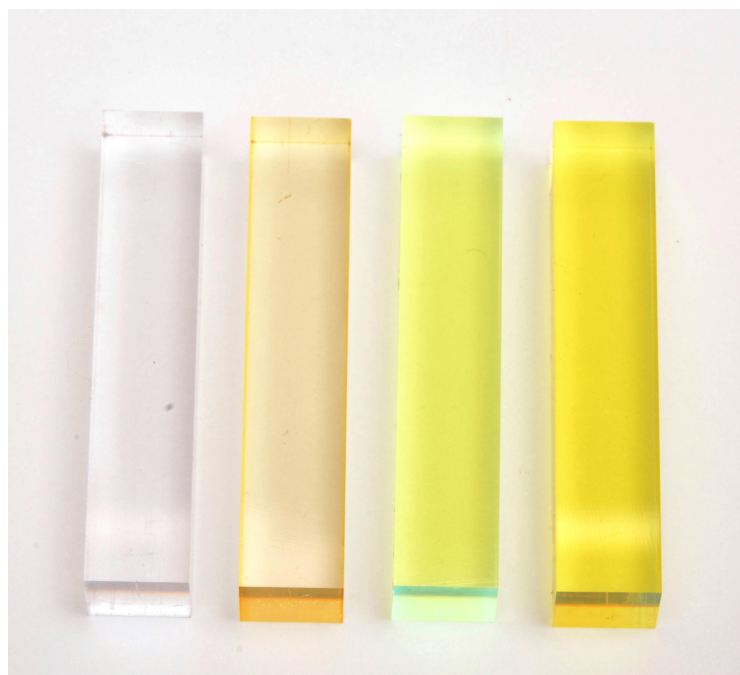


Figure 5.2: [top] A photograph of selected rods, all with nominal doping. From left to right: unirradiated EJ-200, EJ-200 irradiated to 500 kGy at 11 kGy/hr, unirradiated EJ-260, EJ-260 irradiated to 500 kGy at 11 kGy/hr. [bottom] Apparatus for measurements with an alpha source. In use, the apparatus is enclosed in a light-tight box.

In order to facilitate comparison of the spectra from samples with different doses, a pseudo-inverse of D , \mathcal{D}^{-1} , is calculated as a function of wavelength:

$$\mathcal{D}^{-1} = \frac{\ln(T_o) - \ln(T_f)}{d} \quad (5.9)$$

where T_o and T_f are the transmission as a function of wavelength before and after irradiation, respectively.

5.5 Results

Figure 5.4 shows the ratio of the light output of a rod before and after irradiation as a function of d . The rod's matrix is PVT, and the irradiation \mathcal{R} was 460 Gy/hr. Each point corresponds to a separate rod. Some of the rods presented in this figure experienced pauses of 1-3 days, with the full annealing time for this material being approximately 1 month. The results at this \mathcal{R} are well described by an exponential for doses below 40 kGy. Above this, some saturation may be occurring. Since many of our results are based on irradiation of 70 kGy (see A), this may indicate the values are an underestimate of the damage for lower doses. For the CMS detector in HL-LHC running, doses up to a few kGy are expected in the scintillator part of the high granularity calorimeter [91].

Figure 5.5 shows D versus \mathcal{R} for scintillator rods with the EJ-200 fluors at the manufacturer's nominal concentration and with nominal antioxidant concentration, for both PS and PVT matrices. The values of D for the two matrices are similar for \mathcal{R} s between 2 and 100 Gy/hr, and are approximately linear in the logarithm of the \mathcal{R} . For $\mathcal{R} > 100$ Gy/hr, D is larger at larger \mathcal{R} for PVT, while for PS it is smaller or constant at

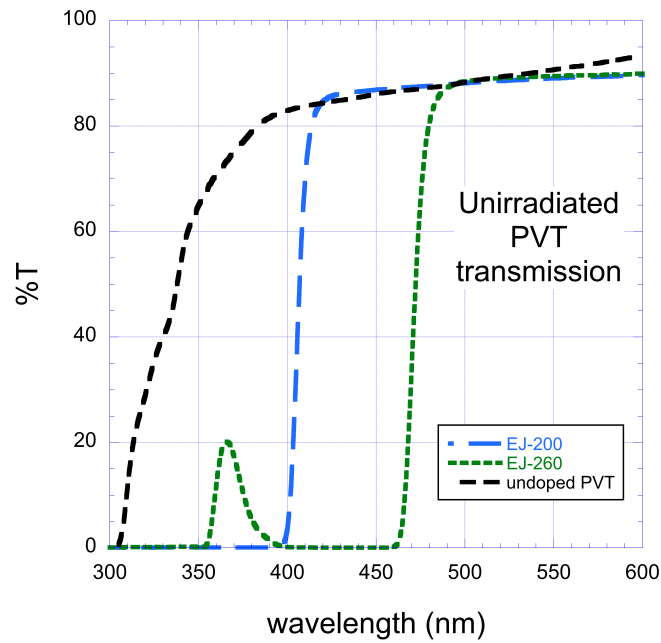
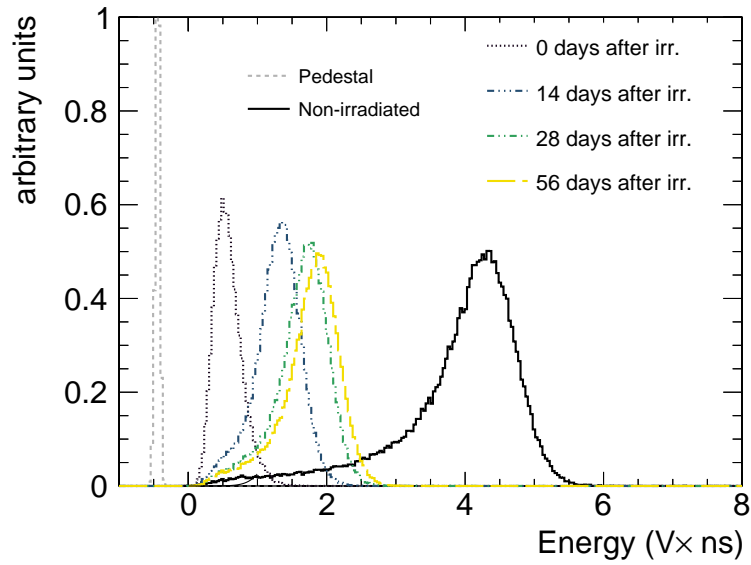


Figure 5.3: [top] Measured energy spectrum from a rod irradiated at 3640 Gy/hr to a dose of 70 kGy when excited using an alpha source at various times since irradiation, showing the annealing process. [bottom] Typical transmission spectra for rods with nominal fluor and antioxidant concentrations and with a PVT matrix, with no fluors (black, medium dashes), EJ-260 fluors (green, short dashes), and for EJ-200 fluors (blue, long dashes).

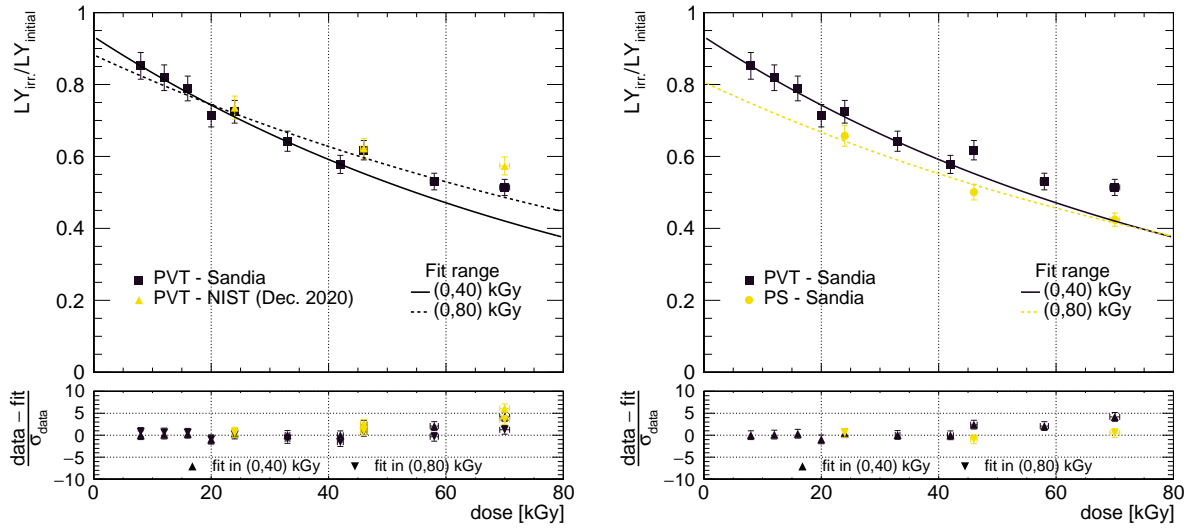


Figure 5.4: [left] Ratio of the light output of rods after receiving a dose d to their unirradiated light output, versus d . The rods' matrix is PVT, and the irradiation dose rate was 0.46 kGy/hr. The different colors correspond to different irradiation dates and facilities. Rods irradiated at Sandia National Laboratories and NIST are represented with black and yellow markers, respectively. The lines are fits of the Sandia data to exponentials, one using only the lower dose data and the other using all data. Uncertainties are dominated by systematic uncertainties. [right] Same, comparing PS and PVT. All rods included in this plot have been irradiated at Sandia National Laboratories.

larger \mathcal{R} . The scatter in the data reveals an uncontrolled systematic, perhaps related to changes in manufacturing over the period of the purchases, or due to uncontrolled environmental variables. The radiation hardness of PS and PVT is similar at low \mathcal{R} . At high \mathcal{R} , PVT is more radiation tolerant for EJ-200 (blue).

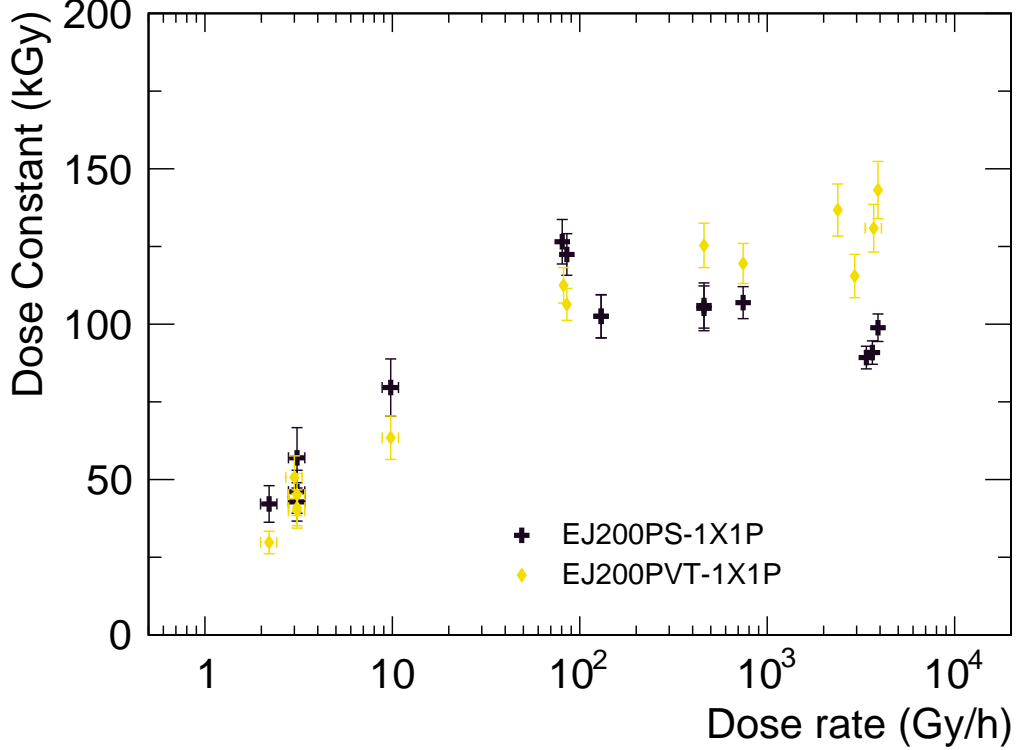


Figure 5.5: The value of D versus \mathcal{R} for scintillator rods with the EJ-200 fluors at the manufacturer's nominal concentration and with nominal antioxidant concentration, for PVT (blue markers) and PS (black markers).

Figure 5.6 shows D versus \mathcal{R} for scintillator rods with the EJ-260 fluors at the manufacturer's nominal concentration and nominal antioxidant concentration, for both PS and PVT matrices. The results are similar to those for the EJ-200 fluors at \mathcal{R} s below about 100 Gy/h. At higher \mathcal{R} s, the results for PVT are similar to those of EJ-200, while the radiation resistance of PS is improved.

Figure 5.7 shows the \mathcal{D}^{-1} results for the PS and PVT versions of the EJ-200 and EJ-

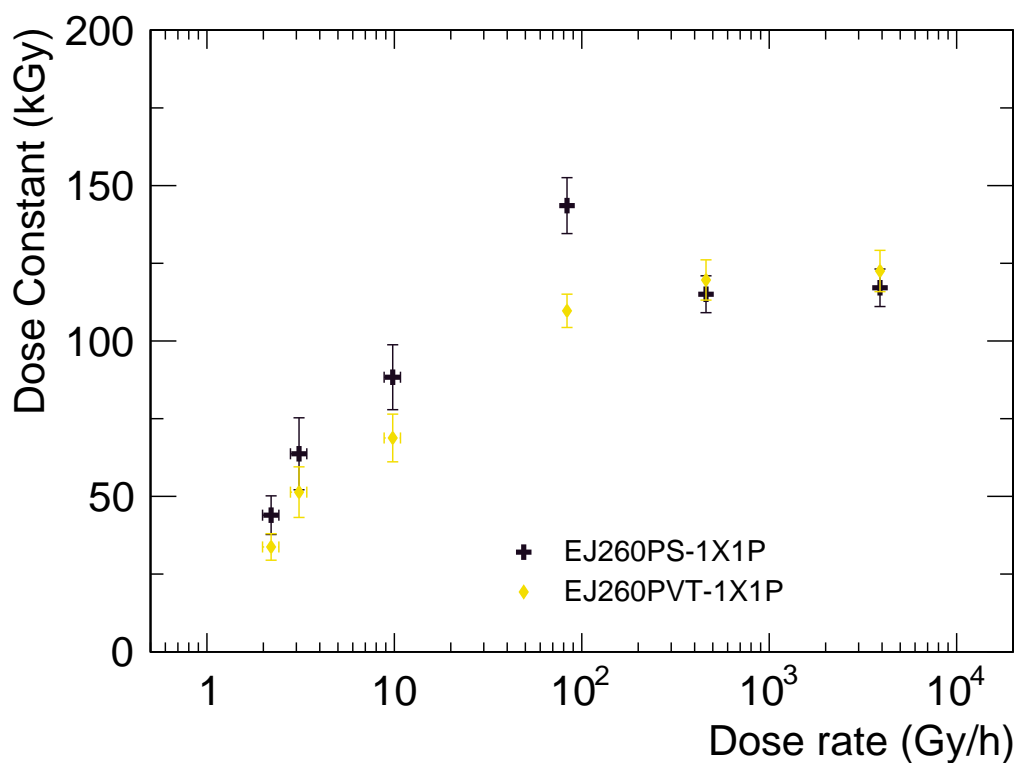


Figure 5.6: The value of D versus \mathcal{R} for scintillator rods with the EJ-260 fluors at the manufacturer's nominal concentration and with nominal antioxidant concentration, for PS and PVT matrices.

260 scintillators for \mathcal{R} s of 3.1 Gy/hr and 3900 Gy/hr. Larger positive values correspond to more damage. Negative values of \mathcal{D}^{-1} are consistent with destruction of the fluor, resulting in less light self-absorption. For EJ-200, the emission and absorption spectra for the secondary fluor overlap in the range $370 \text{ nm} < \lambda < 390 \text{ nm}$. Figure 5.8 shows ratios of \mathcal{D}^{-1} values for high and low \mathcal{R} , and for PS and PVT. For EJ-200, in the region of secondary emission above 410 nm, there is more damage at low \mathcal{R} than at high \mathcal{R} . The damage is larger at lower wavelengths as expected from previous results [94]. The values at low \mathcal{R} for PS and PVT are similar. The value of \mathcal{D}^{-1} is negative in the region where the absorption and emission bands of the primary overlap, indicating some destruction of the secondary fluor.

For EJ-260, the damage was smaller, and the rods were too thin to allow for accurate measurement in this case. There is an indication of color center formation just below 475 nm, which is at the start of the region of the primary emission. In both PS and PVT, this feature did not appear in EJ-200. These color centers formed more at low \mathcal{R} than at high, more in PVT than in PS at low \mathcal{R} , and at about the same rate in PS and PVT at high \mathcal{R} . Absorption from the color centers is low enough in wavelength, though, that it does not affect the light output very much. The ratios show that, except for the comparison between PVT and PS for EJ-200, the effects are roughly independent of wavelength.

5.6 Thickness, fluor concentration, and antioxidant concentrations

Changes in light output due to color center formation can be distinguished from a decrease in initial light production through the dependence of D on the rod thickness.

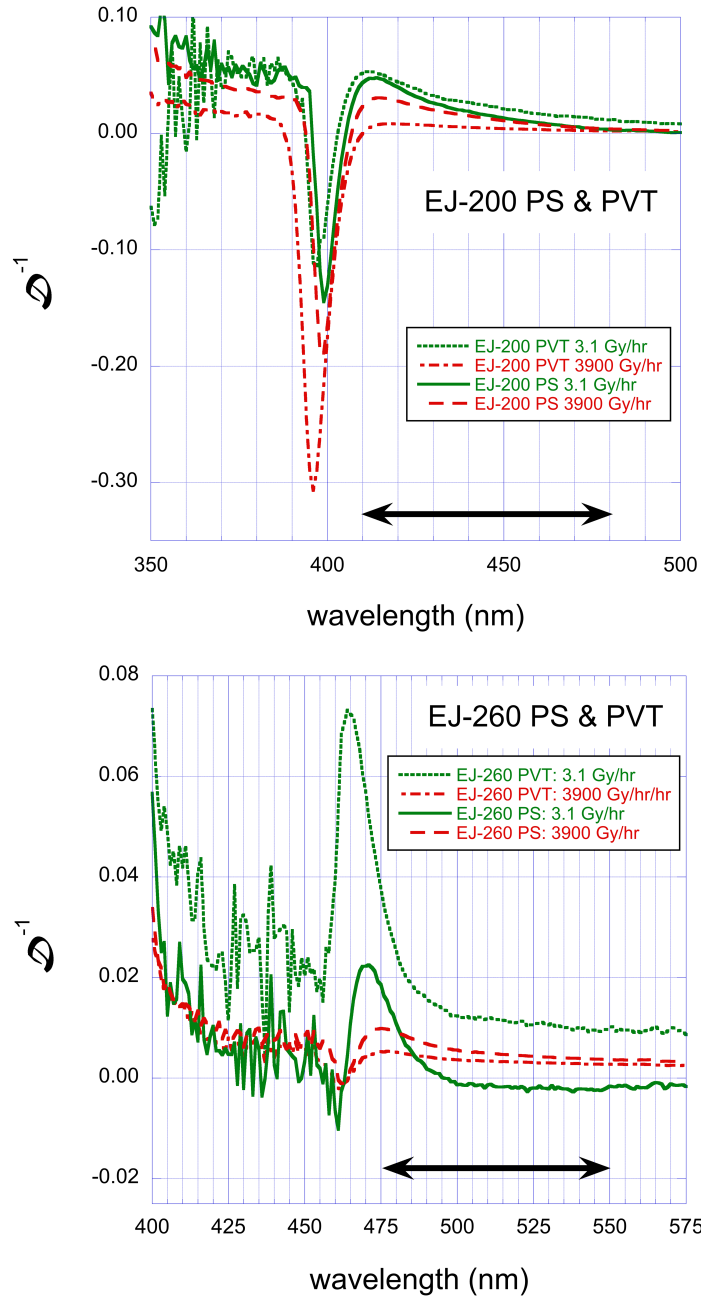


Figure 5.7: [top] The value of \mathcal{D}^{-1} for scintillator with the EJ-200 fluors, for both PS and PVT, at \mathcal{R} s of 3.1 Gy/hr to a total dose of 12.6 kGy and 3900 Gy/hr to a total dose of 70 kGy. [bottom] The value of \mathcal{D}^{-1} for scintillator with the EJ-260 fluors, for both PS and PVT, at \mathcal{R} s of 3.1 Gy/hr to a total dose of 12.6 kGy and 3900 Gy/hr to a total dose of 70 kGy. In both plots, the emission range for the secondary fluor is indicated by a double arrow. Negative values of \mathcal{D}^{-1} correspond to increases in the transmission after irradiation.

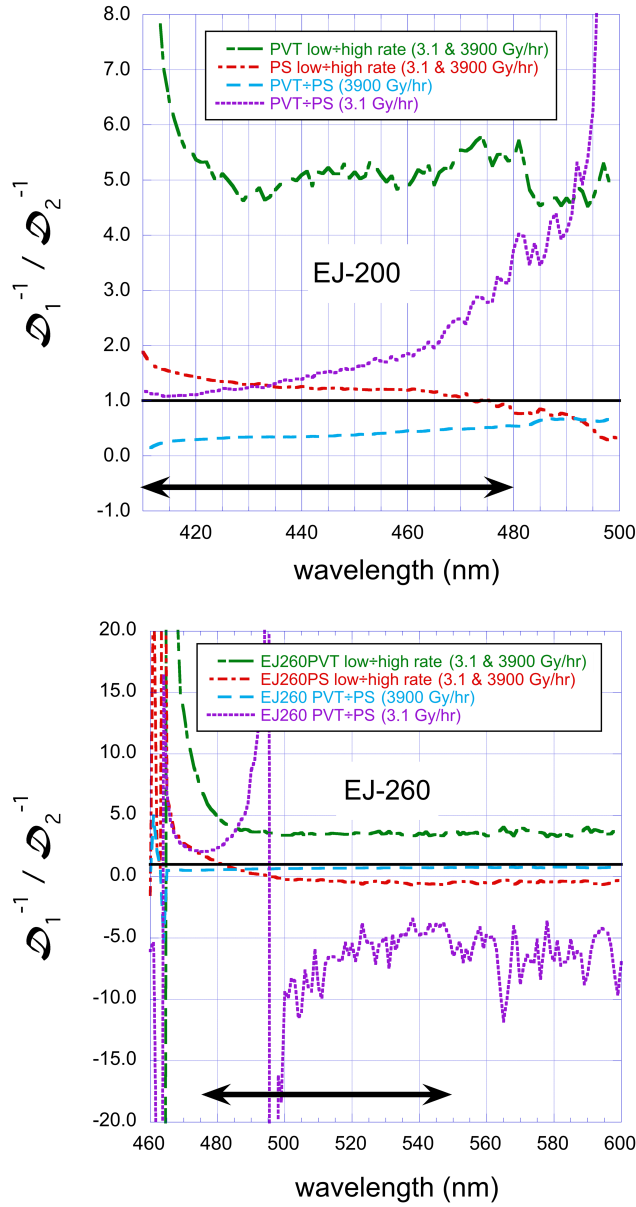


Figure 5.8: Ratios $\mathcal{D}_1^{-1} / \mathcal{D}_2^{-1}$ are plotted versus wavelength, where \mathcal{D}_1^{-1} and \mathcal{D}_2^{-1} are values of \mathcal{D}^{-1} corresponding to different cases of irradiations or irradiated materials. The precise cases are defined separately for each ratio. Two different irradiations are included, a high \mathcal{R} one at 3900 Gy/hr (total dose: 70 kGy) and a low \mathcal{R} one at 3.1 Gy/hr (total dose: 12.6 kGy). [top] EJ-200 for PVT at low \mathcal{R} divided by high \mathcal{R} (green dash), PS at low \mathcal{R} divided by high \mathcal{R} (red dot-dash), PVT divided by PS both at low \mathcal{R} (purple dot), PVT divided by PS both at high \mathcal{R} (red dot-dash) [bottom] EJ-260 for PVT at low \mathcal{R} over high \mathcal{R} (green dash), PS at low \mathcal{R} over high \mathcal{R} (red dot-dash), PVT over PS both at low \mathcal{R} (purple dot), PVT over PS both at high \mathcal{R} (red dot-dash) In both plots, the emission range for the secondary fluor is indicated by a double arrow. The solid black line indicates a value of 1.0.

If the color center formation is independent of whether or not the region is oxidized, D will scale as l^{-1} . If the color centers form predominantly in the oxidized regions, this scaling will only occur once the entire sample is permeated with oxygen, and will be independent of thickness above this value, as the effective thickness is $2z_0$. For PS, at our lowest \mathcal{R} , oxygen permeates the rod for thicknesses below 0.6 cm. If the damage is to initial light production, D will not depend on the thickness. Because all our rods are thin, the color center density must be large to produce measurable light attenuation.

Figure 5.9 shows the results for PS rods with EJ-200 fluors. The results for PVT rods are similar. The top figure shows D versus date since the end of irradiation. At 14 days since irradiation, the value of D for the 1.0 cm rod is 1.5 times smaller (more damage) than that of the 0.4 cm rod, while at 56 days the ratio is 1.1. The ratio of the thicknesses is 2.5. Just after irradiation, when the density of color centers is higher, D depends more strongly on the thickness. After annealing, the dependence is small. This indicates that for small pieces like this, where the path length in the scintillator is small, the dominant source of light loss after annealing is the change in the initial light production. The bottom figure shows the value of D after annealing as a function of \mathcal{R} . Loss of initial light dominates at all measured \mathcal{R} s.

Oxidized polymers tend to absorb light with wavelengths corresponding to emission by the primary fluor. Because of this, we investigated the effect of varying the dopant and antioxidant concentrations. Figures 5.10 [top] and [bottom] show D versus \mathcal{R} for scintillator rods with the EJ-200 fluors, PS and PVT matrix, respectively, and the manufacturer's nominal antioxidant concentration, for nominal fluor concentrations (1X1P), with twice the nominal primary concentration (1X2P) and with twice the nominal secondary

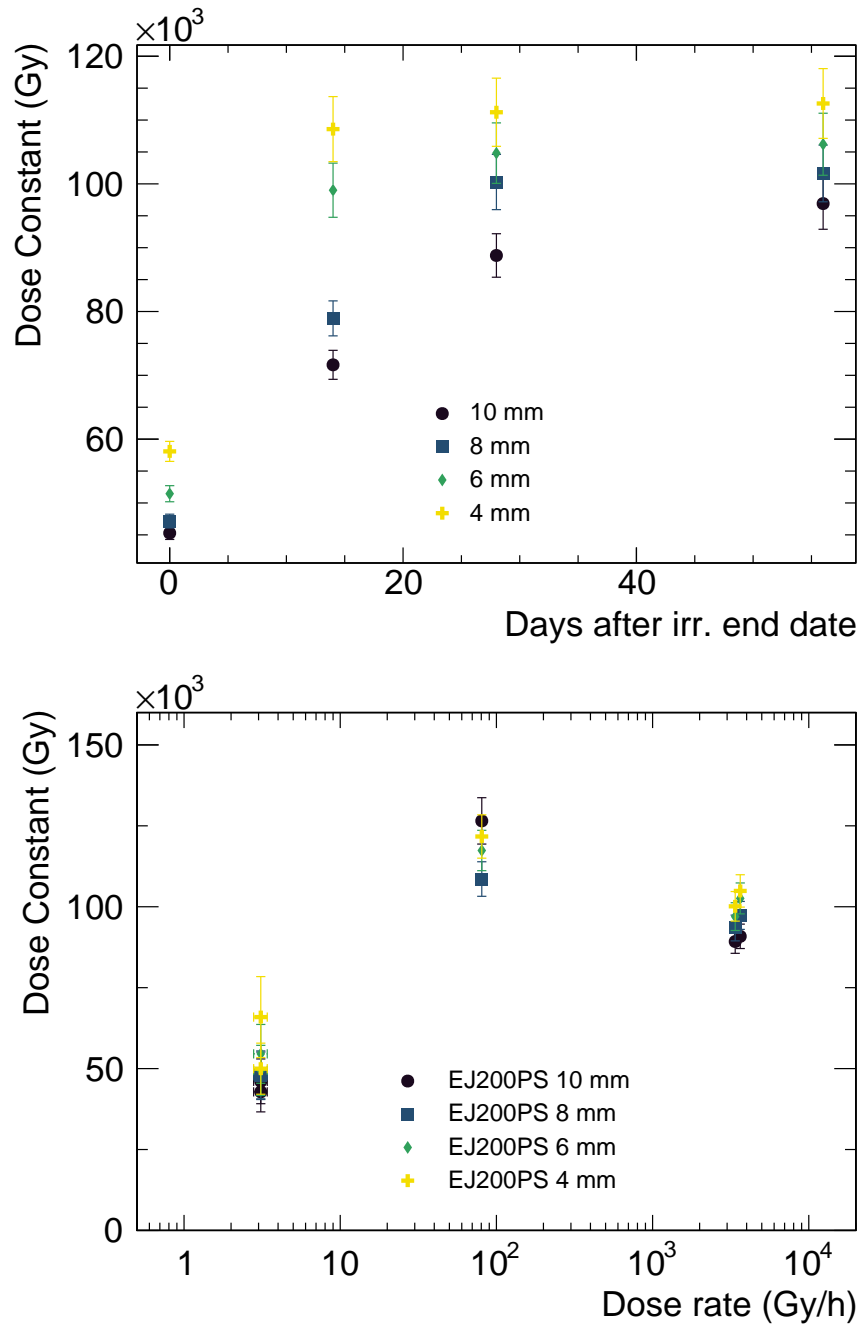


Figure 5.9: For rods with EJ-200 fluors made of PS: [top] value of D versus day since end of irradiation for a \mathcal{R} of 3640 Gy/hr, for rod thicknesses of 0.4 cm, 0.6 cm, 0.8 cm, and 1.0 cm; [bottom] value of D after annealing versus \mathcal{R} for rod thicknesses of 0.4 cm, 0.6 cm, 0.8 cm, and 1.0 cm.

concentration (2X1P). The results reveal increased radiation tolerance at high \mathcal{R} s for PS-based scintillators with twice the nominal primary fluor concentration (PS-1X2P). The rest of the results are independent of the fluor concentration within uncertainties.

Figure 5.11 shows the results for the EJ-200 fluors at the nominal concentration in PVT without antioxidants (AO-0), with the nominal antioxidant concentration (AO-1), and with twice the nominal concentration (AO-2). The results are independent of antioxidant concentration within uncertainties. This is expected, since antioxidants are in the amorphous and not the crystalline regions of the matrix. PVT is in a glassy state at room temperature. It is almost impossible for the antioxidant molecules to move around and react with the C-centered radicals or the peroxy radicals.

5.7 Conclusions

Results on the effects of ionizing radiation on the signal produced by plastic scintillating rods manufactured by Eljen Technology company were presented. Assuming an exponential decrease in the light output with dose, the change in light output was quantified using the exponential dose constant D .

The D values are similar for primary and secondary doping concentrations of 1 and 2 times, and for antioxidant concentrations of 0, 1, and 2 times, the default manufacturer's concentration, which suggests that the default concentrations are optimal. The D value depends approximately linearly on the logarithm of the dose rate for dose rates between 2.2 Gy/hr and 100 Gy/hr for all materials. For the EJ-200 polyvinyltoluene-based (PVT) scintillator, the dose constant is approximately linear in the logarithm of the dose rate

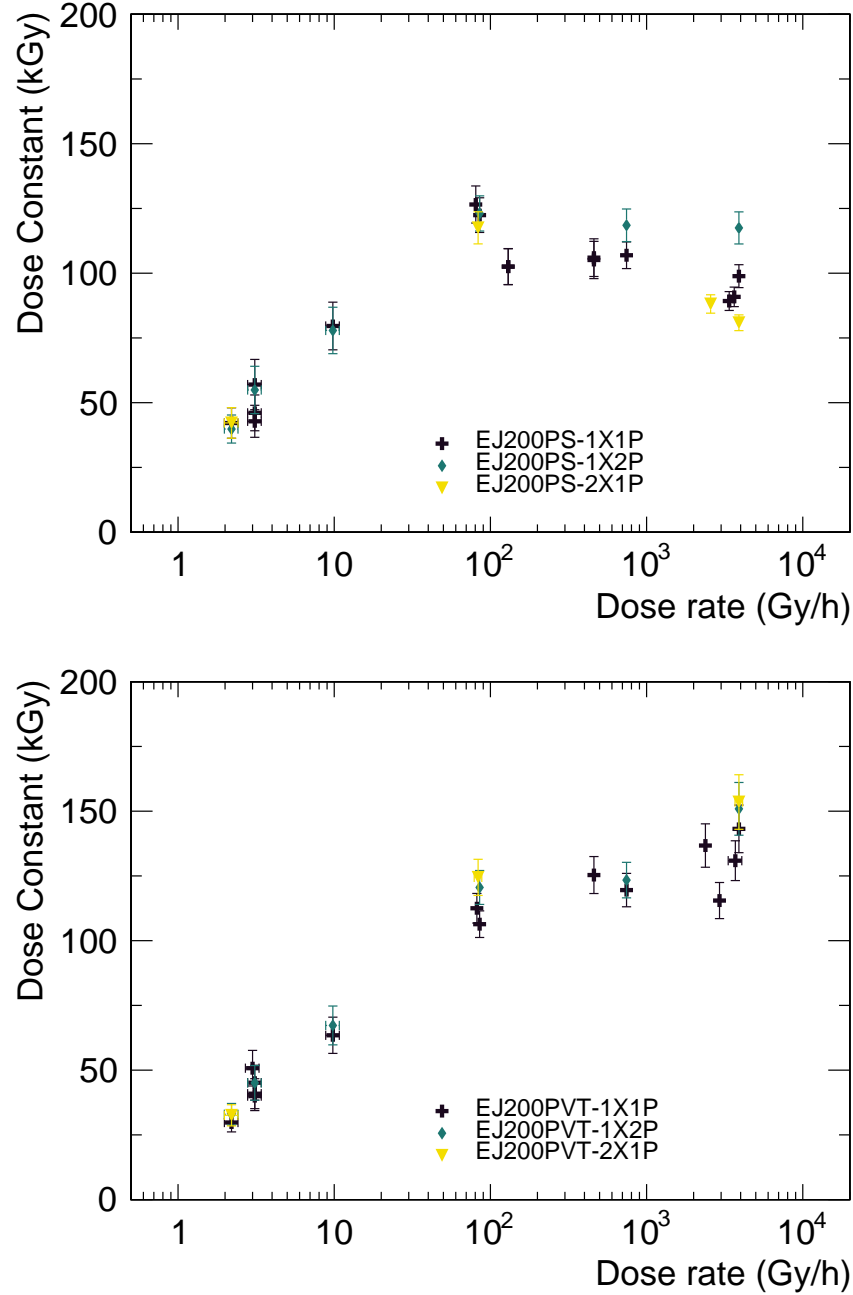


Figure 5.10: [top] The value of D versus \mathcal{R} for PS scintillator rods with the EJ-200 fluors at the manufacturer's nominal concentration for antioxidants for the nominal concentration of fluors (1X1P), for double the concentration of the primary fluor (1X2P), and double the concentration of the secondary fluor (2X1P). [bottom] The value of D versus \mathcal{R} for PVT scintillator rods with the EJ-200 fluors at the manufacturer's nominal concentration for antioxidants for the nominal concentration of fluors (1X1P), for double the concentration of the primary fluor (1X2P), and double the concentration of the secondary fluor (2X1P).

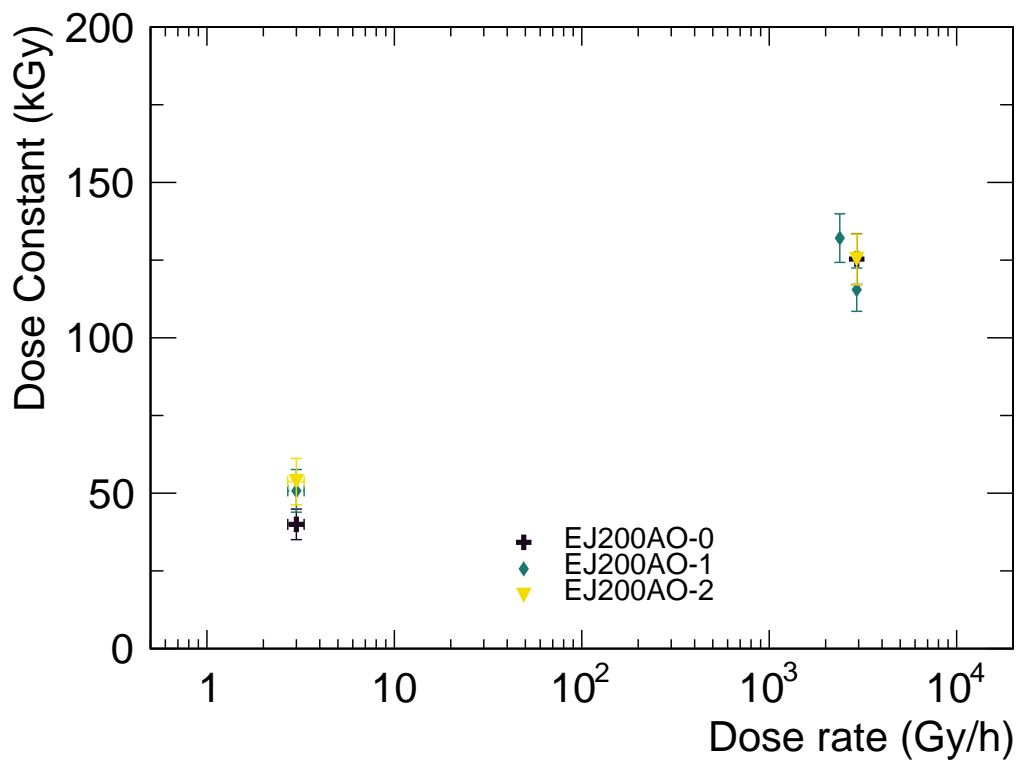


Figure 5.11: The value of D versus \mathcal{R} for scintillator rods with the EJ-200 fluors in PVT at the manufacturer's nominal concentration for fluors without antioxidant additives (AO-0), with the nominal concentration (AO-1), and with twice the nominal (AO-2).

up to 3900 Gy/hr, while for the polystyrene-based (PS) scintillator or both materials with EJ-260 fluors, it remains constant or decreases (depending on doping concentration) above about 100 Gy/hr.

These results show that the conventional wisdom that PVT is more radiation-resistant than PS is only true at high dose rates, for the short paths to the photodetector tested here. Shifting the wavelength from blue to green again only aids in radiation resistance for dose rates higher than typically found at collider detectors for short path lengths.

The results from rods of varying thickness and the different fluors suggest that damage to the initial light output is a larger effect than color center formation for scintillator thickness ≤ 1 cm. For the blue scintillator (EJ-200), the transmission measurements indicate damage to the fluors.

Chapter 6: Effects of radiation damage on optical properties of scintillators and the role of oxygen.

This Chapter presents our studies on the effect of radiation damage and oxygen presence on the optical properties of plastic scintillators. This work is published in Ref. [79], and the text here relies heavily on the content of this publication. I was the first person to notice the refractive index effect in the laboratory. I contributed the majority of the text, conceptualization, software development, data analysis, and plotting. As mentioned at the beginning of Chapter 4, I am the first author of this publication. The design of the methodology for the refraction index measurements was performed equally with M. Y. Aamir. The measurements of the refractive indices were performed by M. Y. Aamir, who at the time was an undergraduate student whom I supervised. Initial code for the CUDA simulation was provided by B. Kronheim and underwent significant changes by me to produce the presented results.

6.1 Oxygen diffusion theory

This section presents an overview of the oxygen diffusion theory in polymers, followed by a discussion of two models that incorporate the effect of oxidation on oxygen diffusion. These two models follow two different approaches, the first having

been developed for oxidation induced by ionizing radiation and the second for photo-oxidation.

6.1.1 Oxygen diffusion in polymers

The diffusion of a gas into a solid or liquid material is described by Fick's two laws of diffusion [125, 126]. The first Fick's law is for the diffusion flux J

$$J = -D \frac{dC}{dx}, \quad (6.1)$$

where D is the diffusion coefficient, and C is the concentration. The second Fick's law is the diffusion equation

$$\frac{\partial C}{\partial t} = D \frac{\partial^2 C}{\partial x^2}. \quad (6.2)$$

The dissolved amount of a gas in a solid or liquid at equilibrium is described by Henry's law [127]

$$C = Sp, \quad (6.3)$$

where p is the partial pressure of the gas at the surface of the material, and S is the solubility (or Henry) coefficient. The polymers used in scintillators are usually amorphous and have a low degree of crystallinity. For these polymers, which are commonly characterized as glassy, two solubilities can be defined, one for diffusion in the material, following Henry's law, and one for diffusion in the voids in the material that is described by Langmuir isotherms [128, 129].

For a thin membrane, Fick's second law can be rewritten using Henry's law as

$$J = -DS \frac{\Delta p}{\delta} = -\bar{P} \frac{\Delta p}{\delta}, \quad (6.4)$$

where Δp is the pressure difference between the two sides of the membrane, δ is its thickness, and \bar{P} is the permeability.

The quantities described in the previous paragraphs have temperature dependencies. Specifically, the solubility S obeys a van 't Hoff equation [130]

$$S = S_0 e^{-\frac{\Delta H_S}{RT}}, \quad (6.5)$$

where ΔH_S is the enthalpy change, R is the universal gas constant, and T is the temperature in degrees Kelvin. The diffusivity and the permeability are known to be described by the Arrhenius equation [128, 130]

$$\bar{P} = \bar{P}_0 e^{-\frac{E_p}{RT}}, \quad (6.6)$$

where E_p is the apparent energy of activation of the permeation process, and

$$D = D_0 e^{-\frac{E_d}{RT}}, \quad (6.7)$$

where E_d is the activation barrier for diffusion.

In the following section, the polymer model that was introduced by Seguchi *et al.* in [131, 132] is studied. The model, a schematic of which is shown in Fig. 6.1, describes a

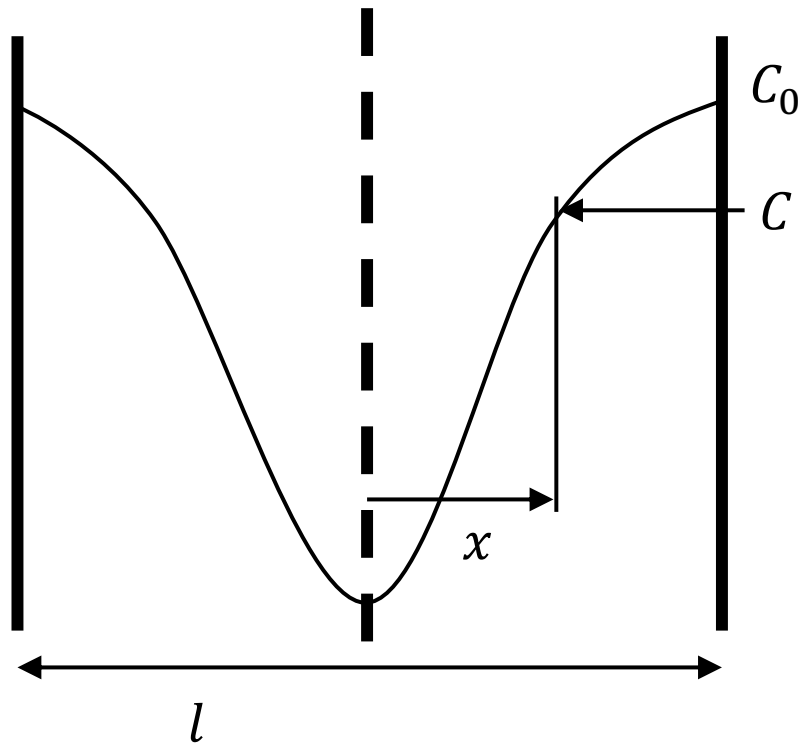


Figure 6.1: A 1-dimensional description of oxygen diffusion in the polymer. The thickness is l , C_0 , and $C(x, t)$ are the oxygen concentrations at the surface and the interior of the polymer, and x is the distance from the center.

polymer film of thickness l with oxygen concentration $C(x, t)$ that obeys the following boundary conditions

1. $C = C_0$ at $x = \frac{l}{2}, -\frac{l}{2}$ for all t ,
2. $C = 0$ for $t = 0$ and $-\frac{l}{2} < x < \frac{l}{2}$,
3. $\frac{\partial C}{\partial x} = 0$ at $x = 0$ for all t .

Fick's second law of diffusion (Eq. 6.2) describes this situation. The solution to this equation is well-known in literature [131, 133]:

$$\frac{C(x, t)}{C_0} = \sum_{n=0}^{\infty} (-1)^n \operatorname{erfc} \frac{(2n+1)\frac{l}{2} - x}{2\sqrt{Dt}} + \sum_{n=0}^{\infty} (-1)^n \operatorname{erfc} \frac{(2n+1)\frac{l}{2} + x}{2\sqrt{Dt}}. \quad (6.8)$$

6.1.2 JAERI model for oxidation during irradiation

The work by Seguchi *et al.* in [131, 132] describes in detail the chemical reactions involved with oxidation during irradiation and studies the effect of oxygen diffusion at equilibrium for that reaction chain. In this section, these calculations are rederived following the manner of [131, 132].

The reactions related to irradiation and oxygen for a polymer P can be described by the following formulas that describe the radical formation process



where P^\bullet is the symbol for the polymer radicals, Y is the specific rate of radical formation, and \mathcal{R} is the dose rate; the radical recombination processes, including crosslinking, have the general form



where k_1 is the rate constant for radical recombination; and the radical oxidation process



where k_2 is the rate constant for the oxidation process.

The equation that describes the balance between the polymer radicals and oxygen concentration can be formulated as

$$\frac{d[P^\bullet]}{dt} = Y\mathcal{R} - k_1[P^\bullet]^2 - k_2[P^\bullet]C(x, t), \quad (6.12)$$

where $[P^\bullet]$ is the density of polymer radicals, $C(x, t)$ is the oxygen concentration, and x is the distance from the center of the polymer's cross-section. In steady state, the first time derivative is 0, and Eq. 6.12 becomes

$$[P^\bullet] = \frac{-k_2C(x) + \sqrt{(k_2C(x))^2 + 4k_1Y\mathcal{R}}}{2k_1}. \quad (6.13)$$

Beginning from the oxygen diffusion equation, we find the equation for the oxygen

concentration balance

$$\frac{\partial C(x, t)}{\partial t} = D \frac{\partial^2 C(x, t)}{\partial x^2} - k_2[P^\bullet]C(x, t), \quad (6.14)$$

where D is the diffusion coefficient for oxygen in the polymer. The following boundary conditions are assumed

1. $C = C_0$ for $t = 0$ and $-\frac{l}{2} \leq x \leq \frac{l}{2}$,
2. $\frac{dC}{dx} = 0$ at $x = 0$ and for all t ,
3. $C = C_0$ at $x = \pm \frac{l}{2}$ and for all t .

6.1.2.1 If $\frac{4k_1Y\mathcal{R}}{(k_2C)^2} \ll 1$ for all x

When the combined rate of radical creation and crosslinking is much lower than the oxygen bonding rate throughout the sample, then the inequality $\frac{4k_1Y\mathcal{R}}{(k_2C)^2} \ll 1$ is true for all x , and Eq. 6.13 can be simplified by Taylor-expanding the square root to

$$[P^\bullet] = \frac{Y\mathcal{R}}{k_2C(x, t)}. \quad (6.15)$$

By substituting this result into Eq. 6.14, we arrive at

$$\frac{\partial C(x, t)}{\partial t} = D \frac{\partial^2 C(x, t)}{\partial x^2} - Y\mathcal{R}. \quad (6.16)$$

For the steady-state case, Eq. 6.16 becomes

$$D \frac{\partial^2 C(x)}{\partial x^2} = Y\mathcal{R}. \quad (6.17)$$

The solution to this differential equation is

$$1 - y = \beta \left(\frac{1}{4} - \lambda^2 \right), \quad (6.18)$$

where $y \equiv \frac{C}{C_0}$, $\lambda \equiv \frac{x}{l}$, and

$$\beta = \frac{Y\mathcal{R}l^2}{2DC_0}. \quad (6.19)$$

The steady-state solutions for different β are shown in Fig. 6.2 . The code that reproduces this figure is available in Ref. [20]. For low values of β , the effect on oxygen concentration is small. The concentration in the center of the sample becomes lower as the value of β grows until the limiting case in which $\beta = 4$ and $y = 0$ for $\lambda = 0$. Eq. 6.18 is not a good description for $\beta \gtrsim 4$.

If the system is not in steady state, then Eq. 6.16 can only be solved numerically by approximating the derivatives of $C(x, t)$ via a finite differences method.

6.1.2.2 If $\frac{4k_1Y\mathcal{R}}{(k_2C)^2} \ll 1$ is not true for all x

In some cases, oxygen is consumed at rates that cannot be replenished by diffusion, and the concentration can become 0 in the central region of the polymer. This is true when the dose rate is sufficiently high for a given set of the rate constants k_1 , k_2 , and Y . The differential equation is not analytically solvable in this case, but it can be approximated

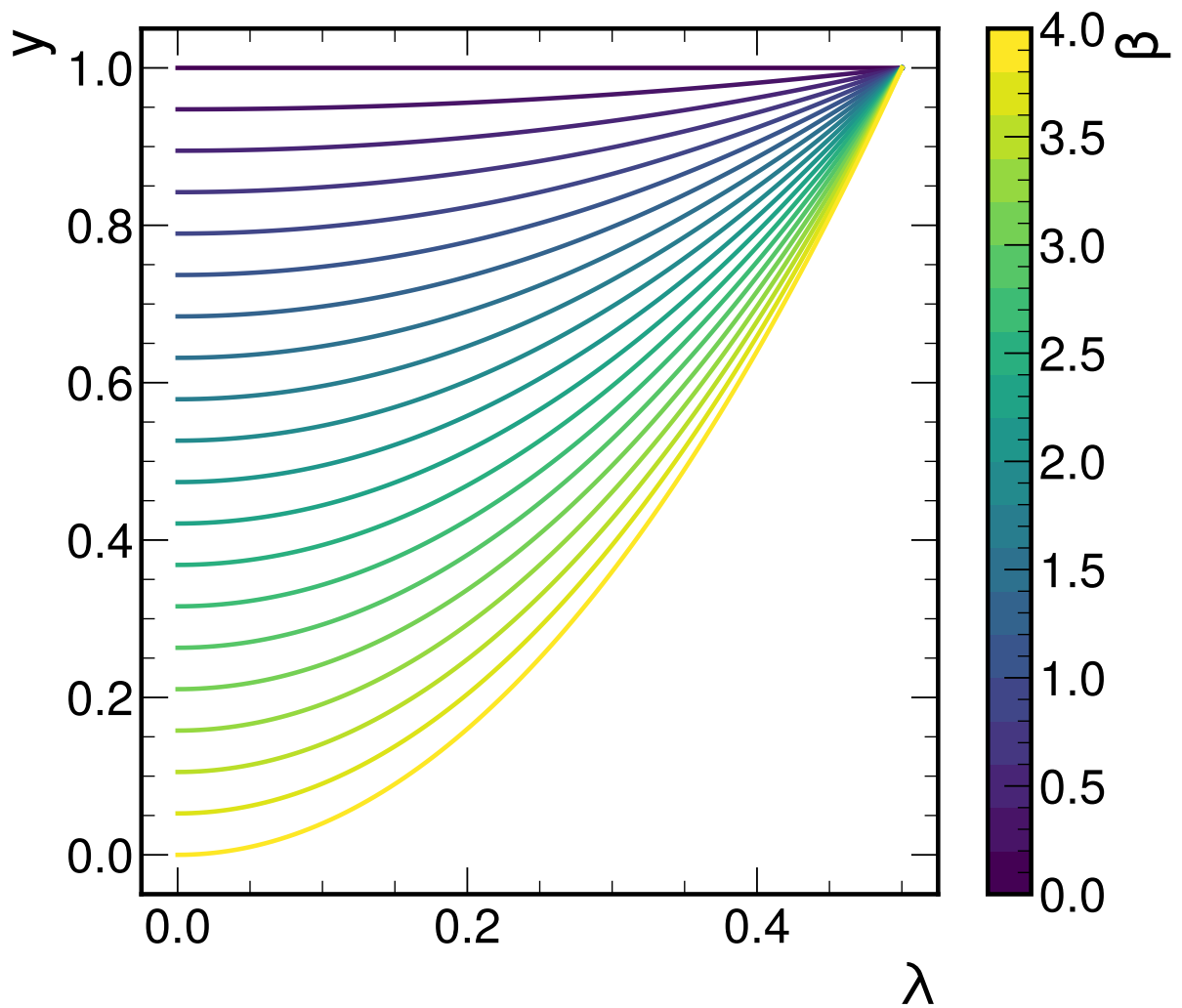


Figure 6.2: The normalized oxygen concentration y at the stationary state under irradiation is plotted for the limiting case $\frac{4k_1Y\mathcal{R}}{(k_2C)^2} \ll 1$ and for a range of values of β .

using a finite difference method. In considering the limiting case $C(0, t) = 0$, according to Eq. 6.18, $\beta = 4$. Then

$$l^2 = \frac{8DC_0}{Y\mathcal{R}}. \quad (6.20)$$

For the oxygen penetration depth $z \equiv l/2$, thus

$$z^2 = \frac{2DC_0}{Y\mathcal{R}}. \quad (6.21)$$

6.1.2.3 Numerical solution

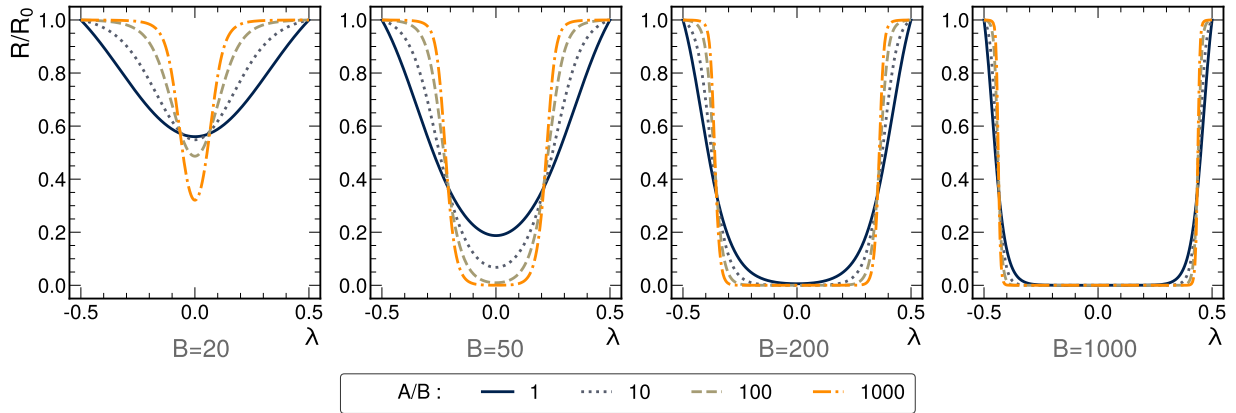


Figure 6.3: Numerical solutions to Eq. 6.22 for various combinations of values for the parameters $A \equiv \frac{C_0 k_2^2}{2Dk_1}$ and $B \equiv \frac{2Y\mathcal{R}}{DC_0}$. The parameter A is expressed through its ratio to B . The normalized reaction rate R/R_0 is shown for the entire normalized length λ . For the code used see Ref. [20].

The system of Equations 6.13 and 6.14 can be solved numerically by using `scipy`'s [134] ODE solver for boundary value problems. The full code is available in Ref. [20].

The formula to be solved is

$$\frac{d^2 y}{d\lambda^2} = Ay(\sqrt{y^2 + \frac{B}{A}} - y), \quad (6.22)$$

where $A \equiv \frac{C_0 k_2^2}{2Dk_1}$, $B \equiv \frac{2Y\mathcal{R}}{DC_0}$. Fig. 6.3 shows solutions of the normalized reaction rate R/R_0 for different combinations of the input parameters A and B . Parameter B determines whether an oxygen-depleted region will form in the middle of the sample, as well as how deep in the scintillator the boundary of the region will be. The ratio A/B controls how steep the transition will be. In particle colliders, plastic scintillators are usually placed in relatively low \mathcal{R} regions, so the curves corresponding to lower values of B and higher values of A/B should be more relevant. These results are in agreement with the approximating solutions made in the previous sections for specific ranges of the model parameters.

Understanding the dynamical evolution of the system requires a full simulation of Eqs. 6.12 and 6.14. For that reason, a custom CUDA implementation of the model is used to create a finite differences simulation of the 3-dimensional sample. The simulation utilizes a $500 \times 100 \times 100$ grid for the $5 \times 1 \times 1$ cm samples, and the input parameters are D , $Y\mathcal{R}$, k_1 , and k_2 . The diffusion coefficient D is set to a value of $0.1 \frac{(\text{lattice units})^2}{\text{time steps}}$ in order to keep the simulation runtime manageable. This value is equivalent to $10^{-8} \text{ cm}^2 \text{ s}^{-1}$ after considering that the experimental annealing time is approximately 30 days. The system is initialized with a nominal value of the oxygen concentration $C_0 = 1$ throughout the sample volume, and this value is kept steady at the outer boundary of the sample, thus imposing a Dirichlet boundary condition. Both the oxygen and the polymer radical concentrations are evolved for 10,000 time steps, simulating the irradiation. Subsequently, the $Y\mathcal{R}$ parameter is set to 0 and the system is evolved for another 10,000 steps, simulating the annealing period. Fig. 6.4 shows the normalized oxygen concentration and oxidation

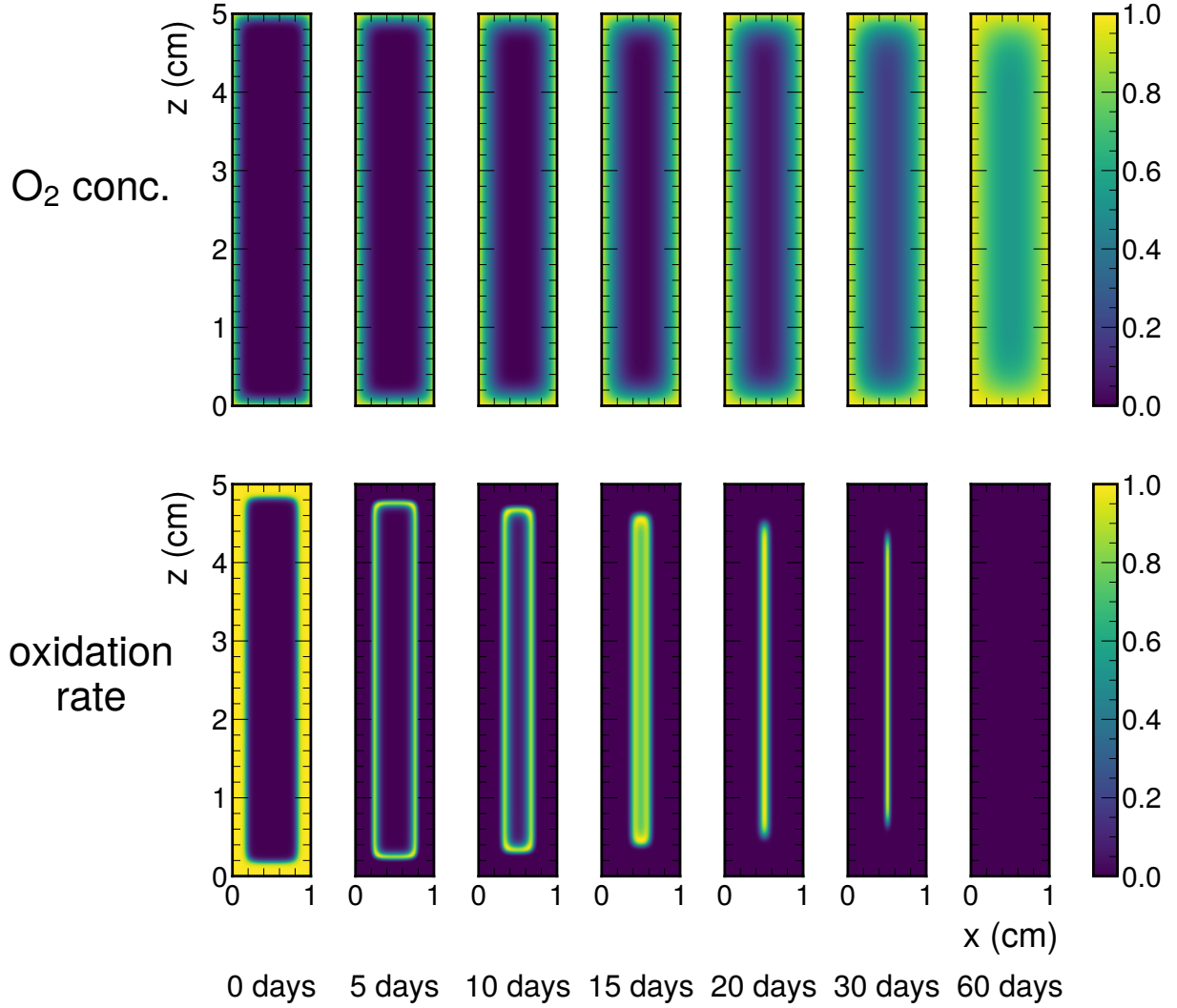


Figure 6.4: Distributions of the normalized O_2 concentration and the oxidation rate for different points in time during the annealing process for the 3D finite differences simulation of the JAERI model. The input parameters are $k_1 = 5 \cdot 10^{-11} \text{ cm}^3\text{s}^{-1}$, $k_2 = 2 \cdot 10^{-10} \text{ cm}^3\text{s}^{-1}$, and $Y\mathcal{R} = 0.6 \text{ cm}^{-3}\text{s}^{-1}$. At $t = 0$, the irradiation stops and the annealing period begins.

rate for the slice at $y = 50$ (middle of that dimension) over different times during the annealing process and for input parameters $k_1 = 5 \cdot 10^{-11} \text{ cm}^3\text{s}^{-1}$, $k_2 = 2 \cdot 10^{-10} \text{ cm}^3\text{s}^{-1}$, and $Y\mathcal{R} = 0.6 \text{ cm}^{-3}\text{s}^{-1}$. The first time step, at $t = 0$, represents the time when the irradiation is turned off. The snapshots of the system at that point in time reveal that the rate of oxidation is very high in the periphery of the sample and drops suddenly to 0 at a certain depth. At the same time, the O_2 concentration is very low throughout the sample and practically 0 in the area with no oxidation rate. As the annealing progresses, the oxygen diffuses inside the sample, and the O_2 concentration increases gradually. The oxidation rate is high only in a short band inside the sample, which corresponds to the area that has sufficient oxygen and radicals to sustain the reaction. This band moves towards the center of the sample with increasing time, until the time when all the radicals have been oxidized and the sample is considered fully annealed. Fig. 6.5 shows

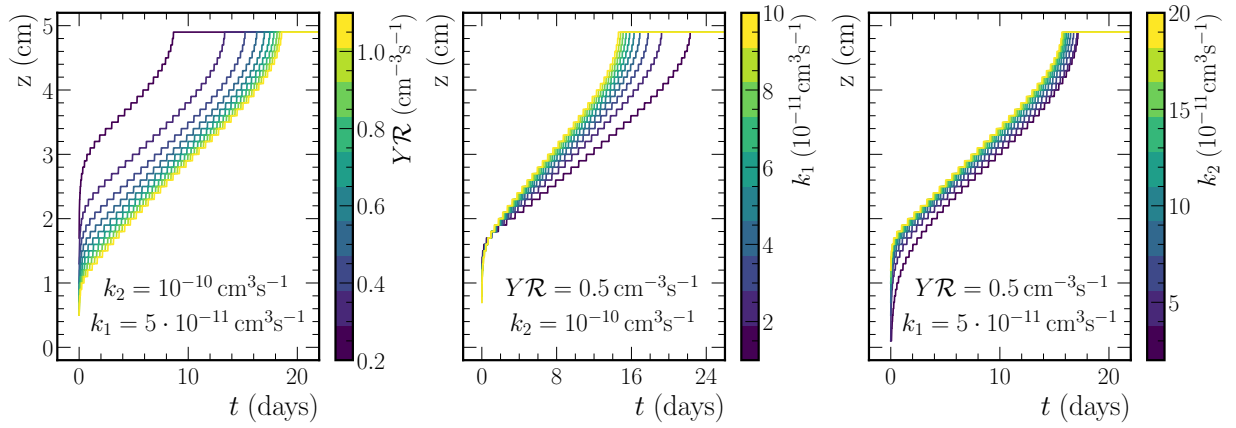


Figure 6.5: The 3D finite differences simulation of the JAERI model for various combinations of the input parameters $Y\mathcal{R}$, k_1 , and k_2 . In each plot, two of the parameters are kept constant, and the third is varied over some range. The diffusion coefficient is $D = 10^{-8} \text{ cm}^2\text{s}^{-1}$ in all cases.

a comparison of the annealing process for a variety of combinations of the parameter values. The annealing is represented by the depth z of the area with a high oxidation rate

at the middle of the sample ($y = 50, z = 250$). For each one of the three plots, two out of three parameters are kept stable, and the third parameter is varied over a certain range. The dose rate times the specific rate of radical formation, expressed as the combined parameter $Y\mathcal{R}$, significantly affects the initial depth, the duration, and the shape of the annealing curve. Lower values tend to place the initial position deeper into the sample and make the annealing curve look less linear. The rate of radical crosslinking k_1 mainly affects the annealing duration, with lower values extending its length. Finally, the rate of radical oxidation k_2 has a significant effect on the initial position, which also affects the annealing duration.

6.1.3 Photo-oxidation model

A different approach is followed by Cunliffe and Davis in [115] for describing the dynamics between oxygen diffusion and light-induced oxidation (which apply to ionizing radiation as well). This description is based on a similar chemical description of the phenomenon that is accounted for by the addition of a reaction rate term $R(C(x, t))$ to the diffusion equation (Eq. 6.2)

$$\frac{\partial C(x, t)}{\partial t} = D \frac{\partial^2 C(x, t)}{\partial x^2} - R(C(x, t)), \quad (6.23)$$

where $R(C(x, t))$ is the rate of oxygen consumption. For a free radical reaction chain with initiation, propagation, and termination steps [135–139], this rate can be described by the

formula

$$\begin{aligned}
 R(C(x, t)) &= \frac{c'_1 C(x, t)}{c'_2 C(x, t) + c'_3} \\
 &= \frac{c_1 C(x, t)}{c_2 C(x, t) + 1},
 \end{aligned} \tag{6.24}$$

where c'_1 , c'_2 , c'_3 , and therefore $c_1 \equiv \frac{c'_1}{c'_3}$ and $c_2 \equiv \frac{c'_2}{c'_3}$, can be expressed in terms of the rate constants for the initiation, propagation, and termination steps. By comparing Eq. 6.24 with Eq. 6.14, it is evident that $-k_2[P^\bullet]C(x, t)$ is replaced by $R(C(x, t))$, and the creation and termination of the radicals are modeled via the propagation and termination. Therefore, this model features a more simplified handling of the radical processes. The steady-state differential equation becomes

$$D \frac{\partial^2 C(x)}{\partial x^2} = \frac{c_1 C(x)}{c_2 C(x) + 1}, \tag{6.25}$$

and after reusing $y \equiv \frac{C}{C_0}$, $\lambda \equiv \frac{x}{l}$,

$$\begin{aligned}
 \frac{d^2 y}{d\lambda^2} &= \frac{\left(\frac{c_1 l^2}{D}\right) y}{c_2 C_0 y + 1} \\
 &= \frac{E y}{F y + 1},
 \end{aligned} \tag{6.26}$$

where $E \equiv \frac{c_1 l^2}{D}$, and $F \equiv c_2 C_0$. The boundary conditions remain the same as before.

6.1.3.1 If $F \ll 1$

For F to have a very small value, either the initial concentration of oxygen C_0 needs to be very low or the rate constants for the radical oxidation process and the termination process for oxidized radicals need to be much lower than the rate constant for the termination of non-oxidized radicals. In this case, the reaction rate is proportional to C . For small E values, which correspond to a combination of small sample thickness, low radical formation rates, low dose rates, and low radical oxidation rates, the oxygen diffusion offsets the reaction sufficiently, and the decrease of C towards the center of the sample is small. For larger values of E , the decrease of C becomes more pronounced.

6.1.3.2 If $Fy \gg 1$ for all y

In this case, there is sufficient oxygen concentration throughout the sample, and the rate constants for the processes that involve oxygen are sufficiently high that the reaction rate is approximately constant throughout the sample. For larger values of E , the demand for oxidation increases, and the oxygen concentration can be depleted within an inner region of the sample.

6.1.3.3 If $Fy \approx 1$ for some y

Considering the case where $F \gg 1$, the reaction rate should be approximately constant as long as $Fy \gg 1$ holds. However, the validity of this statement depends as well on the value of E . Specifically, for small values of E , the condition $Fy \gg 1$ is valid for all values of y . As the value of E increases, oxygen concentration falls more and more

rapidly with depth into the sample. For large values of E , a balance is created between the oxygen concentration and the oxidative part of the reaction chain in some regions of the sample, and as a result, there are some y for which $Fy \approx 1$. In this case, C has a plateau region with almost constant oxygen concentration, and then at some critical depth λ_c the concentration collapses dramatically to very low values. The effect is more pronounced for larger values of E and F , provided that E is sufficiently larger than F . The critical depth can be estimated by beginning with the condition $Fy \gg 1$. Then

$$\frac{d^2y}{d\lambda^2} = \frac{E}{F}. \quad (6.27)$$

After integrating twice and applying the boundary conditions,

$$y = 1 - \frac{E}{8F} + \frac{E\lambda^2}{2F}. \quad (6.28)$$

Considering the critical condition when y falls below y_c given by $Fy_c \approx 1 \Leftrightarrow y_c \approx \frac{1}{F}$ in the middle of the sample,

$$\frac{E}{8F} \geq 1 - \frac{1}{F}. \quad (6.29)$$

For large F values,

$$\frac{E}{8F} = \frac{c_1 l^2}{8Dc_2 C_0} \geq 1. \quad (6.30)$$

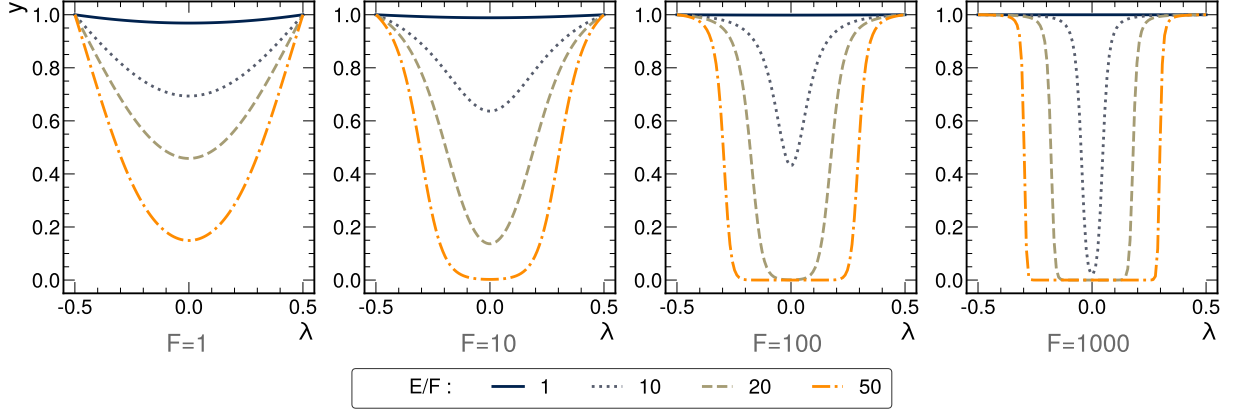


Figure 6.6: Numerical solutions to Eq. 6.26 for various combinations of values for the parameters $E \equiv \frac{c_1 l^2}{D}$ and $F \equiv c_2 C_0$. The parameter E is expressed through its ratio to F . The normalized reaction rate R/R_0 is shown for the entire normalized length λ . For the code used see Ref. [20].

This critical value y_c is very small and therefore the roots of Eq. 6.28 can give an approximation of the location of the sharp decreases:

$$\lambda_c^2 = \frac{1}{4} - \frac{2F}{E} = \frac{1}{4} - \frac{2c_2 D C_0}{c_1 l^2}. \quad (6.31)$$

Writing for z_c , which is measured from the surface of the sample

$$z_c^2 = \frac{2c_2 D C_0}{c_1} \quad (6.32)$$

This formula is very similar to Eq. 6.21 provided that the ratio c_1/c_2 is approximately equal to $Y\mathcal{R}$.

6.1.3.4 Numerical solution

Equation 6.26 can be solved numerically using `scipy`'s ODE solver for boundary value problems. The full code can be found in [20]. Fig. 6.6 shows solutions of the normalized reaction rate R/R_0 for different values of the model parameters A and B . Parameter B controls the shape of the solution, which forms shoulder regions in the outer parts of the sample and drops steeply in the middle for values $\gtrsim 10$. The ratio A/B defines the depth where the transition between the two regions occurs.

For the sake of completeness, Eq. 6.25 was also solved for the two-dimensional case that matches the physical size of our samples, which are described in detail in Section 6.3. The dynamic system was evolved over time on a 350×70 grid until a steady solution was reached. In Fig. 6.7, the solution is shown for the normalized concentration C/C_0 and the normalized reaction rate R/R_0 for a choice of the model parameters $c_1 = c_2 = 100$ and $D = 0.01$. These values were chosen because they produce a steady state in which the oxygen concentration drops significantly very close to the surface of the material, and the reaction rate is high close to the surface but then suddenly drops at some critical depth z_c .

6.2 Refractive index theory

The refractive index n for a material can be expressed as

$$n = \sqrt{\epsilon_r \mu_r}, \quad (6.33)$$

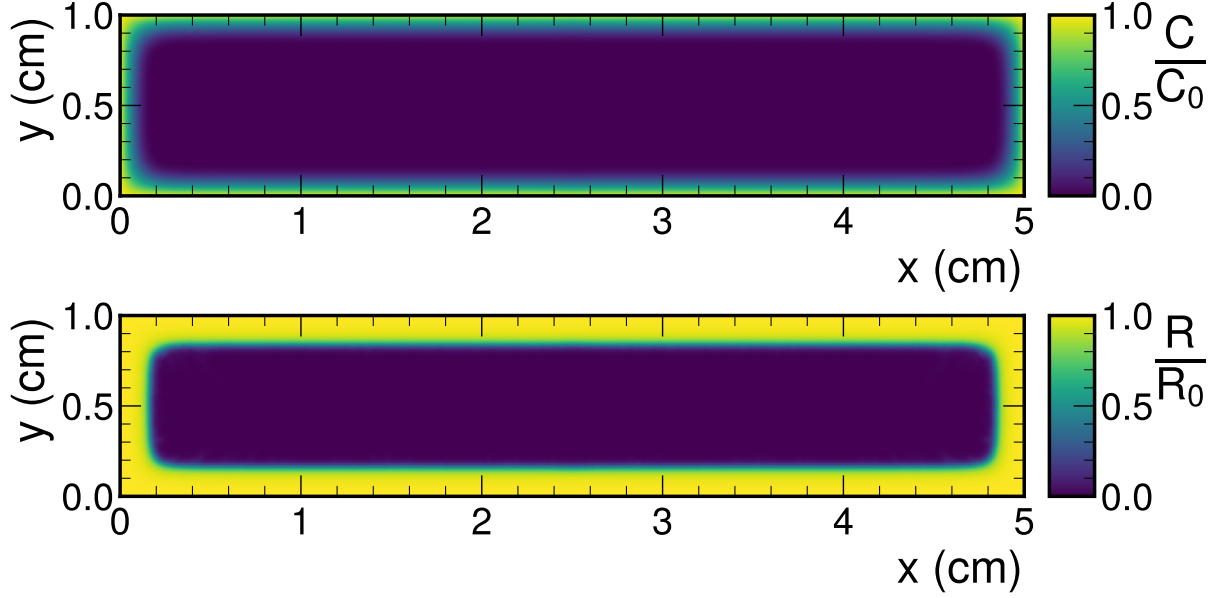


Figure 6.7: The solution to the 2D PDE for the normalized concentration and reaction rate at steady state for a scintillator that is $1 \text{ cm} \times 1 \text{ cm} \times 5 \text{ cm}$. For the code used see Ref. [20].

where ϵ_r and μ_r are the relative permittivity and permeability, respectively. For non-ferromagnetic materials, the relative magnetic permeability is very close to unity. So for plastic scintillators, the formula is a good approximation.

$$n \simeq \sqrt{\epsilon_r} \quad (6.34)$$

A connection between ϵ_r and the microscopic description of a material can be established by the Clausius-Mossotti equation [140]

$$\frac{\epsilon_r - 1}{\epsilon_r + 2} = \frac{N\alpha}{3\epsilon_0}, \quad (6.35)$$

where N is the number density of molecules and $\alpha \equiv \frac{\|\mathbf{p}\|}{\|\mathbf{E}\|}$ is the molecular polarizability of the material, which is defined as the tendency of the molecules to acquire a dipole

moment \mathbf{p} when exposed to an external electric field \mathbf{E} .

This can be rewritten for the refractive index n in a form known as the Lorentz-Lorenz equation [141–143]

$$\frac{n^2 - 1}{n^2 + 2} = \frac{4\pi}{3} N \alpha_m, \quad (6.36)$$

where α_m is the average molecular polarizability volume (that is, the polarizability expressed in CGS units in order to give the convenient dimension of volume). Therefore, the refractive index can be predicted using only one microscopic quantity, α_m .

The average molecular polarizability depends on the atomic polarizabilities of the atoms that form the substance's molecules, as well as on the bond strengths and the molecular structure. This fact was realized by chemists in the late 18th century, trying to associate the structure of organic molecules with their refractive indices. Brühl pioneered a method [144, 145] to predict the molecular refractivity

$$MR \equiv \frac{n^2 - 1}{(n^2 + 2)N} \quad (6.37)$$

by assigning a weighted sum of the atomic refractivities to it. He calculated the atomic refractivities for the atoms that are most commonly found in organic molecules and the additional factors associated with double and triple bonds, and he was able to predict the correct structure for benzene. Table 6.1 shows the values that Brühl derived for the

Table 6.1: Brühl's weights. The sum of these weights gives the molecular refractivity for a compound.

Atom/bond	C	H	O	C=C	C≡C	C=O
weight r_i	2.48	1.04	1.58	1.78	2.18	0.76

weights of the constituents of organic compounds. Calculations according to Brühl theory are shown in Table 6.2 , where the values for the molecular weight P of the monomers,

Table 6.2: Brühl theory predictions and experimental values for three common organic substrate materials.

Polymer	$\sum r_i$	P (g/mol)	d (g/mL)	$n_{\text{Brühl}}$	$n_{\text{experiment}}$
PMMA	26.22	100.12	1.15	1.510	1.49
PVT	38.06	118	1.023	1.574	1.58
PS	33.50	104.15	1.05	1.591	1.59

the density d , and the experimental value of the refractive index $n_{\text{experiment}}$ are retrieved from [146, 147]. Subsequently, the same equation can predict the difference δn in the refractive index when the chemical composition of the material changes, as is expected to happen during irradiation. For example, substituting two hydrogen atoms for a double carbon bond in styrene is expected to change the refractive index by $\delta n = 0.008$ while replacing two hydrogen atoms in the same monomer with a carboxyl bond gives $\delta n = -0.079$. Therefore, it is expected that the presence or absence of oxygen during the irradiation is going to affect the refractive index since the neutralization of the radicals will differ.

The characterization of materials based on their refractive index is often performed by fitting empirical formulas that describe the dispersion with light wavelength to experimental data. The most popular formulas are the Cauchy equation

$$n(\lambda) = A + \frac{B}{\lambda^2} + \frac{C}{\lambda^4} + \dots \approx A + \frac{B}{\lambda^2}, \quad (6.38)$$

where A and B are material-dependent coefficients whose values are determined experi-

mentally, and the Sellmeier equation [148]

$$n^2(\lambda) = 1 + \sum_{i=1}^N \frac{B_i \lambda^2}{\lambda^2 - C_i}, \quad (6.39)$$

where B_i and C_i are the Sellmeier coefficients, and they are experimentally determined. This equation is considered an improvement over Cauchy's formula as it is better at modeling the refractive index in a broad wavelength range from the infrared to the ultraviolet part of the spectrum. Usually, up to third-order coefficients are used to characterize glasses, although keeping two or even one order is sufficient for many applications.

6.3 Experimental setup and procedures

6.3.1 Samples and irradiations

All scintillators discussed in this work are rectangular rods of dimension $1 \text{ cm} \times 1 \text{ cm} \times 5 \text{ cm}$, supplied by Eljen Technology. The substrate material is either polystyrene (PS) or polyvinyltoluene (PVT), while the primary and secondary fluors are p-Terphenyl and POPOP-type, respectively. These scintillators are commercially available from Eljen Technology as EJ-200 with PVT substrate material. The PS-based scintillators were prepared by Eljen specifically for these studies as a custom request.

The rods were irradiated with different dose rates at room temperature in three irradiation facilities. Irradiations from 80.6 Gy/h to 3.9 kGy/h with integrated doses of 70 kGy were performed at the National Institute for Standards and Technology (NIST) in

Gaithersburg, MD, using ^{60}Co . Lower dose rate irradiations from 3.0 to 9.8 Gy/h with total doses ranging from 12.6 to 42 kGy were performed at Goddard Space Flight Center, using also ^{60}Co . The lowest dose rate irradiations were performed at the GIF++ facility at CERN [149] using ^{137}Cs with a dose rate of 2.2 Gy/h to a total dose of 13.2 kGy. The dose and dose rate uncertainties are 1.2% for the NIST irradiations and 10% for the Goddard and GIF++ irradiations. All samples were stored in a dark container after irradiation until annealing was complete.

6.3.2 After irradiation

Irradiated plastic scintillator acquires distinctive optical features that can be used to indicate the recovery status or even measure any abrupt changes in the reaction rate between oxygen and the radiation-induced radicals. Visual inspection of the samples immediately after exiting the irradiator reveals an internal region with a characteristic green coloration from radical color centers that is surrounded by a boundary, which indicates a rapid change in the refractive index of the material. During the recovery process, the green coloration gradually shrinks toward the center of the sample until it eventually disappears. The time needed for the completion of this process varies by substrate material and depends on the storage conditions. For the samples discussed in this work, the average time to full recovery is between 1 and 2 months. This process is already well documented in the literature and is known as scintillator "bleaching" or annealing. Provided enough oxygen is available during recovery, all radicals will get oxidized and therefore the green coloration will be neutralized. After complete annealing,

the only visual remnant of the irradiation is the boundary at which the refractive index of the material changes sharply. Fig. 6.8 [Left] shows the 1×1 cm face of a PS scintillating

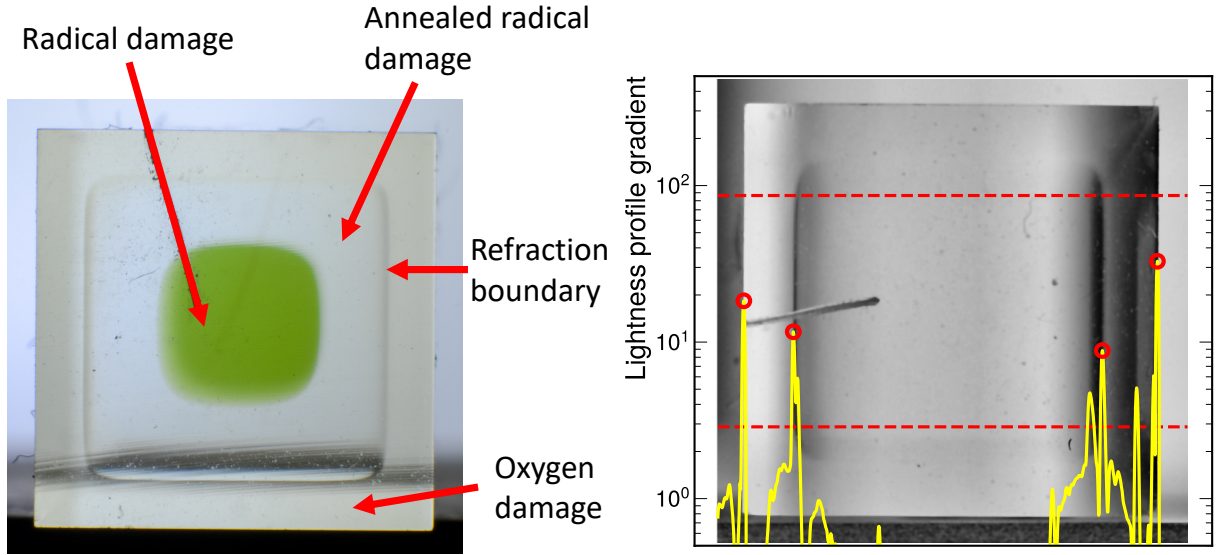


Figure 6.8: [Left] One of the irradiated scintillator samples with a visible refractive index change boundary 15 days after the irradiation end. Irradiation was performed using ^{60}Co at NIST to a total dose of 70 kGy at a dose rate of 460 Gy/h. [Right] The processed lightness channel of a scintillator sample. The gradient of the profile is shown in yellow color, the range used for the profile is defined by red dashed horizontal lines, and the peaks are identified with red circles.

rod 15 days after the end of its irradiation with 460 Gy/h for an integrated dose of 70 kGy.

6.3.3 Refractive index boundary depth

The refractive index change is present in all scintillator rods irradiated with dose rates > 10 Gy/h. The refractive index boundary depths were measured using an OpenCV-based method [150] with photographs and video frames of the samples taken in front of high-contrast backgrounds. The method consists of the following steps:

1. Select pictures/frames with the cleanest views of the boundaries.

2. Process with a bilateral filter to reduce noise and dust.
3. Extract the lightness channel.
4. Improve contrast with Contrast Limited Adaptive Histogram Equalization (CLAHE) [151, 152].
5. Extract the lightness profile along the axis used for depth calculation.
6. Calculate the gradient of the lightness profile to reveal any abrupt changes.
7. Apply a Savitzky–Golay filter [153] for noise removal.
8. Find the positions and widths of the gradient peaks.
9. Calculate the image scale in mm/px and the depth of the refractive index boundaries using the peak positions.
10. Use the peak widths and the variance over a few different pictures to estimate the uncertainties.

Fig. 6.8 [Right] shows the lightness profile gradient overlaid over the processed lightness channel for one of the samples. The discovered peaks that are later used for calculating the image scale and the boundary depth are shown with red circles. The code and the data that can fully reproduce all the results can be found in Ref. [20].

6.3.4 Refractive index measurement

The refractive index of the scintillator rods was measured using the setup shown in Fig. 6.9. A Nikon D7000 DSLR was aligned with the axis of an MPositioning precision

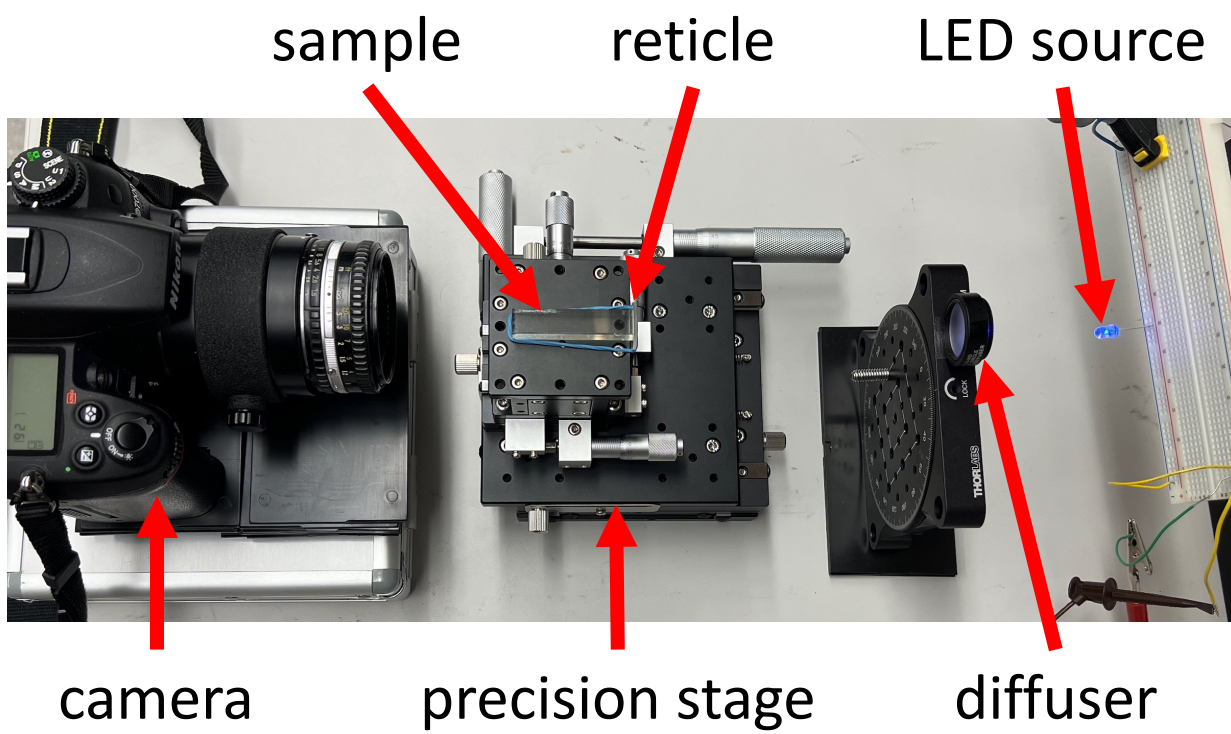


Figure 6.9: The setup for measurements of the index of refraction using a Nikon D7000 digital camera, an MPositioning precision stage with a sample adjacent to a Boli Optics $10 \times 10 \text{ mm}/100 \times 100$ reticle, a Thorlabs 20° circle pattern diffuser, and a 470 nm LED source.

translation stage. The rods were placed on the translation stage with a Boli Optics 0.1 mm division net grid reticle attached to the face opposite the camera. The rod-reticle system was illuminated evenly from behind using an LED of known wavelength with a Thorlabs 20° circle pattern engineered diffuser.

The camera lens focus was fixed on the front face of the rod. Then, the precision stage was translated forward up to the distance at which the divisions of the reticle at the other end of the rod appeared to be in focus. The total distance traversed from the front to the apparent end of the rod was the measured apparent depth L' . This procedure was performed for both the inside and outside regions of the rods, as is shown in Fig. 6.10. The rod lengths L were measured using a caliper. For a sample without an internal boundary, the index of refraction is given by [154]

$$n_{in} = \frac{L}{L'}. \quad (6.40)$$

Accounting for two regions with different refractive indices n_{in} and n_{out} inside the rod, the index of the internal region is

$$n_{in} = \frac{(L - 2d)n_{out}}{L'n_{out} - 2d}, \quad (6.41)$$

where d is the depth of the boundary, and n_{out} is measured using Eq. 6.40 in the part of the sample where only the outer region is visible.

The method was validated using two $\text{Bi}_4\text{Ge}_3\text{O}_{12}$ (BGO) crystal samples. The validation was performed by measuring the index of the material at eight different wavelengths

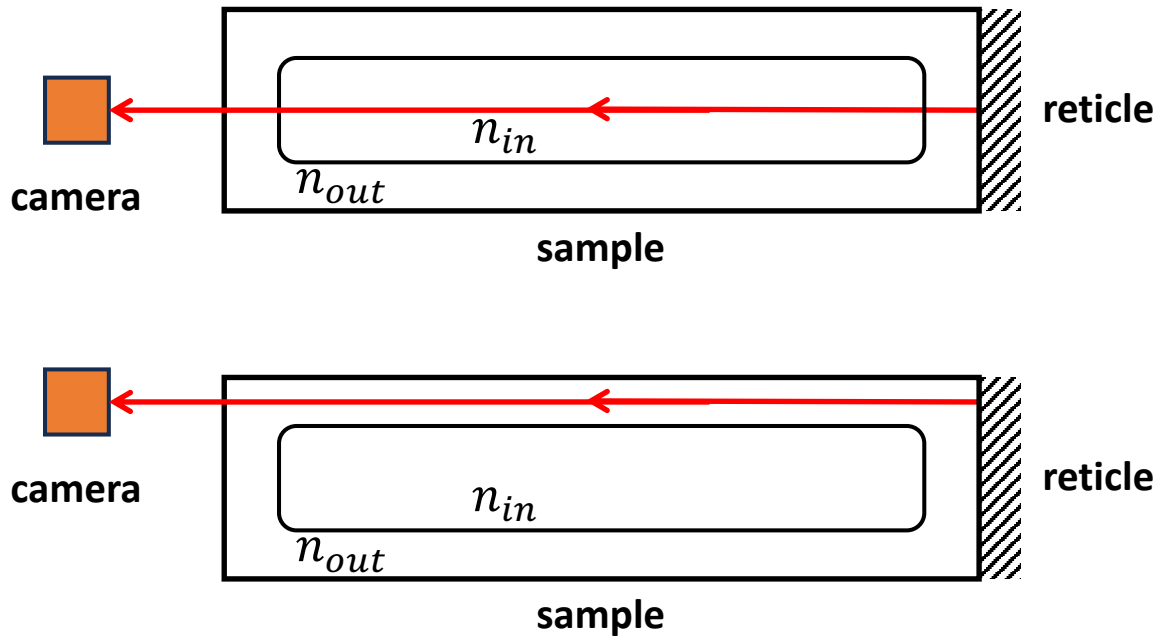


Figure 6.10: A schematic showing the configurations for measuring the refractive indices in samples with two regions. The index of the inner region n_{in} is measured using the configuration shown at the top, in which the light passing through the middle of the sample is used. The index of the outer region n_{out} is measured according to the configuration shown at the bottom, which uses light passing through the periphery of the sample, thus avoiding the inner region. The fact that light traversing the inner region also traverses some of the material in the outer region requires a correction term to the inner region's measured index, as described in the text.

and then comparing their distribution with the relationship predicted by Eq. 6.39. The reference values for B_1 and C_1 for BGO crystals can be found in Ref. [155]. Fig. 6.11 shows

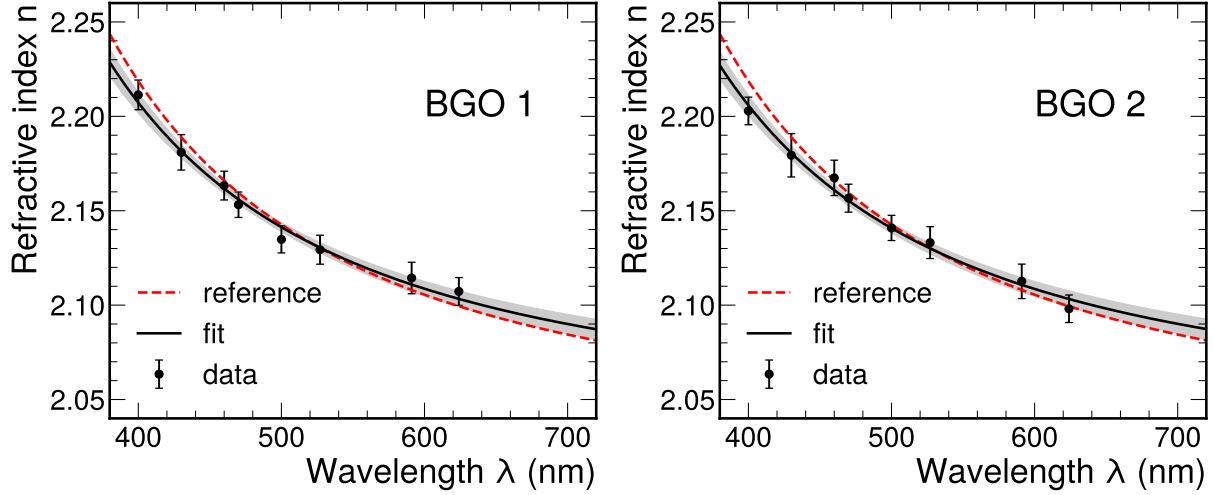


Figure 6.11: A validation of the refractive index measurement method performed against the Sellmeier equation for two BGO crystal samples. The plots show measurements of the index of refraction versus light wavelength. The red curve is the Sellmeier equation using the first-order Sellmeier coefficients that can be found in the literature. A fit of the data to the first-order Sellmeier equation is shown in black. The 1σ band is shown in gray color around the fit line.

the comparison between the reference Sellmeier equation and a fit of the same equation to our data for both samples. The fitted lines match reasonably well with the predictions throughout the visible light spectrum.

6.4 Results

Fig. 6.12 shows all measurements of depth versus the dose rate for PS and PVT rods. As expected by the hypothesis that this boundary is related to the oxygen penetration depth, the depth reduces with increasing dose rate because the oxygen diffusion is not enough to replenish the oxygen molecules consumed by the radicals. The data points are fitted with an equation of the form $z = A/\sqrt{\mathcal{R}}$ since this is the expected formula

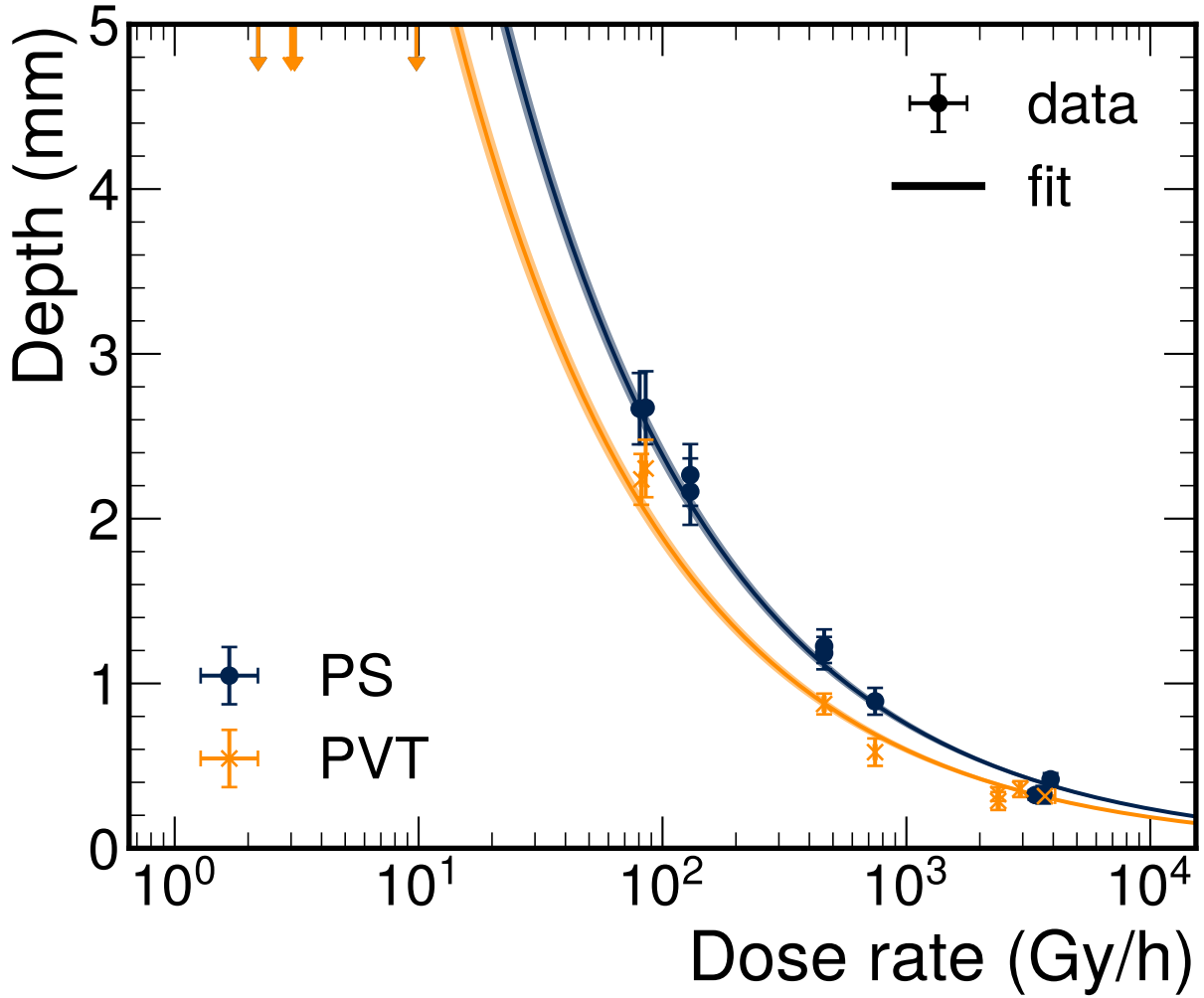


Figure 6.12: The measured depths of the refractive index change boundaries for irradiated PS and PVT scintillator samples as a function of dose rate. Irradiations at 2.2 Gy/h were done using a ^{137}Cs source, the rest using ^{60}Co . The samples that were irradiated with dose rates lower than 80 Gy/h do not have a visible boundary, indicating the depth is larger than half the sample thickness. For that reason, these samples are represented by lower-pointing arrows at 5 mm whose length indicates the uncertainty of having a boundary so close to the surface that it is impossible to measure or observe. The data above 80 Gy/h are fitted with a function of the form $z = \frac{A}{\sqrt{R}}$. The 1σ bands are also shown around the fit lines.

according to Eq. 6.21. The values of the parameter A are estimated to be $A_{PS} = 23.8 \pm 0.7 \text{ mm} \cdot \text{h}^{1/2} \text{Gy}^{-1/2}$ for PS and $A_{PVT} = 18.8 \pm 0.6 \text{ mm} \cdot \text{h}^{1/2} \text{Gy}^{-1/2}$ for PVT. Converting these values to dose rates that allow full oxygen penetration to 5 mm (half the sample width) gives $R_{PS}^{full} = 22.7 \pm 1.3 \text{ Gy/h}$ for PS and $R_{PVT}^{full} = 14.2 \pm 0.9 \text{ Gy/h}$ for PVT.

The annealing process was monitored closely, and the depth of the colored region was measured periodically for a PS sample that was irradiated with 460 Gy/h for a total of 69 kGy. According to Ref. [98], the progression of the annealing is expected to follow the relationship

$$z_{color}^2 = At. \quad (6.42)$$

The measurements of the colored region are shown in Fig. 6.13 along with predictions of the finite differences simulation from Sec. 6.1.2.3, the position of the refractive index boundary, and a fit of Eq. 6.42 to the data. The measurements evolve in accordance with the finite differences simulation whose input parameters have been tuned by minimizing the χ^2 distance between the data and the prediction. Both the data and the simulation deviate from Eq. 6.42 after the initial part of the annealing process. Possible explanations for this might include the shape of the sample (the equation is derived for thin sheets) and the effect of the active radicals on oxygen diffusion. The fit result for the parameter in Eq. 6.42 is $A_{PS} = 7.351 \pm 0.015 \cdot 10^{-3} \text{ mm}^2/\text{h}$, which is lower than the value $0.025 \text{ mm}^2/\text{h}$ from Ref. [98]. This is expected since the fit is obviously underestimating the evolution rate.

The same method was used to measure the refractive indices of unirradiated EJ-200 PS and PVT scintillator samples. Fig. 6.14 shows the measured indices over the visible

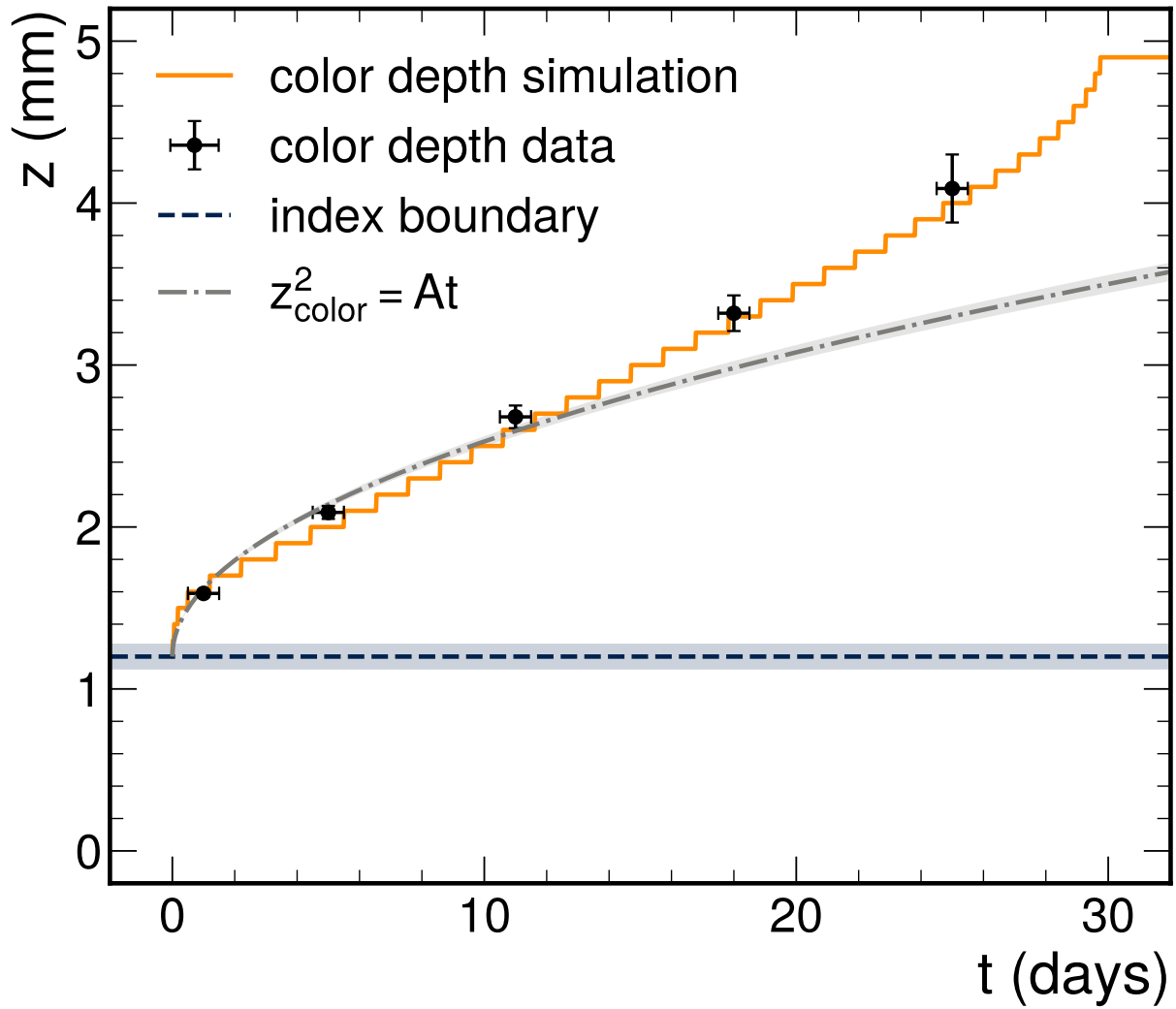


Figure 6.13: Measurements of the annealing process of an irradiated scintillator. The data points represent the depth of the colored region. The finite differences simulation of the colored region depth is shown with an orange line. The depth of the refractive index boundary is shown with a dashed black line. A fit of Eq. 6.42 to the annealing data is shown as a gray line. The Eq. 6.42 doesn't explain the data fully since it is derived for thin films.

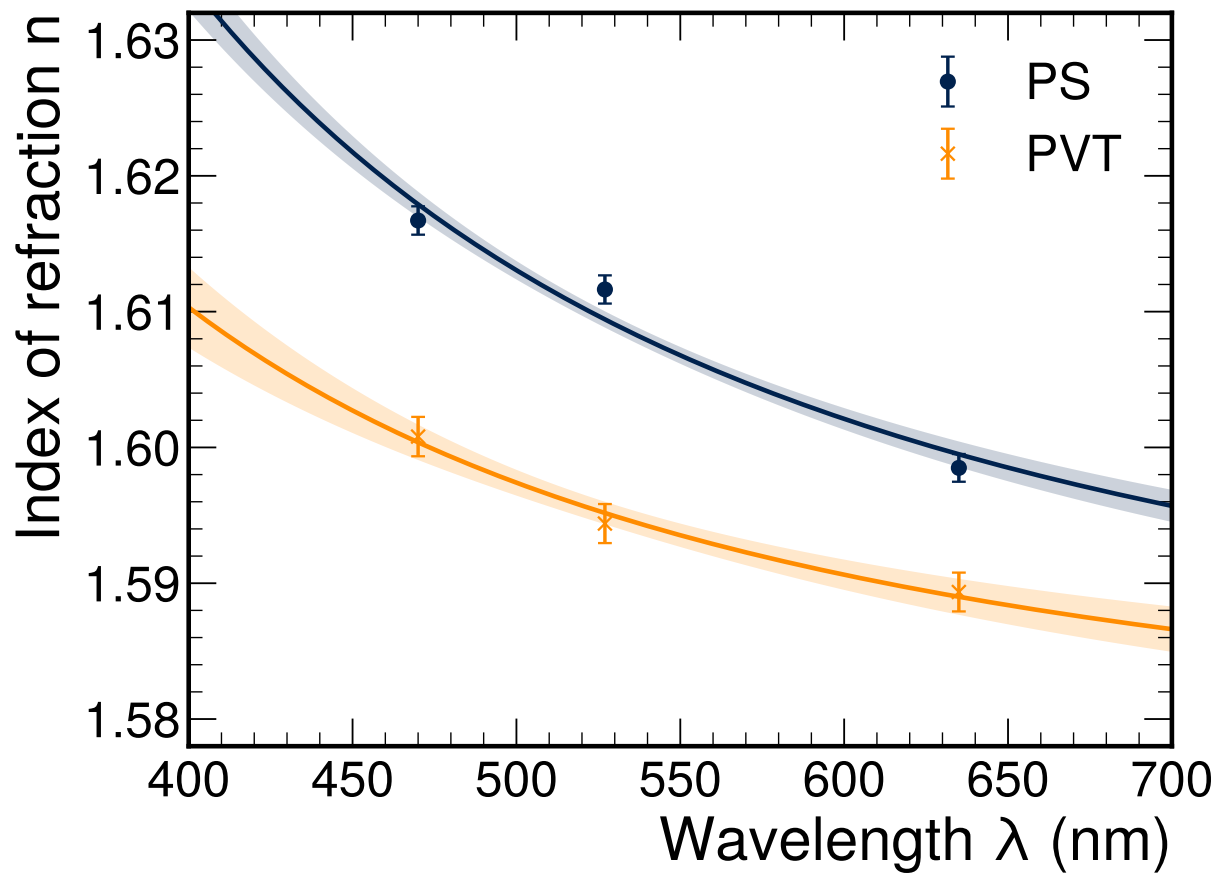


Figure 6.14: The refractive indices for unirradiated EJ-200 PS and PVT. The lines represent fits to the first-order Sellmeier equation. The 1σ bands are shown around the fit lines.

spectrum. Fits to the first-order Sellmeier equation are also included. The calculated Sellmeier coefficients for EJ-200 PS are $B_1^{\text{PS}} = 1.492 \pm 0.007$ and $C_1^{\text{PS}} = 1.71 \pm 0.13 \cdot 10^{-2} \mu\text{m}^2$, and for EJ-200 PVT are $B_1^{\text{PVT}} = 1.483 \pm 0.011$ and $C_1^{\text{PVT}} = 1.10 \pm 0.19 \cdot 10^{-2} \mu\text{m}^2$.

Scintillator samples of both substrates, which were irradiated over a very wide range of dose rates, were measured using the same technique. Fig. 6.15 shows measurements

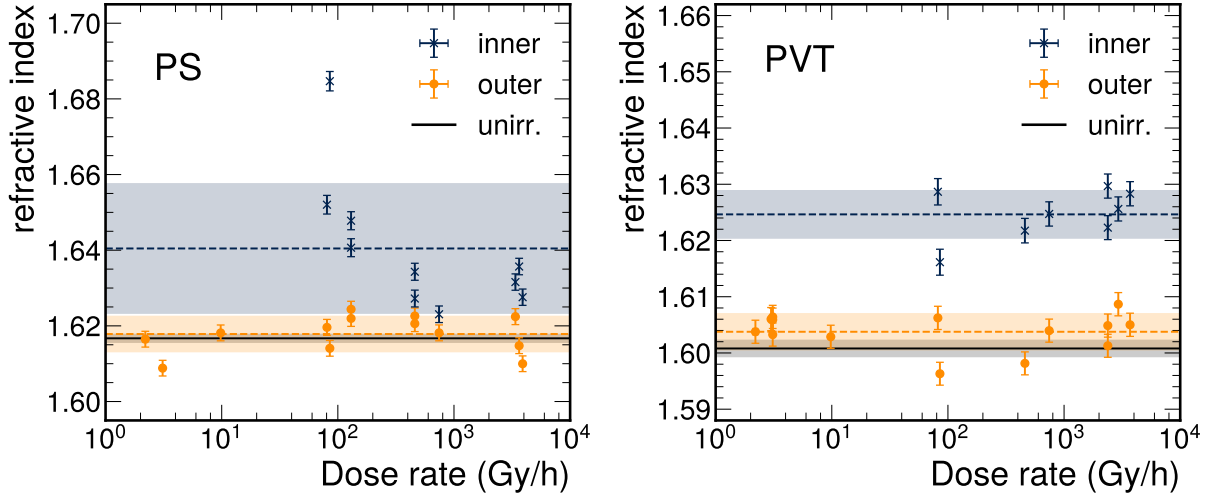


Figure 6.15: Measurements of the refractive index at $\lambda = 470 \text{ nm}$ after irradiation and annealing for EJ-200 PS (left plot) and PVT (right plot) for both the inner (blue) and outer (yellow) regions that are defined by the internal boundary. The average value for each region is shown with a dashed line and the standard deviation with a band around that line. The average of the measurements of the unirradiated samples is shown with a solid black line accompanied by a black-shaded area that represents the uncertainty.

of the index of refraction at the wavelength of 470 nm for irradiated scintillator samples of both PS (left plot) and PVT (right plot) substrates. For both materials, the index of the region inside the boundary is higher than the index in the outer region by approximately $\delta n \approx 0.02$ on average. The samples at lower dose rates, that do not feature an internal boundary, have indices consistent with the values from the outer regions of the samples with boundaries. This is consistent with the hypothesis that these samples have been fully penetrated by oxygen during the irradiation. The values of the index for unirradiated

samples are compatible with the indices of the outer regions within the experimental uncertainties. This suggests that non-oxidative processes, like radical crosslinking, are contributing more (at least collectively) to changes in the refractive index. Finally, there is no indication of dependence of the refractive index on the dose rate of the irradiation for the outer regions of both materials and the inner region of PVT. The refractive index of the inner region for the PS scintillators indicates a decreasing trend with increasing dose rate until it reaches a plateau slightly above the values of the outer region. The available data and their uncertainties prohibit the drawing of any conclusions regarding this trend, and therefore, more measurements with comprehensive coverage of the dose rate values are needed to evaluate this relationship.

6.5 Conclusions

The effects of oxidation during irradiation on the optical properties of plastic scintillators were studied both theoretically and experimentally. Numerous models of oxygen diffusion in polymers, which can be solved numerically or analytically in limiting cases, exist in the literature. Numerical solutions to the differential equations for two of these models show that the normalized oxygen reactivity can undergo a steep decrease from 1 to 0 at a certain depth within the material for a subset of the parameter space of the models. This prediction is in accordance with the optical observations made on irradiated polymeric scintillators that exhibit an optical boundary of sharp change in the refractive index, which separates the material into two regions. The depths at which these boundaries occur were measured and compared with the dose rates of the irradiations.

The data show a dependence on the inverse of the square root of the dose rate, which is in agreement with the predictions of the models. Measurements of the index of refraction of the samples using a photography-based technique reveal that the internal regions defined by those boundaries have slightly elevated index values. The refractive indices of unirradiated samples agree with the values of the outer regions of the irradiated samples. The refractive indices do not depend on the dose rate of the irradiation, with one exception, the inner region for PS, for which a descending trend with increasing dose rate is observed. More studies are needed to clarify the validity and the nature of this trend.

Part III

Search for Soft Unclustered Energy Patterns with muons

Disclaimer

This Part of the dissertation (Part III) relies heavily on the CMS Analysis Note AN-24-084 for the Search for SUEP with muons. I have contributed almost all the text for this note. I developed all the analysis code, and I produced all the plots and tables in the following sections.

This analysis is still in a **blinded stage**, meaning that we are not processing real data in the signal regions. Real data are processed in the control and validation regions. Only the expected final results are reported.

Chapter 7: Introduction to SUEP

CMS has a rich physics program for beyond-the-Standard-Model (BSM) physics. Despite all the efforts, there is still no evidence of exotic physics in the vast number of searches that have been performed. Recently, dark QCD models have been gathering attention, since they are capable of producing a great variety of unique final signatures, many of which have not been explored yet. Examples include but are not limited to long-lived particles [156], semi-visible jets [157], emerging jets [158], and soft unclustered energy patterns (SUEP) [22]. These unusual events can be evidence of a strongly coupled hidden valley.

Hidden valleys are extensions that add a new confining gauge group to the Standard Model (SM) [28]. These hidden valleys can be accessed through a heavy portal state that can be produced in particle colliders like the LHC. The energy directed into the confining hidden valley is used to create dark hadrons, which can then decay back to the visible sector. A schematic representation of this can be seen in Figure 7.1. SUEP are final states with high particle multiplicities that can be produced by a hidden valley characterized by a large 't Hooft coupling combined with a small hadronization scale.

Several works on SUEP have already been published, including overviews [159], strategies for triggering SUEP events [22, 160], definitions of useful metrics [161], machine

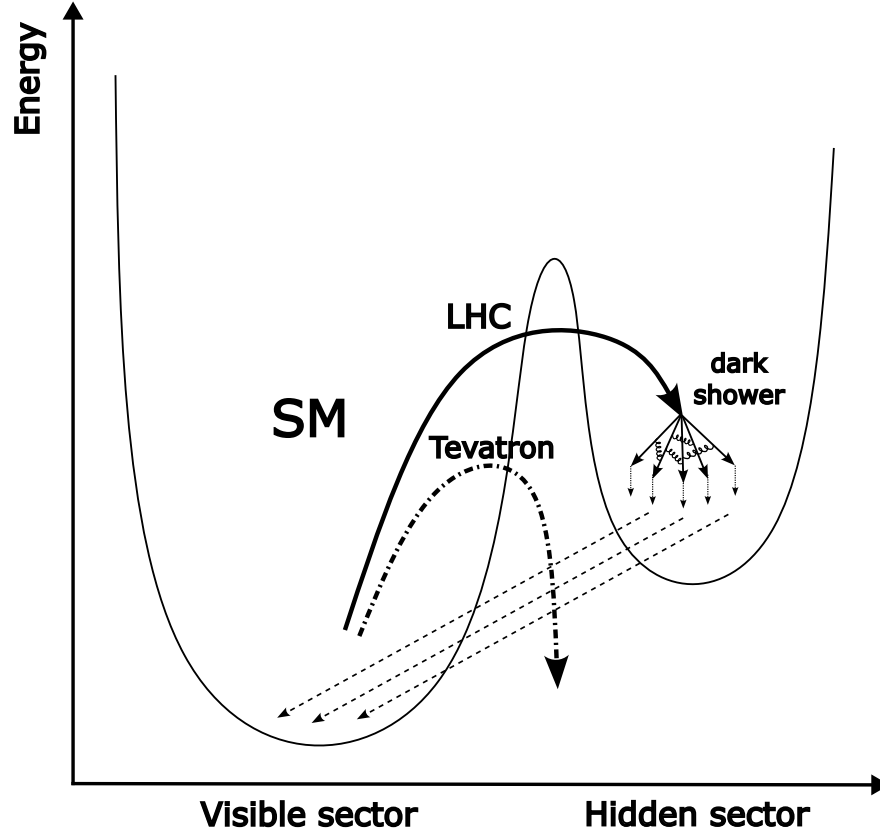


Figure 7.1: Hidden valley conceptual diagram. For the original version of this diagram, see Ref. [21]. The hidden sector is accessible only through the portal created by the LHC. The states created by the dark shower may decay back to the visible sector.

learning approaches like unsupervised learning and autoencoders [24, 162]. CMS has published the first search for SUEP [163, 164] using a strategy that triggers on ISR jets and therefore targets more boosted SUEP final states. Further, effort within the collaboration not published yet includes a search for SUEP that exploits the scouting stream data [165–168] as well as searches for the production of SUEP in association with Z [169, 170] and W [171, 172] bosons.

This analysis aims to look for SUEP with an emphasis on final signatures with high muon multiplicities. The events are selected using triple-muon HLT paths. Further

selections are imposed to obtain collections of higher-quality muons. Control and signal regions are then formed, placing requirements that mainly focus on the number of muons, eventually keeping events with 7 or more muons in the discovery bins of the signal region. The background is estimated by performing an extrapolation on the multiplicity distribution of the QCD MC muons. The resulting extrapolated MC background is fitted to the data and eventually used to calculate upper limits. This search is expected to have great potential and offer nice complementarity with existing CMS searches for SUEP, given the excellent ability of CMS to trigger on muons and reconstruct them.

This Part consists of the following sections: Section 8 describes the signal models, Section 9 presents the datasets used and the Monte Carlo samples that model the signal and the background, Section 10 contains information on the selections applied to the objects used in the analysis, Section 12 has details on the selections used to pre-select the events and then form the control and signal regions, Section 13 describes the background estimation method, Section 14 lists the sources of systematic uncertainty, Section 15 presents the results including upper limits to the production cross section of the signal models.

Chapter 8: Signal models for SUEP

The Soft Unclustered Energy Pattern (SUEP) events are expected to take the form $pp \rightarrow \mathcal{B} + X$, where \mathcal{B} is a state with a very large multiplicity of SM particles that are distributed roughly isotropically around the center-of-mass of \mathcal{B} in its rest frame. The process that is expected to give this kind of final signature involves the production of a scalar boson S that decays to several dark mesons ϕ . Subsequently, the dark mesons decay to pairs of dark photons, A' , which then decay to SM particles [22]. Figure 8.1 shows the Feynman diagram for the entire SUEP process.

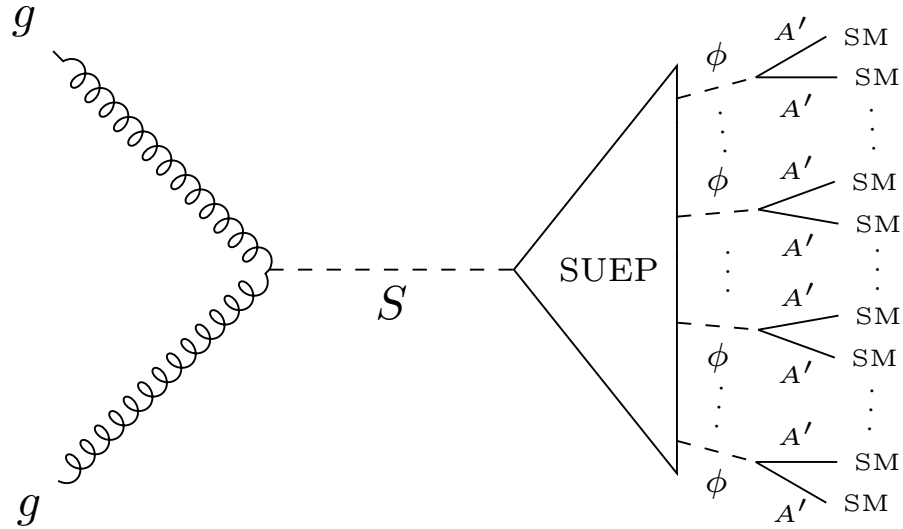


Figure 8.1: Feynman diagram for the SUEP process adapted from Ref. [22]. The scalar mediator is produced via gluon-gluon fusion, and then it decays back to standard model particles after creating a dark shower, hadronizing to ϕ dark mesons, and decaying to A' dark photons.

To produce SUEP events, a mediator particle is needed that acts as a portal to the hidden valley by connecting SM particles to the hidden sector particles. In our case, the mediator particle is assumed to be a heavy scalar boson with properties similar to those of the Higgs boson. The SUEP scalar mediator is produced using gluon-gluon fusion via a quark loop, with main contributions from the top quark, as a narrow-width BSM Higgs boson. Alternative scalar boson production modes, like Vector Boson Fusion (VBF) or associated production with a Z or W boson (ZH or WH), are also possible but are not considered in this work because of their smaller cross sections. Instead, CMS has dedicated analyses that target alternative production modes for SUEP events. Finally, mediation through vector bosons is also possible. The event dynamics are expected to remain similar.

The hidden sector that is accessed by the scalar mediator is assumed to include a dark QCD-like interaction described by a non-Abelian gauge theory. The parton multiplicity generated by a hadronic shower is controlled by the ratio of the energy scale, Q , to the hadronization scale, Λ , Q/Λ . Given a large 't Hooft coupling, $\lambda \equiv g_{dark} N_c^{dark}$, where g_{dark} is the coupling strength and N_c^{dark} is the number of the colors of the dark QCD, the emission of partons carrying a sizeable fraction of the momentum at large angles is expected to become significant, leading to an isotropic distribution of the partons [21, 173–175]. Considering the energy scale to be roughly equivalent to m_S and the hadronization scale to m_ϕ , then the expected parton multiplicity is [176]

$$\langle n \rangle = \frac{m_S}{\Lambda} = \frac{m_S}{m_\phi}. \quad (8.1)$$

Studies of the statistical distribution of meson kinematics have shown that a thermal Maxwell-Boltzmann distribution is followed approximately with temperature at the order of the confinement scale [177, 178]. Similarly, in the SUEP model, it is assumed that the dark mesons ϕ have a Maxwell-Boltzmann momentum distribution

$$\frac{dN}{d^3\mathbf{p}_\phi} \sim \exp\left\{\left(-\frac{\sqrt{\mathbf{p}_\phi^2 + m_\phi^2}}{T}\right)\right\}, \quad (8.2)$$

based on phenomenological studies [179]. Since T is expected to be at the order of the confinement scale, a validity range of $T \sim [0.25, 4] \times m_\phi$ is used when sampling the parameter values.

The dark mesons ϕ are assumed to be coupled to dark photons A' via the operator $\phi A'^{\mu\nu} A'_{\mu\nu}$. The dark photons are not directly coupled with SM particles, but they are kinematically mixed with the SM hypercharge via the operator $\frac{1}{2}\epsilon A'^{\mu\nu} B_{\mu\nu}$. The part of the Lagrangian that encapsulates the decays back to the SM is

$$\mathcal{L}_{decay} = \phi A'^{\mu\nu} A'_{\mu\nu} - \frac{1}{2}m_{A'}^2 A'^\mu A'_\mu + \frac{1}{2}\epsilon A'^{\mu\nu} B_{\mu\nu}, \quad (8.3)$$

where $m_{A'}$ is the mass of the dark photon, ϵ is the strength of the mixing between the dark and the SM photons, ϕ is the dark meson field, $B_{\mu\nu}$ is the field strength tensor for the SM hypercharge gauge field B_μ , and A'_μ and $A'^{\mu\nu}$ are the field and the field strength tensor respectively of the dark photon. This mechanism does not allow tree-level decays of ϕ to SM particles. Instead, a practical limit is imposed on the dark meson mass that $m_\phi > 2m_{A'}$ and therefore the decay to SM can occur through decay to two A' , which then

decay to SM because of the kinematic mixing.

The decay width of A' can be shown to be [23, 180]

$$\Gamma[A' \rightarrow l^+ l^-] \simeq \frac{m_{A'} \alpha \epsilon^2 \cos^2(\theta_W)}{3} \left(1 + \frac{2m_l^2}{m_{A'}^2} \right) \sqrt{1 - \frac{4m_l^2}{m_{A'}^2}}. \quad (8.4)$$

When $m_{A'} \gg m_l$, then the width is approximately $\Gamma[A' \rightarrow l^+ l^-] \propto \epsilon^2 m_{A'}$. The decay rate for $m_{A'} \sim \mathcal{O}(1 \text{ GeV})$ and $\epsilon \gtrsim 10^{-5}$ corresponds to $c\tau \lesssim 1 \text{ mm}$. Therefore, decays back to SM can always be considered prompt for this SUEP model, given a reasonable range for the $m_{A'}$. The branching fractions of A' to SM particles depend strictly on $m_{A'}$. The decay fractions to electrons, muons, and hadrons can be seen in Figure 8.2 [23] as a function of the dark photon mass. For $0.25 \text{ GeV} \lesssim m_{A'} \lesssim 0.6 \text{ GeV}$, the dark photons

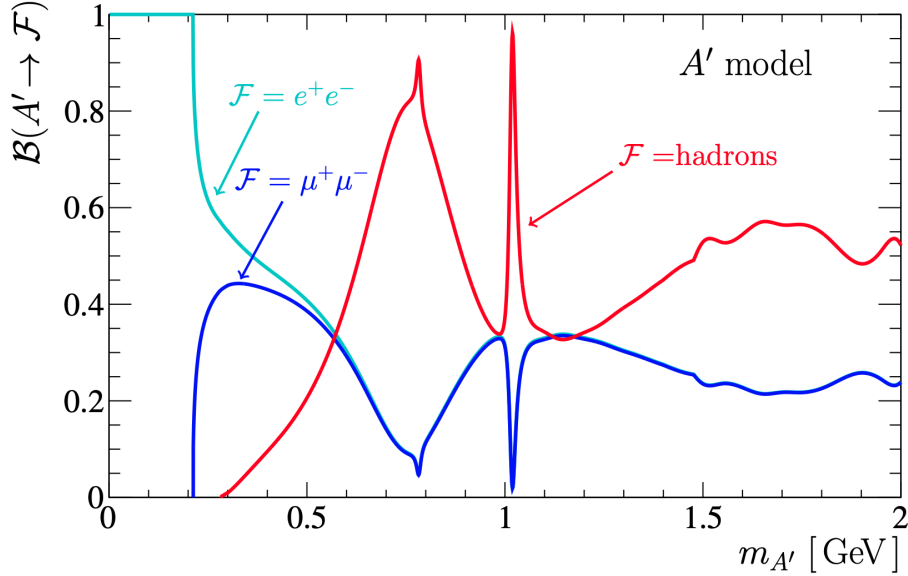


Figure 8.2: The branching fractions of A' to e^+e^- , $\mu^+\mu^-$, and hadrons as a function of the mass of the dark photon $m_{A'}$. [23]

decay predominantly to pairs of electrons and muons with approximately equal numbers of electron and muon pairs. In this regime, the SUEP events are expected to have final

states with very large muon multiplicities.

The SUEP parameter landscape is vast since it contains 4 different parameters that can be varied to alter its behavior. Fortunately, there are constraints that can be used to impose validity ranges. The parameters are the following:

- **Mediator mass m_S :** sets the energy scale of the process. There are no hard limits, but practically limited between the Higgs mass at the lower end and the LHC energy at the higher end. The generated samples are in the $[125, 1000]$ GeV range for this parameter.
- **Dark meson mass m_ϕ :** effectively sets the hadronization scale, Λ . A hard upper limit is set by $\frac{m_S}{2}$ to even allow kinematically the decay $S \rightarrow \phi\phi$. In practice, the parameter is constrained to 8 GeV or less to focus on final states with higher multiplicities and not just a few dark hadrons. The lower limit used is 1 GeV to allow decays back to SM pions. The range used for this parameter in the signal scans is $[1, 8]$ GeV.
- **Temperature T :** controls the kinematic distribution of the ϕ dark mesons. It needs to be approximately at the order of m_ϕ . The actual limit is the range $[0.25, 4] \times m_\phi$ for each value of m_ϕ . Values lower than that are not parametrically sensible, and higher than that would create events with very few and hard dark mesons, resembling events with dark pions. The desirable SUEP range is shown in Figure 8.3 [24] as a purple rectangle covering a range of values for m_ϕ and $\frac{T}{m_\phi}$.
- **Dark photon mass $m_{A'}$:** determines the branching fractions for the decays back to the visible sector. For this search, we make use of two decay scenarios that

correspond to the mass points:

- $m_{A'} = 0.5 \text{ GeV}$: **leptonic dominated decays**. This corresponds to fractions $\mathcal{B}(A' \rightarrow e^+e^-) = \mathcal{B}(A' \rightarrow \mu^+\mu^-) = 0.4$ and $\mathcal{B}(A' \rightarrow \pi^+\pi^-) = 0.2$.
- $m_{A'} = 0.7 \text{ GeV}$: **hadronic dominated decays**. This corresponds to fractions $\mathcal{B}(A' \rightarrow e^+e^-) = \mathcal{B}(A' \rightarrow \mu^+\mu^-) = 0.15$ and $\mathcal{B}(A' \rightarrow \pi^+\pi^-) = 0.7$.

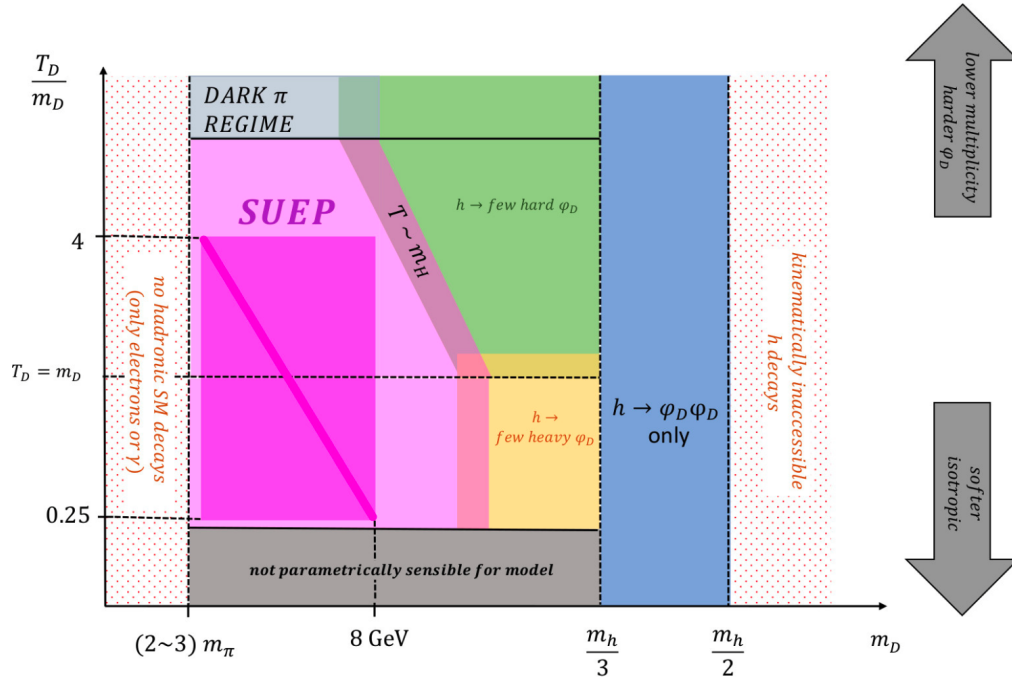


Figure 8.3: The SUEP parameter landscape. Figure taken from Ref. [24]. Sensible ranges for m_ϕ and the ratio $\frac{T}{m_\phi}$ can be set using kinematic restrictions and desired behavior arguments.

The existing efforts for searching for SUEP in CMS include the offline and scouting searches that focus on events with very high track multiplicities [163, 166] and more specialized searches that look for the signature of production associated with vector bosons [169, 171]. The offline and scouting searches excel in lower temperatures and T/m_ϕ ratios, depicted as the lower left half of the purple triangle in Figure 8.3. Additionally,

they hold an advantage in models with higher branching fractions to pairs of pions. The offline search published limits depend on m_S , but they generally exclude SUEP models with temperatures up to 10 GeV for the highest m_S values and lower for lower m_S values.

This analysis is expected to improve current limits for almost all signal points with at least some decays to muons ($m_{A'}$ equal to 0.5 or 0.7 GeV) and have the sensitivity needed to exclude parts of the parameter space with high T and T/m_ϕ values that were not reachable until now. Therefore, this search offers great complementarity to the current CMS analyses and is a step toward realizing sensitivity across the entirety of the SUEP parameter landscape.

Chapter 9: Data and Monte Carlo samples

This search uses data and MC simulation samples that were produced using ultra-legacy (UL) reprocessing during the `RunIISummer20UL` campaigns for all the Run 2 years. The datatier in use is centrally produced `MiniAODv2`. As a first step, all these samples were processed to filter out events that do not pass the preselection requirements and to produce custom-made `NanoAODv9` that include `PFCands` with the remaining events [181]. All three Run 2 data-taking years, from 2016 through 2018, are handled separately both in the MC simulations and in the reconstruction of simulations or data.

9.1 Datasets

The total amount of data from Run 2 in use is 118.28 fb^{-1} and was collected during the years 2016, 2017, and 2018 [182–184] at center-of-mass energy $\sqrt{s} = 13 \text{ TeV}$. The luminosities are calculated using the standard Lumi POG recipes [185], including applying the GoldenJSON masks and running `brilcalc`. The primary dataset is `DoubleMuon` since we use triggers that select events with three muons. Table 9.1 summarizes the data-taking years, the corresponding `MiniAOD` reprocessing used for each one, the eras that compose them, and the run range and luminosity corresponding to each of these eras for Run 2.

Table 9.1: Data taking years for Run 2 (13 TeV) used in the analysis, with the corresponding MiniAOD reprocessing used for each one, the eras that compose them, and the run range and luminosity corresponding to each of these eras. All numbers are for the DoubleMuon primary dataset.

Year	miniAOD processing	Era	Run range	Luminosity (fb ⁻¹)
2016	UL2016_MiniAODv2	2016F	278769–278808	0.58
		2016G	278820–280385	7.65
		2016H	281613–284044	8.74
2017	UL2017_MiniAODv2	2017B	297047–299329	4.80
		2017C	299368–302029	9.57
		2017D	302031–302663	4.25
		2017E	303824–304797	9.31
		2017F	305040–306462	13.54
2018	UL2018_MiniAODv2_GT36	2018A	315257–316995	14.03
		2018B	317080–319310	7.07
		2018C	319337–320065	6.90
		2018D	320500–325175	31.84
Total 2016			278769–284044	16.97
Total 2017			297047–306462	41.47
Total 2018			315257–325175	59.84
Total Run 2 (13 TeV)			272760–325175	118.28

The exact names of all MiniAOD datasets for Run 2 that have been processed can be found in Table 9.2.

9.2 Monte Carlo samples

9.2.1 Background samples

Monte Carlo (MC) simulations are used for all the SM processes that contribute to the background of this search. There are samples for all Run 2 data-taking years 2016, 2017, and 2018 that have been produced during the RunIISummer20UL* campaigns.

One of the largest sources of background originates from QCD jets that contain muons. The QCD samples are generated using PYTHIA [75] at leading order (LO). To

Table 9.2: The full names of the datasets in use for Run 2.

Dataset
/DoubleMuon/Run2016F-UL2016_MiniAODv2-v1/MINIAOD
/DoubleMuon/Run2016G-UL2016_MiniAODv2-v1/MINIAOD
/DoubleMuon/Run2016H-UL2016_MiniAODv2-v2/MINIAOD
/DoubleMuon/Run2017B-UL2017_MiniAODv2-v1/MINIAOD
/DoubleMuon/Run2017C-UL2017_MiniAODv2-v1/MINIAOD
/DoubleMuon/Run2017D-UL2017_MiniAODv2-v1/MINIAOD
/DoubleMuon/Run2017E-UL2017_MiniAODv2-v2/MINIAOD
/DoubleMuon/Run2017F-UL2017_MiniAODv2-v1/MINIAOD
/DoubleMuon/Run2018A-UL2018_MiniAODv2_GT36-v1/MINIAOD
/DoubleMuon/Run2018B-UL2018_MiniAODv2_GT36-v1/MINIAOD
/DoubleMuon/Run2018C-UL2018_MiniAODv2_GT36-v1/MINIAOD
/DoubleMuon/Run2018D-UL2018_MiniAODv2_GT36-v1/MINIAOD

increase the statistics, these QCD samples are muon-enriched by the use of a generator-level filter to select events with a generator-level muon with $p_T > 5 \text{ GeV}$. A significant number of muons in QCD jets can be attributed to π in-flight decays inside the detector. These pions are normally simulated by GEANT4 [186] since they are considered detector-stable particles and therefore do not decay in PYTHIA. However, to increase the efficiency of the muon gen-filter, the decays of π^\pm , K_L^0 , and K^\pm were turned on in PYTHIA. A problem caused by this change is that it was not propagated to the corresponding GEANT4 configuration and, therefore, GEANT4 simulated the decays of the remaining particles using unaltered decay rates. As a result, it is expected that the predicted cross sections are incorrect and that the MC normalization is not expected to match the data well. Nevertheless, this issue is resolved by fitting the QCD with data, and therefore, we keep these MC samples to benefit from the enhanced statistics.

The other sizeable source of background is coming from the Drell-Yan(DY)+jets $\rightarrow l^+l^- + \text{jets}$ process. This process is split into low- and high-mass samples, which differ in

the range of the mass of the generated Z/γ^* propagator. The high-mass samples have $m_{Z/\gamma^*} > 50$ GeV and include the Z peak, while the low-mass samples have $m_{Z/\gamma^*} < 50$ GeV with a lower cutoff at 10 GeV to avoid the infinities at the 0 GeV pole.

For the on-shell part of this process ($m_{Z/\gamma^*} > 50$ GeV), samples binned in the p_T of the Z at the generator level are used for all the Run 2 years because they have the best available statistics. Because of a mistake with the configuration of these samples [187], events with LHE Z p_T exactly equal to 0 GeV are missing. These events are taken from the inclusive `DYJetsToLL` sample.

For the low-mass off-shell part of the DY MC simulation, inclusive samples with a mass range from 10 to 50 GeV are used. The samples for Run 2 have up to 2 jets at the matrix element level, while those for Run 3 have up to 4 jets. These samples were generated using MADGRAPH [76] at LO in QCD and the MLM [188] scheme for jet-matching. The normalization for the low-mass off-shell sample was calculated at NLO in QCD.

Other smaller backgrounds are simulated using either aMC@NLO or POWHEG [189–191] at NLO or MADGRAPH at LO in QCD. For the $W + \text{jets} \rightarrow l\nu_l$ process in the Run 2 years, LO samples, binned in H_T , are used for their enhanced statistics together with the NLO inclusive sample for events with $H_T < 70$ GeV. For the same process in the Run 3 years, jet-binned samples (0 to 2 jets) that have been generated with aMC@NLO at NLO are used. Other notable processes that are included are: $t\bar{t}$ using POWHEG [192], single top, $t\bar{t} + V$, $W + \text{jets}$, VV , VVV , and $H \rightarrow ZZ \rightarrow 4l$. A comprehensive list including the exact name, the normalization, the plotting group name, and the order of generation and normalization is presented in Table 9.3 for Run 2.

For all MC samples, as a first step, the matrix element calculation is performed by one of the external generators or PYTHIA, and then they are passed to PYTHIA tuned with the CMS developed TuneCP5 [193] for parton showering, hadronization, and underlying event simulation. The relevant center-of-mass energies are set accordingly, $\sqrt{s} = 13$ TeV for Run 2 samples. The parton distribution function set NNPDF31_nnlo_as_0118 [194] is used. The next step consists of passing the events generated by PYTHIA to a full-scale simulation of CMS based on GEANT4. The simulation step models the interaction region realistically using a technique named vertex smearing and estimates the interactions between the generated particles and all the passive and active material of the detector. The trajectories of all charged particles are calculated using a detailed map of the magnetic field created by the solenoid magnet. The simulated hits are then passed to a digitization step that simulates the response and the noise of the detector readout electronics. Finally, the effect of pileup (PU) is included in the final result of the simulation using the pre-mixing technique [195].

9.2.2 Signal samples

The MC samples for the signal processes have been generated using the BSM Higgs tools in PYTHIA. The hard process $pp \rightarrow S$ is generated directly in PYTHIA, effectively simulating the gluon-gluon fusion production mode for Higgs. The resulting scalar particle is then passed to a plugin [196] that contains an implementation of the dark showering procedure and has been added to CMSSW as a PYTHIA user-hook. The plugin effectively simulates the dark shower process $S \rightarrow \phi \cdots \phi$ by creating the number of dark

mesons ϕ that is allowed by the energy scale of the hard process and assigning them kinematic properties using a relativistic version of the Maxwell-Boltzmann distribution, also known as Maxwell-Jüttner distribution, with temperature T . The final decays of ϕ to A' and A' to SM particles are handled by PYTHIA.

The generation of the signal samples was performed centrally using the EXO group's MC&I tools [197]. The scan over the signal parameters was performed using `RandomizedParameters` except for the temperature T parameter, which had to be provided as a `UserCustomization`. The following parameter ranges were scanned:

- m_S : values in the $[125, 1000]$ GeV range,
- $m_{A'}$: 0.5 and 0.7 GeV corresponding to the leptonic and hadronic decay scenarios, respectively, as they were described in Section 8,
- m_ϕ : values in the $[1, 8]$ GeV range for the leptonic decay scenario and $[1.4, 8]$ GeV for the hadronic decay scenario,
- T : values in the $[0.25, 4] \times m_\phi$ range, which corresponds to $[0.25, 32]$ GeV and $[0.35, 32]$ GeV for the leptonic and the hadronic decay scenarios, respectively.

The resulting signal sample names, split over the values of T , can be found in Table 9.4 for Run 2. The scan values for m_ϕ and $m'_{A'}$ contained in each sample are presented in separate columns. The scan over the m_S values is common to all samples, so it is not included in separate columns. The scan map over the values of T and m_ϕ is presented in Figure 9.1.

The cross sections for Higgs are used, and the calculations for the cross section

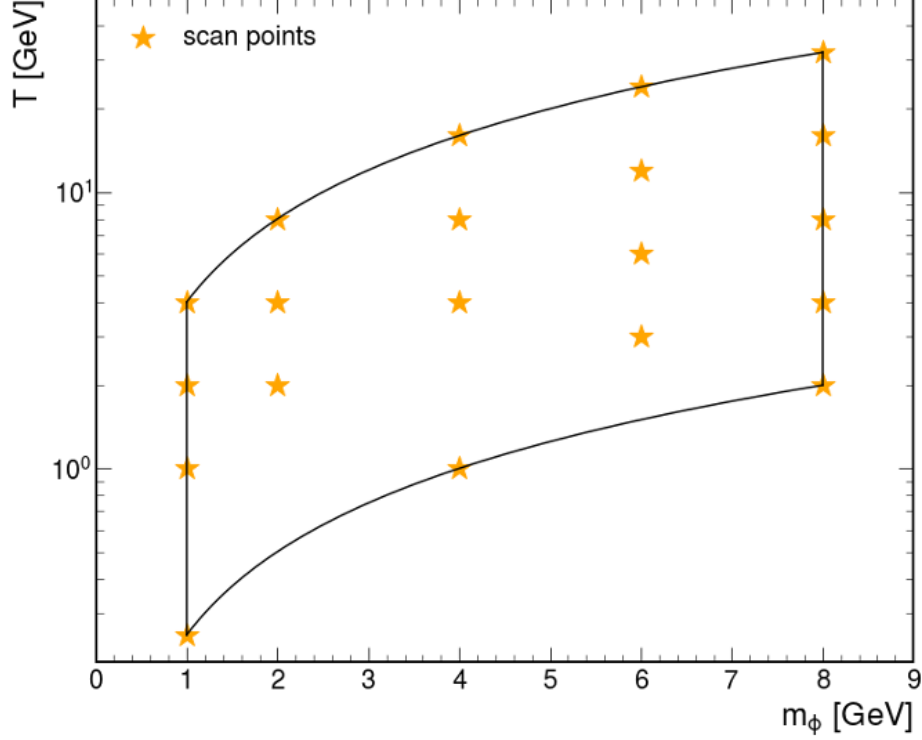


Figure 9.1: The scan points chosen for T and m_ϕ . The bounds of the parametrically sensible region are denoted with black lines

versus the Higgs mass from the LHC Higgs XS WG [198] are utilized for the samples with different values of m_S . The calculation for point-like effective interaction is used, which is N³LO in QCD but without any additional mass or EW corrections. The PDF set is PDF4LHC15_nnlo_100. The values of the cross sections for all the different values of m_S at the center-of-mass energy, 13 TeV, are shown in Table 9.5. The scalar mediator is assumed to decay to a group of dark mesons with $\mathcal{B}(S \rightarrow \phi \cdots \phi) = 1$, which then decay to pairs of dark photons with $\mathcal{B}(\phi \rightarrow A' A') = 1$. Finally, the dark photons, A' , decay to $e^+ e^-$, $\mu^+ \mu^-$, and $\pi^+ \pi^-$ pairs with branching ratios that are set by their mass. Two mass points (equivalent to decay scenarios) are generated: 1) $m_{A'} = 0.5 \text{ GeV}$ with branching ratios $\mathcal{B}(A' \rightarrow e^+ e^-) = \mathcal{B}(A' \rightarrow \mu^+ \mu^-) = 0.4$ and $\mathcal{B}(A' \rightarrow \pi^+ \pi^-) = 0.2$, and 2) $m_{A'} = 0.7 \text{ GeV}$ with branching ratios $\mathcal{B}(A' \rightarrow e^+ e^-) = \mathcal{B}(A' \rightarrow \mu^+ \mu^-) = 0.15$ and

$\mathcal{B}(A' \rightarrow \pi^+ \pi^-) = 0.7$. These branching fractions are used during the generation of the event by Pythia, but they are not needed in the final normalization event weights.

9.3 Corrections

9.3.1 Pileup reweighting

MC events are reweighted to correct discrepancies between the simulated PU distribution and the one seen in data [199]. A histogram ratio of the two distributions is used for the reweighting, and it is applied to the nominal event weight:

$$w = \frac{h_{data}[\text{nTrueInt}]}{h_{MC}[\text{nTrueInt}]} \quad (9.1)$$

The number of true interactions (`nTrueInt`) is used to pick the relevant histogram bin. The recommended nominal value of the inelastic p - p cross section is 69.2 mb with measurement uncertainty 4.6% [200].

9.3.2 L1 prefiring

During 2016 and 2017, the timing of ECAL experienced a gradual shift that was not propagated correctly to L1 trigger primitives (TP). This resulted in a significant fraction of high- η TPs erroneously associated with the previous bunch crossing (BX). L1 rules prevent two consecutive BXs from firing, effectively vetoing events that happen to have a significant amount of energy in the region $2.75 < \eta < 3$. This effect is referred to as L1 prefiring.

The muon system experienced a similar issue with prefiring originating from incorrect BX assignment of muon candidates because of the limited time resolution of the muon detectors. This effect, which was present in the entire Run 2 but more pronounced during 2016, has strong p_T - η dependence and its magnitude ranges from 0.5% to 1.5%.

This effect is not simulated in MC, and therefore, it is corrected using weights derived for each MC event individually after simulation. A prefiring probability is calculated for all offline photons, jets, and muons. The final weight is the product of the non-prefiring probability of all objects:

$$w = 1 - P(\text{prefiring}) = \prod_{i \in \{\text{photons, jets, muons}\}} \left(1 - p_{pref}^i(p_T^i, \eta) \right) \quad (9.2)$$

The recipe for the calculation of these weights [201] is implemented in the NanoAODv9. Since all samples are processed with an extended version of NanoAODv9, these weights are available by default in the samples used in this analysis for Run 2 years.

Table 9.3: Background samples used for Run 2 years in the analysis, their associated cross section times branching fraction, the plotting group in which each one is included in stack plots, and the overall QCD order used in the gen-level simulation (normalization cross section).

Sample name	$\sigma \times B \times \epsilon$ (pb)	Plotting group	Order (normalization)
DYJetsToLL.LHEFilterPtZ-0To50_MatchEWPdG20_TuneCP5.13TeV-amcatnloFFFX-pythia8	1404.0	DY	NLO(NLO)
DYJetsToLL.LHEFilterPtZ-100To250_MatchEWPdG20_TuneCP5.13TeV-amcatnloFFFX-pythia8	363.8	DY	NLO(NLO)
DYJetsToLL.LHEFilterPtZ-250To400_MatchEWPdG20_TuneCP5.13TeV-amcatnloFFFX-pythia8	84.0	DY	NLO(NLO)
DYJetsToLL.LHEFilterPtZ-400To650_MatchEWPdG20_TuneCP5.13TeV-amcatnloFFFX-pythia8	3.23	DY	NLO(NLO)
DYJetsToLL.LHEFilterPtZ-50To100_MatchEWPdG20_TuneCP5.13TeV-amcatnloFFFX-pythia8	0.436	DY	NLO(NLO)
DYJetsToLL.LHEFilterPtZ-650ToInf_MatchEWPdG20_TuneCP5.13TeV-amcatnloFFFX-pythia8	0.041	DY	NLO(NLO)
DYJetsToLL.M-50_TuneCP5.13TeV-amcatnloFFFX-pythia8	5804.0	DY	NLO(NNLO)
DYJetsToLL.M-10to50_TuneCP5.13TeV-madgraphMLM-pythia8	20590.0	DY	LO(NLO)
QCD_Pt-15To20_MuEnrichedPt5_TuneCP5.13TeV-pythia8	2800000.0	QCD	LO(LO)
QCD_Pt-20To30_MuEnrichedPt5_TuneCP5.13TeV-pythia8	2527000.0	QCD	LO(LO)
QCD_Pt-30To50_MuEnrichedPt5_TuneCP5.13TeV-pythia8	1367000.0	QCD	LO(LO)
QCD_Pt-50To80_MuEnrichedPt5_TuneCP5.13TeV-pythia8	381700.0	QCD	LO(LO)
QCD_Pt-80To120_MuEnrichedPt5_TuneCP5.13TeV-pythia8	87740.0	QCD	LO(LO)
QCD_Pt-120To170_MuEnrichedPt5_TuneCP5.13TeV-pythia8	21280.0	QCD	LO(LO)
QCD_Pt-170To300_MuEnrichedPt5_TuneCP5.13TeV-pythia8	7000.0	QCD	LO(LO)
QCD_Pt-300To470_MuEnrichedPt5_TuneCP5.13TeV-pythia8	622.6	QCD	LO(LO)
QCD_Pt-470To600_MuEnrichedPt5_TuneCP5.13TeV-pythia8	58.9	QCD	LO(LO)
QCD_Pt-600To800_MuEnrichedPt5_TuneCP5.13TeV-pythia8	18.12	QCD	LO(LO)
QCD_Pt-800To1000_MuEnrichedPt5_TuneCP5.13TeV-pythia8	3.318	QCD	LO(LO)
QCD_Pt-1000_MuEnrichedPt5_TuneCP5.13TeV-pythia8	1.085	QCD	LO(LO)
TTToHadronic_TuneCP5.13TeV-powheg-pythia8	377.96	TT	NLO(NLO)
TTToSemiLeptonic_TuneCP5.13TeV-powheg-pythia8	365.34	TT	NLO(NLO)
TTTo2L2Nu_TuneCP5.13TeV-powheg-pythia8	88.29	TT	NLO(NLO)
TTWJetsToQQ_TuneCP5.13TeV-amcatnloFFFX-madspin-pythia8	0.4432	TTV	NLO(NLO)
TTWJetsToLNU_TuneCP5.13TeV-amcatnloFFFX-madspin-pythia8	0.2163	TTV	NLO(NLO)
TTZToQQ_TuneCP5.13TeV-amcatnlo-pythia8	0.5113	TTV	NLO(NLO)
TTZToLL_TuneCP5.13TeV-amcatnlo-pythia8	0.07468	TTV	NLO(NLO)
ST_t-channel_top_4f_InclusiveDecays_TuneCP5.13TeV-powheg-madspin-pythia8	113.4	ST	NLO(NLO)
ST_t-channel_antitop_4f_InclusiveDecays_TuneCP5.13TeV-powheg-madspin-pythia8	67.93	ST	NLO(NLO)
ST_s-channel_4f_leptonDecays_TuneCP5.13TeV-amcatnlo-pythia8	3.549	ST	NLO(NLO)
ST_tW_Dilept_5f_DR_TuneCP5.13TeV-amcatnlo-pythia8	3.289	ST	NLO(NLO)
WJetsToLNU_TuneCP5.13TeV-amcatnloFFFX-pythia8	66680.0	WJets	NLO(NLO)
WJetsToLNU_HT-70To100_TuneCP5.13TeV-madgraphMLM-pythia8	1283.0	WJets	LO(NLO)
WJetsToLNU_HT-100To200_TuneCP5.13TeV-madgraphMLM-pythia8	1244.0	WJets	LO(NLO)
WJetsToLNU_HT-200To400_TuneCP5.13TeV-madgraphMLM-pythia8	337.8	WJets	LO(NLO)
WJetsToLNU_HT-400To600_TuneCP5.13TeV-madgraphMLM-pythia8	44.93	WJets	LO(NLO)
WJetsToLNU_HT-600To800_TuneCP5.13TeV-madgraphMLM-pythia8	11.19	WJets	LO(NLO)
WJetsToLNU_HT-800To1200_TuneCP5.13TeV-madgraphMLM-pythia8	4.926	WJets	LO(NLO)
WJetsToLNU_HT-1200To2500_TuneCP5.13TeV-madgraphMLM-pythia8	1.152	WJets	LO(NLO)
WJetsToLNU_HT-2500ToInf_TuneCP5.13TeV-madgraphMLM-pythia8	0.02646	WJets	LO(NLO)
WWTo1L1Nu2Q_4f_TuneCP5.13TeV-amcatnloFFFX-pythia8	51.65	VV+VVV	NLO(NLO)
WWTo2L2Nu_TuneCP5.13TeV-powheg-pythia8	11.09	VV+VVV	NLO(NLO)
WZTo1L1Nu2Q_4f_TuneCP5.13TeV-amcatnloFFFX-pythia8	9.119	VV+VVV	NLO(NLO)
WZTo2Q2L_mllmin4p0_TuneCP5.13TeV-amcatnloFFFX-pythia8	6.565	VV+VVV	NLO(NLO)
WZTo3LNU_mllmin4p0_TuneCP5.13TeV-powheg-pythia8	4.664	VV+VVV	NLO(NLO)
ZZTo2L2Nu_TuneCP5.13TeV-powheg-pythia8	0.9738	VV+VVV	NLO(NLO)
ZZTo2Q2L_mllmin4p0_TuneCP5.13TeV-amcatnloFFFX-pythia8	3.676	VV+VVV	NLO(NLO)
ZZTo4L_TuneCP5.13TeV-powheg-pythia8	1.325	VV+VVV	NLO(NLO)
WWW_4F_TuneCP5.13TeV-amcatnlo-pythia8	0.2158	VV+VVV	NLO(NLO)
WWZ_4F_TuneCP5.13TeV-amcatnlo-pythia8	0.1707	VV+VVV	NLO(NLO)
ZZZ_TuneCP5.13TeV-amcatnlo-pythia8	0.01476	VV+VVV	NLO(NLO)
GluGluHToZZTo4L_M125_TuneCP5.13TeV-powheg2_minloHJJ_JHUGenV7011.pythia8	0.01334	Higgs	NLO(NNLO)
VBF_HToZZTo4L_M125_TuneCP5.13TeV-powheg2_JHUGenV7011.pythia8	0.001038	Higgs	NLO(NNLO)
ZH_HToZZ_4LFilter_M125_TuneCP5.13TeV-powheg2_minlo-HZJ_JHUGenV7011.pythia8	0.001602	Higgs	NLO(NNLO)
WminusH_HToZZTo4L_M125_TuneCP5.13TeV-powheg2_minlo-HWJ_JHUGenV7011.pythia8	0.0001463	Higgs	NLO(NNLO)
WplusH_HToZZTo4L_M125_TuneCP5.13TeV-powheg2_minlo-HWJ_JHUGenV7011.pythia8	0.0002306	Higgs	NLO(NNLO)
WminusH_HToBB_WToLNU_M-125_TuneCP5.13TeV-powheg-pythia8	0.1031	Higgs	NLO(NNLO)
WplusH_HToBB_WToLNU_M-125_TuneCP5.13TeV-powheg-pythia8	0.1649	Higgs	NLO(NNLO)
GluGluToZH_HToZZTo4L_M125_TuneCP5.13TeV-jhugenv723-pythia8	$2.33 \cdot 10^{-5}$	Higgs	NLO(NNLO)
ttH_HToZZ_4LFilter_M125_TuneCP5.13TeV-powheg2_JHUGenV7011.pythia8	0.0009022	Higgs	NLO(NNLO)

Table 9.4: Signal samples used in the analysis for the Run 2 years. The scan values for m_ϕ and $m_{A'}$ that are contained in each sample are listed in separate columns. For all samples, the scanned values for m_S are 125, 200, 300, 400, 500, 600, 800, and 1000 GeV.

Sample name	m_ϕ (GeV)	$m_{A'}$ (GeV)
	scan values	scan values
GluGluToSUEP_T0p25_TuneCP5_13TeV_pythia8	1	0.5
GluGluToSUEP_T0p35_TuneCP5_13TeV_pythia8	1.4	0.7
GluGluToSUEP_T1p00_TuneCP5_13TeV_pythia8	1, 4	0.5, 0.7
GluGluToSUEP_T1p40_TuneCP5_13TeV_pythia8	1.4	0.5, 0.7
GluGluToSUEP_T2p00_TuneCP5_13TeV_pythia8	1, 2, 8	0.5, 0.7
GluGluToSUEP_T2p80_TuneCP5_13TeV_pythia8	1.4	0.5, 0.7
GluGluToSUEP_T3p00_TuneCP5_13TeV_pythia8	6	0.5, 0.7
GluGluToSUEP_T4p00_TuneCP5_13TeV_pythia8	1, 2, 4, 8	0.5, 0.7
GluGluToSUEP_T5p60_TuneCP5_13TeV_pythia8	1.4	0.5, 0.7
GluGluToSUEP_T6p00_TuneCP5_13TeV_pythia8	6	0.5, 0.7
GluGluToSUEP_T8p00_TuneCP5_13TeV_pythia8	2, 4, 8	0.5, 0.7
GluGluToSUEP_T12p00_TuneCP5_13TeV_pythia8	6	0.5, 0.7
GluGluToSUEP_T16p00_TuneCP5_13TeV_pythia8	4, 8	0.5, 0.7
GluGluToSUEP_T24p00_TuneCP5_13TeV_pythia8	6	0.5, 0.7
GluGluToSUEP_T32p00_TuneCP5_13TeV_pythia8	8	0.5, 0.7

Table 9.5: Cross sections for all values of m_S for center-of-mass energy 13 TeV.

m_S	125	200	300	400	500	600	800	1000
$\sigma(\sqrt{s} = 13 \text{ TeV})$ (pb)	45.2	16.9	6.59	3.19	1.71	1.0	0.402	0.185

Chapter 10: Object selection

This chapter presents the selection criteria for the objects used in this search. The main objects used are `Muon` and `PFCandidates`.

10.1 Muons

10.1.1 General muon selection

Muons are selected using the cut-based identification criteria at the `mediumId` level to reject badly reconstructed muons [202]. This criterion is chosen over the `SoftId` criterion because of its compatibility with the Particle Flow description of the event that is needed, since the `PFCandidates` are also in use. The kinematic selections are $p_T > 3 \text{ GeV}$ and $|\eta| < 2.4$. An additional requirement on the longitudinal impact parameter ($|d_z| < 0.2 \text{ cm}$) is applied to reduce bad reconstructions and the presence of muons from pileup (PU). In summary, the following cleaning selections are applied to muons:

- $p_T^\mu > 3 \text{ GeV}$,
- $|\eta| < 2.4$,
- $|d_z^\mu| < 0.2 \text{ cm}$,

- MediumId

10.1.2 Selections for the analysis subregions

This analysis categorizes the events into subregions, which are defined in great detail in Section 12.4. In short, two control regions are defined, one for QCD events and one for Drell-Yan events, and two signal regions, targeting low- and high-temperature SUEP events, which are further split into loose and tight selections. The muon selections for all the subregions are explained in detail in Section 12.4 and summarized in Table 12.5.

10.1.3 Muon corrections

The general muon efficiency can be described by the expression [203]

$$\epsilon_{\text{overall}}^{\mu} = \epsilon_{\text{TRK}}^{\mu} \cdot \epsilon_{\text{RECO}|\text{TRK}}^{\mu} \cdot \epsilon_{\text{ID}|\text{RECO}}^{\mu} \cdot \epsilon_{\text{Iso}|\text{ID}}^{\mu} \cdot \epsilon_{\text{Trigger}|\text{Iso}}^{\mu}, \quad (10.1)$$

where $\epsilon_{\text{TRK}}^{\mu}$ is the tracking efficiency, $\epsilon_{\text{RECO}|\text{TRK}}^{\mu}$ the reconstruction efficiency, $\epsilon_{\text{ID}|\text{RECO}}^{\mu}$ the cut-based identification efficiency, $\epsilon_{\text{Iso}|\text{ID}}^{\mu}$ the isolation efficiency, and $\epsilon_{\text{Trigger}|\text{Iso}}^{\mu}$ the trigger efficiency. The tracking efficiency is very close to unity; therefore, the general recommendation in CMS is to consider it equal to 1. For the purposes of this study, the isolation and triggering efficiencies can also be considered to be very close to 1 and, therefore, are ignored. The reconstruction and identification efficiencies are provided by the Muon Physics Object Group (POG) [204, 205]. The Tag-and-Probe method is utilized to calculate the efficiencies using the J/ψ peak for low- p_{T} muons ($p_{\text{T}} < 15$ GeV) and the Z peak for medium- p_{T} muons ($15 \text{ GeV} < p_{\text{T}} < 100$ GeV).

Corrections for the discrepancies of the muon reconstruction and identification efficiency between data and MC are applied to the events in the form of scale factor weights using per-muon weights that are combined multiplicatively to obtain a single weight for each event.

10.2 Tracks

Two collections are used to obtain all high-quality tracks, `PFCandidates` and `LostTracks`. The following quality criteria are imposed on the objects of these collections:

- $\text{fromPV} > 1$,
- $p_{\text{T}}^{\text{track}} \geq 0.75 \text{ GeV}$,
- $|\eta| \leq 2.5$ for `PFCandidates`, $|\eta| \leq 1$ for `LostTracks`,
- $|d_z| < 10 \text{ cm}$,
- $\delta d_z < 0.05 \text{ cm}$.

These cleaning selections require a tight fit to the primary vertex ($\text{fromPV} > 1$) [206] and limit the amount of displacement along the z axis (d_z) and its uncertainty (δd_z). After applying these cleaning requirements, the two collections are combined to form a tracks collection.

At this point, it should be noted that there are no cross-cleaning criteria to prevent any muons from being a track as well. This is in contrast to the strategy followed by the SUEP with associated vector boson searches (ZH and WH). Those analyses expect muons

from Z and W decay, and therefore, they have to remove them from the tracks that form the SUEP candidates. Such constraints do not exist in this analysis and are not utilized.

Chapter 11: Analysis strategy

In this chapter, we outline our strategy for background estimation. Our search consists of two sets of selection criteria defining two signal regions SRs, one optimized for high temperature and the other for low temperature, SUEP models. Both require at least three muons (that pass additional selections described in Chapter 12). The “loose” signal region is all such events, while the “tight” SR, used for the cut-and-count search for SUEP, requires at least 7 muons. For backgrounds containing vector bosons, including those from top decays and/or Higgs bosons, some of the muons are prompt. The rest come from meson decays, especially b or c mesons, or from decays in flight from charged pions and kaons.

We will show from the MC simulation that for all backgrounds containing prompt muons, except for Drell-Yan production, the background in each tight SR is negligible.

For DY production and QCD multijet production, we will show that the background is small (less than 0.2 events) but not negligible. For QCD backgrounds, a data-driven method is usually needed, as the modeling of, e.g., jet multiplicity, is not reliable. For QCD muons and muons in DY events beyond the two prompt muons, we will argue that the distribution falls exponentially. An exponential has two parameters, the normalization and the decay constant.

We fit exponential functions simultaneously to the loose and tight MC n_{muon} distributions. The fit uses three parameters for the two functions: two normalization parameters, one for loose and one for tight, and one common decay constant. This fitting procedure is performed separately on DY and QCD MC. The signal region histograms for MC are supplemented with the prediction of those fits since the MC samples for DY and QCD have insufficient statistics for high n_{muon} . These histograms are passed to CMS `Combine` [207] as signal regions. To obtain better normalizations for the background processes and constrain the systematic uncertainties, histogram distributions of n_{muon} using selections that are enhanced in backgrounds, with low signal contamination, referred to as control regions, are also fed into `Combine`. Finally, `Combine` adjusts the predictions within the uncertainties, including the part supplemented by the fit.

We will also define a validation region, which has selections similar to the signal region, but adjusted to ensure low signal contamination. The efficacy of the entire procedure is tested using this validation region.

Chapter 12: Event selection

The event selections target final states with large muon multiplicities. Initially, a pre-selection is imposed based on the desired HLT paths and requirements that ensure operation at the trigger plateau. Additional selections are placed to form the control, signal, and validation regions used throughout the analysis.

12.1 Triggers

All events are required to pass a selection based on a logical OR combination of HLT paths. The exact selections are shown in Table 12.1 and they depend on the year and the data-taking era within each year.

The individual HLT paths in use vary slightly between the data-taking eras and years, and sometimes even within the same era when there was a trigger menu update. However, all HLT paths share the requirement for at least three muons in the final state. There are three different configurations regarding the p_T cuts for the muons. These are: (12, 10, 5) GeV, (10, 5, 5) GeV, and (5, 5, 3) GeV. Some additional requirements that are present in some of the paths are:

- $|d_z^{\mu^+\mu^-}| < 0.2 \text{ cm}$ – difference in z between the two muons in each pair, denoted with `_DZ` in the path name.

Table 12.1: Summary of the HLT selection used in the pre-selection of events for the analysis for each associated data-taking period.

Period	HLT selection	Eff. luminosity (fb^{-1})
2016 Eras F-G	HLT_TripleMu_12_10_5	24.88
2016 Era H	HLT_TripleMu_5_3_3_DZ_Mass3p8 OR HLT_TripleMu_12_10_5	8.76
2017 Eras B-D	HLT_TripleMu_10_5_5_DZ OR HLT_TripleMu_12_10_5	17.27
2017 Eras D-F	HLT_TripleMu_5_3_3_Mass3p8to60_DZ OR HLT_TripleMu_10_5_5_DZ OR HLT_TripleMu_12_10_5	24.27
2018 Era A	HLT_TripleMu_5_3_3_Mass3p8to60_DZ OR HLT_TripleMu_10_5_5_DZ OR HLT_TripleMu_12_10_5	5.30
2018 Eras A-D	HLT_TripleMu_5_3_3_Mass3p8_DZ OR HLT_TripleMu_10_5_5_DZ OR HLT_TripleMu_12_10_5	54.67

- $m_{\mu^+\mu^-} > 3.8 \text{ GeV}$ – invariant mass of the two muons in each pair for all combinations, denoted with `_Mass3p8` in the path name.
- $m_{\mu^+\mu^-} < 60 \text{ GeV}$ – similar to above. Used only together with the requirement above and denoted with `_Mass3p8to60` in the path name.

Tables 12.2 show the exact data-taking eras and the effective luminosity (that is, the actual luminosity scaled by PU) for each HLT path for Run 2.

Table 12.2: Summary of the trigger paths used in the pre-selection of events for the analysis and their associated data-taking periods for Run 2 years.

Trigger paths	Periods	Eff. luminosity (fb^{-1})
HLT_TripleMu_5_3_3_DZ_Mass3p8	2016 Era H	8.74
HLT_TripleMu_5_3_3_Mass3p8to60_DZ	2017 Eras D-F, 2018 Era A	29.55
HLT_TripleMu_5_3_3_Mass3p8_DZ	2018 Eras A-D	54.54
HLT_TripleMu_10_5_5_DZ	2017 Eras B-F, 2018 Eras A-D	101.31
HLT_TripleMu_12_10_5	2016 Eras F-H, 2017 Eras B-F, 2018 Eras A-D	137.62

The HLT paths are seeded with logic combinations of L1 trigger bits. The exact L1 seeds are shown in Table 12.3, and they vary between different HLT paths, but they share the common feature of requiring three muons at the L1 level.

Table 12.3: Summary of the L1 seeds for each HLT path separated by the data-taking years.

Year	HLT path	L1 seed
2016	HLT_TripleMu_5_3_3_DZ_Mass3p8_v*	L1_TripleMu0 OR L1_TripleMu_5_0_0 OR L1_TripleMu_5_5_3
	HLT_TripleMu_12_10_5_v*	L1_TripleMu0 OR L1_TripleMu_5_5_3
2017–2018	HLT_TripleMu_5_3_3_Mass3p8to60_DZ_v*	L1_TripleMu0 OR L1_TripleMu_5_5_3 OR L1_TripleMu_5_3_3 OR L1_TripleMu3_SQ
2017–2018	HLT_TripleMu_10_5_5_DZ_v*	
	HLT_TripleMu_12_10_5_v*	
	HLT_TripleMu_5_3_3_Mass3p8_DZ_v*	

These HLT paths ran unscaled for almost the entirety of the physics data-taking runs (except for emergency columns).

This analysis focuses on final states with many muons. Specifically, at least 7 muons are required for the SR discovery bins and at least 3 for the CRs. As a result, the triggering efficiency is expected to be very close to 1 both in data and MC, and therefore, no scale factor corrections or uncertainties are applied.

12.2 Pre-selection

The pre-selection requires the events to pass one of the HLT paths described in Section 12.1, and then to have at least three reconstructed muons that pass the cleaning criteria described in Section 10.1.

12.3 Muon sources

The sources of muons can be divided into the following categories:

- Prompt muons coming directly from the hard scattering process (e.g., $Z \rightarrow \mu^+ \mu^-$).
- Light flavor hadron decays. For example, pion or kaon in-flight decays to muons.

The pions may be created by either the hard process, the parton shower, or the underlying event.

- Heavy flavor hadron decays. This involves b or c quarks, produced either in the hard scattering process or in the parton shower, that hadronize into D or B mesons that decay leptonically.
- Fake muons from reconstruction failures.

Fortunately, contributions from the last category are insignificant thanks to CMS's great performance as a muon detector and the stringent quality criteria that are imposed during object selection. Jets are expected to contain muons coming from light or heavy flavor decays. Therefore, for each SM process, a combination of prompt muons originating from the hard process and muons coming from light or heavy-flavored jets must be considered.

MC matching is used to determine the source of the muons in the MC signal and background samples. Each reconstructed muon is matched to the corresponding generator-level muon with final status (`status==1`), and then its generator history is traversed to determine the source. The muons are placed into 6 categories, and the result

is stored in the `Muon_genPartFlav` column in the NanoAOD files [208]. The values of `Muon_genPartFlav` are summarized in Table 12.4.

Table 12.4: The values of `Muon_genPartFlav` and muon sources.

<code>Muon_genPartFlav</code>	Muon Source
0	unmatched
1	prompt muon (including $\gamma^* \rightarrow \mu^+ \mu^-$)
3	
4	
5	muon from c
15	muon from b
	muon from prompt tau

This gen-matching procedure was utilized during the design of the analysis regions, and it is used in the next section to establish the optimal selection sets by separating the muons according to their source.

12.4 Selection regions

After pre-selection and object selection, further selections are imposed in order to form regions that isolate background events coming from specific sources, named Control Regions (CR), and regions with high purity of signal events, named Signal Regions (SR). In addition, a Validation Region (VR) is also defined to facilitate studying the validity of the background estimation method that will be described in the next chapter.

12.4.1 Control regions (CR)

We define two control regions with the intention of quantifying the two main sources of SM background: QCD multijet events with muons and DY to dimuons plus jets with muons.

12.4.1.1 QCD control region (CR_{QCD})

For the CR_{QCD}, the target is to isolate events coming from QCD multijets with muons. It is expected that most muons in these events originate from π , K , D , and B meson decays, which have been produced by the hadronic showers in the jets. These mesons are expected to have significant detector lifetimes, $c\tau$, and therefore the muons often have large impact parameters. Figure 12.1 presents the distribution of d_{xy}^μ broken down by the MC process (left plot) and by the muon source (right plot). It is evident that the dominant source of muons in QCD is b -flavored mesons, followed by c -flavored mesons. All other sources have insignificant contributions.

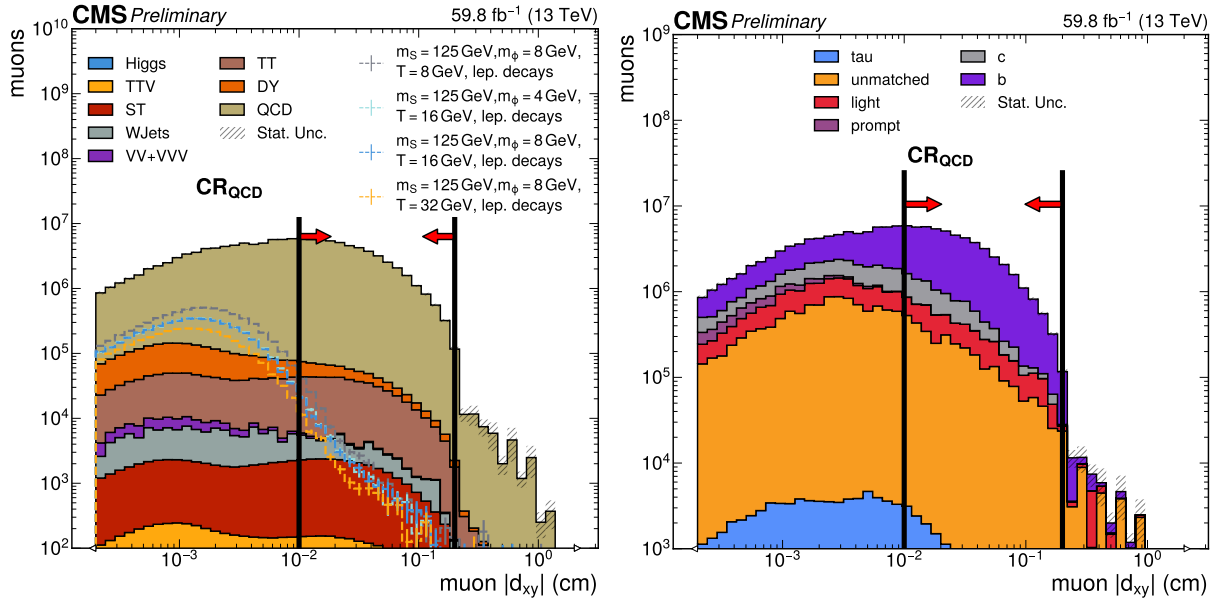


Figure 12.1: Distribution of d_{xy}^μ for 2018 MC simulation. The left plot shows this split by the MC process, and the right plot shows the grouped contributions of each muon source.

For this reason, the transverse impact parameter, d_{xy}^μ , of the muons in this region is required to be in the range $0.01 \text{ cm} \leq |d_{xy}^\mu| \leq 0.2 \text{ cm}$ to ensure that a pure sample of b -

origin muons. Ultimately, the CR_{QCD} is formed by counting the number of muons passing that selection and keeping events that have at least one such muon. The histogram for this region, binned in n_{muon} , can be seen in Figure 12.2 for both data and MC, including a plot of their ratio. The last bin also includes contributions from events with more than 4 muons. The MC histogram for each year is normalized to the data using k-factors that are estimated by subtracting the total yields of all non-QCD MC processes from the total yields of the data and then dividing by the total QCD MC yield in the region. The QCD k-factors range between 0.62 and 0.71.

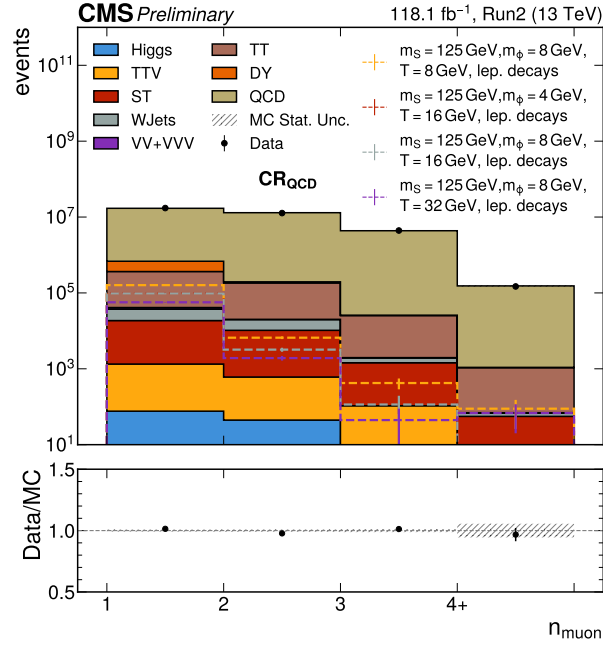


Figure 12.2: CR_{QCD} for Run 2. The ratio between data and MC is also shown. A k -factor has been applied to QCD to normalize the total MC yield to data.

12.4.1.2 DY control region (CR_{DY})

Similarly, the CR_{DY} isolates events that contain the results of the Drell-Yan process with the Z/γ^* eventually decaying to a pair of muons. These events can have more than

two muons because of extra muons coming from jets. To create this region, all possible pairs of opposite-sign muons are formed, and the dimuon with invariant mass closest to the Z mass is kept as the Z candidate. Events that don't have opposite-sign muon pairs are rejected. To further reduce all non-DY processes, an extra requirement for the invariant mass of the Z candidates to be within $2\Gamma_Z = 4.99 \text{ GeV}$ of the Z mass:

$$|m_{\mu^+\mu^-} - m_Z| < 2\Gamma_Z \Leftrightarrow |m_{\mu^+\mu^-} - 91.19 \text{ GeV}| < 4.99 \text{ GeV} \quad (12.1)$$

Similarly with CR_{QCD} , this region is also binned in n_{muon} . For this reason, the prompt muons coming from the hard process and the soft muons produced by jets need to be counted and added together for each event. The prompt muons are the same ones that form the Z candidates with the following additional selections that improve their purity:

- $p_T^\mu > 25 \text{ GeV}$
- Muon_miniIsoId at least tight ($\text{Muon_miniPFRelIso_all} < 0.1$)
- $|d_{xy}^\mu| < 0.008 \text{ cm}$
- $|d_z^\mu| < 0.01 \text{ cm}$
- $|IP_{3D}^\mu| < 0.01 \text{ cm}$

The $N - 1$ plot for the d_{xy}^μ distribution of the prompt muons is shown in Figure 12.3. The cut is placed at the point of transition from prompt muons to b muons. The other selections are chosen similarly. All $N - 1$ plots can be found in Appendix B.

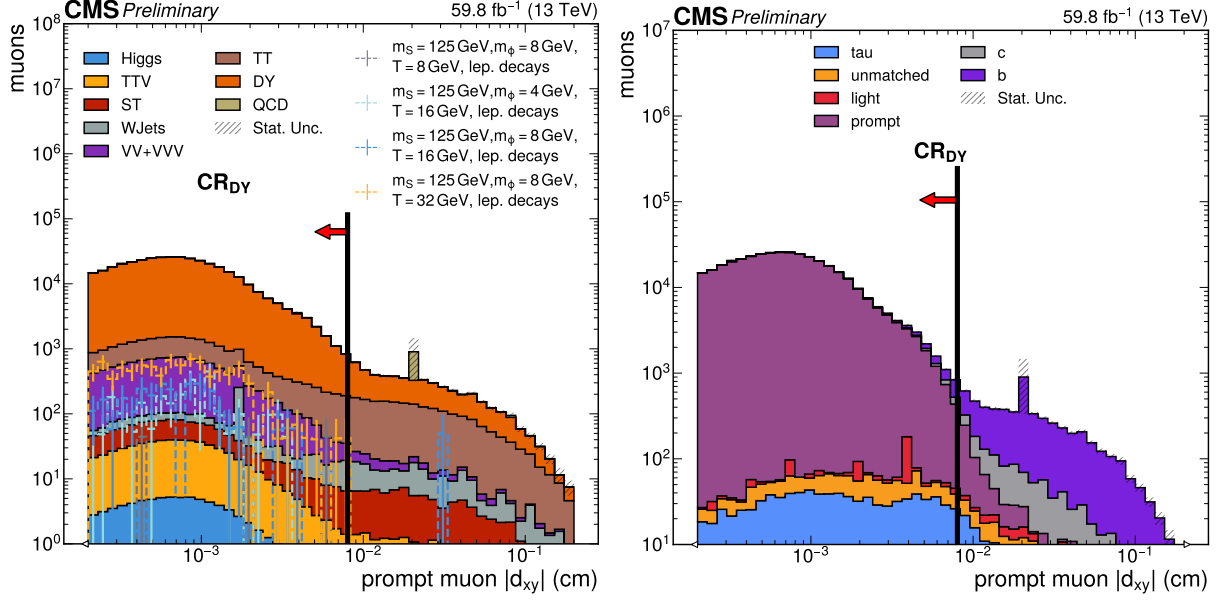


Figure 12.3: $N-1$ distribution of d_{xy}^μ of prompt muons for 2018 MC simulation. The left plot shows this split by the MC process, and the right plot shows the grouped contributions of each muon source.

The QCD-originating muons (applicable to all MC processes – not only QCD MC) are counted from all other muons that pass the following selection:

- Muon_minIPRelIso_all > 0.1
- $|d_{xy}^\mu| > 0.01$ cm
- $|d_z^\mu| > 0.01$ cm
- $|IP_{3D}^\mu| > 0.015$ cm

which is approximately the reverted selection of the one used to select the prompt muons.

The $N-1$ plot for the distribution of the muon isolation is presented in Figure 12.4.

Evidently, the isolation cut is placed in a way that selects the b muons that exist in DY events. All other cuts are constructed with similar objectives, and they can be found in

Appendix B.

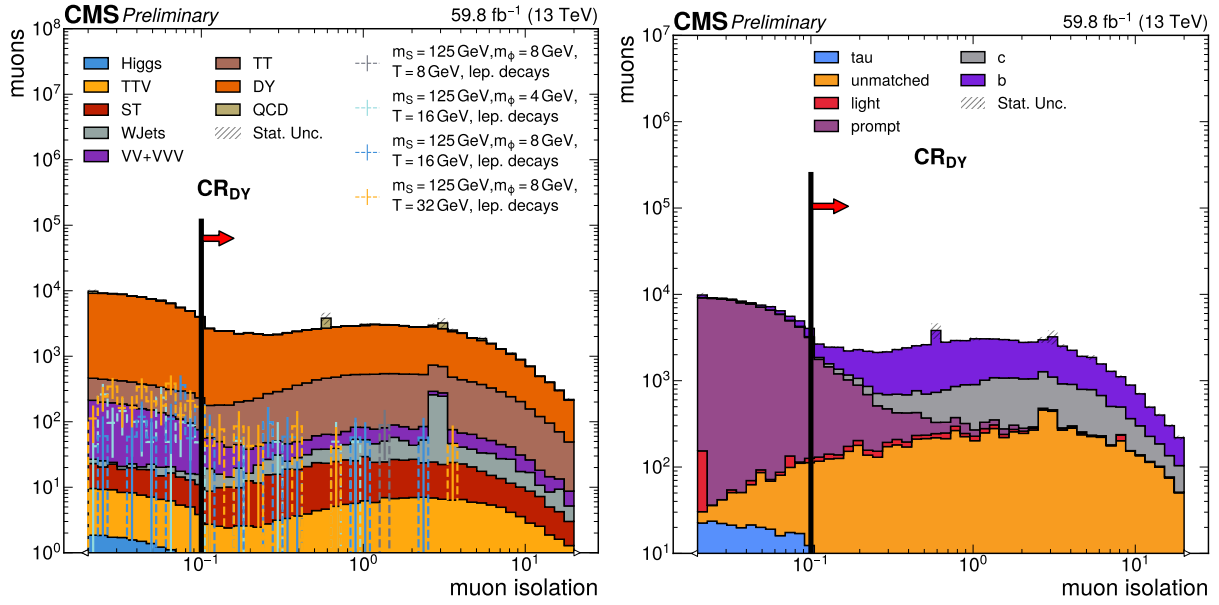


Figure 12.4: $N - 1$ distribution of the muon isolation for 2018 MC simulation. The left plot shows this split by the MC process, and the right plot shows the grouped contributions of each muon source.

The CR_{DY} is formed using the muon counts $n_{\text{muon}} = n_{\text{prompt muon}} + n_{\text{QCD muon}}$. The region is defined using this n_{muon} sum because it selects many DY events while keeping the signal contamination low. Selecting multiple prompt muons is possible by removing the dimuon mass constraint, but it would introduce large contamination from high-temperature signal. On the other hand, selecting muons using only the criteria for QCD muons populates the region mostly with QCD events. Eventually, events with at least two muons are kept, and the region is binned in the n_{muon} distribution. The resulting histogram is shown in Figure 12.5 for both data and MC, including a plot of their ratio. In a similar fashion to CR_{QCD} , the last bin includes the overflow contributions from events with more than 5 muons. The MC histograms for each year are normalized to data with the use of DY k-factors that are derived in a similar manner to the k-factors for QCD in CR_{QCD} . The DY k-factors for Run 2 are between 0.93 and 0.97.

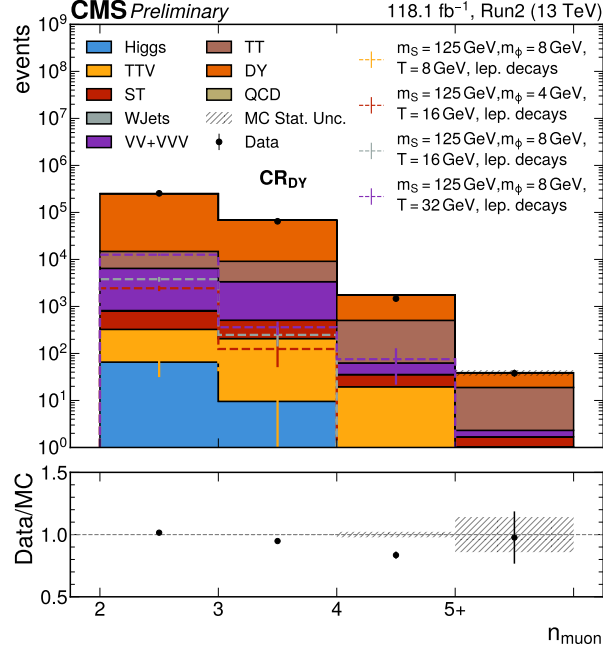


Figure 12.5: CR_{DY} for Run 2. The ratio between data and MC is also shown. A k -factor has been applied to QCD to normalize the total MC yield to data.

12.4.2 Signal regions (SR)

The behavior of the signal model can vary vastly between the edges of a given parameter range. A particularly notable example is the effect of the model's temperature T on the multiplicity of the final state. The hadronization scale of the dark shower is effectively controlled by the value of this input parameter. Low temperature values result in events with very high multiplicities of soft particles, giving unique final states that diverge significantly from the outcomes of SM processes. In the opposite edge of the temperature range, high T values give final states with fewer particles with larger momenta that are more similar to SM events. For that reason, two signal regions are defined, the first targeting the high-temperature models ($SR_{high\ T}$) and the second being optimized for low-temperature models ($SR_{low\ T}$).

Furthermore, as it will become obvious over the next few paragraphs, these signal regions are plagued by insufficient MC statistics, making any MC-based background estimation prohibitive. This issue is overcome by an extrapolation method that extracts the slope of the n_{muon} distribution from a region with looser selections that allow for better MC statistics and then applies it to the distribution in the tight signal region to extrapolate the yields of empty bins. This method is explained in great detail in Section 13. Therefore, the $\text{SR}_{\text{low } T}$ and $\text{SR}_{\text{high } T}$ are further divided into loose and tight variants.

For both SRs, the final discovery bin used in the final fit to data, as described in Section 6.4, is formed by keeping events with $n_{\text{muon}} \geq 7$. These discovery bins are the only parts of the signal regions that are directly utilized in looking for new physics and setting upper limits.

12.4.2.1 Low temperature signal region ($\text{SR}_{\text{low } T}$)

SUEP models with low or medium temperatures are expected to create very large multiplicities of particles that are isotropically distributed in the rest frame of the scalar mediator particle. An attempt to exploit this distribution is made using a SUEP identification procedure that involves picking a high multiplicity track cluster, boosting its constituents to the cluster's rest frame, and calculating event shape variables using the boosted tracks. In more detail, the cleaned tracks are reclustered using FASTJET [209] with the anti- k_T algorithm [210] and cone size $\Delta R = 1.5$. The clusters are ordered by p_T and up to two are kept (two or one if there is only one cluster). The cluster with the largest number of constituents is marked as the SUEP candidate. Since the SUEP candidate is a

very large radius jet, it is not expected to be a very accurate reconstruction of the actual scalar mediator. However, the energy distribution of the cluster is still expected to be relatively spherical in its rest frame. The SUEP candidate constituents are boosted back to the AK15 jet's rest frame and then are used to calculate the sphericity tensor

$$S_{ab}^{(r)} = \frac{\sum_i |p_i|^{r-2} p_{i_a} p_{i_b}}{\sum_i |p_i|^r}, \quad (12.2)$$

where $a, b \in \{x, y, z\}$, p_i is the momentum of one particle, and r is a free parameter that in this analysis is set to 1 to keep the calculation infrared and collinear (IRC) safe. After the tensor is calculated, the sphericity event shape variable, S , is calculated as

$$S_1 = \frac{3}{2} (\lambda_2 + \lambda_3), \quad (12.3)$$

where λ_2 and λ_3 are the two lowest eigenvalues of the sphericity tensor. The value of this variable is close to 1 for very spherical events, like the ones originating from the signal process, and close to 0 for non-spherical events, like traditional QCD dijet events. Cuts on this variable are used when selecting events for both $\text{SR}_{\text{high } T}^{\text{loose}}$ and $\text{SR}_{\text{high } T}^{\text{tight}}$.

The $\text{SR}_{\text{low } T}$ regions are formed by selecting events with S_1 values above some threshold and $n_{\text{muon}} \geq 3$. For the muons, an extra upper limit is imposed on their p_T values to reject muons coming from DY, multiboson, and $t\bar{t}$ events without significantly affecting the selection of signal muons, which are expected to be softer. The values for all the selections have been optimized by using $N - 1$ plots for all the quantities of interest and the final expected yield for the background in the discovery bin of the signal region.

The thresholds for the cuts were adjusted to levels that reduce the expected background to 0.3 events or less while taking care not to overly penalize the signal selection efficiency by consulting the corresponding $N - 1$ plots.

The muon requirements are chosen to accommodate the soft and prompt muons that are expected in signal events. The dimuon resonances in signal events have very low masses. Therefore, the mass of the OS dimuon pairs is restricted to low values. Finally, a cut is placed on sphericity since signal events typically attain values > 0.5 . The summary of the selections for the $\text{SR}_{\text{low } T}^{\text{tight}}$ placed on top of the generic SR selections is:

- $p_T^\mu < 35 \text{ GeV}$ for all muons
- $IP_{3D}^\mu < 0.007 \text{ cm}$ for all muons
- $n_{\text{muon}} \geq 3$
- $S_1 > 0.7$
- $m_{\mu^+\mu^-} < 35 \text{ GeV}$ over all opposite-sign (OS) dimuon pairs

The same selections are relaxed to form $\text{SR}_{\text{low } T}^{\text{loose}}$ with better statistics:

- $p_T^\mu < 45 \text{ GeV}$ for all muons
- $IP_{3D}^\mu < 0.1 \text{ cm}$ for all muons
- $n_{\text{muon}} \geq 3$
- $S_1 > 0.2$
- $m_{\mu^+\mu^-} < 45 \text{ GeV}$ over all opposite-sign (OS) dimuon pairs

The remaining events are binned in n_{muon} both for $\text{SR}_{\text{low } T}^{\text{loose}}$ and $\text{SR}_{\text{low } T}^{\text{tight}}$.

The $N - 1$ plots for the distributions of S_1 and $m_{\mu^+\mu^-}$ are shown in Figure 12.6. The

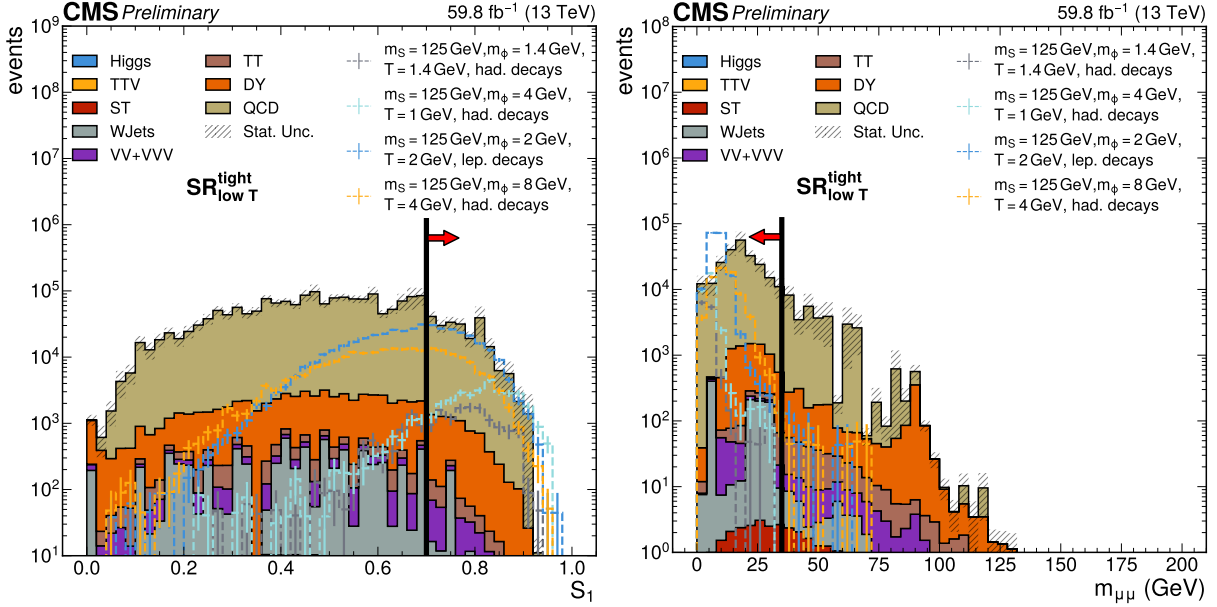


Figure 12.6: $N - 1$ distributions of S_1 (left) and $m_{\mu^+\mu^-}$ (right) in $\text{SR}_{\text{low } T}^{\text{tight}}$ for 2018 MC simulation. The chosen cuts are indicated with black lines and red arrows on the plots.

values of the cuts are selected so that the background rejection is as strong as possible without compromising significantly the signal retention efficiency. All $N - 1$ plots are included in Appendix B.

The remaining events are binned in n_{muon} . The histograms for $\text{SR}_{\text{low } T}^{\text{loose}}$ and $\text{SR}_{\text{low } T}^{\text{tight}}$ are shown in Figure 12.7 for Run 2. The last bin is inclusive in n_{muon} higher than 7 and is marked as the discovery bin.

12.4.2.2 High temperature signal region ($\text{SR}_{\text{high } T}$)

When dealing with signal models that have higher temperatures ($> 4 \text{ GeV}$), the final states often do not have high enough multiplicities to make advantageous the use

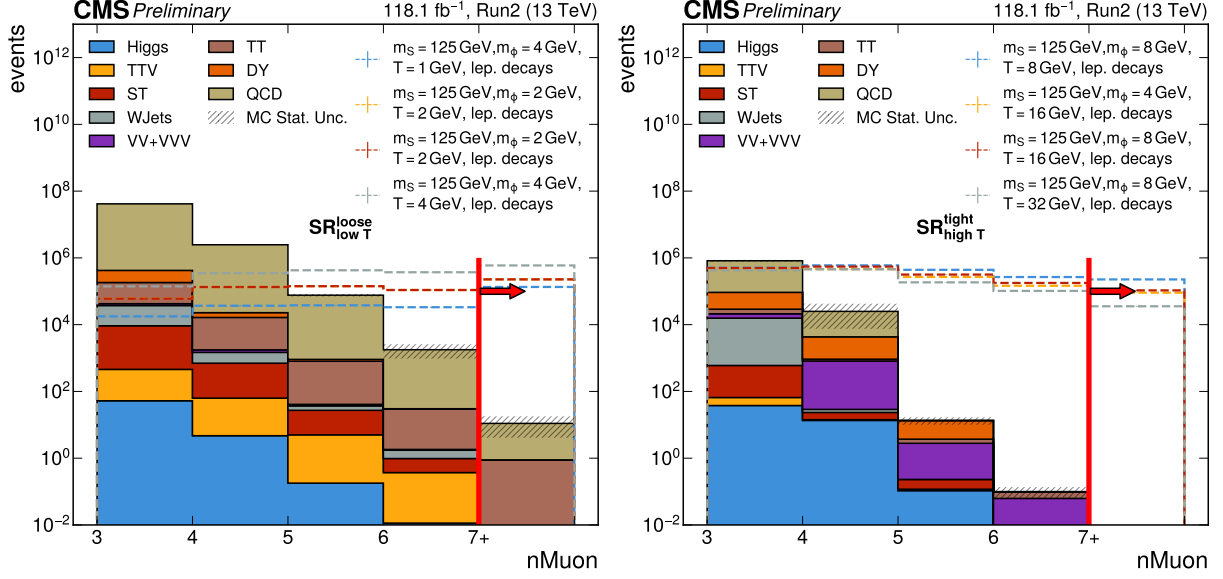


Figure 12.7: $SR_{low\ T}$ regions for Run 2 MC. Left is $SR_{low\ T}^{loose}$ and right is $SR_{low\ T}^{tight}$. The discovery bin is annotated with a separate red line and a pointing arrow.

of sphericity, a variable very sensitive to the input number of particles. Instead, cuts on muon isolation are a better choice since less hadronic activity is expected in the vicinity of the muons. Additionally, it is known that the dark photons decay to pairs of charged SM particles, namely e^+e^- , $\mu^+\mu^-$, and $\pi^+\pi^-$. Therefore, a cut on the neutral component of the isolation, which is defined as the difference between the isolations for all and charged particles, $Muon_miniPFRelIso_all - Muon_miniPFRelIso_chg$, is also applied.

The selections for the $SR_{high\ T}^{tight}$ on top of the generic SR selections are:

- $IP_{3D}^\mu < 0.007\text{ cm}$
- $Muon_miniPFRelIso_all < 0.65$
- $Muon_miniPFRelIso_all - Muon_miniPFRelIso_chg < 0.5$
- $n_{muon} \geq 3$
- $m_{\mu^+\mu^-} < 70\text{ GeV}$

Again, these selections are relaxed to form $SR_{high\ T}^{loose}$ with better statistics:

- $IP_{3D}^{\mu} < 0.1\text{ cm}$
- $Muon_miniPFRelIso_all < 5$
- $Muon_miniPFRelIso_all - Muon_miniPFRelIso_chg < 3$
- $n_{muon} \geq 3$
- $m_{\mu^+\mu^-} < 70\text{ GeV}$

The $N - 1$ plots for the distributions of muon isolation and IP_{3D}^{μ} are shown in Figure 12.8. The cuts are placed slightly above the peaks of the signal muons. All $N - 1$

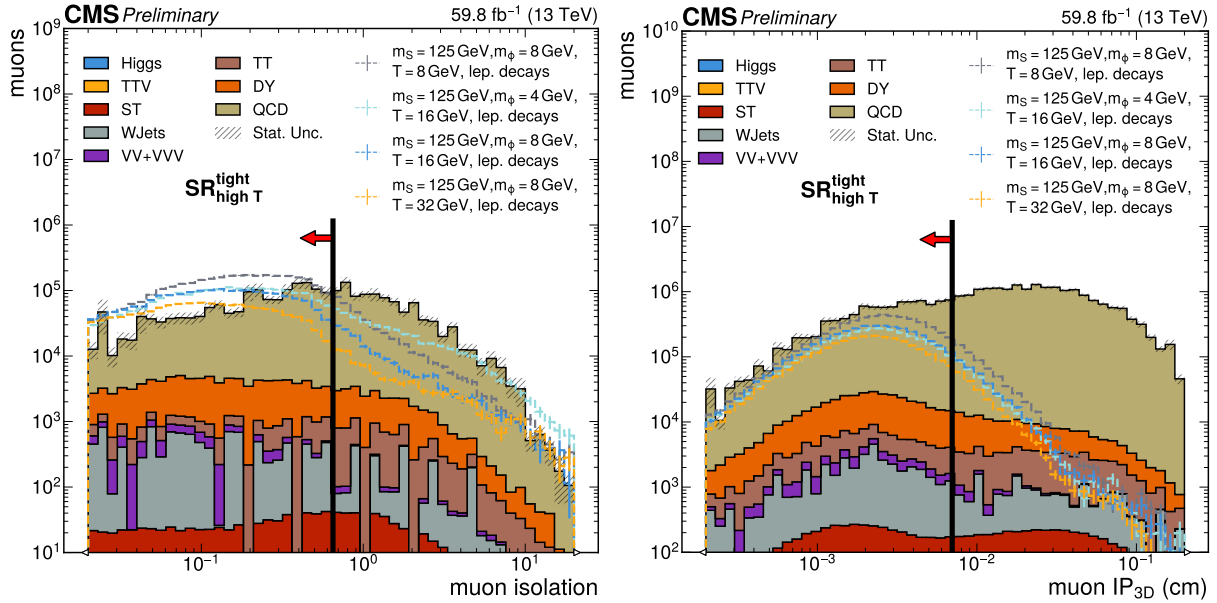


Figure 12.8: $N - 1$ distributions of muon isolation (left) and IP_{3D}^{μ} (right) in $SR_{high\ T}^{tight}$ for 2018 MC simulation. The chosen cuts are indicated with black lines and red arrows on the plots.

plots are included in Appendix B.

The remaining events are binned in n_{muon} . The histograms for $\text{SR}_{\text{high } T}^{\text{loose}}$ and $\text{SR}_{\text{high } T}^{\text{tight}}$ are shown in Figure 12.9 for Run 2. The last bin is inclusive in n_{muon} higher than 7 and is marked as the discovery bin.

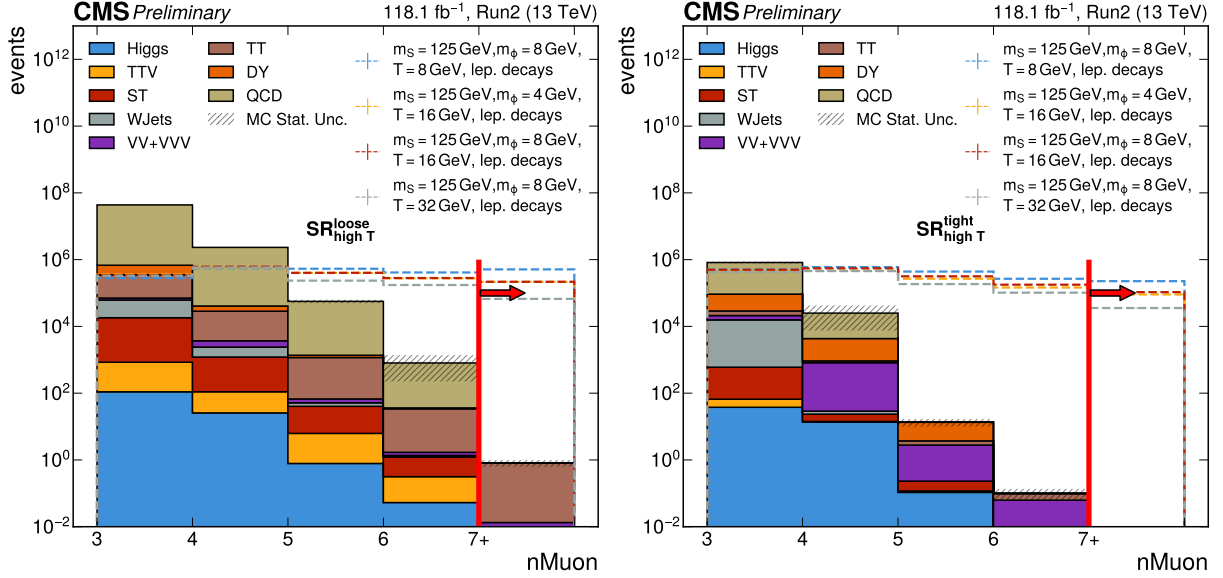


Figure 12.9: $\text{SR}_{\text{high } T}$ regions for Run 2 MC. Left is $\text{SR}_{\text{high } T}^{\text{loose}}$ and right is $\text{SR}_{\text{high } T}^{\text{tight}}$. The discovery bin is annotated with a separate red line and a pointing arrow.

A last note on the signal regions is that the contributions to the muons of the background processes in the events that survive all the cuts are mainly from b muons. This is demonstrated in Figure 12.10 that features the $N - 1$ plots for the IP_{3D}^{μ} distributions grouped by the muon sources in $\text{SR}_{\text{low } T}^{\text{tight}}$ (left) and $\text{SR}_{\text{high } T}^{\text{tight}}$ (right). These distributions justify the choices made for the cuts of the control regions to isolate contributions coming from b muons.

12.4.3 Validation region (VR)

A Validation Region (VR) is utilized to facilitate the evaluation of the MC-based extrapolation method for the background estimation. The VR is also divided into loose

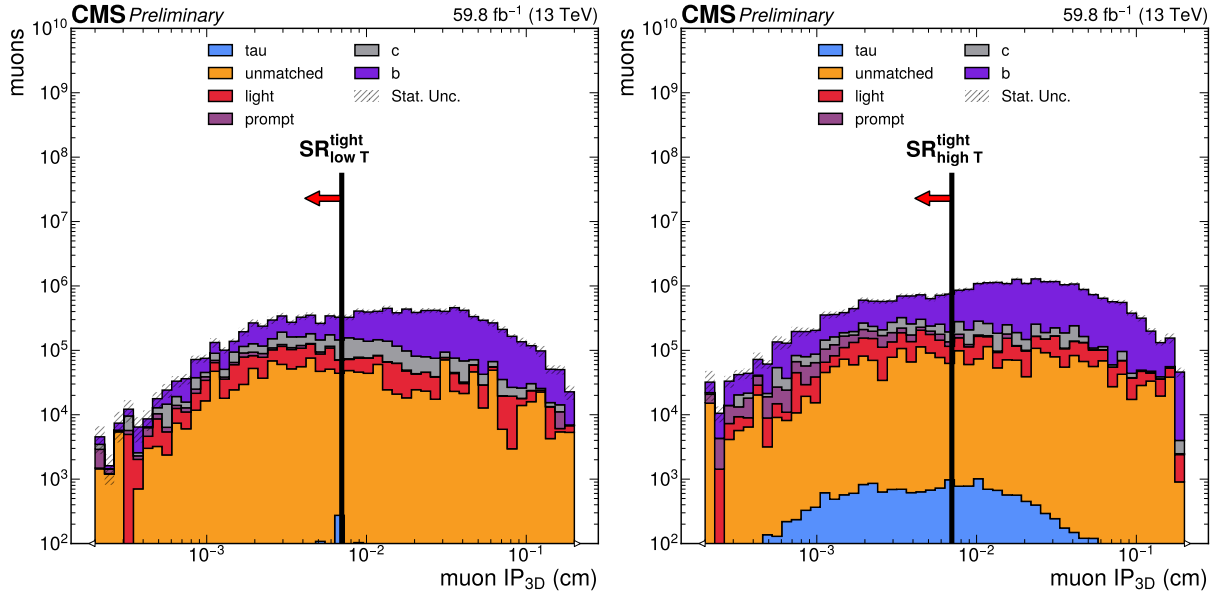


Figure 12.10: $N - 1$ plots for the IP_{3D}^μ distributions grouped by the muon sources for 2018 MC simulation. The left plot is for $SR_{low\ T}^{tight}$ and the right plot is for $SR_{high\ T}^{tight}$.

and tight variants, as it needs to be suitable for testing the background estimation technique developed for the SRs. There are two guiding principles for the definition of the VR. The first is to have enough statistics to validate the extrapolation technique explained in Section 13 in the high n_{muon} bins, and the second is to avoid contamination with signal events as much as possible. The latter requirement is the more stringent one since the scan on the parameters of the signal model creates a wide range of final states. The most powerful selection against all signal events comes from a cut on the 3D impact parameter of the muons. Low-temperature signal events are further reduced by using a lower cut on the p_T of the muons. For high-temperature signal events, vetoing events with isolated muons and all OS dimuon pairs having low invariant mass is necessary to remove contamination to a satisfactory level.

In summary, the selections for the tight VR (VR_{tight}) are:

- $p_T^\mu > 5 \text{ GeV}$
- $IP_{3D}^\mu > 0.02 \text{ cm}$
- `Muon_miniPFRelIso_all` > 0.4
- $\max_{\forall \mu^+ \mu^- \text{ pairs}} m_{\mu^+ \mu^-} > 20 \text{ GeV}$
- $n_{\text{muon}} \geq 3$

These selections are loosened to form the loose VR (VR_{loose}) to increase the statistics:

- $p_T^\mu > 5 \text{ GeV}$
- $IP_{3D}^\mu > 0.01 \text{ cm}$
- `Muon_miniPFRelIso_all` > 0.2
- $\max_{\forall \mu^+ \mu^- \text{ pairs}} m_{\mu^+ \mu^-} > 20 \text{ GeV}$
- $n_{\text{muon}} \geq 3$

The remaining events are binned in n_{muon} . The histograms for VR_{loose} and VR_{tight} are shown in Figure 12.11 for Run 2, including both data and MC, and plots of their ratio and pull.

12.5 Selection summary

A summary of all the selections is presented in Table 12.5.

The purposes of all defined regions are outlined in Table 12.6. These are explained in much greater detail in Sections 13 and 15.

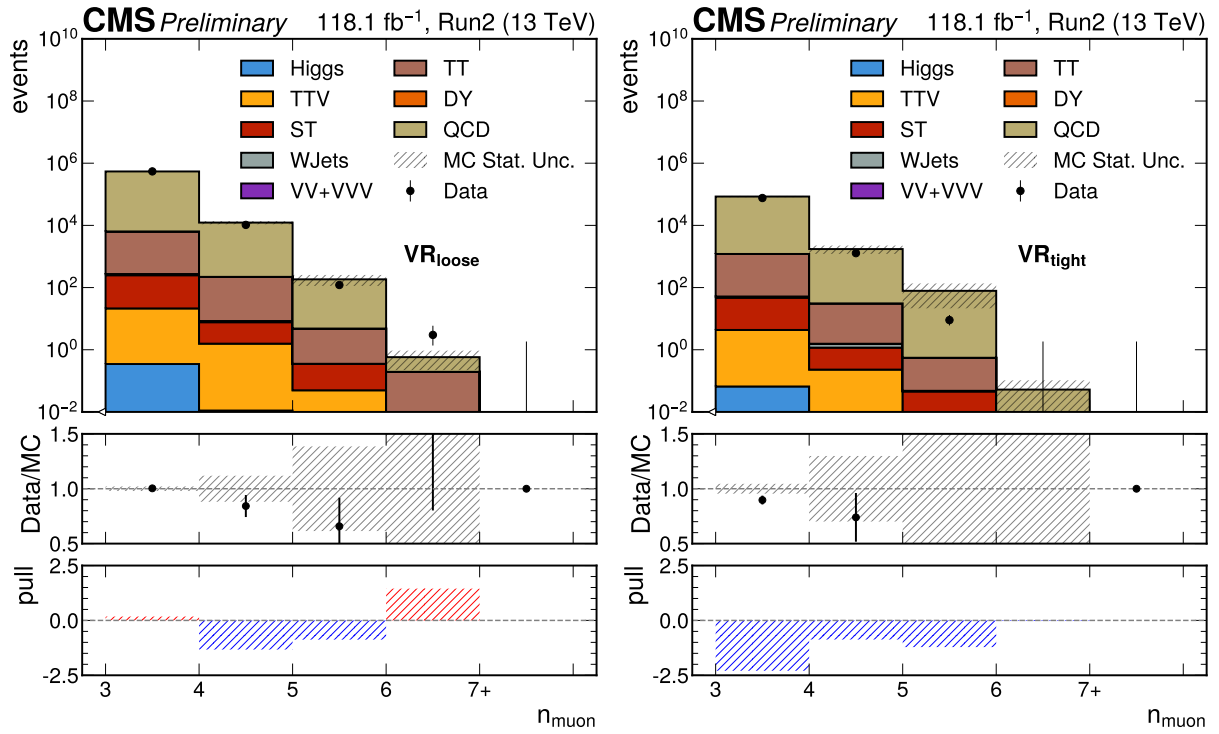


Figure 12.11: VR regions for Run 2. The left plot is VR_{loose} and the right plot is VR_{tight}. The ratio between data and MC, along with the pull plot, is also shown below each plot.

Table 12.5: Summary of the selections.

Regions		muon selections	$m_{\mu\mu}$	n_{muon}	S_1
CR _{QCD}		$0.01 \text{ cm} \leq dxy \leq 0.2 \text{ cm}$	-	≥ 2	-
CR _{DY}	prompt μ	$p_T > 25 \text{ GeV}$ $ dxy < 0.008 \text{ cm}$ $ dz < 0.01 \text{ cm}$ $IP_{3D} < 0.01 \text{ cm}$ $iso < 0.1$	$> 86.2 \text{ GeV}$ and $< 96.2 \text{ GeV}$	≥ 3	-
		$ dxy > 0.01 \text{ cm}$ $ dz > 0.01 \text{ cm}$ $IP_{3D} > 0.015 \text{ cm}$ $iso > 0.1$	$< 50 \text{ GeV}$		
SR _{low T}	loose	$p_T < 45 \text{ GeV}$ $IP_{3D} < 0.1 \text{ cm}$	$< 45 \text{ GeV}$	≥ 3	> 0.2
	tight	$p_T < 35 \text{ GeV}$ $IP_{3D} < 0.007 \text{ cm}$	$< 35 \text{ GeV}$	≥ 3	> 0.7
	discovery	$p_T < 35 \text{ GeV}$ $IP_{3D} < 0.007 \text{ cm}$	$< 35 \text{ GeV}$	≥ 7	> 0.7
SR _{high T}	loose	$IP_{3D} < 0.1 \text{ cm}$ $iso < 5$ neutral $iso < 3$	$< 70 \text{ GeV}$	≥ 3	-
	tight	$IP_{3D} < 0.007 \text{ cm}$ $iso < 0.65$ neutral $iso < 0.5$	$< 70 \text{ GeV}$	≥ 3	-
	discovery	$IP_{3D} < 0.007 \text{ cm}$ $iso < 0.65$ neutral $iso < 0.5$	$< 70 \text{ GeV}$	≥ 7	-
VR	loose	$p_T > 5 \text{ GeV}$ $IP_{3D} > 0.01 \text{ cm}$ $iso > 0.2$	$> 20 \text{ GeV}$	≥ 3	-
	tight	$p_T > 5 \text{ GeV}$ $IP_{3D} > 0.02 \text{ cm}$ $iso > 0.4$	$> 20 \text{ GeV}$	≥ 3	-

Table 12.6: Purpose of each region.

Regions		Usage
CR_{QCD}		Included in the Combine fit to estimate the QCD normalization and help constrain the nuisances.
CR_{DY}		Included in the Combine fit to estimate the DY normalization and help constrain the nuisances.
$\text{SR}_{\text{low } T, \text{high } T}$	loose	Used to extract the slope of the n_{muon} distribution.
	tight	Used to extract the slope of the n_{muon} distribution and extrapolate its values in the empty bins.
	discovery	The bin of the tight region that is included in the Combine fit to look for new physics and set limits.
VR	loose	Used to extract the slope of the n_{muon} distribution for validation purposes.
	tight	Used to extract the slope of the n_{muon} distribution and extrapolate its values in the empty bins for validation purposes.

Chapter 13: Background Estimation

The background for this search arises either from SM processes that produce large numbers of muons, misreconstructions that can fake muons, or combinations thereof. The MC simulation is used to estimate the expected background in the signal region. It is demonstrated in the next sections that most MC processes have insignificant contributions to the background in the discovery bins of the signal regions. The two processes that are expected to have dominant albeit still small contributions are QCD and DY. For these two processes, the MC statistics are proven to be insufficient, and an extrapolation method is devised to predict the missing event yields using the distributions from regions with better MC statistics. In the subsections below, the sources of multi-muon final states are studied in depth, the expected contributions to the background are outlined, and, finally, the method that extrapolates the background estimation to regions with poor statistics is presented and validated.

13.1 Expected backgrounds

It is clear from the discussion in Section [12](#) that there are two main sources of muons: those from the hard process and those originating from meson decays. Given the hadronic nature of the collisions, QCD jets are expected to be present in all events,

overwhelming them with mesons. The consequence is that all SM processes have the potential to generate events with very large muon multiplicities given enough meson decays and hard muons.

In practice, the probability of producing these events is minuscule since the SM hard processes that deliver 4 muons have small cross sections (e.g., $pp \rightarrow ZZ \rightarrow 4\mu$ or $pp \rightarrow H \rightarrow ZZ^* \rightarrow 4\mu$) and those with > 4 muons are even rarer. The meson decays to muons can be effectively treated as independent, with a small individual probability of success. This description naturally leads to the employment of a binomial distribution to characterize the distribution of the total number of muons produced in each event by meson decays. In the limit of small success probability, a binomial can be approximated by a falling exponential distribution

$$f(n_{\text{muon}}) \sim A \exp\{-Bn_{\text{muon}}\}. \quad (13.1)$$

A large number of samples with MC simulations for various SM processes, as can be seen in Table 9.3, have been processed and are included in the CR and SR histograms (Figures 12.2, 12.5, 12.7, and 12.9). Looking at the loose SRs and the populated bins of the tight SRs, it is straightforward to point out that almost all contributions come from QCD, DY, $t\bar{t}$, and double and triple vector boson production. The MC samples for the $t\bar{t}$ and multi-vector boson processes have very good statistics and achieve statistical uncertainties up to a few percent, even for bins with expected yields less than 1 event. For these processes, the MC samples are deemed sufficient and are utilized as-is. In fact, all MC processes have 0 event yields in the bins of interest, the discovery bins of the

signal regions. Tables 13.2 and 13.1 show the highest n_{muon} bins that are populated with MC events for each MC process. There is no process with statistics in the $n_{\text{muon}} = 7$ bins. The effective MC weight for the last populated bin is also shown (denoted as scale) along with the effective raw MC events and the corresponding Poisson (Garwood) interval for a bin with the same effective weight and 0 event yield. The term effective is introduced here because most of these samples contain events with different weights.

Table 13.1: MC statistics table for $\text{SR}_{\text{low } T}$ for 2018. The yields for all MC processes in the discovery bin ($n_{\text{muon}} = 7$) are 0. The columns show the highest n_{muon} that is populated with MC events, its event yields, the effective total weight for that bin, the effective raw number of MC events for that bin, and the Poisson (Garwood) intervals for a bin with the same effective weight and 0 yield.

process	highest populated n_{muon} bin	event yield	eff. MC weight ($\sum w^2 / \sum w$)	eff. MC events ($(\sum w)^2 / \sum w^2$)	Poisson unc. band for $y = 0$
Higgs	5	0.00044 ± 0.00022	0.00011	4	(0.0, 0.0002)
TTV	5	0.003 ± 0.0021	0.0015	1.9	(0.0, 0.0028)
ST	4	0.36 ± 0.14	0.057	6.2	(0.0, 0.11)
WJets	4	0.67 ± 0.46	0.31	2.2	(0.0, 0.57)
VV+VVV	5	0.037 ± 0.023	0.014	2.7	(0.0, 0.026)
TT	5	0.076 ± 0.054	0.038	2	(0.0, 0.07)
DY	4	117 ± 38	12	9.6	(0.0, 22)
QCD	5	3.9 ± 3.9	3.8	1	(0.0, 7.1)

It is evident from the discussion in the previous paragraph and the statistical properties outlined in Tables 13.2 and 13.1 that all processes except QCD and DY have sufficiently low statistical uncertainties. The MC distributions for these processes initially follow a power law-like falling distribution, but at some point, they become statistically depleted and their yields suddenly drop to or close to zero events, accompanied by huge statistical uncertainties. The situation is especially problematic for QCD since it is the MC sample with both the largest total event yields and statistical uncertainties, and it was generated using the unorthodox setting of allowing the light flavor meson decays in

Table 13.2: MC statistics table for $\text{SR}_{\text{high } T}$ for 2018. The yields for all MC processes in the discovery bin ($n_{\text{muon}} = 7$) are 0. The columns show the highest n_{muon} that is populated with MC events, its event yields, the effective total weight for that bin, the effective raw number of MC events for that bin, and the Poisson (Garwood) intervals for a bin with the same effective weight and 0 yield.

process	highest populated n_{muon} bin	event yield	eff. MC weight $(\sum w^2 / \sum w)$	eff. MC events $((\sum w)^2 / \sum w^2)$	Poisson unc. band for $y = 0$
Higgs	6	0.0015 ± 0.00078	0.00041	3.7	(0.0, 0.00075)
TTV	5	0.0055 ± 0.0052	0.0048	1.1	(0.0, 0.0089)
ST	5	0.053 ± 0.053	0.053	1	(0.0, 0.097)
WJets	4	3.1 ± 1.4	0.65	4.8	(0.0, 1.2)
VV+VVV	6	0.03 ± 0.0048	0.00078	37.9	(0.0, 0.0014)
TT	6	0.037 ± 0.037	0.037	1	(0.0, 0.067)
DY	5	3.2 ± 1.6	0.82	4	(0.0, 1.5)
QCD	4	19145 ± 19079	19013	1	(0.0, 35004)

PYTHIA to increase the generator-level filter efficiency. A method to remediate the low MC statistics hindrance is presented in the next section.

13.2 Extrapolation method

The usual practice for searches involving regions that require prohibitively large numbers of MC events to be properly sampled is to employ data-based background estimation methods. However, in this case, this is not feasible since it is very difficult to isolate regions close to the signal region that are not severely contaminated with signal events. This is also evident in the SR plots in Figures 12.7 and 12.9. The solution chosen is to derive a scaling power law for the MC distributions in the loose SRs and then apply it to the MC distribution in the tight SRs in order to eventually obtain an extrapolation for the MC yields in the discovery bins of the SRs. The n_{muon} distribution is expected to be consistent with a falling power law in regions dominated by meson decays to

muons. This includes all QCD events, assuming operation at the trigger plateau, and DY events with $n_{\text{muon}} \geq 3$. The SRs adhere to these requirements by construction, and they indeed follow approximately a power law as can be seen in Figures 12.7 and 12.9, excluding bins that are statistically depleted. Furthermore, plotting the normalized n_{muon} distribution densities for the loose and tight versions of the same region for the same MC sample facilitates comparing the shapes between them. This is shown for $\text{SR}_{\text{high } T}$ in Figure 13.1 for QCD (left plot) and DY (right plot), and for $\text{SR}_{\text{low } T}$ in Figure 13.2

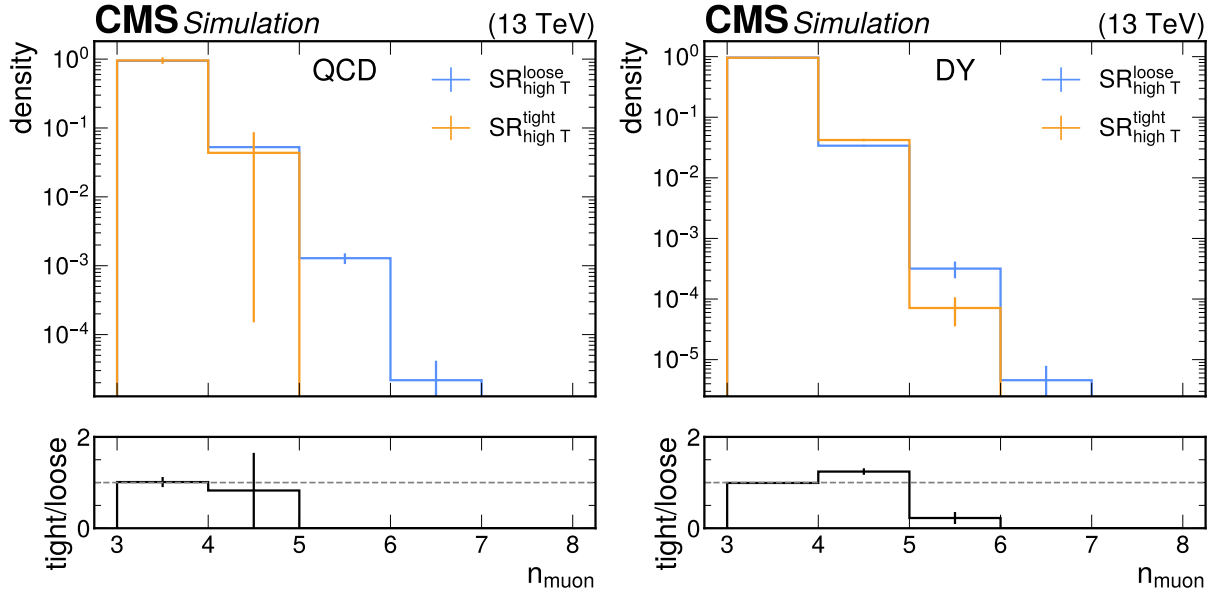


Figure 13.1: The normalized to unity densities for the n_{muon} distributions for $\text{SR}_{\text{high } T}^{\text{loose}}$ and $\text{SR}_{\text{high } T}^{\text{tight}}$ for QCD MC (left) and DY MC (right). The tight over loose ratios are also plotted below each histogram.

for QCD (left plot) and DY (right plot). The ratio of tight to loose is also shown below each histogram. The tight regions are, unfortunately, too statistically depleted to allow comprehensive comparisons of the slopes of the distributions. However, comparing the values for $n_{\text{muon}} = 3$ and 4, which are populated for all regions and MC samples, the ratios for those bins are moderately consistent with unity within the uncertainties.

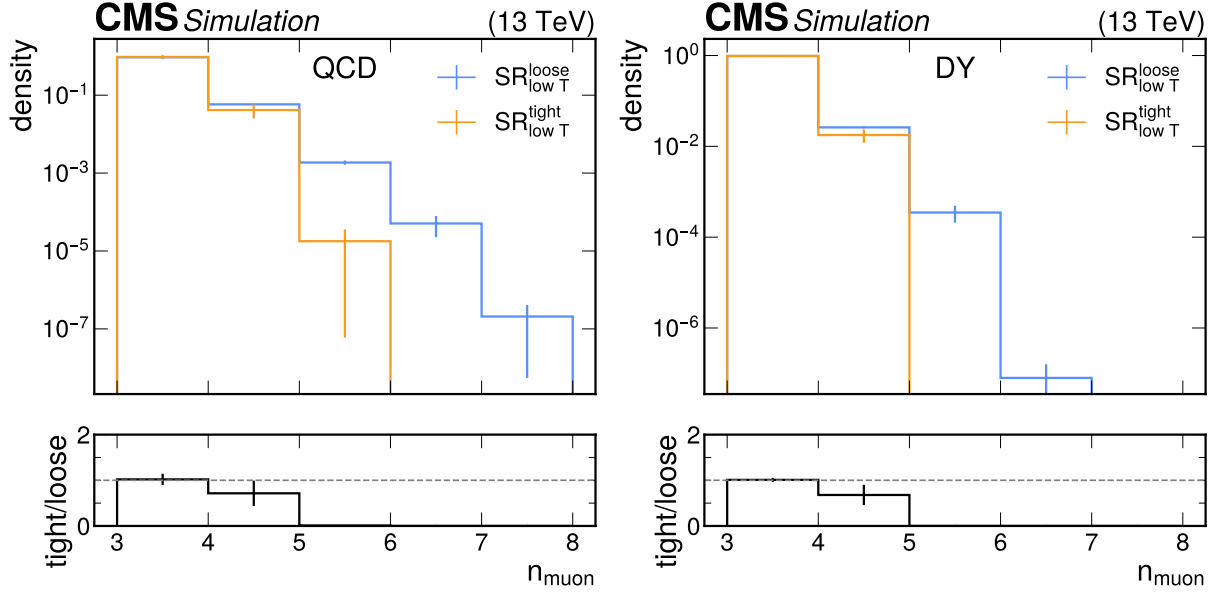


Figure 13.2: The normalized to unity densities for the n_{muon} distributions for $\text{SR}_{\text{low } T}^{\text{loose}}$ and $\text{SR}_{\text{low } T}^{\text{tight}}$ for QCD MC (left) and DY MC (right). The tight over loose ratios are also plotted below each histogram.

Given this partial independence of the n_{muon} distribution from the cut thresholds, it is a reasonable strategy to use the well-populated loose signal regions to extract the rate of decrease component of the distribution and then use it to extrapolate the yields in the tight signal regions. Assuming a distribution that follows the form described in Equation 13.1, simultaneous fits are performed on $\text{SR}_{\text{high } T}^{\text{loose}}$ and $\text{SR}_{\text{high } T}^{\text{tight}}$, and $\text{SR}_{\text{low } T}^{\text{loose}}$ and $\text{SR}_{\text{low } T}^{\text{loose}}$ to extract the distributions using a common parameter. The actual fitted functions are:

$$y_{\text{loose}} = A_{\text{loose}} - Bn_{\text{muon}} \quad (13.2)$$

$$y_{\text{tight}} = A_{\text{tight}} - Bn_{\text{muon}}, \quad (13.3)$$

where y_{loose} and y_{tight} are the logarithms of the event yields in the tight and loose regions,

B is the shared rate of drop parameter, and A_{loose} and A_{tight} are the normalization parameters for the loose and tight regions, respectively. A least squares fit is performed to find the optimal values for A_{loose} , A_{tight} , and B using MINUIT2 [211,212]. Finally, for the uncertainty, the parametric uncertainty of the fit is obtained using error propagation by transforming the covariance matrix C with the Jacobian of the fit function

$$C' = JCJ^T, \quad (13.4)$$

where $J_{ij} = \frac{\partial y_i}{\partial p_j}$ with $y = f(x, p)$ the fit function and p the parameter set, and taking the square roots of the diagonal elements. This uncertainty is added in quadrature with the relative MC uncertainty of each bin. For bins with no content, the relative statistical MC uncertainty of the nearest populated bin is used. This may result in large total uncertainties that in some cases surpass 100%, but is representative of the low amount of available MC statistics.

The extrapolation fit for $\text{SR}_{\text{high } T}$ is shown for QCD MC in Figure 13.3 and for DY MC in Figure 13.4, while for $\text{SR}_{\text{low } T}$ is shown for QCD MC in Figure 13.5 and for DY MC in Figure 13.6. Plots for the ratios between MC and fit result, and the pulls are also shown below the histograms. The MC distributions are not far off from the fit to the power law in the $n_{\text{muon}} = 4, 5, 6$ bins of the loose regions, where the contributions are expected to be almost entirely from meson decays and still not statistically depleted. The MC is statistically depleted in the $n_{\text{muon}} \geq 7$ bin for the loose regions and the $n_{\text{muon}} = 5, 6, \geq 7$ bins for the tight regions. The bins for $n_{\text{muon}} = 3$ in the loose regions do not follow the power law very well, and they tend to dominate the fits, so they are not included in the

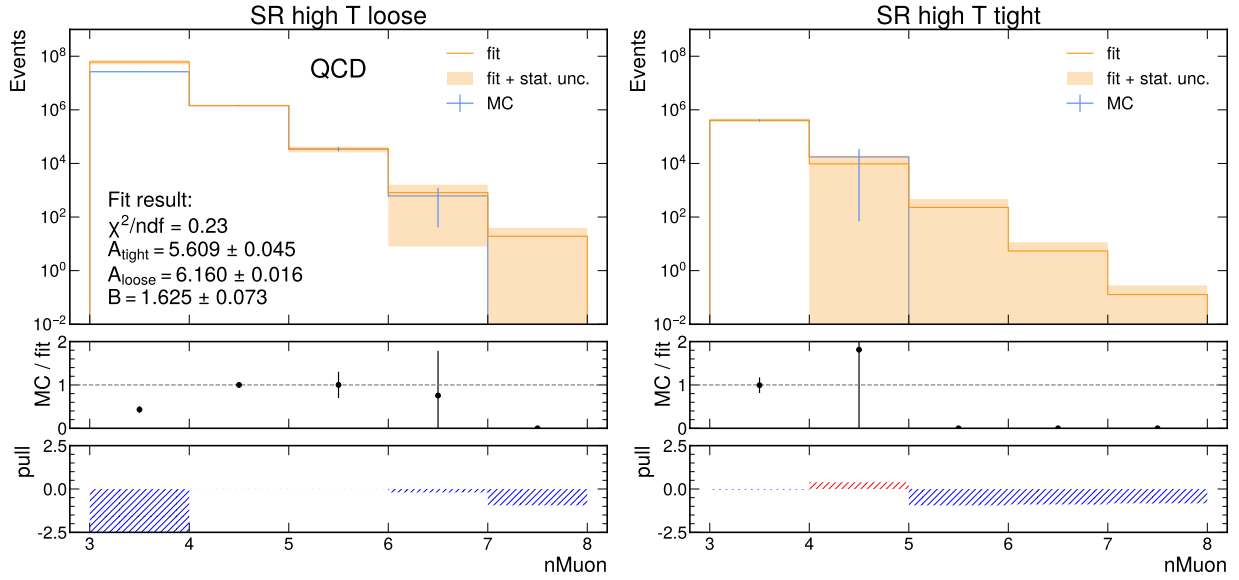


Figure 13.3: Extrapolation fit for QCD MC in $\text{SR}_{\text{high } T}$. Left is $\text{SR}_{\text{high } T}^{\text{loose}}$ and right is $\text{SR}_{\text{high } T}^{\text{tight}}$. The MC/fit ratio and the pull plots are also shown below.

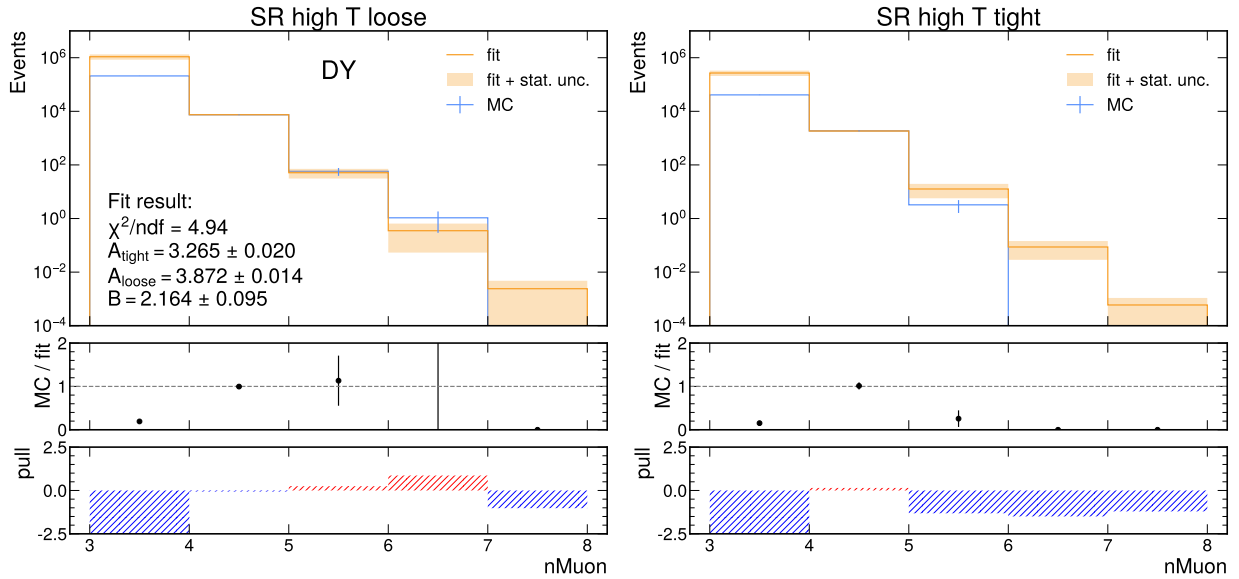


Figure 13.4: Extrapolation fit for DY MC in $\text{SR}_{\text{high } T}$. Left is $\text{SR}_{\text{high } T}^{\text{loose}}$ and right is $\text{SR}_{\text{high } T}^{\text{tight}}$. The MC/fit ratio and the pull plots are also shown below.

fits. These bins are still shown in the plots, accompanied by their evaluated fit values to show the amount of disagreement. In most cases, the reduced χ^2 values are a bit high, at around 5, because of the high-statistics low- n_{muon} bins. The MC distributions for the

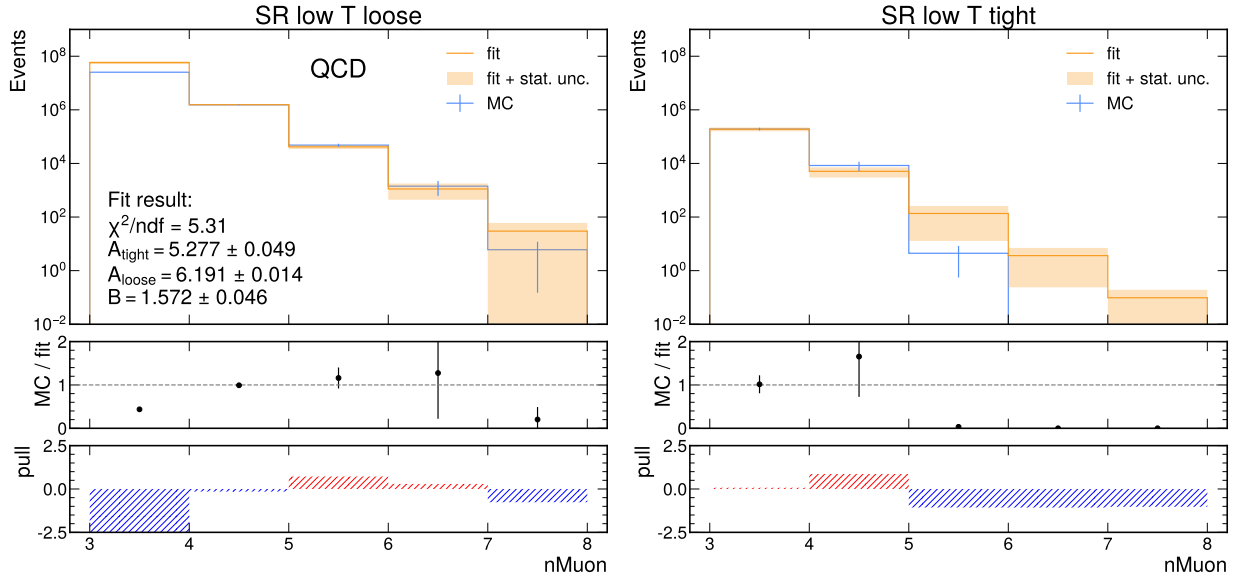


Figure 13.5: Extrapolation fit for QCD MC in $\text{SR}_{\text{low } T}$. Left is $\text{SR}_{\text{low } T}^{\text{loose}}$ and right is $\text{SR}_{\text{low } T}^{\text{tight}}$. The MC/fit ratio and the pull plots are also shown below.

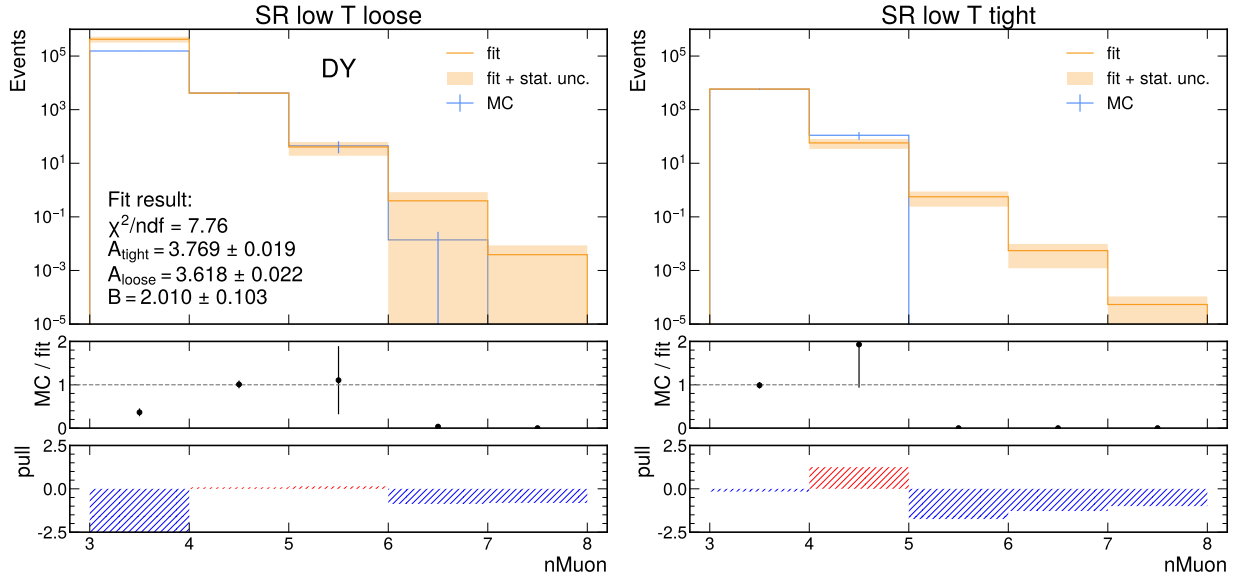


Figure 13.6: Extrapolation fit for DY MC in $\text{SR}_{\text{low } T}$. Left is $\text{SR}_{\text{low } T}^{\text{loose}}$ and right is $\text{SR}_{\text{low } T}^{\text{tight}}$. The MC/fit ratio and the pull plots are also shown below.

loose, tight, extrapolated loose, and extrapolated tight regions are overlaid in the same plots in Figure 13.7 for QCD and in Figure 13.8 for DY to demonstrate the common slope between all regions.

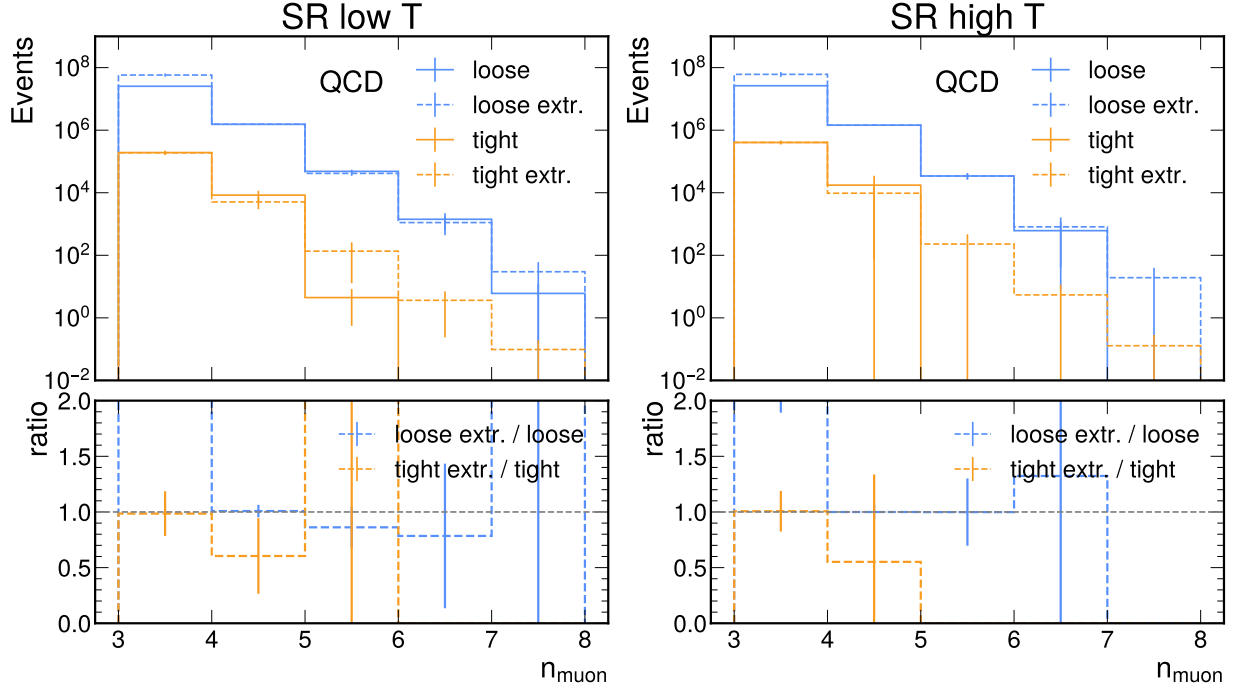


Figure 13.7: Overlays of the distributions of the loose, tight, and extrapolated tight regions for QCD MC. Left is $SR_{\text{low } T}$ and right is $SR_{\text{high } T}$.

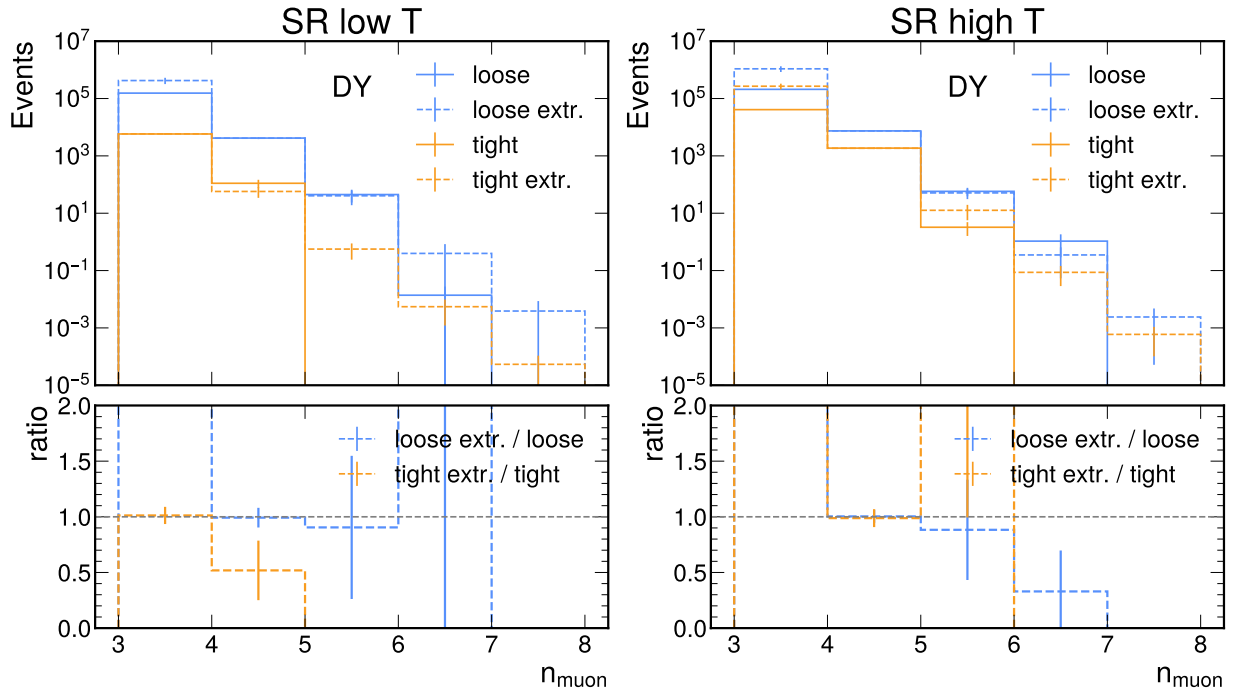


Figure 13.8: Overlays of the distributions of the loose, tight, and extrapolated tight regions for DY MC. Left is $SR_{\text{low } T}$ and right is $SR_{\text{high } T}$.

The final result of this extrapolation method is shown for $SR_{low\ T}$ in Figure 13.9 for Run 2, and for $SR_{high\ T}$ in Figure 13.9 for Run 2. The final numbers for the expected

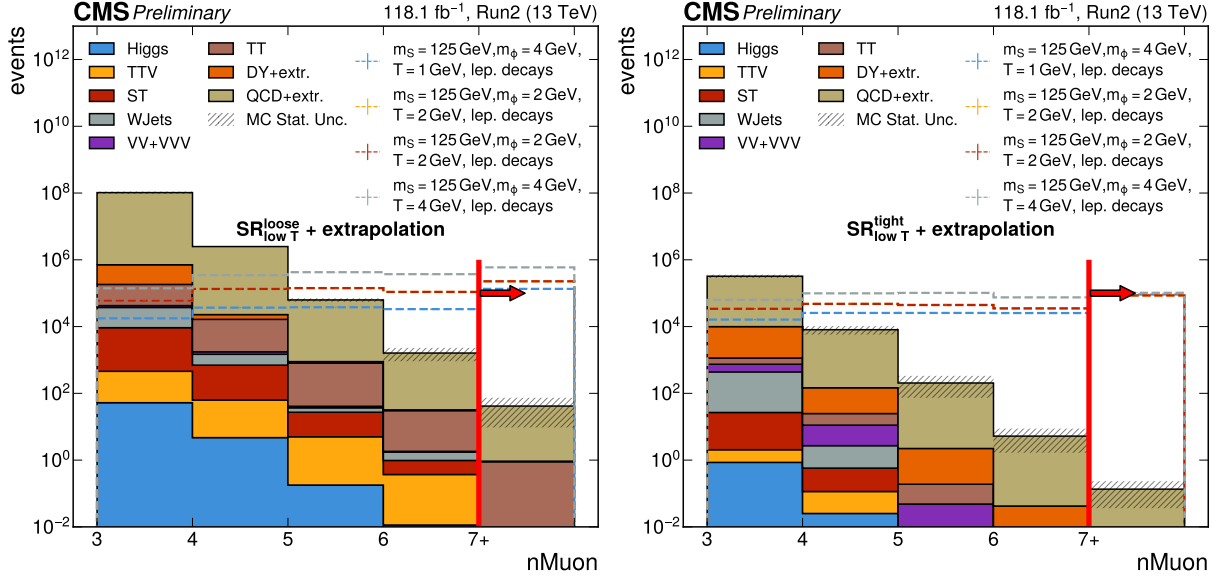


Figure 13.9: $SR_{low\ T}$ regions for Run 2, including the extrapolated distributions for QCD and DY MC. Left is $SR_{low\ T}^{loose}$ and right is $SR_{low\ T}^{tight}$. The discovery bin is annotated with a separate red line and a pointing arrow.

number of events for DY and QCD MC in the discovery bins of the signal regions after applying the extrapolation method are presented in Table 13.3. All other processes have negligible contributions. The total expected background is 0.19 ± 0.16 events in $SR_{high\ T}$ and 0.135 ± 0.099 events in $SR_{low\ T}$.

13.3 Validation of the extrapolation method

To validate the extrapolation method, the VR region that is defined in Section 13.3 is utilized. The fit procedure described in Section 13.2 is performed in the VR both for QCD MC. Then, the results of the method on QCD MC are compared with data. The fit method is also performed on data to check the consistency of the method.

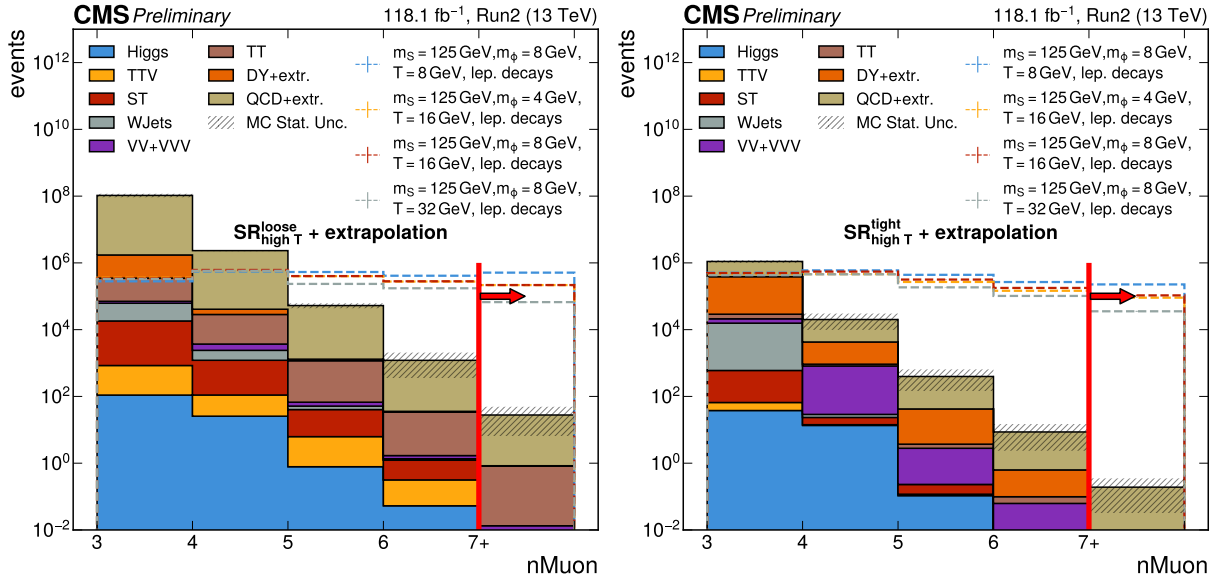


Figure 13.10: $SR_{high\ T}$ regions for Run 2, including the extrapolated distributions for QCD and DY MC. Left is $SR_{high\ T}^{loose}$ and right is $SR_{high\ T}^{tight}$. The discovery bin is annotated with a separate red line and a pointing arrow.

The fit in VR_{loose} and VR_{tight} is shown for QCD MC in Figure 13.11 and for data

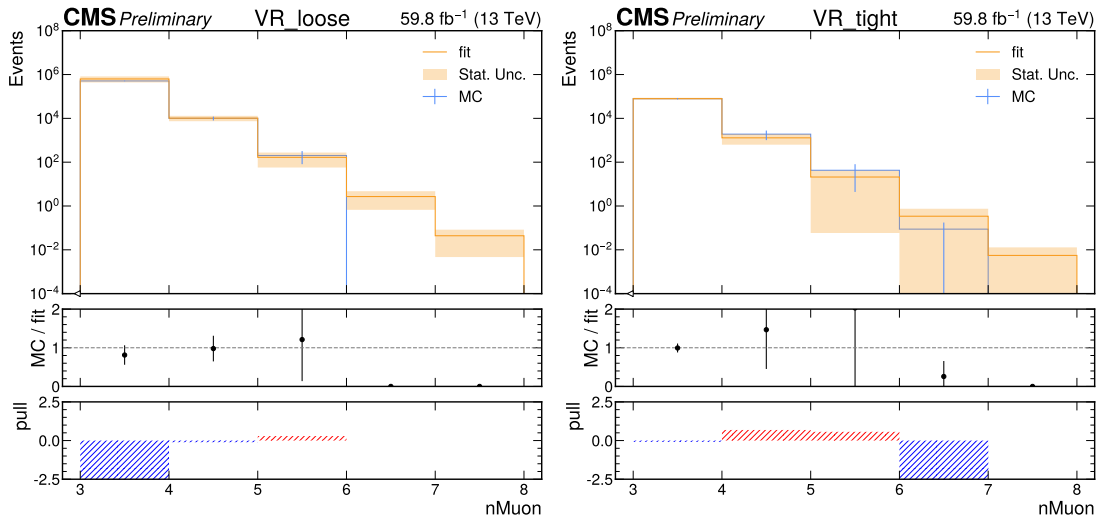


Figure 13.11: Extrapolation fit for QCD MC in VR. Left is VR_{loose} and right is VR_{tight} . The MC/fit ratio and the pull plots are also shown below. There is closure between the fit and the MC.

in Figure 13.12. The ratios and the pulls are also plotted below the histograms. The

year	process	$SR_{\text{high } T}$ discovery bin	$SR_{\text{low } T}$ discovery bin
2016	DY + extr.	0.0018 ± 0.0022	0.00050 ± 0.0019
	QCD + extr.	0.015 ± 0.019	$(6.7 \pm 7.1) \times 10^{-5}$
	Total bkg	0.017 ± 0.019	0.00057 ± 0.0019
2017	DY + extr.	0.0058 ± 0.0044	0.00047 ± 0.00085
	QCD + extr.	0.039 ± 0.031	0.037 ± 0.027
	Total bkg	0.045 ± 0.031	0.037 ± 0.027
2018	DY + extr.	0.00059 ± 0.00049	$(5.4 \pm 5.4) \times 10^{-5}$
	QCD + extr.	0.13 ± 0.15	0.097 ± 0.095
	Total bkg	0.13 ± 0.15	0.097 ± 0.095
Total bkg Run2		0.19 ± 0.16	0.135 ± 0.099

Table 13.3: The final event yields for the QCD and DY MC background processes in the discovery bins of the two signal regions. These numbers are produced using the extrapolation method outlined in Section 13.2.

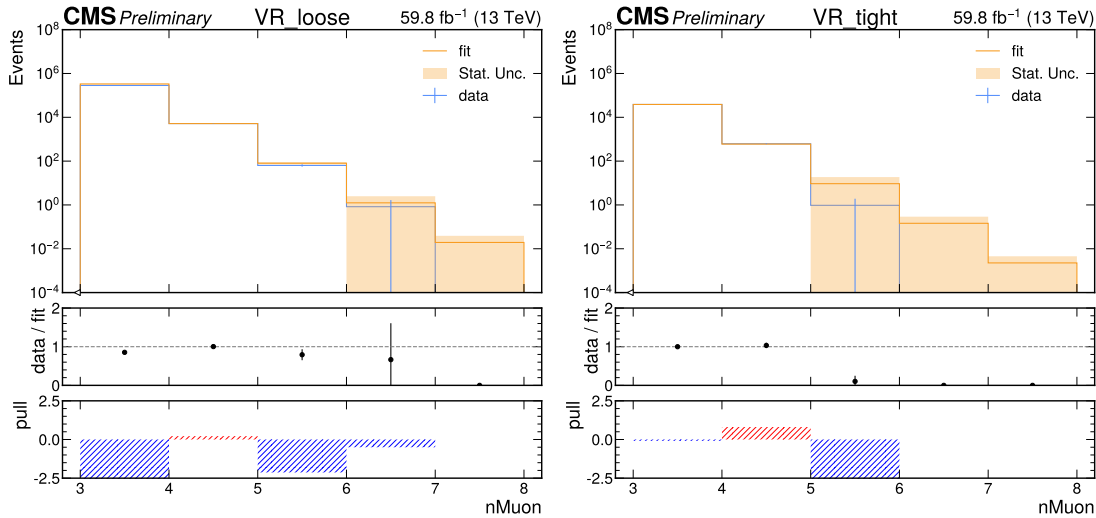


Figure 13.12: Extrapolation fit for data in VR. Left is VR_{loose} and right is VR_{tight} . The data/fit ratio and the pull plots are also shown below. There is closure between the fit and the data.

distributions predicted by the fit results are consistent both in the case of the QCD MC fit and the data fit, except for some statistically depleted bins in the high ends of the distributions. Overlays of the VR_{tight} and VR_{tight} with extrapolation on top of VR_{loose} are

shown in Figure 13.13, both for QCD MC and data. These plots support the hypothesis

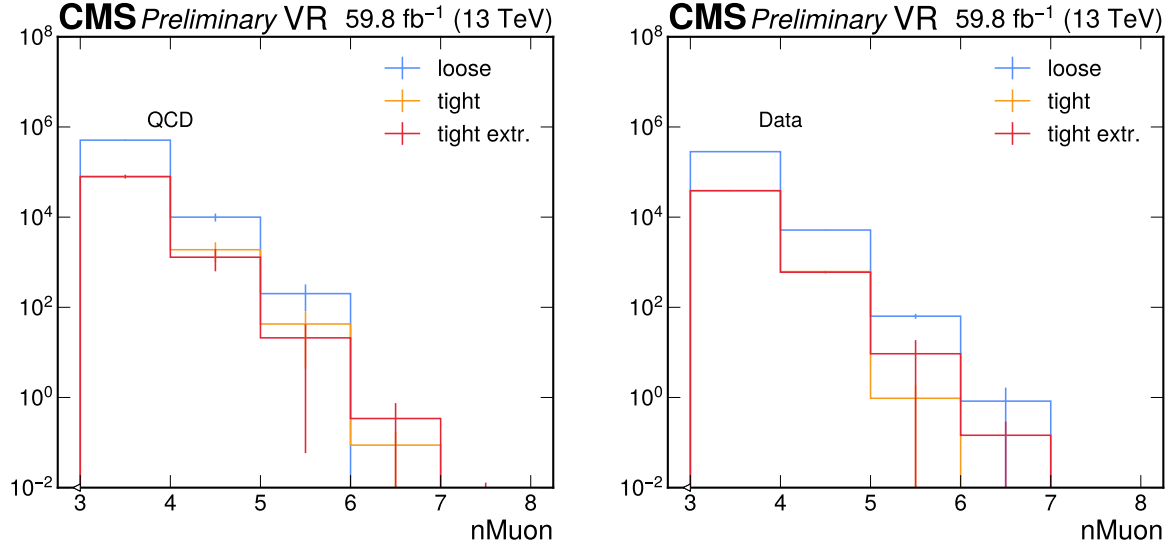


Figure 13.13: Overlays of the distributions of the loose, tight, and extrapolated tight regions of the VR. Left is QCD MC and right is data.

that the rate of drop of the power law distribution does not change between the loose and tight regions.

The n_{muon} distributions for VR_{loose} and VR_{tight} that include the results of the extrapolations for QCD MC are presented in Figure 13.14 for Run 2. In these plots, the distributions from the data are overlaid on top of the prediction from the MC and the extrapolated distributions for QCD. The final predicted distribution is consistent with the data, except for the $n_{\text{muon}} = 5$ bin in VR_{tight} for which the predicted yield seems to be overestimated by about $1\text{-}\sigma$ compared to data.

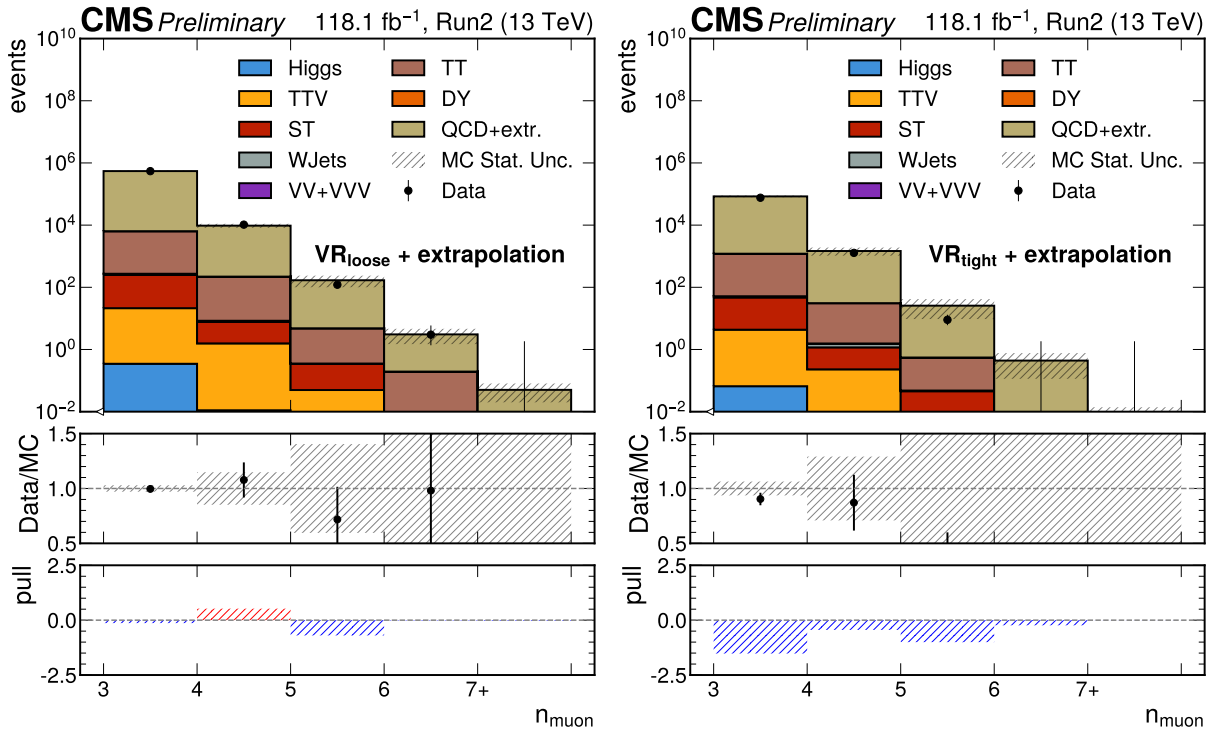


Figure 13.14: VR regions for Run 2 with extrapolated QCD MC. The left plot is VR_{loose} and the right plot is VR_{tight}. The ratio between data and MC, along with the pull plot, is also shown below each plot. There is good closure between the fitted MC and the data.

Chapter 14: Systematic Uncertainties

In this section, the sources of systematic uncertainty taken into consideration are listed.

14.1 Experimental uncertainties

14.1.1 Pileup

The measurement uncertainty of 4.6% of the inelastic p - p cross section [200] is used to obtain up and down variations for the PU reweighting weights. The data histogram is scaled up and down by 4.6%, resulting in variations of the weights that produce shape systematic variations [199]. This uncertainty applies to all MC processes (signal and background) and is correlated across years and processes.

14.1.2 L1 prefiring

The uncertainty for L1 prefiring is provided [201] in the form of up and down variations of the total prefire weight that are used to produce shape systematics. The weight variations are created using the object prefire uncertainties, which are 20%, and

the p_T - η bin's statistical uncertainty added in quadrature:

$$\delta p_{pref}^i = \sqrt{\left(0.2 p_{pref}^i\right)^2 + \sigma_{stat}^2}. \quad (14.1)$$

These variations are already precalculated in NanoAOD for all MC processes (signal and background). This uncertainty is correlated across the MC processes and uncorrelated across the data-taking years.

14.1.3 Muon scale factors

The uncertainties of the muon scale factors have a systematic component that is correlated across years and simulated processes, and a statistical component that is uncorrelated across the years and correlated across the MC processes. The systematic part of the uncertainty is the dominant one, and therefore, it is the one used to vary the scale factor weights up and down to obtain shape variations. Given the multiplicative nature of these scale factors and the very large muon multiplicities in this search, it is expected that this uncertainty is one of the largest. This is even more prominent in the case of lower temperature signal events, which are expected to contain up to tens of muons. This uncertainty applies to all MC processes (signal and background).

14.1.4 Luminosity

The recommended minimal correlation scheme for Run 2 is used for the luminosity uncertainty [185]. This scheme divides the uncertainty into:

1. uncorrelated parts that are separate for each year,

2. correlated for 2017 and 2018, and
3. correlated for all years.

When the uncertainty sources for each year are added quadratically, the numbers are 1.2%, 2.3%, and 2.5% for 2016, 2017, and 2018, respectively. These uncertainties apply to all MC processes (signal and background) and are correlated across all the simulated processes, and they are applied only as scaling uncertainties (not changing the shapes).

14.1.5 Track efficiency

The systematic uncertainties for the track reconstruction efficiency are calculated using the *track-killing* method suggested by the TRACKING POG [213] to account for the difference in the reconstruction efficiencies between data and MC. In this method, the tracks are removed randomly from the MC samples to account for higher reconstruction efficiency in simulation over data. This is performed using probabilities derived in D^* meson studies [214] that vary between years and p_T ranges. The killing probabilities are 2.1% for 2018, 2.2% for 2017, and 2.7% for 2016 for tracks with $p_T < 20$ GeV. For tracks with $p_T > 20$ GeV, the probability is 1% for all years.

This uncertainty applies only to $SR_{\text{low } T}$, which is formed again after recalculating sphericity using the new track collection after the random removal. The new event yields are taken as the down variation of a shape systematic uncertainty. The relative difference between the nominal values and the down variation is used to symmetrize the variations and obtain the up variation.

This uncertainty is correlated between the processes and uncorrelated between

data-taking years.

14.2 Theoretical uncertainties

14.2.1 Matrix element renormalization and factorization scales

These theoretical uncertainties represent the uncertainty of the renormalization and factorization scales, μ_R^{LHE} and μ_F^{LHE} , at the matrix element calculation level. The variations are 2 and 0.5 times the nominal values for μ_R^{LHE} and μ_F^{LHE} , which is consistent with theoretical studies [215,216]. Two three-point uncertainty sets, where one of the two scales is kept at the nominal value and the other is varied at 0.5 and 2 times the nominal, are considered only. The resulting sets of up and down weights are propagated to the total event weight to create shape variations.

These uncertainties are available by default only for MC processes generated via an external matrix element calculator. For samples generated with PYTHIA (signal and QCD), they were calculated manually by varying the scale of the hard process, Q , using the information available in the `Generator` branch of NanoAOD for the hard scattering partons. For μ_R^{LHE} , the running coupling constants α_S and α_{EM} were recalculated at the varied levels of Q . One QCD vertex is considered for QCD MC events, and two QCD vertices for the signal events. The weights are given by the ratios of the varied scale to the nominal in the power given by the corresponding number of vertices

$$w_{\mu_R} = \left(\frac{\alpha_{EM}(Q'^2)}{\alpha_{EM}(Q^2)} \right)^{n_{EM}} \cdot \left(\frac{\alpha_S(Q'^2)}{\alpha_S(Q^2)} \right)^{n_{QCD}}, \quad (14.2)$$

where Q and Q' are the nominal and the varied scales of the process, and n_{EM} and n_{QCD} are the number of electroweak and QCD vertices.

For μ_F^{LHE} , the parton distribution functions, $xf(x)$, are recalculated at the varied levels of Q . The weights are given by the ratios of the varied PDFs to the nominal ones

$$w_{\mu_F} = \frac{x_1 f(\text{id}_1, x_1, Q'^2) \cdot x_2 f(\text{id}_2, x_2, Q'^2)}{x_1 f(\text{id}_1, x_1, Q^2) \cdot x_2 f(\text{id}_2, x_2, Q^2)}, \quad (14.3)$$

where x_1, x_2 are the momentum fractions for the two partons, id_1 and id_2 are their flavors, and Q and Q' are the nominal and the varied scales of the process.

These uncertainties are correlated across MC processes and data-taking years.

14.2.2 Matrix element parton distribution function

The parton distribution function's (PDF) uncertainty at the matrix element level calculation can be accounted for using variations of the central PDF. In more detail, up and down weights are calculated for each event using the formula

$$w_{\pm}^{PDF} = 1 \pm \frac{\text{std}(w_i/w_0)}{\text{mean}(w_i/w_0)} \quad (14.4)$$

where w_i/w_0 are the normalized weights of the members of the NNPDF3.1 PDF set (default PDF, central + 100 variations, $\alpha_s = 0.130$), with the normalization being the nominal LHE weight w_0 . The up and down weights are propagated to the nominal event weights to create shape variations. These uncertainties are available by default only for MC processes generated via an external matrix element calculator. For the processes

generated using PYTHIA (signal and QCD), they were added manually by evaluating the PDFs, $xf(x)$, for all the replicas in `NNPDF31_nnlo_as_0118_mc_hessian_pdfas` [194] using the info available in `NanoAOD`. These uncertainties are correlated across MC processes and data-taking years.

14.2.3 Parton shower

The parton shower uncertainties are calculated automatically by PYTHIA [217] by varying the renormalization scale, μ_R^{PS} , and the inclusion of non-singular terms for QCD emissions for the initial state radiation (ISR) and the final state radiation (FSR). The up and down variations are 2 and 0.5 times the nominal values for ISR and FSR. This results in per-event up and down weights, separate for ISR and FSR, that are propagated to the total event weight to produce shape variations. Unfortunately, these variations are not available for the muon-enriched MC QCD samples used in this analysis. These uncertainties are correlated across the data-taking years and MC processes.

14.3 Summary of systematic uncertainties

The mapping between the systematic uncertainties and the MC processes, along with their type and correlation, is shown in Table 14.1. The checkmarks indicate that a given systematic uncertainty is included for the given MC process. These systematics are included in the fit to data that is presented in Section 15, and they affect the shapes and the normalization of the MC processes in the CRs and the normalization of the yields in the discovery bins of SRs. For the yields of QCD and DY MC in the discovery

Table 14.1: Mapping between systematics and MC processes.

Syst. Unc.	Type	Corr.	QCD	DY	TT	VV+VVV	WJets	ST	TTV	Higgs	SUEP
lumi.13TeV	scale	part.	✓	✓	✓	✓	✓	✓	✓	✓	✓
PUReweight	shape	corr.	✓	✓	✓	✓	✓	✓	✓	✓	✓
L1Prefire	shape	part.	✓	✓	✓	✓	✓	✓	✓	✓	✓
MuonSF	shape	corr.	✓	✓	✓	✓	✓	✓	✓	✓	✓
TrkEff	shape	part.	✓	✓	✓	✓	✓	✓	✓	✓	✓
LHEScaleMuR	shape	corr.	✓	✓	✓	✓	✓	✓	✓	✓	✓
LHEScaleMuF	shape	corr.	✓	✓	✓	✓	✓	✓	✓	✓	✓
LHEPdf	shape	corr.	✓	✓	✓	✓	✓	✓	✓	✓	✓
ISR	shape	corr.		✓	✓	✓	✓	✓	✓	✓	✓
FSR	shape	corr.		✓	✓	✓	✓	✓	✓	✓	✓

bins, the extrapolation procedure that is described in Section 13 is applied separately on each histogram with up and down variations to create an extrapolation for each varied histogram.

The magnitude of the shift to the yields of the discovery bin is shown as a percentage of the nominal yield for $\text{SR}_{\text{high } T}$ in Table 14.2 and $\text{SR}_{\text{low } T}$ in Table 14.3. The

Table 14.2: Impacts of systematic uncertainties on the yields of the discovery bin of $\text{SR}_{\text{high } T}$ for 2018. The maximum up/down shift is displayed as a percentage of the nominal value.

Syst. Unc.	SUEP ($m_{A'} = 0.5 \text{ GeV}$)						QCD	DY
	$m_S = 125 \text{ GeV}$	$m_S = 400 \text{ GeV}$	$m_S = 1000 \text{ GeV}$	$m_S = 125 \text{ GeV}$	$m_S = 125 \text{ GeV}$			
	$m_\phi = 8 \text{ GeV}$	$m_\phi = 8 \text{ GeV}$	$m_\phi = 8 \text{ GeV}$	$m_\phi = 8 \text{ GeV}$	$m_\phi = 4 \text{ GeV}$			
	$T = 32 \text{ GeV}$	$T = 32 \text{ GeV}$	$T = 32 \text{ GeV}$	$T = 16 \text{ GeV}$	$T = 4 \text{ GeV}$			
lumi.13TeV	2.5	2.5	2.5	2.5	2.5	2.5	2.5	2.5
PUReweight	0.9	0.9	0.3	1.2	1.7	20.5	2	
L1PreFire	-1.7	-2.7	-4.1	-1.3	-0.4	-0.1	-2.4	
MuonSF	13.3	12.3	14.5	16.9	27	14.5	7.1	
LHEScaleMuR	-22.2	-17.1	-15.3	-22.2	-22.2	-12.7	-2.8	
LHEScaleMuF	-5.9	-5	-11.8	-5.9	-5.7	16.3	-63	
LHEPdf	-0.3	0.2	-0.3	0.3	-0.2	-0.3	-0.4	
ISR	-1	-0.4	-0.1	-1.8	-2.6	-	-4	
FSR	0.8	-1.7	-2.5	-3	0.4	-	-4.8	

values on these tables represent the maximum percent up or down shifts caused by the corresponding systematics, with only the shifts with the maximum absolute values being shown. Various examples of signal models that match the different SRs are included in

Table 14.3: Impacts of systematic uncertainties on the yields of the discovery bin of $\text{SR}_{\text{low } T}$ for 2018. The maximum up/down shift is displayed as a percentage of the nominal value.

Syst. Unc.	SUEP ($m_\phi = 4 \text{ GeV}, T = 1 \text{ GeV}$)				QCD	DY
	$m_S = 400 \text{ GeV}$	$m_S = 400 \text{ GeV}$	$m_S = 600 \text{ GeV}$	$m_S = 600 \text{ GeV}$		
	$m_{A'} = 0.5 \text{ GeV}$	$m_{A'} = 0.7 \text{ GeV}$	$m_{A'} = 0.5 \text{ GeV}$	$m_{A'} = 0.7 \text{ GeV}$		
lumi_13TeV	2.5	2.5	2.5	2.5	2.5	2.5
PUReweight	0.3	1.4	0.8	0.4	14.0	-10.6
MuonSF	69.4	45.7	86.5	57.3	-42.8	13.9
L1PreFire	0.1	-0.2	0.1	0.1	-0.6	-0.9
TrkEff	0.3	-0.2	0.3	0.4	99.2	1318.5
LHEScaleMuR	-17.1	-17.1	-16.3	-16.3	-9.9	-11.8
LHEScaleMuF	-5.1	-5.4	-8.2	-8.4	+7.0	-21.8
LHEPdf	0.2	0.2	-0.2	0.2	-0.3	-0.3
ISR	-6.3	-7.6	-3.4	-8	-	13.8
FSR	-0.9	2.4	-0.5	1.4	-	38.1

each table.

According to Tables 14.2 and 14.3, the MuonSF uncertainty is the experimental uncertainty with the most significant impact, especially for the signal models with lower temperatures, which can experience shifts up to $\sim 87\%$. For QCD in $\text{SR}_{\text{high } T}$, the PUReweight uncertainty can cause shifts up to 21%. In the $\text{SR}_{\text{low } T}$, the TrkEff uncertainty has a very significant upward impact on QCD and DY. From the theory uncertainties, the renormalization scale, μ_R , uncertainty is the largest one, reaching impacts up to 22% for some signal processes. Additionally, the factorization scale uncertainty has a sizeable effect on DY, reaching up to -63% in the $\text{SR}_{\text{high } T}$.

Chapter 15: Results

The CR histograms, together with the estimated background and signal yields in the discovery bins of the SRs, accompanied by their systematic uncertainties, are included in a fit to data, performed by CMS `Combine` [207], to obtain upper limits for all points in the signal parameter scan.

15.1 Prefit plots

The prefit plot that includes the two control regions and the discovery bins from the two signal regions can be seen in Figure 15.1 for Run 2. The MC yields for the QCD and DY processes in the discovery bins are the products of the extrapolation method described in Section 13. The histograms in this plot are normalized using only the cross sections listed in Table 9.3 and, unlike the plots in Section 12, they do not have any k-factors applied to them. This is easy to notice in the ratio plot below the main histogram. The normalization in the control regions is obviously off. These histograms are the input to `Combine` to fit the MC to data and extract the 95% upper limits. Extracting the k-factors for QCD and DY is part of the fit to data.

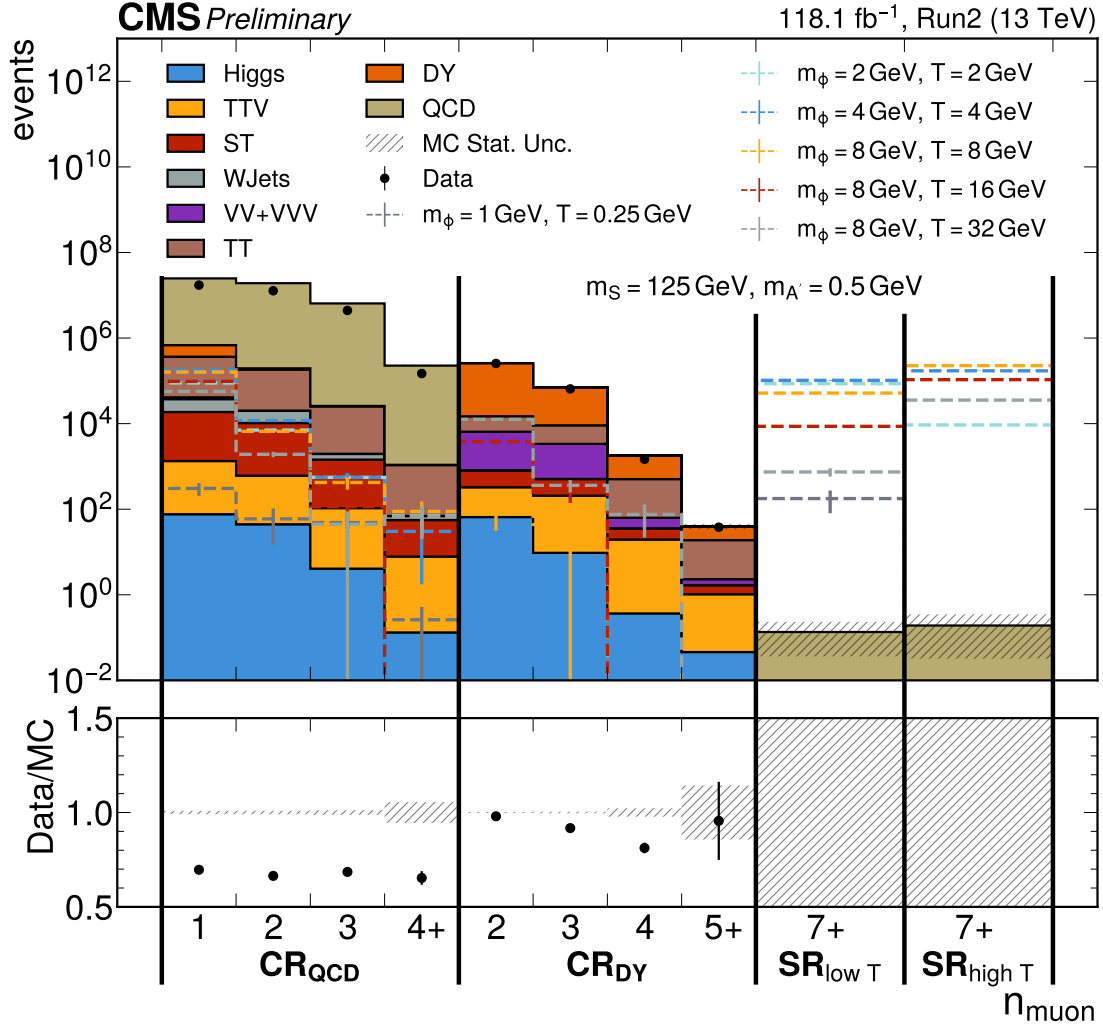


Figure 15.1: The prefitted n_{muon} distributions for all regions for Run 2.

15.2 Signal model assignment for the SRs

The expected background yields in the discovery bins of the signal regions are numbers that are both below 1 and not very different. Consequently, the signal retention efficiency is the main contributing factor to the sensitivity of each signal region to a given scan point of the signal model. The choice between $\text{SR}_{\text{high } T}$ and $\text{SR}_{\text{low } T}$ for each scan point is made solely by choosing the region with the larger event yield. Signal models with lower temperatures, larger m_ϕ/T ratios, and hadronically dominated decays tend to

choose the $\text{SR}_{\text{low } T}$. All signal yields are shown in Table C.1 of Appendix C. The selected region is annotated with bold text on the event yields.

15.3 Combine fit and postfit plots

We perform maximum likelihood template fits between the data and the MC prediction. All the systematic uncertainties are included in the form of nuisance parameters in the fit. The relevant likelihood has the form

$$\mathcal{L} = \prod_{\text{years}} \prod_{\text{regions}} \prod_{\text{bins}} \text{Pois}(n_{\text{obs}}; n_{\text{exp}}(r, \vec{v})) \cdot \prod_{\text{nuisances}} p(v; y), \quad (15.1)$$

where r is the signal strength parameter, \vec{v} is the vector of all the nuisance parameters, $p(v; y)$ is the probability density for the nuisance v given some previous observation y . The parameter of interest (POI) in this case is the signal strength parameter, r , that is just a free parameter that scales the signal processes multiplicatively.

The `Combine` cards include three histograms: CR_{QCD} , CR_{DY} , and either $\text{SR}_{\text{low } T}$ or $\text{SR}_{\text{high } T}$. For $\text{SR}_{\text{low } T}$ and $\text{SR}_{\text{high } T}$, only the discovery bins are included, so they are single-bin histograms. All the systematics listed in Section 14 are also included in the datacards. The luminosity systematics are included as log-normal scaling systematics affecting only the normalization, and all other systematics are treated as shape systematics that use `Combine`'s shape morphing method to interpolate the shapes. For the two dominant MC processes, QCD and DY, their normalizations are left to float freely by introducing the rate parameters k_{QCD} and k_{DY} to the fit. The control regions have decently isolated samples of the two processes, permitting the determination of the normalizations by the

fit. For the statistical uncertainties of the MC in the CRs, the Barlow-Beeston method [218], which introduces nuisance parameters for the bins of the MC templates, is employed by using `Combine's autoMCStats` option. For bins with total yields larger than 5 events, the Barlow-Beeston lite approach [219] is used by introducing one nuisance parameter covering all MC processes. Bins with total yields of less than 5 events use the full Barlow-Beeston, which introduces one nuisance for each MC process in the bin. For the uncertainties in the signal regions, the `autoMCStats` is also used, but the Gaussian constraint is forced regardless of the event yields. This is done because the bin errors of the background histograms in the SRs contain the uncertainty predicted by the extrapolation method, which is a combination of the MC statistical uncertainty and the systematic uncertainty introduced by the fit, as explained in Section 13.2.

The postfit plot for the Run 2-only fit for signal point: $m_S = 125 \text{ GeV}$, $m_\phi = 8 \text{ GeV}$, $T = 32 \text{ GeV}$, $m_{A'} = 0.5 \text{ GeV}$ (mostly leptonic decays to SM) is shown in Figure 15.2. The MC templates match the data very well after the fit. The signal region is blinded. The exact values of the fitted parameters are estimated using the command [220]:

```
combine -M FitDiagnostics workspace.root --rMin -1 --rMax 5 \
--robustFit 1 --cminDefaultMinimizerStrategy 1
```

and they are presented in Table 15.1. The k-factors for QCD and DY are $k_{\text{QCD}} = 0.6971 \pm 0.0002$ and $k_{\text{DY}} = 0.993 \pm 0.004$.

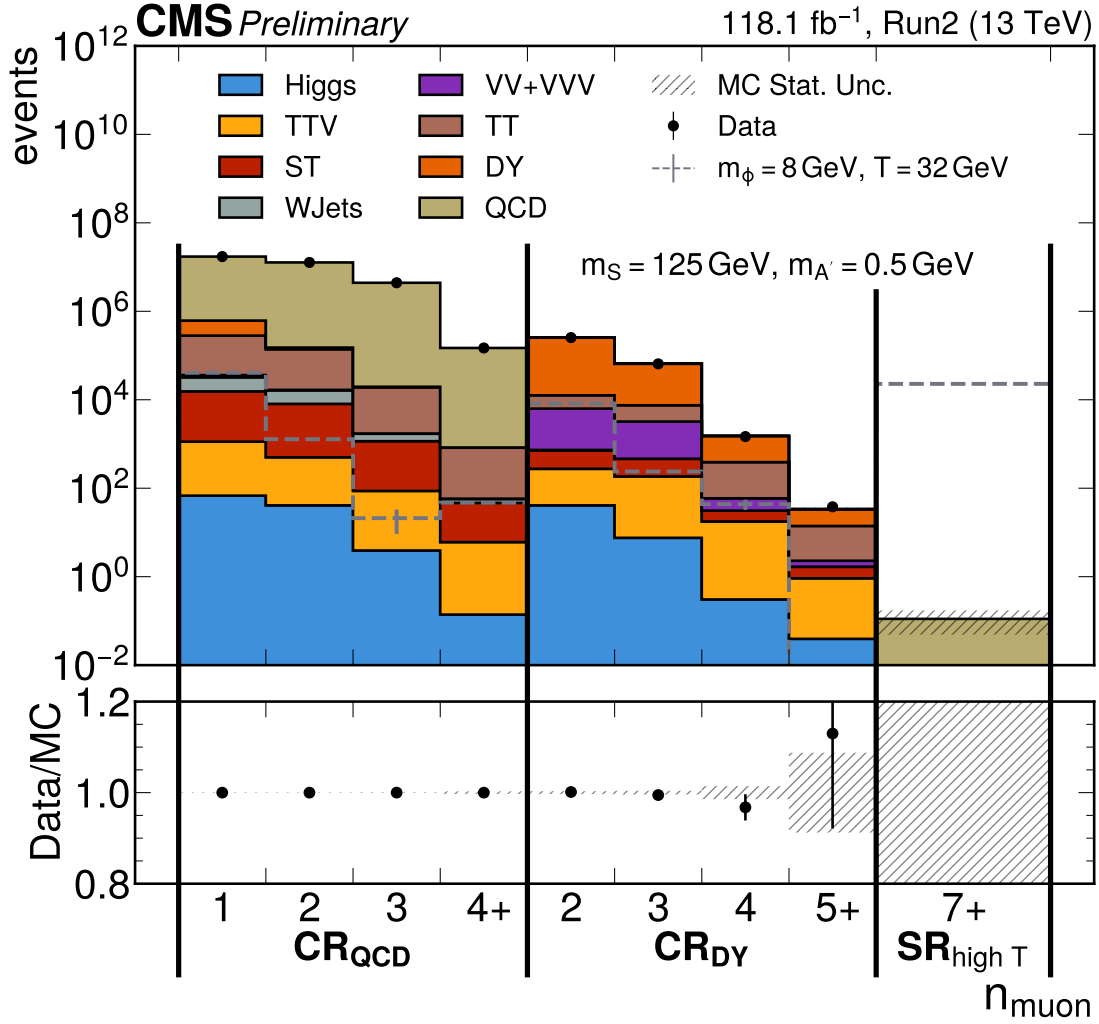


Figure 15.2: The postfit n_{muon} distributions for the CRs and blinded SR_{high T} for the Run 2-only fit. The MC matches very well the data in the bins with many entries, because they have the statistical power to constrain the fit.

15.4 Impact plots

The likelihoods of all the fitted parameters (nuisance parameters and k-factors) are profiled, and their 1- σ postfit uncertainties are determined. Then, all parameters are shifted up and down according to their postfit uncertainties to determine the impact on the parameter of interest (POI), which in this case is the signal strength r .

The following commands are used to create impact plots using the Asimov dataset [220]:

```

combineTool.py -M Impacts -d workspace.root -m 125 --rMin -5 \
    --rMax 20 --robustFit 1 --cminDefaultMinimizerStrategy 0 \
    -t -1 --expectSignal 0 --doInitialFit
combineTool.py -M Impacts -d workspace.root -m 125 --rMin -5 \
    --rMax 20 --robustFit 1 --cminDefaultMinimizerStrategy 0 \
    -t -1 --expectSignal 0 --doFits
combineTool.py -M Impacts -d workspace.root -m 125 --rMin -5 \
    --rMax 20 --robustFit 1 --cminDefaultMinimizerStrategy 0 \
    -t -1 --expectSignal 0 --output impacts.json
plotImpacts.py -i impacts.json -o impacts

```

The impact plot using the Asimov dataset with expected signal strength, r , set to 0, is shown in Figure 15.3 for the Run 2 fit. The same plot but for $r = 1$ is shown in Figure 15.4. The impact plot using data in the CRs and blinded SR is shown in Figure 15.5 for the Run 2 fit. In this case, the `-t -1 --expectSignal 0` options are replaced with `--setParameters k_QCD=0.7,k_DY=0.9`, which is an initial guess for the values of the free parameters, and it is needed for the fit to converge successfully.

The impact plots for fits with the Asimov dataset for $r = 0$ and $r = 1$ show correct fit values for the parameter of interest (POI). No shifts or pulls from the nominal values are observed, as is expected for these fits. The systematic uncertainties with the highest impacts are the MC nuisances for the SR in the case with $r = 0$, and μ_{onSF} in the case with $r = 1$. In the case of the fit with data in the CRs and blinded SR with data yield set to 0 events, there are strong pulls away from the nominal values, with the

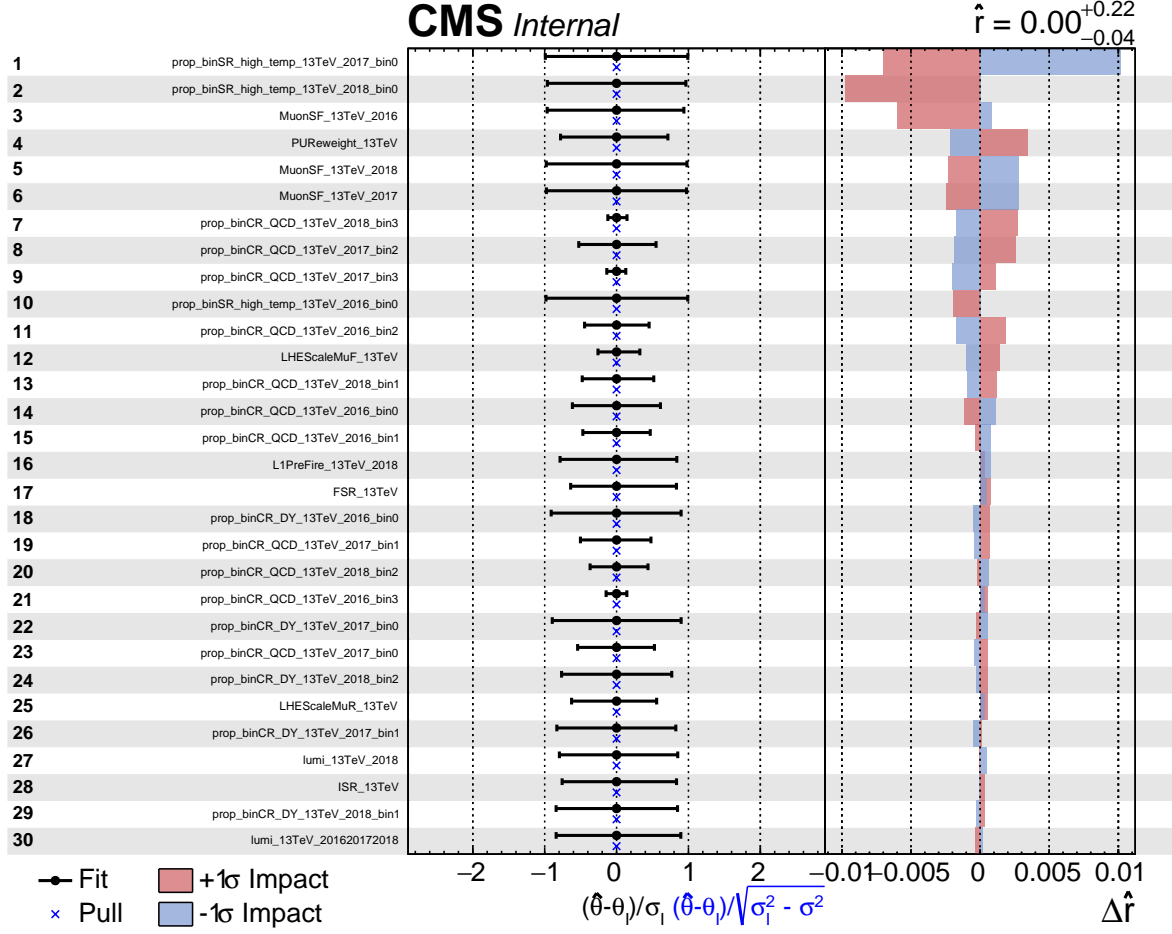


Figure 15.3: Impact plot with top 30 nuisances for Run 2 fit with Asimov dataset and signal strength set to $r = 0$.

most notable examples being `LHEScaleMuR`, `ISR`, `FSR`, and some of the MC template nuisance parameters.

15.4.1 Expected limits

The expected %95CL limits are calculated using the Asymptotic approximation method [221]. The exact command used has the form [220]:

```
combine workspace.root -M AsymptoticLimits --cl 0.95 --run blind
```

The expected 95% upper limits for the SUEP production cross section at center-of-mass

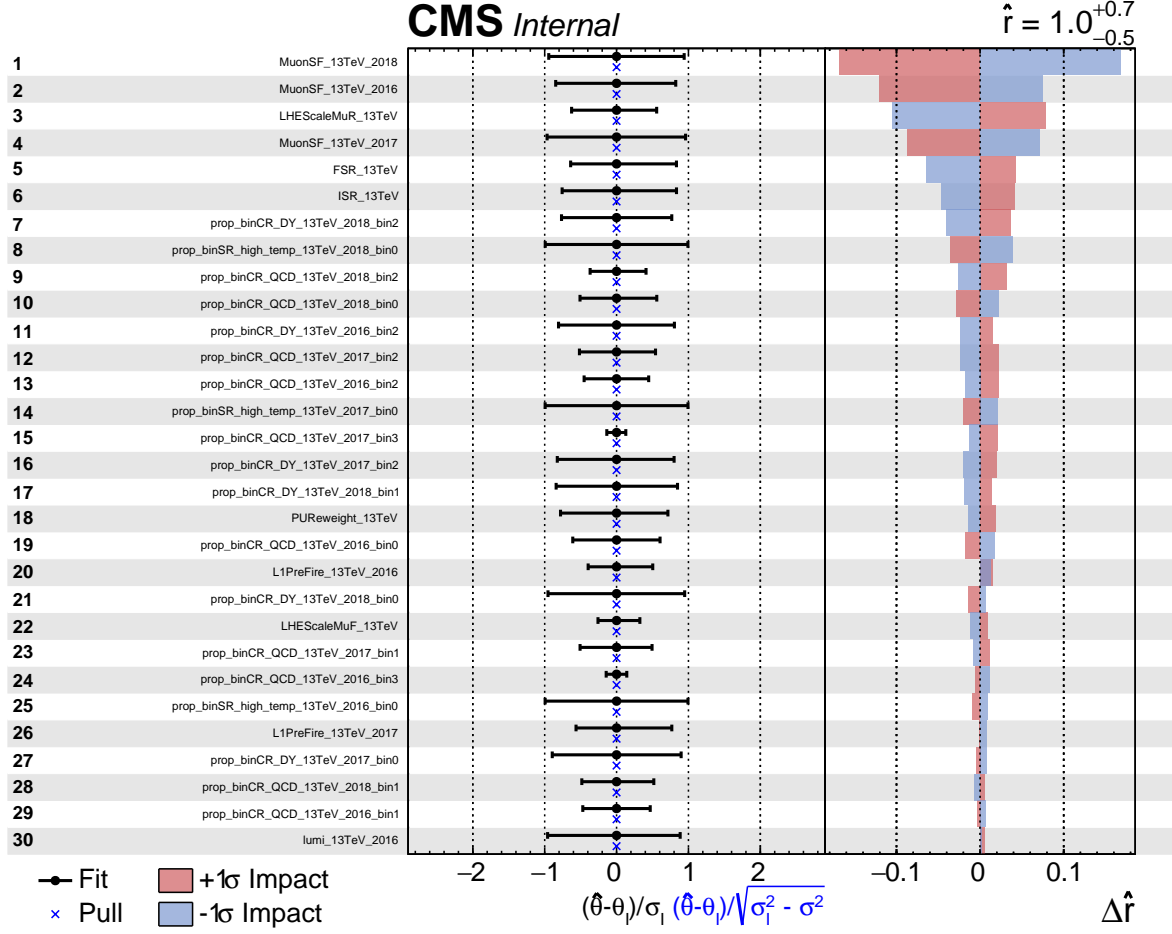


Figure 15.4: Impact plot with top 30 nuisances for Run 2 fit with Asimov dataset and signal strength set to $r = 1$.

energy $\sqrt{s} = 13$ TeV are presented in Figure 15.6 using both Run 2 (118 fb^{-1} at 13 TeV) for signal points with $m_\phi = 2$ GeV and $T = 2$ GeV (top left), $m_\phi = 4$ GeV and $T = 1$ GeV (top right), $m_\phi = 4$ GeV and $T = 4$ GeV (bottom left), and $m_\phi = 8$ GeV and $T = 32$ GeV (bottom right) as a function of the entire scanned range of $m_{S'}$. The limits are plotted with blue color for the leptonically dominated decays ($m_{A'} = 0.5$ GeV) and with red color for the hadronically dominated decays ($m_{A'} = 0.7$ GeV). The theoretical prediction for the cross section of the production of a scalar boson via gluon-gluon fusion as a function is also plotted as a dashed black line. The upper limits are also presented in terms of the

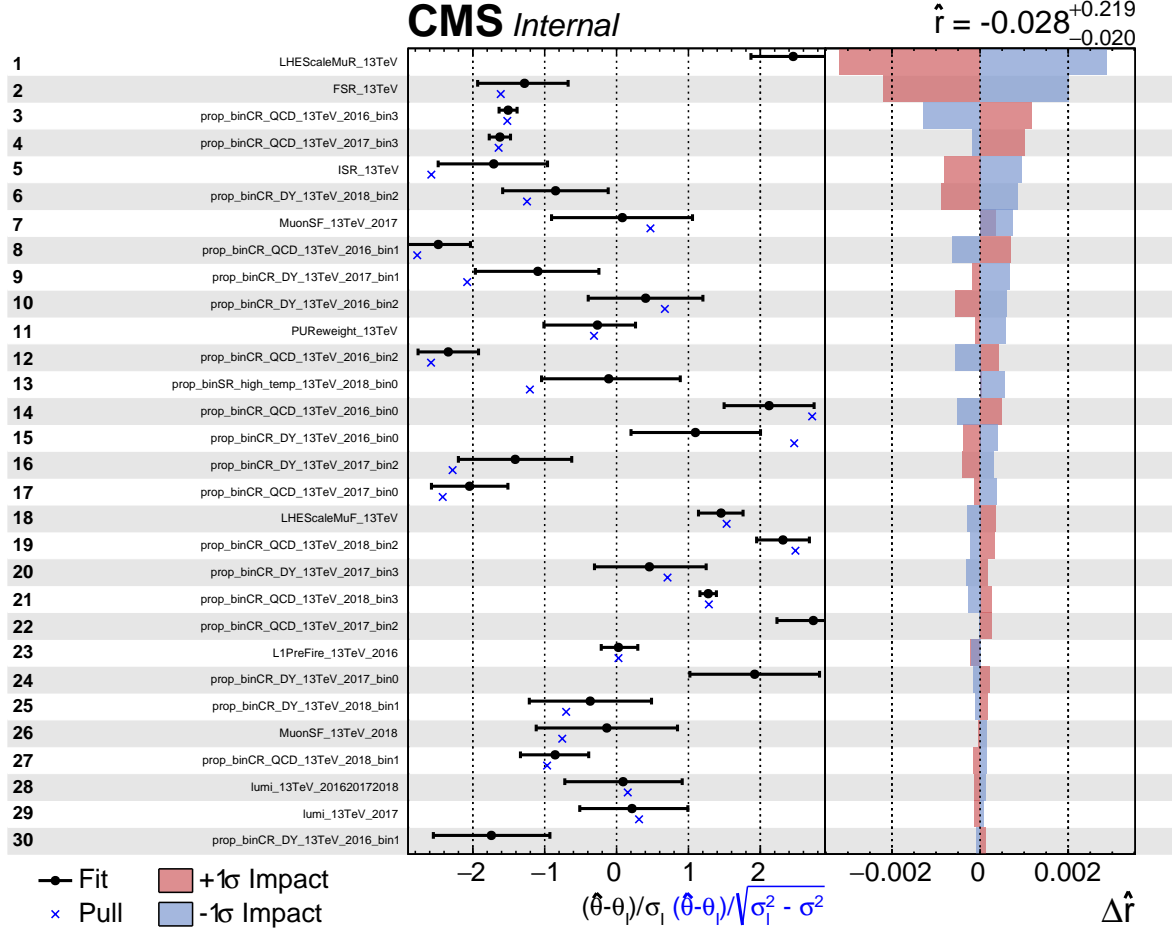


Figure 15.5: Impact plot for fit with data and blinded SRs. Fit is only for Run 2. The data yields have been set to 0 in the SRs.

dimensionless signal strength parameter, r , in Figure 15.7. The signal strength parameter is independent of the center-of-mass energy.

The expected upper limits are three to four orders of magnitude tighter than the theory predictions along the entire scalar mediator mass range, with the limits for the leptonically dominated decay scenario being stronger by one to two orders of magnitude compared to the semi-hadronic decay scenario. Only the limits for models with very low temperatures ($T = 0.25 \text{ GeV} - 0.35 \text{ GeV}$) do not exclude the entire scalar mediator mass range since the signal MC is statistically depleted because of poor triggering efficiency.

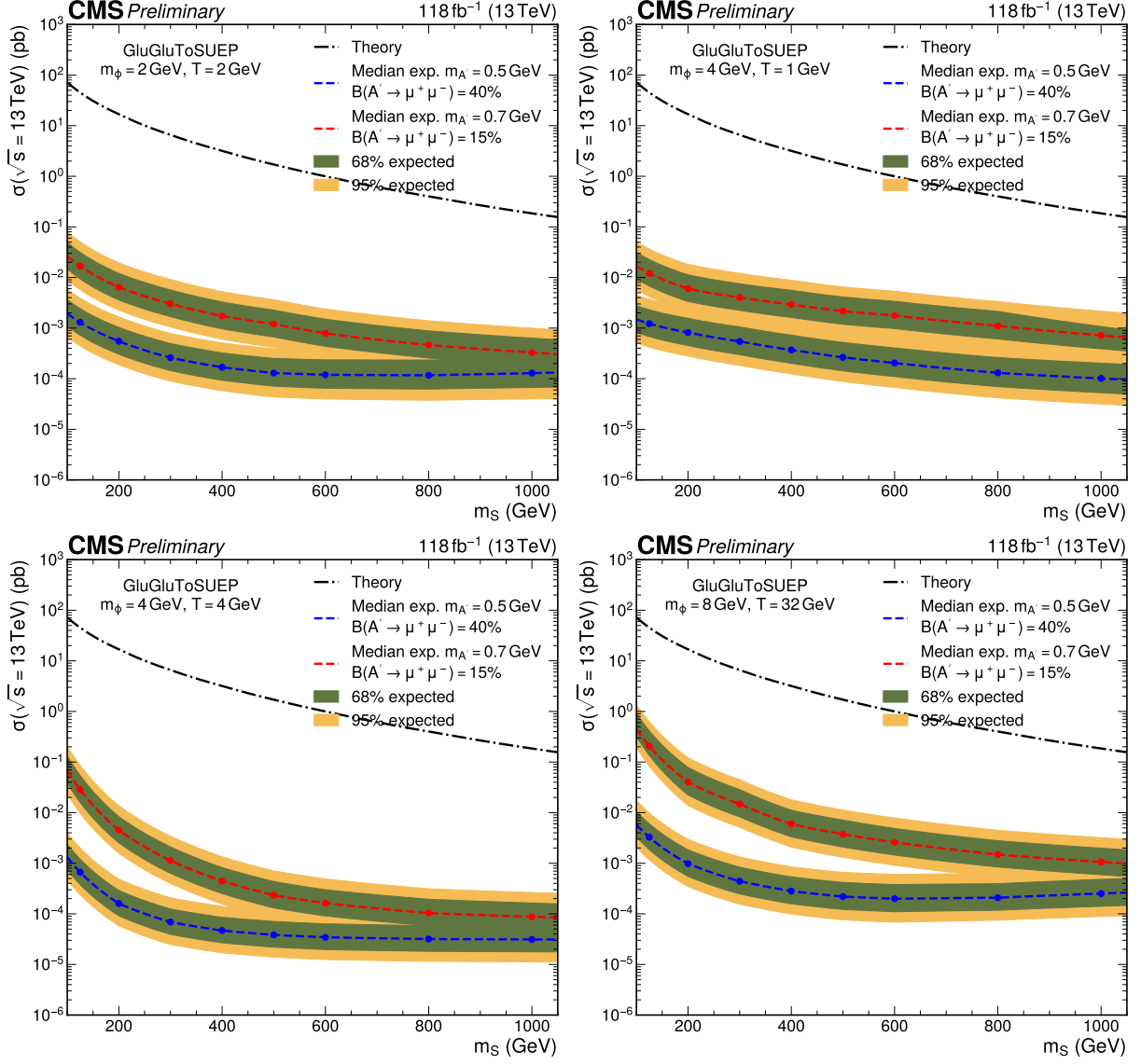


Figure 15.6: Expected 95% upper limits for the SUEP production cross section at $\sqrt{s} = 13$ TeV using the asymptotic approximation method as a function of the scalar mediator's mass, m_S , with $m_\phi = 4$ GeV and $T = 4$ GeV (left) and $m_\phi = 8$ GeV and $T = 32$ GeV (right) both for hadronically (red) and leptonically (blue) dominated decay scenarios.

All the 1D expected limits (all model parameters fixed except m_S) are included in the Appendix D.

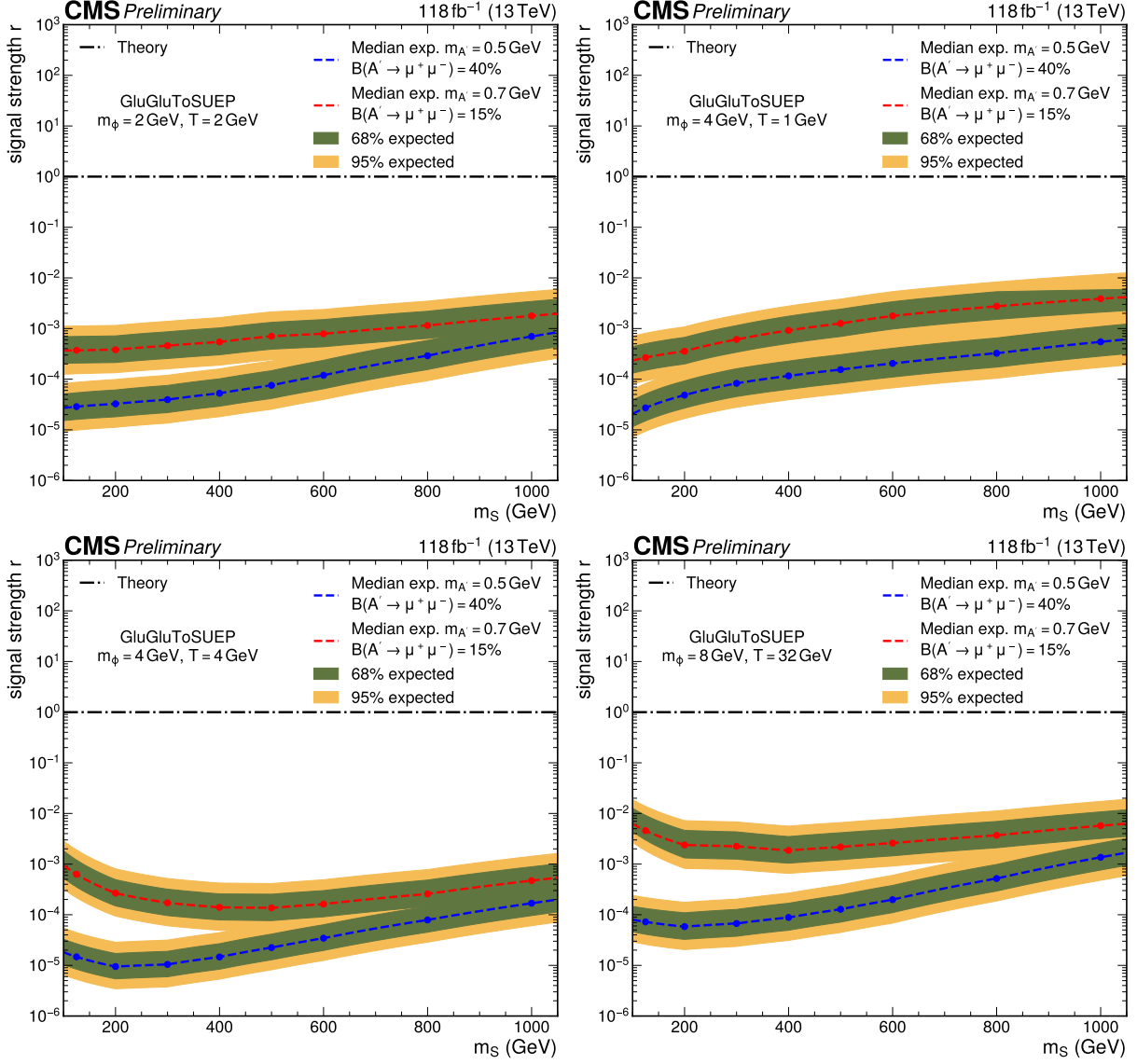


Figure 15.7: Expected 95% upper limits for the signal strength parameter, r , using the asymptotic approximation method as a function of the scalar mediator's mass, m_S , with $m_\phi = 4$ GeV and $T = 4$ GeV (left) and $m_\phi = 8$ GeV and $T = 32$ GeV (right) both for hadronically (red) and leptonically (blue) dominated decay scenarios.

Table 15.1: Result for b-only fit for Run 2 with data in the CRs and blinded $SR_{\text{high } T}$ with yields set to 0. The initial value for all nuisance parameters is 0. The k-factors have initial value 1.

Floating Parameter	Final Value \pm Error
FSR_13TeV	-1.2873 ± 0.714
ISR_13TeV	-1.7174 ± 0.130
L1PreFire_13TeV_2016	$+0.0354 \pm 0.170$
L1PreFire_13TeV_2017	$+1.0743 \pm 0.019$
L1PreFire_13TeV_2018	$+0.0116 \pm 0.444$
LHEScaleMuF_13TeV	$+1.4515 \pm 0.0028$
LHEScaleMuR_13TeV	$+2.4494 \pm 0.0074$
MuonSF_13TeV_2016	-1.0994 ± 0.144
MuonSF_13TeV_2017	$+0.0714 \pm 0.183$
MuonSF_13TeV_2018	-0.1409 ± 0.266
PUReweight_13TeV	-0.2710 ± 0.111
k_DY_13TeV	$+0.9930 \pm 0.0044$
k_QCD_13TeV	$+0.6971 \pm 0.000196$
lumi_13TeV_2016	-0.5417 ± 0.0629
lumi_13TeV_201620172018	$+0.1006 \pm 0.0266$
lumi_13TeV_2017	$+0.1932 \pm 0.0120$
lumi_13TeV_20172018	$+0.0952 \pm 0.0843$
lumi_13TeV_2018	$+0.2532 \pm 0.0135$
prop_binCR_DY_13TeV_2016_bin0	$+1.1098 \pm 0.468$
prop_binCR_DY_13TeV_2016_bin1	-1.7354 ± 0.538
prop_binCR_DY_13TeV_2016_bin2	$+0.4037 \pm 0.525$
prop_binCR_DY_13TeV_2016_bin3	$+0.0907 \pm 0.575$
prop_binCR_DY_13TeV_2017_bin0	$+1.9254 \pm 0.495$
prop_binCR_DY_13TeV_2017_bin1	-1.1052 ± 0.503
prop_binCR_DY_13TeV_2017_bin2	-1.4146 ± 0.526
prop_binCR_DY_13TeV_2017_bin3	$+0.4571 \pm 0.537$
prop_binCR_DY_13TeV_2018_bin0	-0.8197 ± 0.575
prop_binCR_DY_13TeV_2018_bin1	-0.3649 ± 0.534
prop_binCR_DY_13TeV_2018_bin2	-0.8522 ± 0.474
prop_binCR_DY_13TeV_2018_bin3	$+0.5654 \pm 0.452$
prop_binCR_QCD_13TeV_2016_bin0	$+2.1161 \pm 0.0557$
prop_binCR_QCD_13TeV_2016_bin1	-2.4825 ± 0.0428
prop_binCR_QCD_13TeV_2016_bin2	-2.3473 ± 0.0518
prop_binCR_QCD_13TeV_2016_bin3	-1.5096 ± 0.0431
prop_binCR_QCD_13TeV_2017_bin0	-2.0529 ± 0.0607
prop_binCR_QCD_13TeV_2017_bin1	-2.9321 ± 0.0437
prop_binCR_QCD_13TeV_2017_bin2	$+2.7287 \pm 0.0413$
prop_binCR_QCD_13TeV_2017_bin3	-1.6275 ± 0.0413
prop_binCR_QCD_13TeV_2018_bin0	$+2.9460 \pm 0.0606$
prop_binCR_QCD_13TeV_2018_bin1	-0.8701 ± 0.0490
prop_binCR_QCD_13TeV_2018_bin2	$+2.3034 \pm 0.0237$
prop_binCR_QCD_13TeV_2018_bin3	$+1.2716 \pm 0.0499$
prop_binSR_high_temp_13TeV_2016_bin0	-0.0054 ± 0.693
prop_binSR_high_temp_13TeV_2017_bin0	-0.0182 ± 0.693
prop_binSR_high_temp_13TeV_2018_bin0	-0.1095 ± 0.693

Part IV

Final remarks

Chapter 16: Summary and conclusions

This dissertation presented two studies on the effects of radiation damage in plastic scintillator, and a search for a signature called Soft Unclustered Energy Patterns (SUEP) using data from LHC collisions collected by the CMS experiment.

The first study, shown in Chapter 5, examined the effects of ionizing radiation on the scintillation signal produced by plastic scintillators. The scintillation light yield reduction was quantified using the concept of the dose constant, D . Several different concentrations of fluors and antioxidants were tested. The manufacturer's default values were found to be optimal for use in detectors in hadron colliders. It was found that D scales linearly with the logarithm of the dose rate for dose rates < 100 Gy/h. For PVT-based scintillator, D continues to scale linearly even at higher dose rates, while for PS-based scintillator, the dose constant plateaus at higher dose rates. Therefore, PVT scintillator is more resistant only at higher dose rates. Furthermore, the results from samples of varying thickness and different dopants indicate that damage to the initial light output is the dominant effect for samples with thickness ≤ 1 cm compared to color center formation.

The plastic scintillator studies, summarized above, contribute to our understanding of the aging effects of a material that is ubiquitous in modern particle physics experiments. Performing scintillator irradiations at very low dose rates is necessary for building a

realistic picture of the radiation damage mechanism relevant to the conditions at hadron colliders. Given the time and the precision needed to perform such irradiations, it is evident that such studies can easily become prohibitively complex and costly. The analysis presented in this thesis represents a significant step in this direction; however, further irradiations at even lower dose rates are necessary to corroborate its findings.

The second study of Part II, presented in Chapter 6, studied the effects of oxidation on the optical properties of plastic scintillators during irradiation and annealing. Two models of oxygen diffusion in polymers were investigated and solved numerically. The results indicate that the reactivity can experience a significant change from approximately 100% to almost 0% at a certain depth of the material, which can be varied depending on the model parameters. This change matches our visual observations of irradiated plastic scintillator samples, which have both a green-colored inner region and a sharp change in the refractive index at specific depths depending on the dose rate.

Those depths were measured for the refractive index boundary, and they seem to be compatible with an inverse square root of dose rate dependence, which is in accordance with the predictions of the models. The depths of the inner green-colored regions increase during annealing after the irradiation, until the colored regions disappear. The evolution of the depths of the colored region during annealing was measured for an irradiated PS sample. These measurements can be explained by the diffusion of oxygen inside the sample during annealing. The simulation of one of the diffusion models agrees with the experimental data.

Additionally, the refractive indices of both the internal and the external regions were measured using a photography-based technique. The internal regions have elevated

values of the index of refraction compared to the outer ones. The indices of the outer regions match the index of unirradiated samples. These results suggest that the irradiation affects primarily the substrate material, and in the absence of oxygen, the substrate can experience chemical changes that can affect its refractive index. The refractive indices generally do not show a dose rate dependence, except for the inner region of PS, which shows a descending trend with increasing dose rate. More studies are needed to confirm this effect.

This study highlights the connections between oxidation and radiation damage through the visible effects on the irradiated material. Such studies are deemed critical given the current push for plastic scintillators in hypoxic environments with the presence of ionizing radiation, like the High Granularity Calorimeter in CMS. Our understanding of those effects can be further solidified with further experiments with low-dose rate irradiations of samples of varying shapes, sizes, and thicknesses.

Lastly, a search for soft unclustered energy patterns using decays to muons was presented in Part III of this dissertation. The triple-muon triggers are used to select events during data taking. Further offline selections are applied to form two control regions, targeting events from QCD and DY, and two signal regions with ≥ 7 muons, focusing on events from signal models with low and high temperatures. The MC background in the signal regions is obtained by fitting a power law in extended versions of the regions and extrapolating them to the regions of interest. The expected background is 0.2 events or lower in the signal regions. The final histograms for the control regions and the extrapolated signal regions are used to fit with data and extract the 95% CL upper limits. The expected limits appear to be between 3 and 5 orders of magnitude lower than the

theory predictions. Once unblinded, this search is expected to be able to exclude almost all proposed signal models.

This analysis nicely complements the existing efforts in CMS for SUEP searches, and it offers unprecedented sensitivity for a considerable part of the model's parametric space. Significant improvements in the searches for SUEP can be realized after the Phase 2 upgrade of the CMS detector. The addition of tracking to the L1 trigger will offer the ability to trigger on events with high multiplicities of soft objects that follow specific distributions and patterns. A first step in this direction would be the development of an HLT path specialized for SUEP signatures.

Part V

Appendices

Chapter A: List of scintillator samples

This appendix contains lists of the samples used throughout the paper. For the samples with varying fluor concentrations, the scintillator label in the first column has the form “<scintillator color><substrate>”. The scintillator color can be either “EJ200” or “EJ260”. The substrate can be PS or PVT, where PS in the name means the matrix is polystyrene, and PVT means it is polyvinyltoluene. The fluor concentrations are shown as “NXMP”, where “N” refers to the multiplication factor for the secondary fluor and “M” to the primary fluor. For the samples with varying antioxidant concentrations, the scintillator label in the first column has the form “<scintillator color><antioxidant concentrations>”, where antioxidant concentrations are expressed by numbers 0, 1, 2 which represent 0.5, 1, and 2 times the nominal value.

⁸There are 3 samples for this irradiation.

⁹There are 2 samples for this irradiation.

Scintillator type	Dose (kGy)	Dose rate \mathcal{R} (Gy/hr)	Irr. end date	Irr. facility
EJ200PS-1X1P	13.2	2.2	2018/10/26	GIF++
	12.6	3.1	2018/11/30	GSFC REF ⁸
	42.0	9.8	2018/12/06	GSFC REF
	70.0	80.6	2017/04/12	NIST
	70.0	85.3	2016/11/09	NIST
	69.0	130.0	2021/09/24	NIST ⁹
	70.0	460.0	2021/10/14	NIST ⁹
	70.0	744.0	2016/12/02	NIST
	70.0	3380.0	2017/11/07	NIST
	70.0	3640.0	2017/04/13	NIST
	70.0	3900.0	2016/10/04	NIST
EJ200PS-1X2P	13.2	2.2	2018/10/26	GIF++
	12.6	3.1	2018/11/30	GSFC REF
	42.0	9.8	2018/12/06	GSFC REF
	70.0	85.3	2016/11/09	NIST
	70.0	744.0	2016/12/02	NIST
	70.0	3900.0	2016/10/04	NIST
EJ200PS-2X1P	13.2	2.2	2018/10/26	GIF++
	70.0	83.4	2017/01/11	NIST
	70.0	2570.0	2020/02/14	NIST
	70.0	3900.0	2016/10/05	NIST

Table A.1: List of EJ200PS samples.

Scintillator type	Dose (kGy)	Dose rate \mathcal{R} (Gy/hr)	Irr. end date	Irr. facility
EJ200PVT-1X1P	13.2	2.2	2018/10/26	GIF++
	17.1	3.0	2019/12/04	GSFC REF
	12.6	3.1	2018/11/30	GSFC REF ⁸
	42.0	9.8	2018/12/06	GSFC REF
	70.0	81.9	2017/03/01	NIST
	70.0	85.3	2016/11/09	NIST
	70.0	744.0	2016/12/02	NIST
	70.0	2380.0	2020/09/17	NIST ⁹
	60.0	2930.0	2019/02/22	NIST
	70.0	3700.0	2017/03/02	NIST
	70.0	3900.0	2016/10/04	NIST
EJ200PVT-1X2P	13.2	2.2	2018/10/26	GIF++
	12.6	3.1	2018/11/30	GSFC REF
	42.0	9.8	2018/12/06	GSFC REF
	70.0	85.3	2016/11/09	NIST
	70.0	744.0	2016/12/02	NIST
	70.0	3900.0	2018/10/04	NIST
EJ200PVT-2X1P	13.2	2.2	2018/10/26	GIF++
	70.0	83.4	2017/01/11	NIST
	70.0	3900.0	2016/10/05	NIST

Table A.2: List of EJ200PVT samples.

Scintillator type	Dose (kGy)	Dose rate \mathcal{R} (Gy/hr)	Irr. end date	Irr. facility
EJ260PS-1X1P	13.2	2.2	2018/10/26	GIF++
	12.6	3.1	2018/11/30	GSFC REF
	42.0	9.8	2018/12/06	GSFC REF
	70.0	83.4	2017/01/11	NIST
	70.0	460.0	2020/12/20	NIST
	70.0	3900.0	2016/10/05	NIST
EJ260PVT-1X1P	13.2	2.2	2018/10/26	GIF++
	12.6	3.1	2018/11/30	GSFC REF
	42.0	9.8	2018/12/06	GSFC REF
	70.0	83.4	2017/01/11	NIST
	70.0	460.0	2020/12/20	NIST
	70.0	3900.0	2016/10/05	NIST

Table A.3: List of EJ260PS and EJ260PVT samples.

Scintillator type	Dose (kGy)	Dose rate \mathcal{R} (Gy/hr)	Irr. end date	Irr. facility
EJ200AO-0	17.1	3.0	2019/12/04	GSFC REF
	60.0	2930	2019/02/22	NIST
EJ200AO-1	17.1	3.0	2019/12/04	GSFC REF
	70.0	2380	2020/09/17	NIST
	60.0	2930	2019/02/22	NIST
EJ200AO-2	17.1	3.0	2019/12/04	GSFC REF
	60.0	2930	2019/02/22	NIST

Table A.4: List of varying antioxidant samples.

Chapter B: $N - 1$ plots

This appendix contains all the $N - 1$ plots. In these plots, all the cuts are applied except for the cut on the variable displayed on the horizontal axis. They are tools helpful in evaluating whether our cut working points are at the optimal values. Additionally, these plots are also shown for the MC background broken down by the muon source.

B.1 $N - 1$ plots for CR_{QCD}

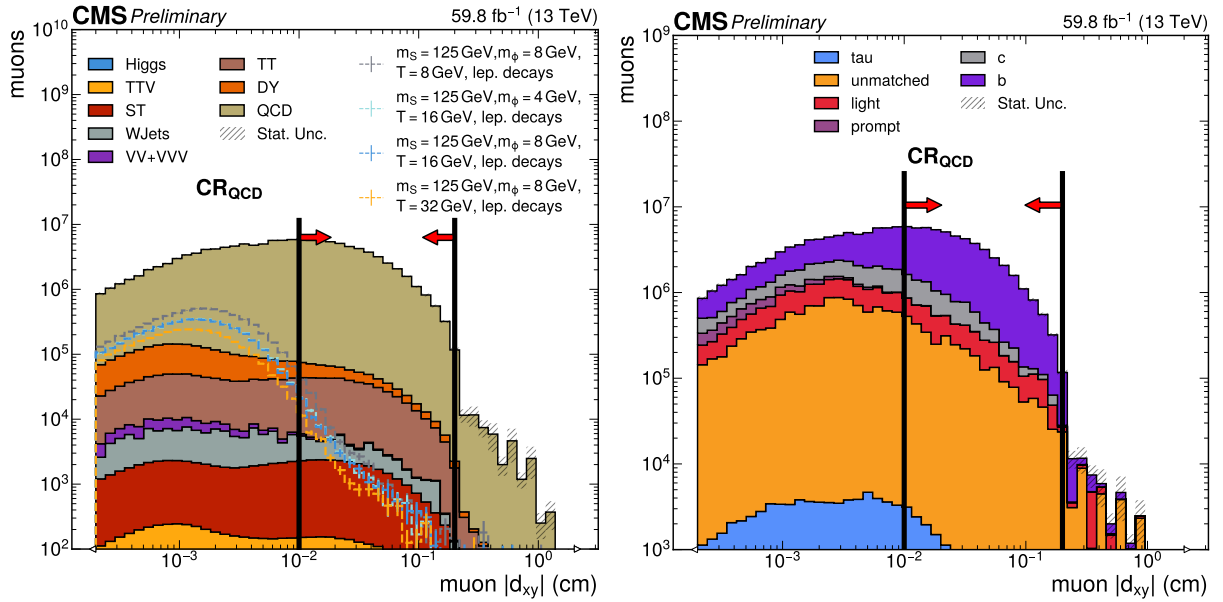


Figure B.1: $N - 1$ plot for CR_{QCD} muon d_{xy} .

B.2 $N - 1$ plots for CR_{DY}

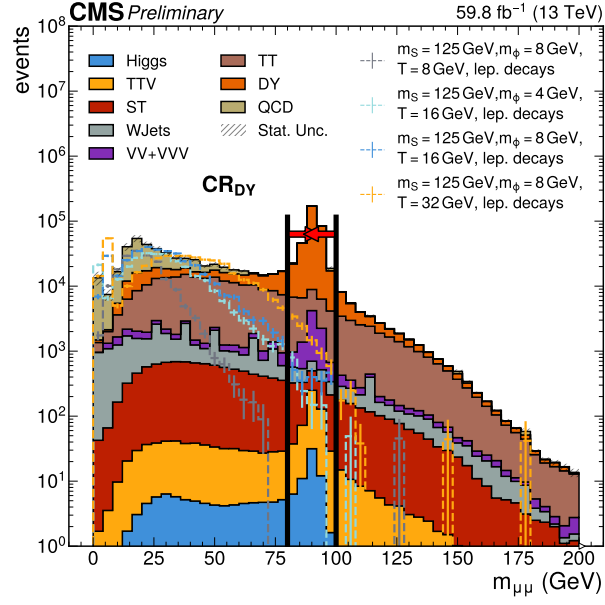


Figure B.2: $N - 1$ plot for CR_{DY} dimuon mass.

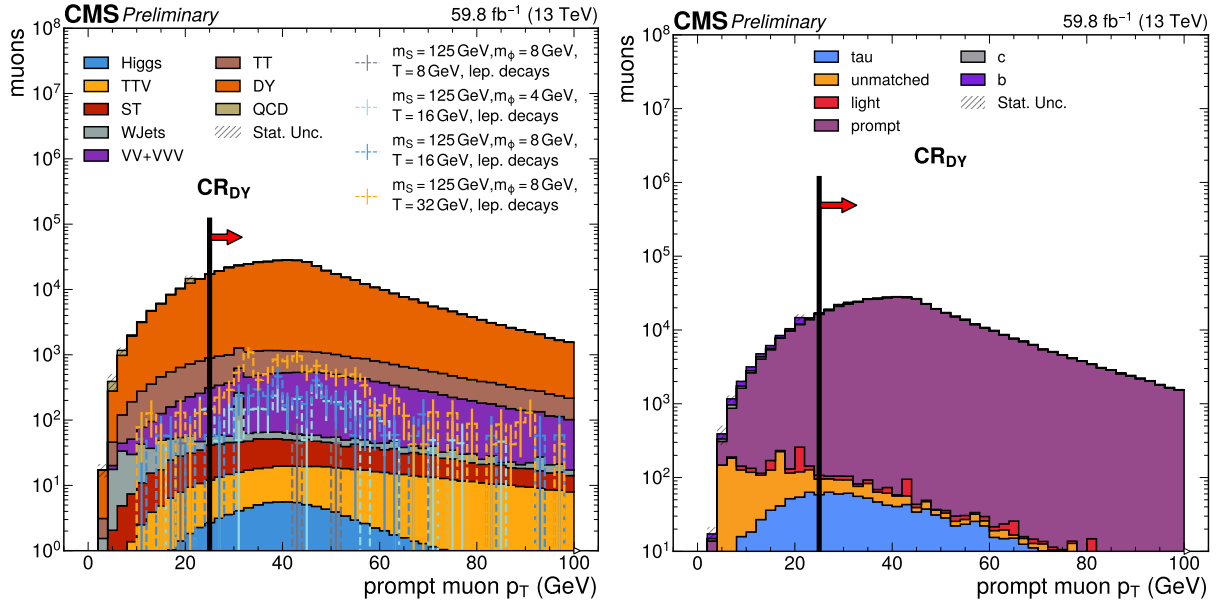


Figure B.3: $N-1$ plot for CR_{DY} and muon p_T .

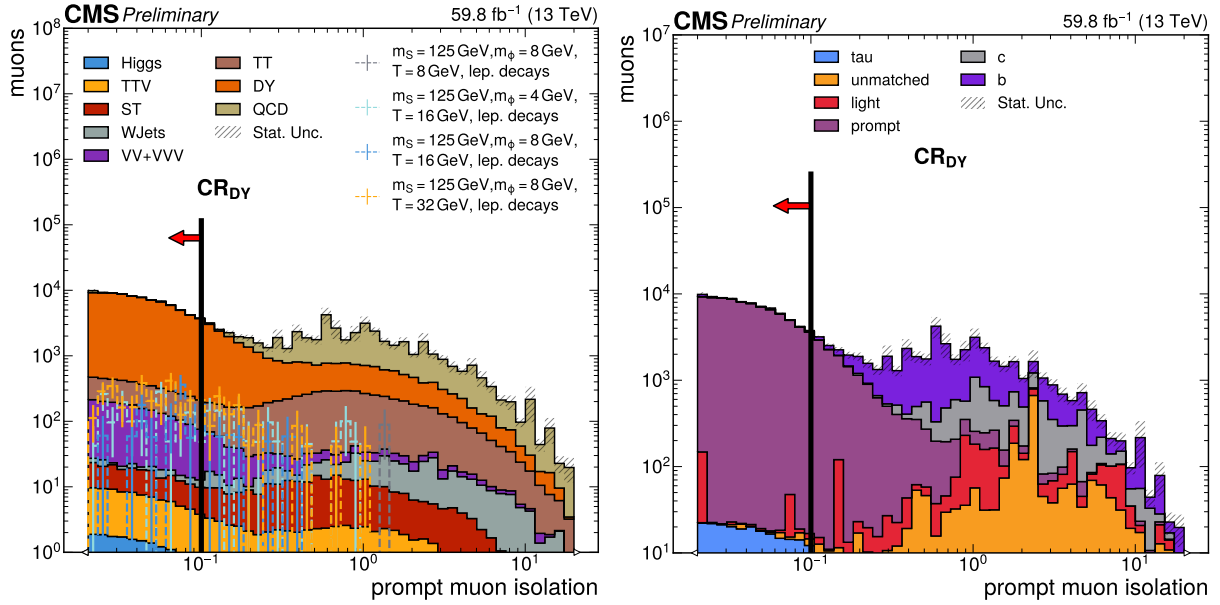


Figure B.4: $N-1$ plot for CR_{DY} and muon iso.

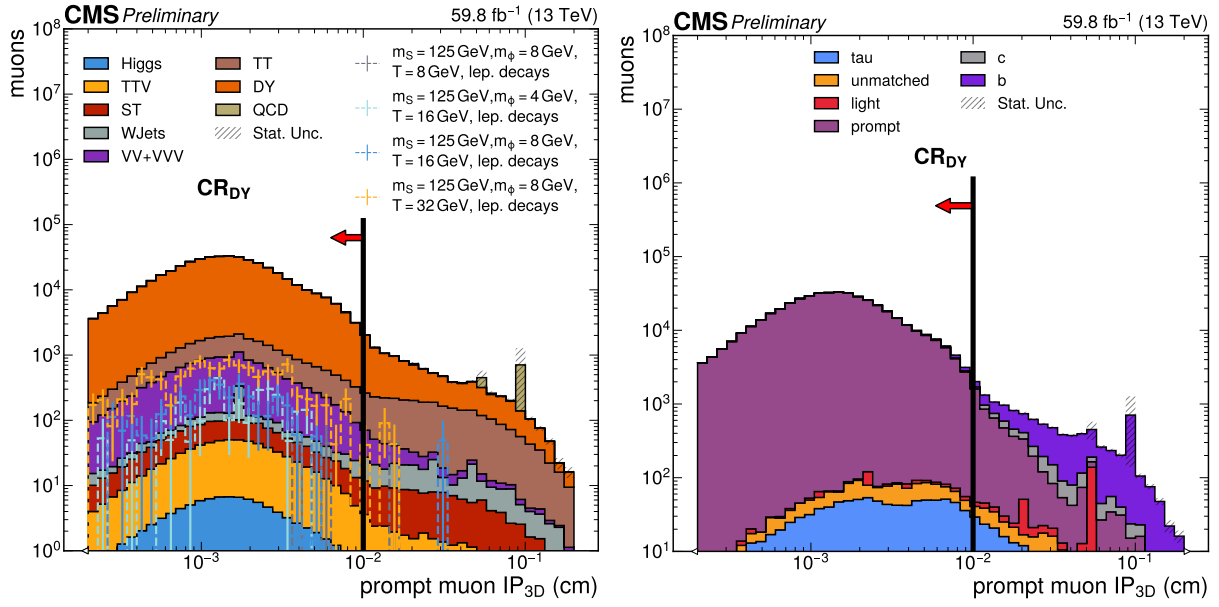


Figure B.5: $N - 1$ plot for CR_{DY} cand muon ip3d.

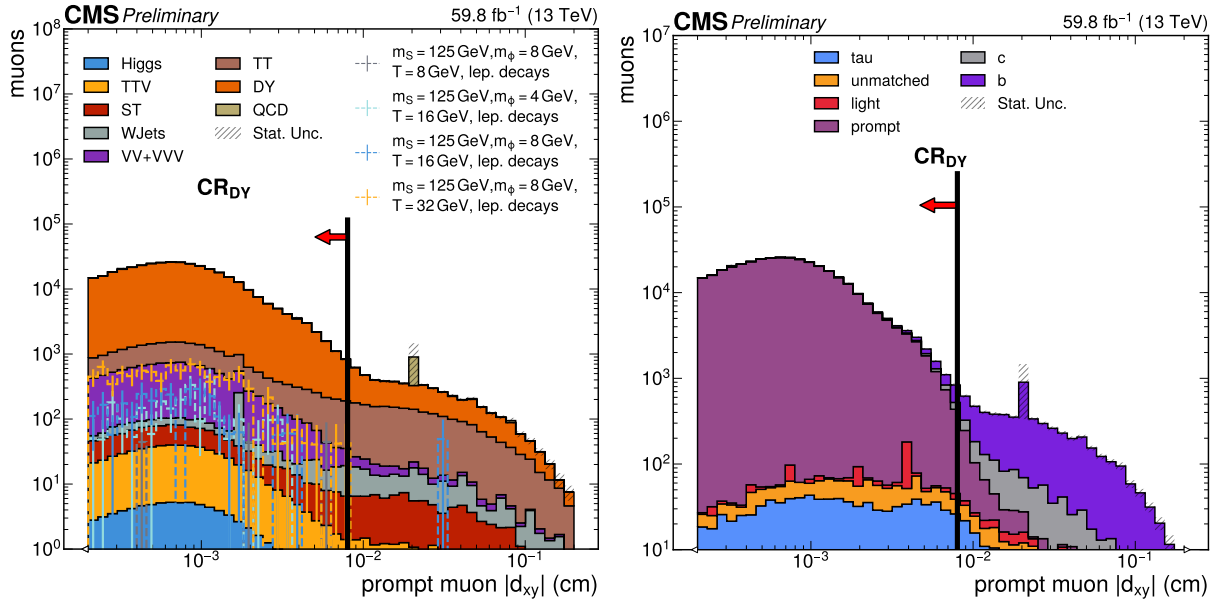


Figure B.6: $N - 1$ plot for CR_{DY} cand muon dxy.

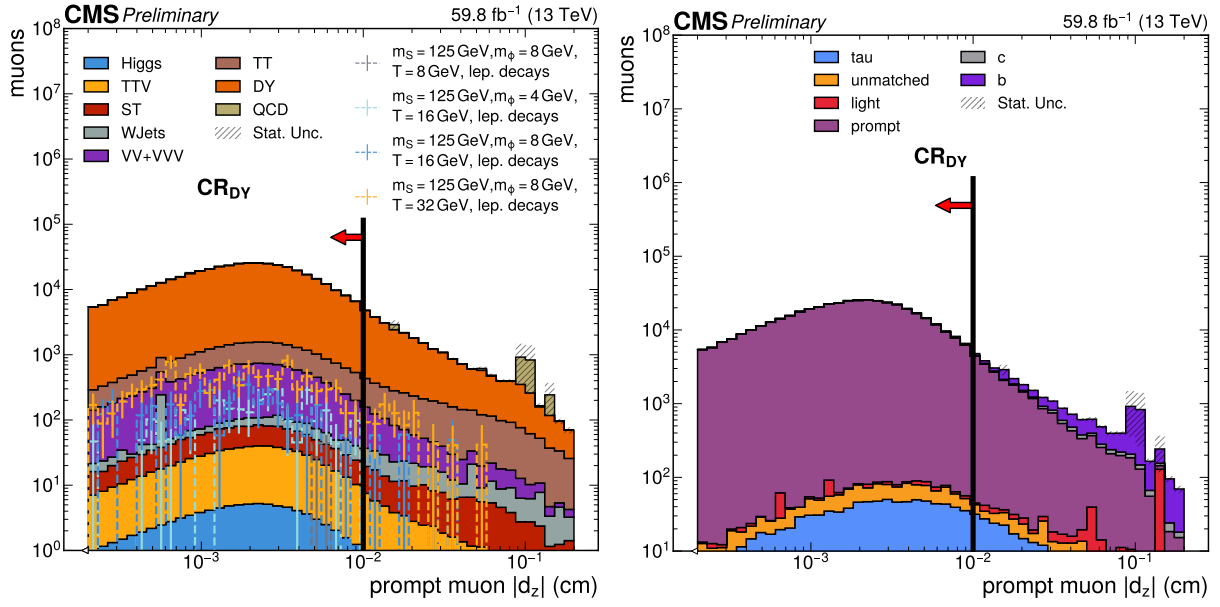


Figure B.7: $N-1$ plot for CR_{DY} and muon dz .

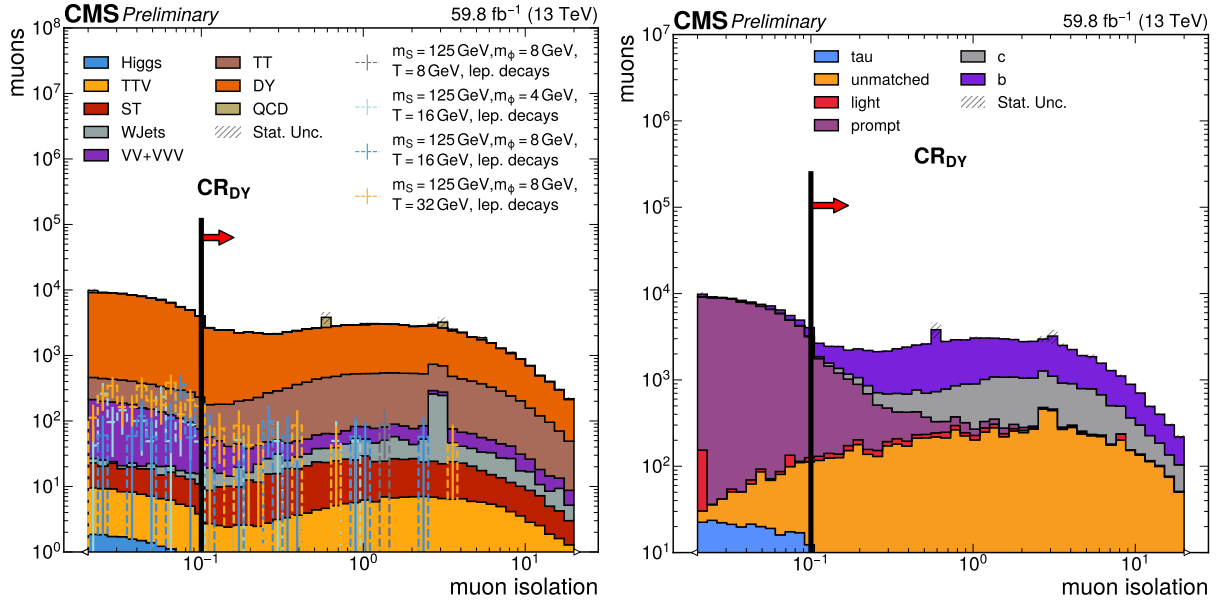


Figure B.8: $N-1$ plot for CR_{DY} muon iso.

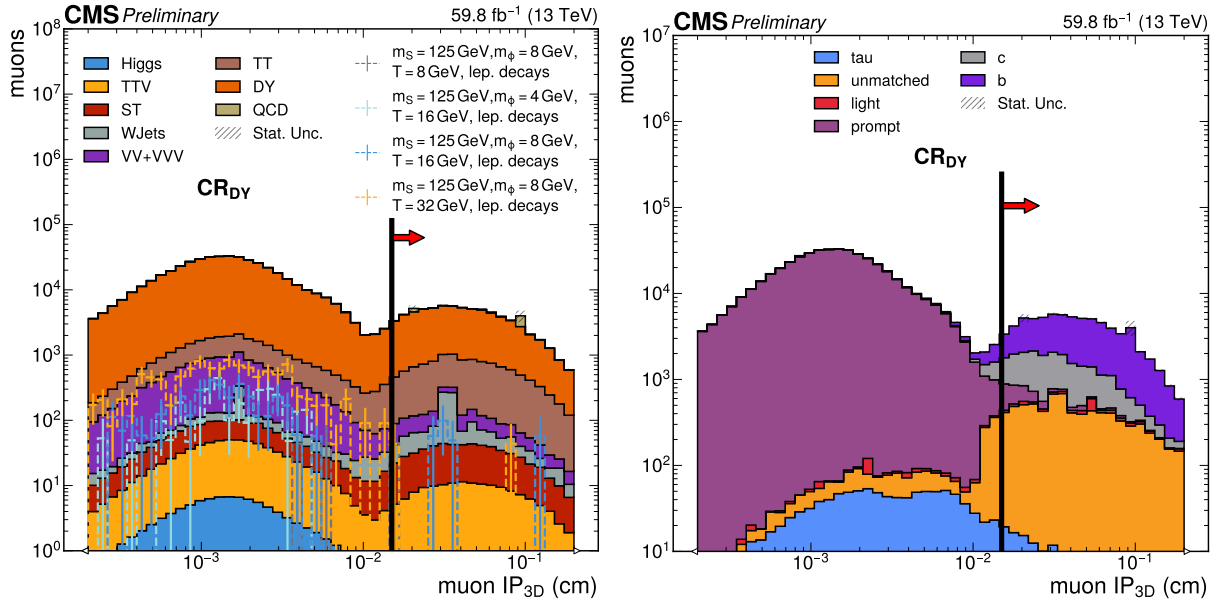


Figure B.9: $N - 1$ plot for CR_{DY} muon ip3d.

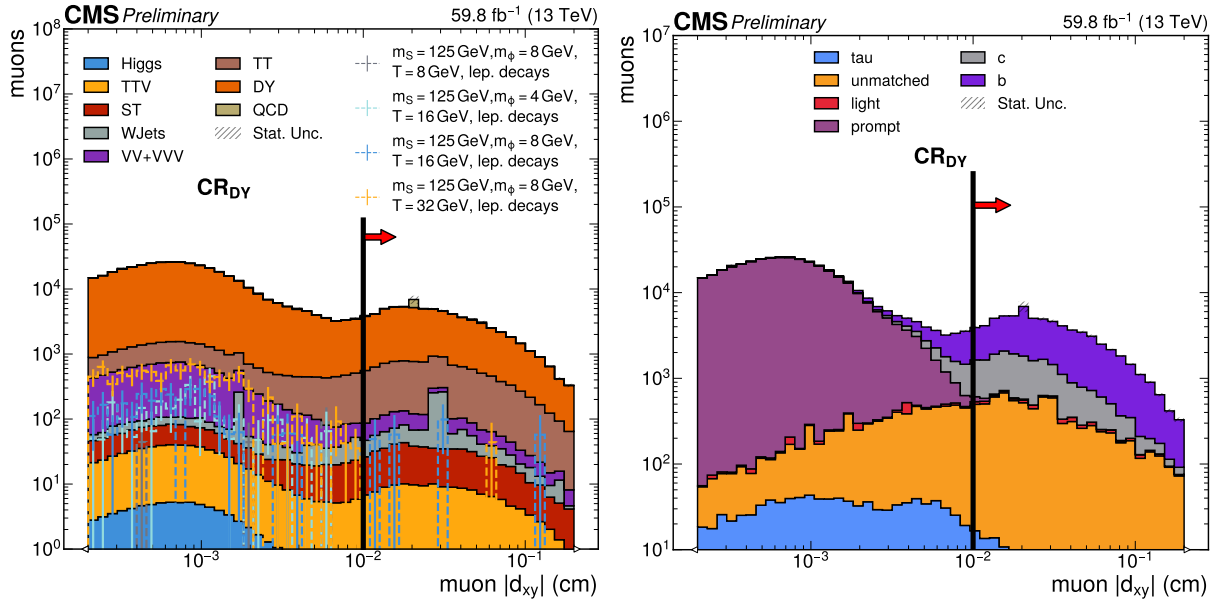


Figure B.10: $N - 1$ plot for CR_{DY} muon dxy.

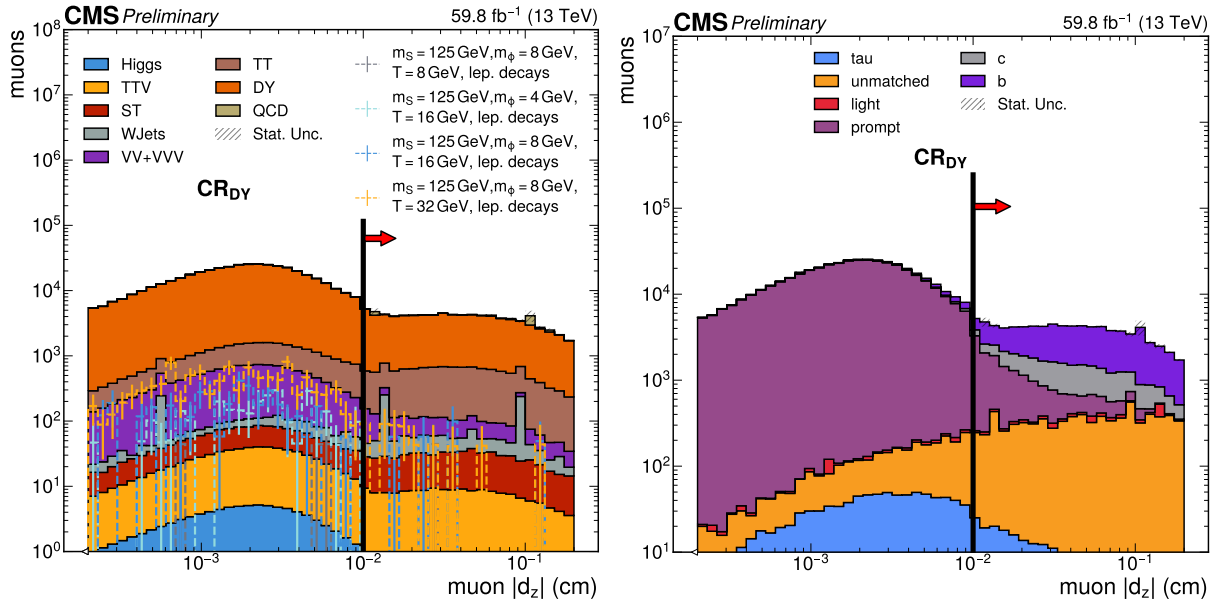


Figure B.11: $N - 1$ plot for CR_{DY} muon dz .

B.3 $N - 1$ plots for $SR_{\text{low } T}$

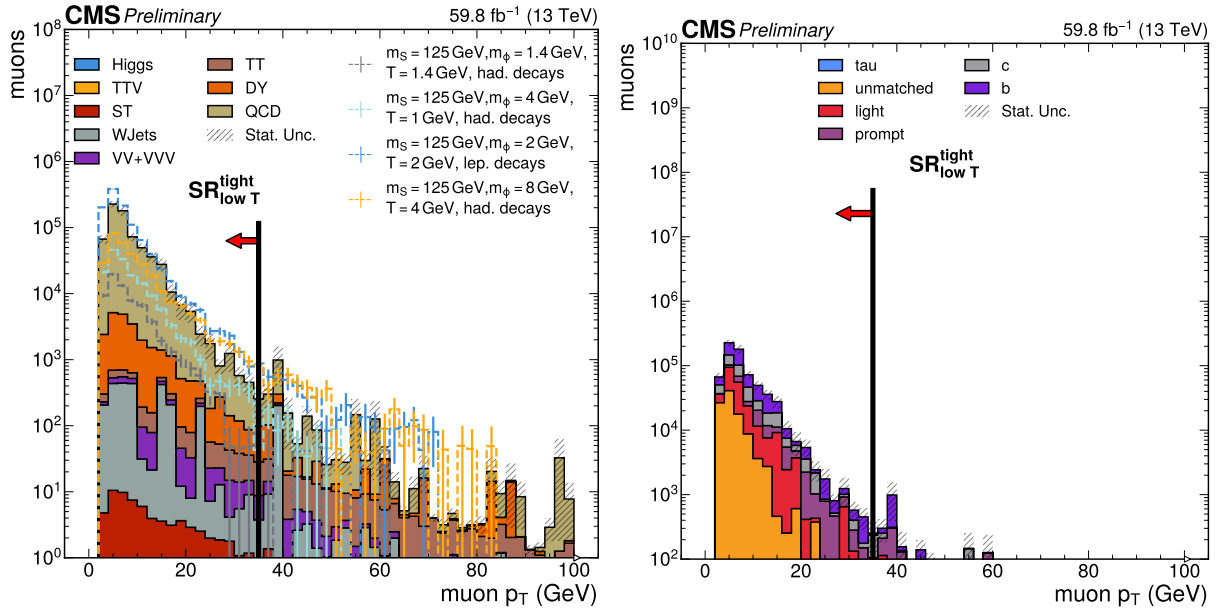


Figure B.12: $N - 1$ plot for $SR_{\text{low } T}^{\text{tight}}$ muon p_T.

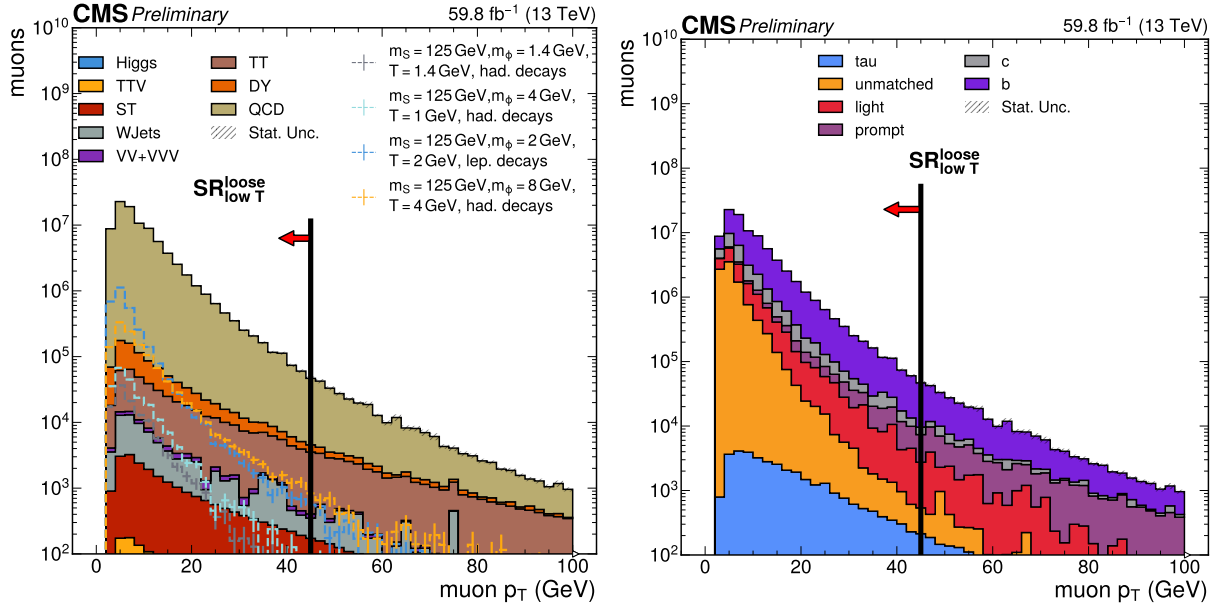


Figure B.13: $N-1$ plot for $SR_{low\ T}^{loose}$ muon p_T .

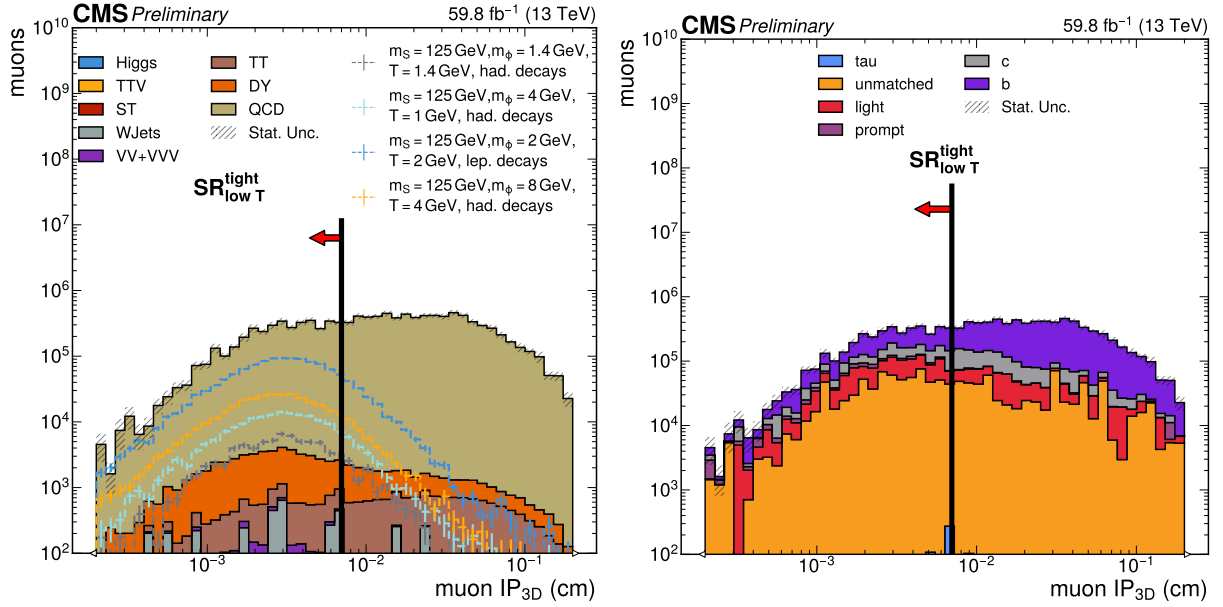


Figure B.14: $N-1$ plot for $SR_{low\ T}^{tight}$ muon ip_{3d} .

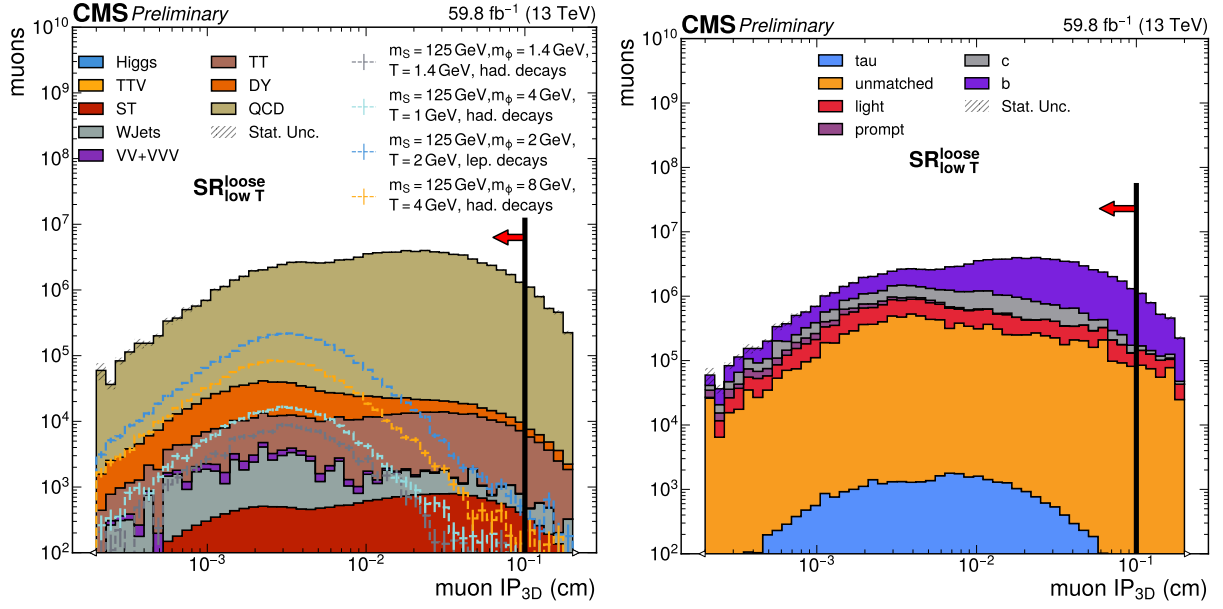


Figure B.15: $N - 1$ plot for $SR_{low\ T}^{loose}$ muon ip_{3d} .

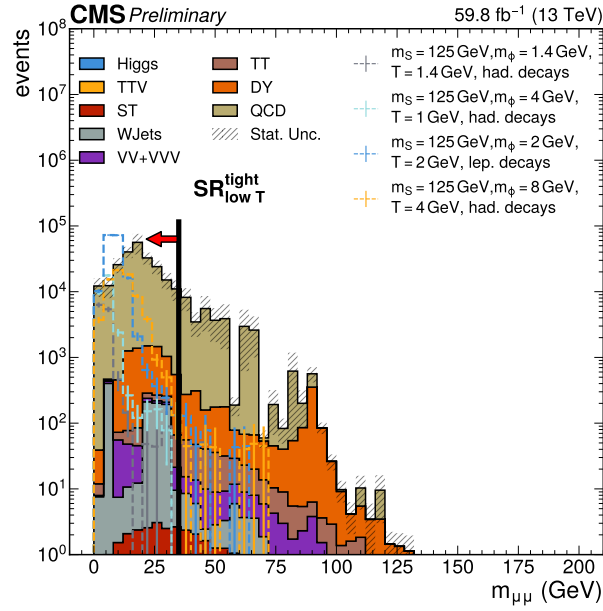


Figure B.16: $N - 1$ plot for $SR_{low\ T}^{tight}$ dimuon mass.

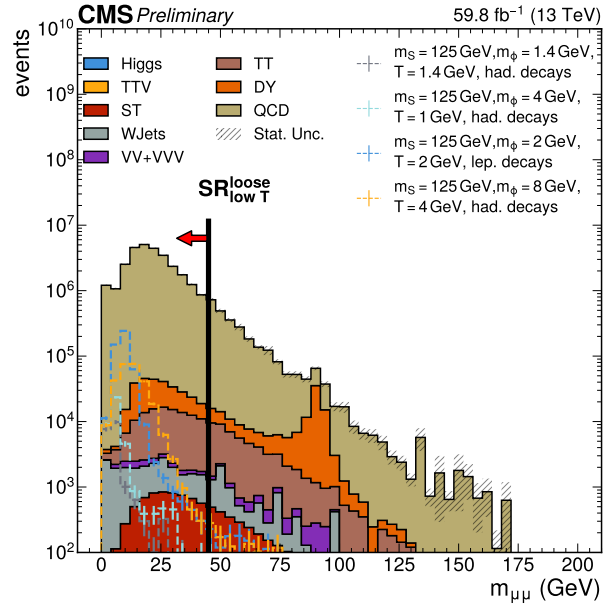


Figure B.17: $N - 1$ plot for SR_{low T}^{loose} dimuon mass.

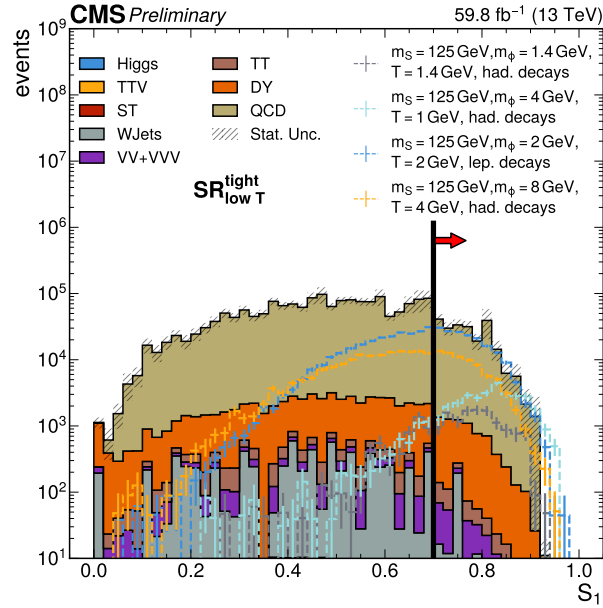


Figure B.18: $N - 1$ plot for SR_{low T}^{tight} sph1.

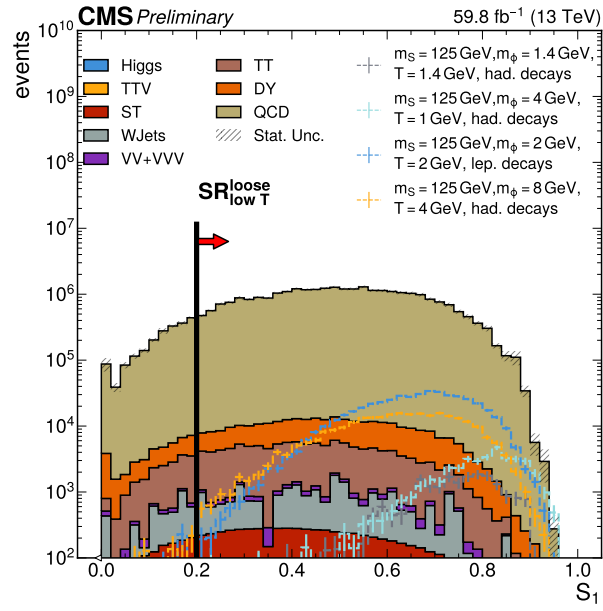


Figure B.19: $N - 1$ plot for $\text{SR}_{\text{low } T}^{\text{loose sph1}}$.

B.4 $N - 1$ plots for $SR_{\text{high } T}$

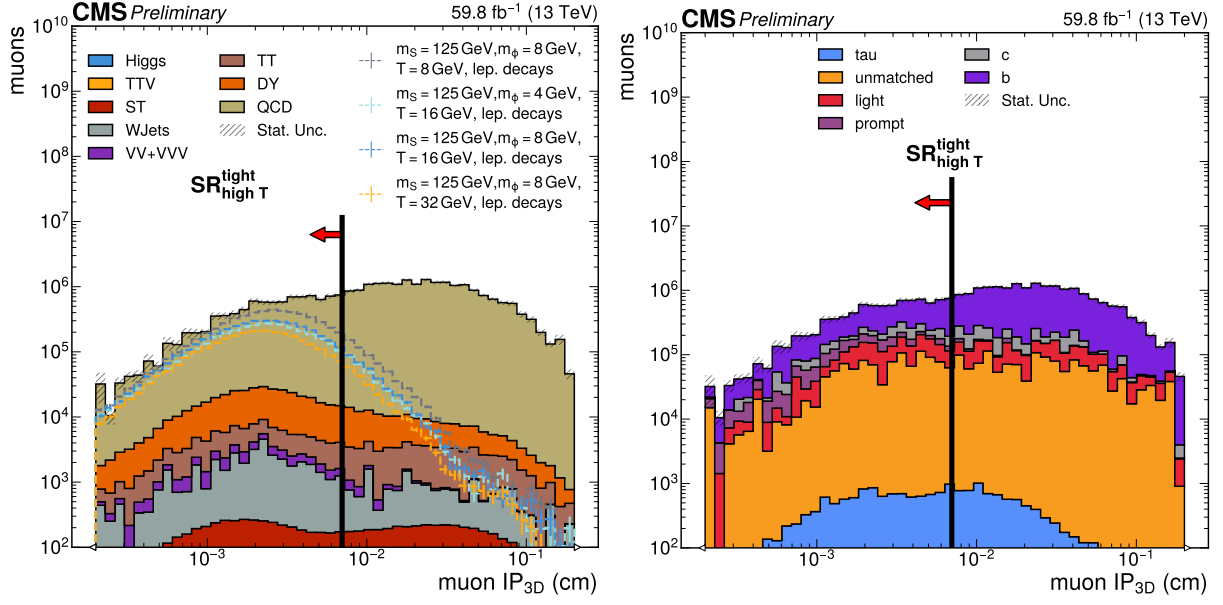


Figure B.20: $N - 1$ plot for $SR_{\text{high } T}^{\text{tight}}$ muon ip3d.

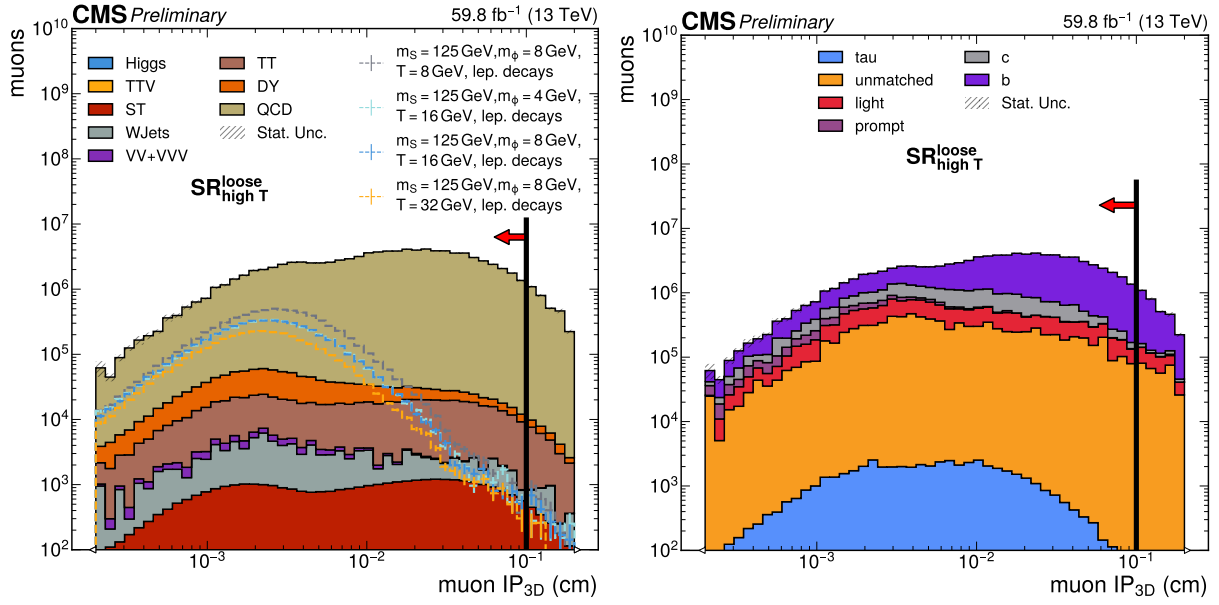


Figure B.21: $N - 1$ plot for $SR_{high\ T}^{loose}$ muon ip3d.

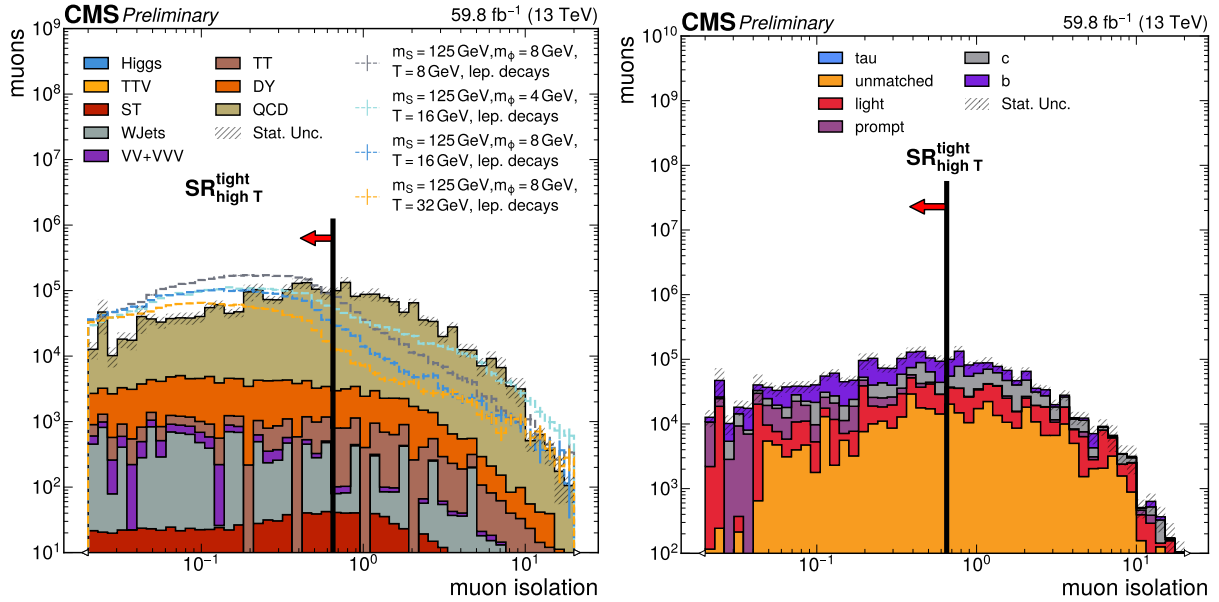


Figure B.22: $N - 1$ plot for $SR_{high\ T}^{tight}$ muon iso.

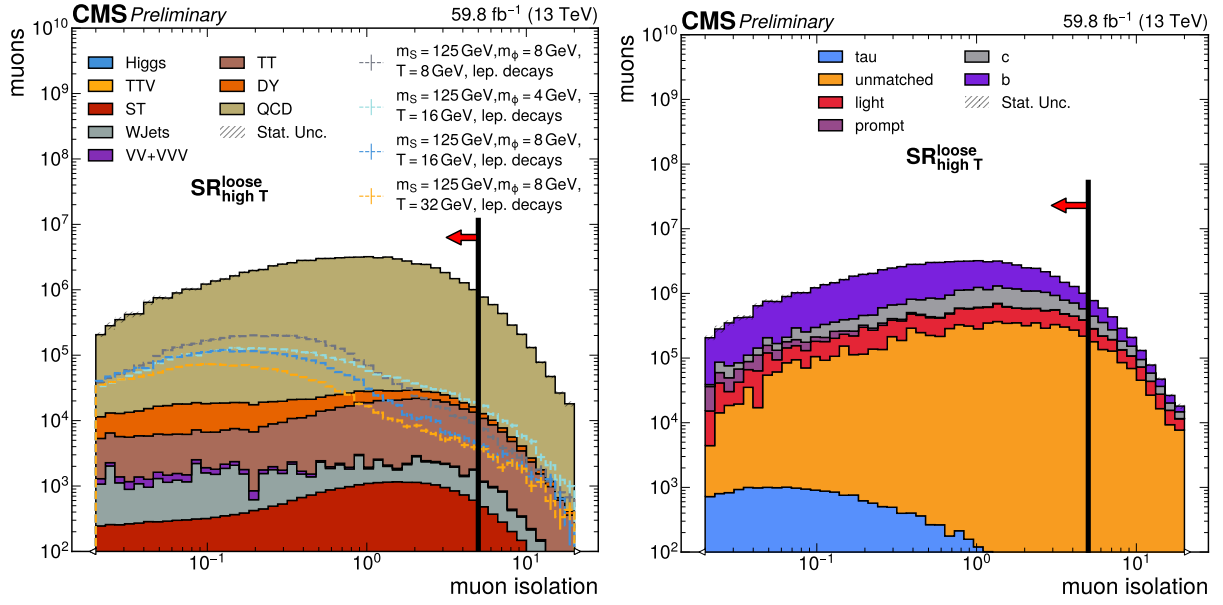


Figure B.23: $N - 1$ plot for $SR_{\text{high } T}^{\text{loose}}$ muon iso.

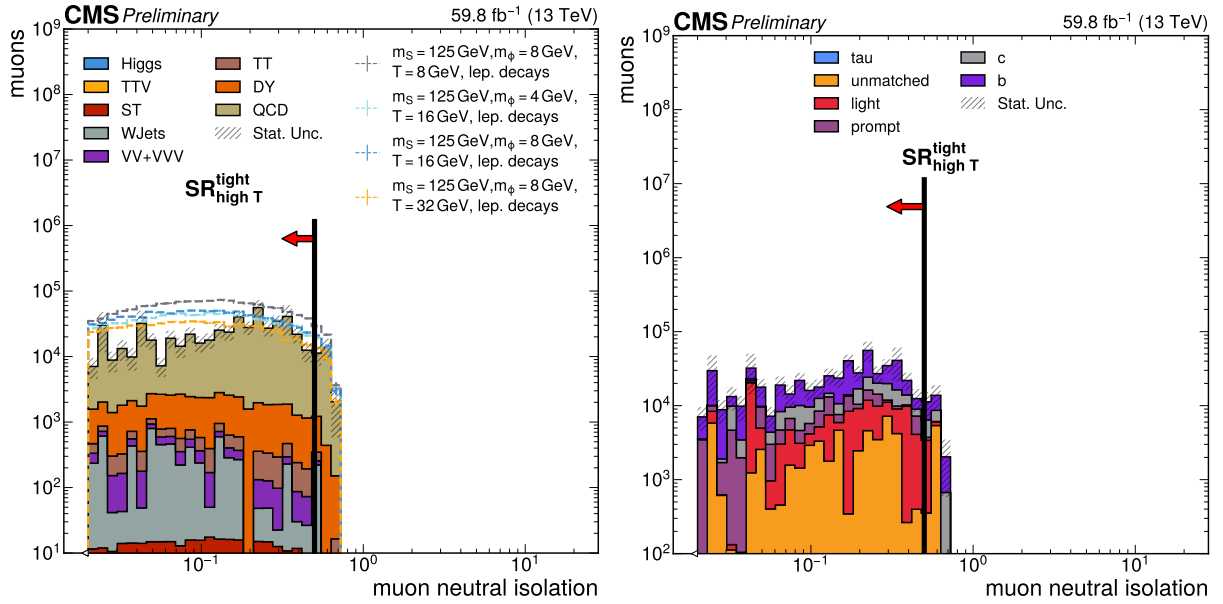


Figure B.24: $N - 1$ plot for $SR_{\text{high } T}^{\text{tight}}$ muon neutral iso.

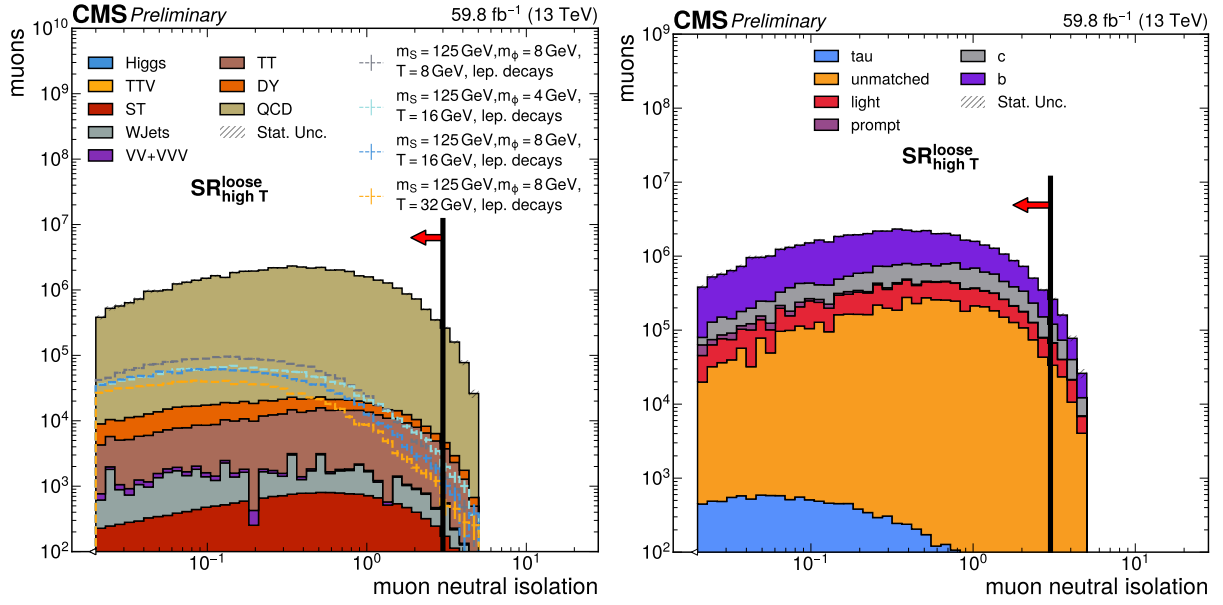


Figure B.25: $N - 1$ plot for $SR_{high\ T}^{loose}$ muon neutral iso.

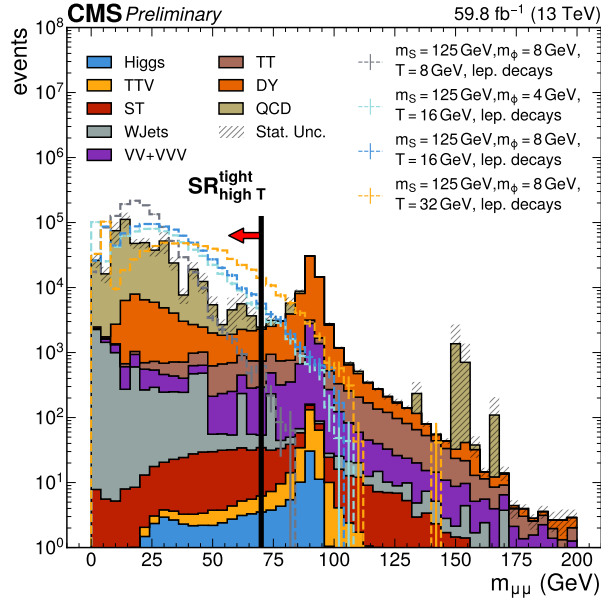


Figure B.26: $N - 1$ plot for $SR_{high\ T}^{tight}$ dimuon mass.

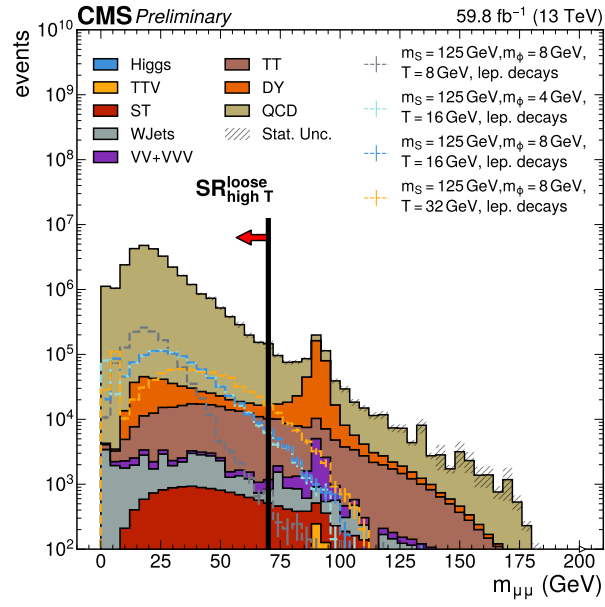


Figure B.27: $N - 1$ plot for $\text{SR}_{\text{high } T}^{\text{loose}}$ dimuon mass.

Chapter C: SR signal yields

The event yields of all signal models in the discovery bins of the two signal regions are presented in Table C.1. The largest event yield for each model is highlighted using bold text. These are used to pick the signal regions for each signal scan point. A small number of points from the very low T models have 0 yields in both SRs. We don't run Combine for these points.

Table C.1: SR signal yields for all years in Run 2 (2016, 2017, and 2018)

SUEP model	SR _{high T}	SR _{low T}
$m_S = 125, m_\phi = 1, T = 0.25$, leptonic	0 ± 0	177 ± 97
$m_S = 200, m_\phi = 1, T = 0.25$, leptonic	0 ± 0	16 ± 16
$m_S = 300, m_\phi = 1, T = 0.25$, leptonic	0 ± 0	0 ± 0
$m_S = 400, m_\phi = 1, T = 0.25$, leptonic	0 ± 0	0 ± 0
$m_S = 500, m_\phi = 1, T = 0.25$, leptonic	0 ± 0	0 ± 0
$m_S = 600, m_\phi = 1, T = 0.25$, leptonic	0 ± 0	0 ± 0
$m_S = 1000, m_\phi = 1, T = 0.25$, leptonic	0 ± 0	0 ± 0
$m_S = 125, m_\phi = 1.4, T = 0.35$, hadronic	0 ± 0	496 ± 133
$m_S = 200, m_\phi = 1.4, T = 0.35$, hadronic	0 ± 0	12 ± 12
$m_S = 300, m_\phi = 1.4, T = 0.35$, hadronic	0 ± 0	5.1 ± 5.1
$m_S = 400, m_\phi = 1.4, T = 0.35$, hadronic	0 ± 0	2.3 ± 2.2
$m_S = 500, m_\phi = 1.4, T = 0.35$, hadronic	0 ± 0	0 ± 0
$m_S = 600, m_\phi = 1.4, T = 0.35$, hadronic	0 ± 0	0.027 ± 0.027
$m_S = 800, m_\phi = 1.4, T = 0.35$, hadronic	0 ± 0	0 ± 0
$m_S = 1000, m_\phi = 1.4, T = 0.35$, hadronic	0 ± 0	0 ± 0
$m_S = 125, m_\phi = 1.4, T = 1.4$, hadronic	0 ± 0	3984 ± 409
$m_S = 200, m_\phi = 1.4, T = 1.4$, hadronic	0 ± 0	2731 ± 228

SUEP model	SR _{high T}	SR _{low T}
$m_S = 300, m_\phi = 1.4, T = 1.4, \text{hadronic}$	0 ± 0	1606 \pm 137
$m_S = 400, m_\phi = 1.4, T = 1.4, \text{hadronic}$	0 ± 0	1001 \pm 88
$m_S = 500, m_\phi = 1.4, T = 1.4, \text{hadronic}$	0 ± 0	451 \pm 47
$m_S = 600, m_\phi = 1.4, T = 1.4, \text{hadronic}$	0 ± 0	353 \pm 38
$m_S = 800, m_\phi = 1.4, T = 1.4, \text{hadronic}$	0 ± 0	143 \pm 14
$m_S = 1000, m_\phi = 1.4, T = 1.4, \text{hadronic}$	0 ± 0	66.1 \pm 7.2
$m_S = 125, m_\phi = 1.4, T = 2.8, \text{hadronic}$	32 ± 32	5660 \pm 471
$m_S = 200, m_\phi = 1.4, T = 2.8, \text{hadronic}$	24 ± 24	6922 \pm 391
$m_S = 300, m_\phi = 1.4, T = 2.8, \text{hadronic}$	7.7 ± 7.7	6531 \pm 245
$m_S = 400, m_\phi = 1.4, T = 2.8, \text{hadronic}$	5.7 ± 4.1	6301 \pm 213
$m_S = 500, m_\phi = 1.4, T = 2.8, \text{hadronic}$	11.4 ± 9.0	5778 \pm 206
$m_S = 600, m_\phi = 1.4, T = 2.8, \text{hadronic}$	1.2 ± 1.2	4941 \pm 128
$m_S = 800, m_\phi = 1.4, T = 2.8, \text{hadronic}$	2.0 ± 1.1	3454 \pm 60
$m_S = 1000, m_\phi = 1.4, T = 2.8, \text{hadronic}$	0.20 ± 0.20	2151 \pm 39
$m_S = 125, m_\phi = 1.4, T = 5.6, \text{hadronic}$	388 ± 137	2283 \pm 327
$m_S = 200, m_\phi = 1.4, T = 5.6, \text{hadronic}$	380 ± 82	6154 \pm 350
$m_S = 300, m_\phi = 1.4, T = 5.6, \text{hadronic}$	401 ± 69	11320 \pm 370
$m_S = 400, m_\phi = 1.4, T = 5.6, \text{hadronic}$	350 ± 53	14376 \pm 344
$m_S = 500, m_\phi = 1.4, T = 5.6, \text{hadronic}$	204 ± 28	14522 \pm 245
$m_S = 600, m_\phi = 1.4, T = 5.6, \text{hadronic}$	171 ± 19	12825 \pm 168
$m_S = 800, m_\phi = 1.4, T = 5.6, \text{hadronic}$	93.3 ± 8.8	8280 \pm 85
$m_S = 1000, m_\phi = 1.4, T = 5.6, \text{hadronic}$	43.0 ± 4.2	4609 \pm 46
$m_S = 125, m_\phi = 2, T = 2, \text{leptonic}$	9320 ± 542	85703 \pm 1762
$m_S = 200, m_\phi = 2, T = 2, \text{leptonic}$	13756 ± 423	76317 \pm 1059
$m_S = 300, m_\phi = 2, T = 2, \text{leptonic}$	12263 ± 319	63933 \pm 786
$m_S = 400, m_\phi = 2, T = 2, \text{leptonic}$	8908 ± 209	48301 \pm 530
$m_S = 500, m_\phi = 2, T = 2, \text{leptonic}$	4960 ± 130	34323 \pm 388
$m_S = 600, m_\phi = 2, T = 2, \text{leptonic}$	2942 ± 73	22501 \pm 235
$m_S = 800, m_\phi = 2, T = 2, \text{leptonic}$	822 ± 28	9742 \pm 115
$m_S = 1000, m_\phi = 2, T = 2, \text{leptonic}$	222.2 ± 8.5	4342 \pm 45
$m_S = 125, m_\phi = 2, T = 2, \text{hadronic}$	30 ± 30	6520 \pm 436
$m_S = 200, m_\phi = 2, T = 2, \text{hadronic}$	63 ± 31	6369 \pm 321
$m_S = 300, m_\phi = 2, T = 2, \text{hadronic}$	21 ± 14	5364 \pm 239
$m_S = 400, m_\phi = 2, T = 2, \text{hadronic}$	16.4 ± 7.6	4566 \pm 144
$m_S = 500, m_\phi = 2, T = 2, \text{hadronic}$	24.7 ± 8.8	3547 \pm 112
$m_S = 600, m_\phi = 2, T = 2, \text{hadronic}$	5.0 ± 2.6	3185 \pm 75
$m_S = 800, m_\phi = 2, T = 2, \text{hadronic}$	0.020 ± 0.020	2207 \pm 46
$m_S = 1000, m_\phi = 2, T = 2, \text{hadronic}$	0.007 ± 0.007	1442 \pm 28
$m_S = 125, m_\phi = 2, T = 4, \text{leptonic}$	97827 \pm 1748	81947 \pm 1622
$m_S = 200, m_\phi = 2, T = 4, \text{leptonic}$	154582 \pm 1611	123881 \pm 1460

SUEP model	$SR_{\text{high } T}$	$SR_{\text{low } T}$
$m_S = 300, m_\phi = 2, T = 4, \text{leptonic}$	149356 \pm 1092	113468 \pm 968
$m_S = 400, m_\phi = 2, T = 4, \text{leptonic}$	112584 \pm 819	76730 \pm 691
$m_S = 500, m_\phi = 2, T = 4, \text{leptonic}$	77300 \pm 529	46471 \pm 423
$m_S = 600, m_\phi = 2, T = 4, \text{leptonic}$	51320 \pm 366	27906 \pm 273
$m_S = 800, m_\phi = 2, T = 4, \text{leptonic}$	22901 \pm 150	10890 \pm 112
$m_S = 1000, m_\phi = 2, T = 4, \text{leptonic}$	10408 \pm 77	4737 \pm 54
$m_S = 125, m_\phi = 2, T = 4, \text{hadronic}$	665 \pm 162	3684 \pm 387
$m_S = 200, m_\phi = 2, T = 4, \text{hadronic}$	1122 \pm 146	7995 \pm 390
$m_S = 300, m_\phi = 2, T = 4, \text{hadronic}$	1170 \pm 104	11491 \pm 327
$m_S = 400, m_\phi = 2, T = 4, \text{hadronic}$	1069 \pm 76	13363 \pm 271
$m_S = 500, m_\phi = 2, T = 4, \text{hadronic}$	891 \pm 59	13018 \pm 227
$m_S = 600, m_\phi = 2, T = 4, \text{hadronic}$	486 \pm 36	11452 \pm 183
$m_S = 800, m_\phi = 2, T = 4, \text{hadronic}$	265 \pm 15	7429 \pm 79
$m_S = 1000, m_\phi = 2, T = 4, \text{hadronic}$	91.9 \pm 7.4	4045 \pm 53
$m_S = 125, m_\phi = 2, T = 8, \text{leptonic}$	134896 \pm 2586	30740 \pm 1256
$m_S = 200, m_\phi = 2, T = 8, \text{leptonic}$	212628 \pm 2071	51671 \pm 1022
$m_S = 300, m_\phi = 2, T = 8, \text{leptonic}$	209633 \pm 1503	51679 \pm 754
$m_S = 400, m_\phi = 2, T = 8, \text{leptonic}$	162588 \pm 1046	35276 \pm 494
$m_S = 500, m_\phi = 2, T = 8, \text{leptonic}$	113582 \pm 700	21266 \pm 306
$m_S = 600, m_\phi = 2, T = 8, \text{leptonic}$	76209 \pm 404	11451 \pm 158
$m_S = 800, m_\phi = 2, T = 8, \text{leptonic}$	34399 \pm 185	3370 \pm 59
$m_S = 1000, m_\phi = 2, T = 8, \text{leptonic}$	16237 \pm 90	1022 \pm 23
$m_S = 125, m_\phi = 2, T = 8, \text{hadronic}$	1165 \pm 244	1495 \pm 288
$m_S = 200, m_\phi = 2, T = 8, \text{hadronic}$	1768 \pm 199	3092 \pm 262
$m_S = 300, m_\phi = 2, T = 8, \text{hadronic}$	2508 \pm 162	6329 \pm 260
$m_S = 400, m_\phi = 2, T = 8, \text{hadronic}$	2896 \pm 133	8671 \pm 228
$m_S = 500, m_\phi = 2, T = 8, \text{hadronic}$	2272 \pm 95	8689 \pm 193
$m_S = 600, m_\phi = 2, T = 8, \text{hadronic}$	2177 \pm 72	8348 \pm 140
$m_S = 800, m_\phi = 2, T = 8, \text{hadronic}$	1437 \pm 38	5407 \pm 73
$m_S = 1000, m_\phi = 2, T = 8, \text{hadronic}$	899 \pm 20	3027 \pm 37
$m_S = 125, m_\phi = 4, T = 1.0, \text{leptonic}$	1481 \pm 233	91296 \pm 1896
$m_S = 200, m_\phi = 4, T = 1.0, \text{leptonic}$	853 \pm 97	52034 \pm 837
$m_S = 300, m_\phi = 4, T = 1.0, \text{leptonic}$	680 \pm 74	31236 \pm 582
$m_S = 400, m_\phi = 4, T = 1.0, \text{leptonic}$	490 \pm 42	22676 \pm 325
$m_S = 500, m_\phi = 4, T = 1.0, \text{leptonic}$	254 \pm 25	17422 \pm 252
$m_S = 600, m_\phi = 4, T = 1.0, \text{leptonic}$	139 \pm 14	13370 \pm 164
$m_S = 800, m_\phi = 4, T = 1.0, \text{leptonic}$	41.7 \pm 4.3	8689 \pm 78
$m_S = 1000, m_\phi = 4, T = 1.0, \text{leptonic}$	8.6 \pm 1.5	5385 \pm 51
$m_S = 125, m_\phi = 4, T = 1.0, \text{hadronic}$	0 \pm 0	9058 \pm 565
$m_S = 200, m_\phi = 4, T = 1.0, \text{hadronic}$	0 \pm 0	6809 \pm 292

SUEP model	SR _{high T}	SR _{low T}
$m_S = 300, m_\phi = 4, T = 1.0$, hadronic	3.2 ± 3.2	4065 \pm 171
$m_S = 400, m_\phi = 4, T = 1.0$, hadronic	2.0 ± 2.0	2722 \pm 109
$m_S = 500, m_\phi = 4, T = 1.0$, hadronic	1.3 ± 1.3	2022 \pm 81
$m_S = 600, m_\phi = 4, T = 1.0$, hadronic	1.7 ± 1.7	1444 \pm 51
$m_S = 800, m_\phi = 4, T = 1.0$, hadronic	0 ± 0	945 \pm 25
$m_S = 1000, m_\phi = 4, T = 1.0$, hadronic	0 ± 0	682 \pm 16
$m_S = 125, m_\phi = 4, T = 4$, leptonic	171631 \pm 2627	102768 \pm 2048
$m_S = 200, m_\phi = 4, T = 4$, leptonic	264953 \pm 2275	161496 \pm 1801
$m_S = 300, m_\phi = 4, T = 4$, leptonic	242496 \pm 1575	139524 \pm 1221
$m_S = 400, m_\phi = 4, T = 4$, leptonic	172260 \pm 904	90995 \pm 674
$m_S = 500, m_\phi = 4, T = 4$, leptonic	112459 \pm 640	54860 \pm 452
$m_S = 600, m_\phi = 4, T = 4$, leptonic	73571 \pm 385	32813 \pm 265
$m_S = 800, m_\phi = 4, T = 4$, leptonic	32219 \pm 203	12767 \pm 135
$m_S = 1000, m_\phi = 4, T = 4$, leptonic	15087 \pm 84	5472 \pm 56
$m_S = 125, m_\phi = 4, T = 4$, hadronic	1913 \pm 270	3953 \pm 409
$m_S = 200, m_\phi = 4, T = 4$, hadronic	4842 \pm 300	9085 \pm 418
$m_S = 300, m_\phi = 4, T = 4$, hadronic	6896 \pm 272	14110 \pm 394
$m_S = 400, m_\phi = 4, T = 4$, hadronic	6778 \pm 173	17236 \pm 279
$m_S = 500, m_\phi = 4, T = 4$, hadronic	5640 \pm 141	17712 \pm 252
$m_S = 600, m_\phi = 4, T = 4$, hadronic	4135 \pm 87	14906 \pm 167
$m_S = 800, m_\phi = 4, T = 4$, hadronic	2077 \pm 55	9423 \pm 118
$m_S = 1000, m_\phi = 4, T = 4$, hadronic	893 \pm 20	5227 \pm 50
$m_S = 125, m_\phi = 4, T = 8$, leptonic	202152 \pm 2736	36186 \pm 1163
$m_S = 200, m_\phi = 4, T = 8$, leptonic	328813 \pm 2601	63971 \pm 1159
$m_S = 300, m_\phi = 4, T = 8$, leptonic	302089 \pm 1755	55421 \pm 760
$m_S = 400, m_\phi = 4, T = 8$, leptonic	215858 \pm 1147	36589 \pm 475
$m_S = 500, m_\phi = 4, T = 8$, leptonic	137769 \pm 819	20210 \pm 315
$m_S = 600, m_\phi = 4, T = 8$, leptonic	87704 \pm 443	10930 \pm 157
$m_S = 800, m_\phi = 4, T = 8$, leptonic	36707 \pm 217	3047 \pm 63
$m_S = 1000, m_\phi = 4, T = 8$, leptonic	16515 \pm 87	832 \pm 20
$m_S = 125, m_\phi = 4, T = 8$, hadronic	3294 \pm 409	939 \pm 223
$m_S = 200, m_\phi = 4, T = 8$, hadronic	7918 \pm 396	3446 \pm 267
$m_S = 300, m_\phi = 4, T = 8$, hadronic	11391 \pm 317	5961 \pm 232
$m_S = 400, m_\phi = 4, T = 8$, hadronic	12682 \pm 306	7661 \pm 237
$m_S = 500, m_\phi = 4, T = 8$, hadronic	11511 \pm 239	8155 \pm 202
$m_S = 600, m_\phi = 4, T = 8$, hadronic	9642 \pm 163	7211 \pm 142
$m_S = 800, m_\phi = 4, T = 8$, hadronic	6395 \pm 84	4869 \pm 74
$m_S = 1000, m_\phi = 4, T = 8$, hadronic	3880 \pm 43	2698 \pm 36
$m_S = 125, m_\phi = 4, T = 16$, leptonic	90738 \pm 1928	5382 \pm 464
$m_S = 200, m_\phi = 4, T = 16$, leptonic	149490 \pm 1867	7099 \pm 407

SUEP model	SR _{high T}	SR _{low T}
$m_S = 300, m_\phi = 4, T = 16$, leptonic	149775 \pm 1272	5794 \pm 252
$m_S = 400, m_\phi = 4, T = 16$, leptonic	118430 \pm 910	3729 \pm 166
$m_S = 500, m_\phi = 4, T = 16$, leptonic	81548 \pm 606	2061 \pm 96
$m_S = 600, m_\phi = 4, T = 16$, leptonic	54351 \pm 360	1109 \pm 51
$m_S = 800, m_\phi = 4, T = 16$, leptonic	22354 \pm 162	242 \pm 17
$m_S = 1000, m_\phi = 4, T = 16$, leptonic	9037 \pm 63	49.4 \pm 4.7
$m_S = 125, m_\phi = 4, T = 16$, hadronic	1585 \pm 278	32 \pm 32
$m_S = 200, m_\phi = 4, T = 16$, hadronic	2845 \pm 236	327 \pm 76
$m_S = 300, m_\phi = 4, T = 16$, hadronic	3499 \pm 195	549 \pm 77
$m_S = 400, m_\phi = 4, T = 16$, hadronic	4229 \pm 148	691 \pm 61
$m_S = 500, m_\phi = 4, T = 16$, hadronic	4266 \pm 169	793 \pm 75
$m_S = 600, m_\phi = 4, T = 16$, hadronic	3684 \pm 87	682 \pm 37
$m_S = 800, m_\phi = 4, T = 16$, hadronic	2779 \pm 48	553 \pm 22
$m_S = 1000, m_\phi = 4, T = 16$, hadronic	1914 \pm 30	314 \pm 12
$m_S = 125, m_\phi = 6, T = 3.0$, leptonic	145539 \pm 2347	147080 \pm 2383
$m_S = 200, m_\phi = 6, T = 3.0$, leptonic	218966 \pm 1917	210201 \pm 1903
$m_S = 300, m_\phi = 6, T = 3.0$, leptonic	204841 \pm 1368	177012 \pm 1292
$m_S = 400, m_\phi = 6, T = 3.0$, leptonic	148040 \pm 988	114787 \pm 894
$m_S = 500, m_\phi = 6, T = 3.0$, leptonic	98308 \pm 632	69013 \pm 556
$m_S = 600, m_\phi = 6, T = 3.0$, leptonic	64576 \pm 496	41710 \pm 414
$m_S = 800, m_\phi = 6, T = 3.0$, leptonic	28561 \pm 189	17018 \pm 157
$m_S = 1000, m_\phi = 6, T = 3.0$, leptonic	13395 \pm 88	7789 \pm 76
$m_S = 125, m_\phi = 6, T = 3.0$, hadronic	1672 \pm 286	7385 \pm 616
$m_S = 200, m_\phi = 6, T = 3.0$, hadronic	4174 \pm 310	12149 \pm 530
$m_S = 300, m_\phi = 6, T = 3.0$, hadronic	5453 \pm 228	18970 \pm 429
$m_S = 400, m_\phi = 6, T = 3.0$, hadronic	5562 \pm 203	20955 \pm 388
$m_S = 500, m_\phi = 6, T = 3.0$, hadronic	4456 \pm 141	21089 \pm 308
$m_S = 600, m_\phi = 6, T = 3.0$, hadronic	3148 \pm 90	17878 \pm 222
$m_S = 800, m_\phi = 6, T = 3.0$, hadronic	1460 \pm 40	11714 \pm 115
$m_S = 1000, m_\phi = 6, T = 3.0$, hadronic	659 \pm 18	6792 \pm 61
$m_S = 125, m_\phi = 6, T = 6$, leptonic	237637 \pm 3002	75519 \pm 1706
$m_S = 200, m_\phi = 6, T = 6$, leptonic	377047 \pm 2693	124270 \pm 1553
$m_S = 300, m_\phi = 6, T = 6$, leptonic	334289 \pm 2083	111189 \pm 1215
$m_S = 400, m_\phi = 6, T = 6$, leptonic	230468 \pm 1199	72353 \pm 685
$m_S = 500, m_\phi = 6, T = 6$, leptonic	143983 \pm 792	40428 \pm 426
$m_S = 600, m_\phi = 6, T = 6$, leptonic	90048 \pm 480	22951 \pm 247
$m_S = 800, m_\phi = 6, T = 6$, leptonic	37631 \pm 240	7425 \pm 111
$m_S = 1000, m_\phi = 6, T = 6$, leptonic	17131 \pm 99	2567 \pm 39
$m_S = 125, m_\phi = 6, T = 6$, hadronic	4049 \pm 397	2025 \pm 293
$m_S = 200, m_\phi = 6, T = 6$, hadronic	9585 \pm 443	6584 \pm 368

SUEP model	SR _{high T}	SR _{low T}
$m_S = 300, m_\phi = 6, T = 6$, hadronic	14588 ± 413	10932 ± 361
$m_S = 400, m_\phi = 6, T = 6$, hadronic	16102 ± 302	14829 ± 293
$m_S = 500, m_\phi = 6, T = 6$, hadronic	15141 ± 292	15143 ± 292
$m_S = 600, m_\phi = 6, T = 6$, hadronic	11990 ± 159	13202 ± 168
$m_S = 800, m_\phi = 6, T = 6$, hadronic	7201 ± 94	8572 ± 105
$m_S = 1000, m_\phi = 6, T = 6$, hadronic	4003 ± 44	4612 ± 47
$m_S = 125, m_\phi = 6, T = 12$, leptonic	149884 ± 2459	16798 ± 832
$m_S = 200, m_\phi = 6, T = 12$, leptonic	259213 ± 2362	23029 ± 706
$m_S = 300, m_\phi = 6, T = 12$, leptonic	255592 ± 1592	19774 ± 448
$m_S = 400, m_\phi = 6, T = 12$, leptonic	188501 ± 1139	12238 ± 291
$m_S = 500, m_\phi = 6, T = 12$, leptonic	124264 ± 748	6555 ± 172
$m_S = 600, m_\phi = 6, T = 12$, leptonic	78456 ± 490	3235 ± 100
$m_S = 800, m_\phi = 6, T = 12$, leptonic	31729 ± 182	714 ± 27
$m_S = 1000, m_\phi = 6, T = 12$, leptonic	13394 ± 89	125.1 ± 8.7
$m_S = 125, m_\phi = 6, T = 12$, hadronic	2947 ± 367	281 ± 124
$m_S = 200, m_\phi = 6, T = 12$, hadronic	7635 ± 387	936 ± 133
$m_S = 300, m_\phi = 6, T = 12$, hadronic	11465 ± 339	2276 ± 153
$m_S = 400, m_\phi = 6, T = 12$, hadronic	11787 ± 274	2334 ± 124
$m_S = 500, m_\phi = 6, T = 12$, hadronic	12038 ± 218	2415 ± 98
$m_S = 600, m_\phi = 6, T = 12$, hadronic	10438 ± 160	2296 ± 76
$m_S = 800, m_\phi = 6, T = 12$, hadronic	7336 ± 82	1673 ± 39
$m_S = 1000, m_\phi = 6, T = 12$, hadronic	4756 ± 49	902 ± 21
$m_S = 125, m_\phi = 6, T = 24$, leptonic	52490 ± 1575	1583 ± 267
$m_S = 200, m_\phi = 6, T = 24$, leptonic	81537 ± 1216	1799 ± 182
$m_S = 300, m_\phi = 6, T = 24$, leptonic	78391 ± 911	1242 ± 116
$m_S = 400, m_\phi = 6, T = 24$, leptonic	59986 ± 630	801 ± 72
$m_S = 500, m_\phi = 6, T = 24$, leptonic	41089 ± 360	498 ± 39
$m_S = 600, m_\phi = 6, T = 24$, leptonic	26458 ± 266	259 ± 26
$m_S = 800, m_\phi = 6, T = 24$, leptonic	10188 ± 99	89.1 ± 9.0
$m_S = 1000, m_\phi = 6, T = 24$, leptonic	3734 ± 46	15.7 ± 2.9
$m_S = 125, m_\phi = 6, T = 24$, hadronic	915 ± 196	66 ± 66
$m_S = 200, m_\phi = 6, T = 24$, hadronic	1771 ± 214	52 ± 38
$m_S = 300, m_\phi = 6, T = 24$, hadronic	2268 ± 152	140 ± 39
$m_S = 400, m_\phi = 6, T = 24$, hadronic	2349 ± 119	76 ± 22
$m_S = 500, m_\phi = 6, T = 24$, hadronic	2140 ± 92	85 ± 19
$m_S = 600, m_\phi = 6, T = 24$, hadronic	1943 ± 73	123 ± 20
$m_S = 800, m_\phi = 6, T = 24$, hadronic	1475 ± 40	74.5 ± 8.8
$m_S = 1000, m_\phi = 6, T = 24$, hadronic	960 ± 21	47.2 ± 4.7
$m_S = 125, m_\phi = 8, T = 2.0$, leptonic	119966 ± 2073	194067 ± 2672
$m_S = 200, m_\phi = 8, T = 2.0$, leptonic	158352 ± 1766	223890 ± 2146

SUEP model	SR _{high T}	SR _{low T}
$m_S = 300, m_\phi = 8, T = 2.0$, leptonic	150184 ± 1197	191391 \pm 1397
$m_S = 400, m_\phi = 8, T = 2.0$, leptonic	114370 ± 791	128927 \pm 878
$m_S = 500, m_\phi = 8, T = 2.0$, leptonic	75728 ± 505	77857 \pm 539
$m_S = 600, m_\phi = 8, T = 2.0$, leptonic	49966 \pm 312	48798 ± 331
$m_S = 800, m_\phi = 8, T = 2.0$, leptonic	22307 \pm 140	20782 ± 155
$m_S = 1000, m_\phi = 8, T = 2.0$, leptonic	10235 \pm 72	10040 ± 87
$m_S = 125, m_\phi = 8, T = 2.0$, hadronic	1407 ± 226	9683 \pm 595
$m_S = 200, m_\phi = 8, T = 2.0$, hadronic	2409 ± 217	14548 \pm 546
$m_S = 300, m_\phi = 8, T = 2.0$, hadronic	3060 ± 159	19332 \pm 406
$m_S = 400, m_\phi = 8, T = 2.0$, hadronic	3421 ± 112	22217 \pm 288
$m_S = 500, m_\phi = 8, T = 2.0$, hadronic	2685 ± 89	21893 \pm 259
$m_S = 600, m_\phi = 8, T = 2.0$, hadronic	1888 ± 75	19641 \pm 245
$m_S = 800, m_\phi = 8, T = 2.0$, hadronic	924 ± 28	13325 \pm 108
$m_S = 1000, m_\phi = 8, T = 2.0$, hadronic	354 ± 11	8079 \pm 57
$m_S = 125, m_\phi = 8, T = 4.0$, leptonic	233122 \pm 2837	136912 ± 2189
$m_S = 200, m_\phi = 8, T = 4.0$, leptonic	353052 \pm 2545	214422 ± 2005
$m_S = 300, m_\phi = 8, T = 4.0$, leptonic	311584 \pm 1498	180067 ± 1146
$m_S = 400, m_\phi = 8, T = 4.0$, leptonic	213570 \pm 1052	114043 ± 780
$m_S = 500, m_\phi = 8, T = 4.0$, leptonic	135724 \pm 624	65976 ± 445
$m_S = 600, m_\phi = 8, T = 4.0$, leptonic	86054 \pm 434	39629 ± 306
$m_S = 800, m_\phi = 8, T = 4.0$, leptonic	36839 \pm 175	15413 ± 116
$m_S = 1000, m_\phi = 8, T = 4.0$, leptonic	17178 \pm 108	6529 ± 68
$m_S = 125, m_\phi = 8, T = 4.0$, hadronic	3448 ± 374	4441 \pm 418
$m_S = 200, m_\phi = 8, T = 4.0$, hadronic	8829 ± 382	11176 \pm 434
$m_S = 300, m_\phi = 8, T = 4.0$, hadronic	12240 ± 375	19915 \pm 484
$m_S = 400, m_\phi = 8, T = 4.0$, hadronic	13078 ± 252	23813 \pm 344
$m_S = 500, m_\phi = 8, T = 4.0$, hadronic	11440 ± 204	24191 \pm 298
$m_S = 600, m_\phi = 8, T = 4.0$, hadronic	9002 ± 144	20345 \pm 217
$m_S = 800, m_\phi = 8, T = 4.0$, hadronic	5238 ± 66	12763 \pm 105
$m_S = 1000, m_\phi = 8, T = 4.0$, hadronic	2744 ± 35	7193 \pm 59
$m_S = 125, m_\phi = 8, T = 8$, leptonic	226495 \pm 3103	51739 ± 1482
$m_S = 200, m_\phi = 8, T = 8$, leptonic	369591 \pm 2891	81278 ± 1360
$m_S = 300, m_\phi = 8, T = 8$, leptonic	332955 \pm 2027	70553 ± 938
$m_S = 400, m_\phi = 8, T = 8$, leptonic	232641 \pm 1129	43699 ± 491
$m_S = 500, m_\phi = 8, T = 8$, leptonic	145744 \pm 767	23641 ± 313
$m_S = 600, m_\phi = 8, T = 8$, leptonic	90523 \pm 508	12047 ± 187
$m_S = 800, m_\phi = 8, T = 8$, leptonic	36861 \pm 185	3092 ± 54
$m_S = 1000, m_\phi = 8, T = 8$, leptonic	16392 \pm 80	854 ± 18
$m_S = 125, m_\phi = 8, T = 8$, hadronic	4809 \pm 441	1307 ± 234
$m_S = 200, m_\phi = 8, T = 8$, hadronic	11378 \pm 461	4089 ± 278

SUEP model	$SR_{\text{high } T}$	$SR_{\text{low } T}$
$m_S = 300, m_\phi = 8, T = 8, \text{hadronic}$	17419 ± 486	6947 ± 313
$m_S = 400, m_\phi = 8, T = 8, \text{hadronic}$	18388 ± 302	9216 ± 214
$m_S = 500, m_\phi = 8, T = 8, \text{hadronic}$	17124 ± 276	9097 ± 200
$m_S = 600, m_\phi = 8, T = 8, \text{hadronic}$	15311 ± 192	8397 ± 143
$m_S = 800, m_\phi = 8, T = 8, \text{hadronic}$	9652 ± 97	5399 ± 73
$m_S = 1000, m_\phi = 8, T = 8, \text{hadronic}$	5807 ± 54	2945 ± 39
$m_S = 125, m_\phi = 8, T = 16, \text{leptonic}$	106404 ± 2269	8638 ± 644
$m_S = 200, m_\phi = 8, T = 16, \text{leptonic}$	185391 ± 1979	9895 ± 458
$m_S = 300, m_\phi = 8, T = 16, \text{leptonic}$	191416 ± 1391	7184 ± 269
$m_S = 400, m_\phi = 8, T = 16, \text{leptonic}$	144488 ± 1156	4772 ± 213
$m_S = 500, m_\phi = 8, T = 16, \text{leptonic}$	95861 ± 630	2754 ± 107
$m_S = 600, m_\phi = 8, T = 16, \text{leptonic}$	60396 ± 432	1288 ± 64
$m_S = 800, m_\phi = 8, T = 16, \text{leptonic}$	23154 ± 151	266 ± 16
$m_S = 1000, m_\phi = 8, T = 16, \text{leptonic}$	9013 ± 76	50.0 ± 5.8
$m_S = 125, m_\phi = 8, T = 16, \text{hadronic}$	2075 ± 294	110 ± 63
$m_S = 200, m_\phi = 8, T = 16, \text{hadronic}$	5128 ± 316	375 ± 86
$m_S = 300, m_\phi = 8, T = 16, \text{hadronic}$	8109 ± 284	636 ± 84
$m_S = 400, m_\phi = 8, T = 16, \text{hadronic}$	9073 ± 241	881 ± 75
$m_S = 500, m_\phi = 8, T = 16, \text{hadronic}$	8744 ± 165	655 ± 45
$m_S = 600, m_\phi = 8, T = 16, \text{hadronic}$	8237 ± 140	782 ± 43
$m_S = 800, m_\phi = 8, T = 16, \text{hadronic}$	5829 ± 76	522 ± 23
$m_S = 1000, m_\phi = 8, T = 16, \text{hadronic}$	3764 ± 37	342 ± 11
$m_S = 125, m_\phi = 8, T = 32, \text{leptonic}$	35486 ± 1147	742 ± 164
$m_S = 200, m_\phi = 8, T = 32, \text{leptonic}$	45120 ± 913	573 ± 104
$m_S = 300, m_\phi = 8, T = 32, \text{leptonic}$	39739 ± 673	473 ± 75
$m_S = 400, m_\phi = 8, T = 32, \text{leptonic}$	30297 ± 492	311 ± 51
$m_S = 500, m_\phi = 8, T = 32, \text{leptonic}$	21128 ± 303	156 ± 26
$m_S = 600, m_\phi = 8, T = 32, \text{leptonic}$	13768 ± 181	96 ± 15
$m_S = 800, m_\phi = 8, T = 32, \text{leptonic}$	5392 ± 82	34.9 ± 6.7
$m_S = 1000, m_\phi = 8, T = 32, \text{leptonic}$	1996 ± 33	8.3 ± 2.4
$m_S = 125, m_\phi = 8, T = 32, \text{hadronic}$	506 ± 148	0 ± 0
$m_S = 200, m_\phi = 8, T = 32, \text{hadronic}$	1132 ± 160	0 ± 0
$m_S = 300, m_\phi = 8, T = 32, \text{hadronic}$	1215 ± 124	0 ± 0
$m_S = 400, m_\phi = 8, T = 32, \text{hadronic}$	1428 ± 98	12.3 ± 9.2
$m_S = 500, m_\phi = 8, T = 32, \text{hadronic}$	1231 ± 75	0 ± 0
$m_S = 600, m_\phi = 8, T = 32, \text{hadronic}$	1014 ± 43	17.1 ± 5.5
$m_S = 800, m_\phi = 8, T = 32, \text{hadronic}$	707 ± 27	13.1 ± 3.7
$m_S = 1000, m_\phi = 8, T = 32, \text{hadronic}$	462 ± 15	9.7 ± 2.2

Chapter D: Limits

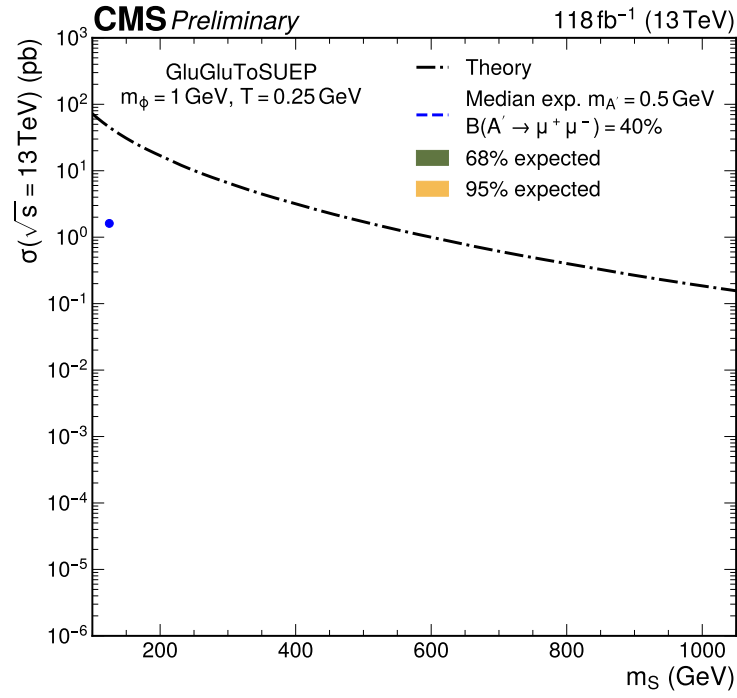


Figure D.1: 1D limit for $m_\phi = 1 \text{ GeV}$, $T = 0.25 \text{ GeV}$ (both decay modes) as a function of m_S .

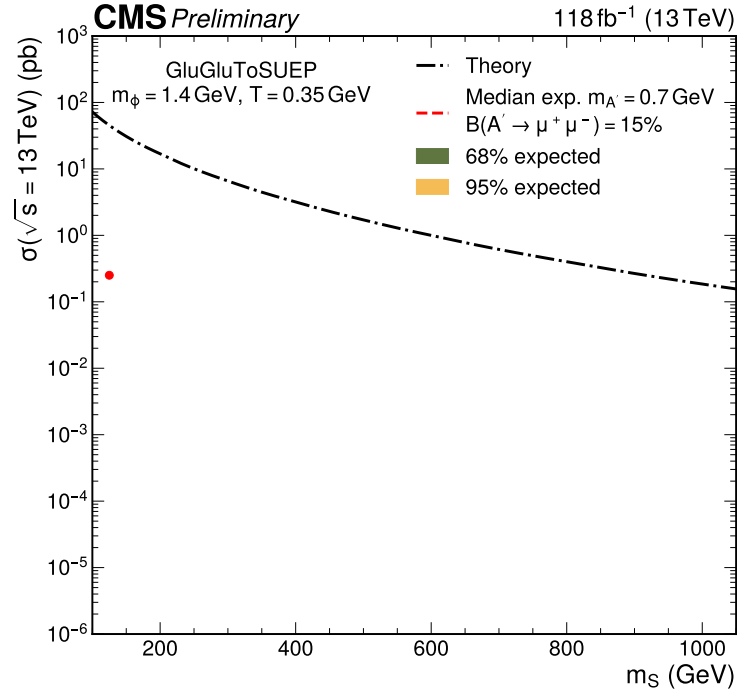


Figure D.2: 1D limit for $m_\phi = 1.4$ GeV, $T = 0.35$ GeV (both decay modes) as a function of m_S .

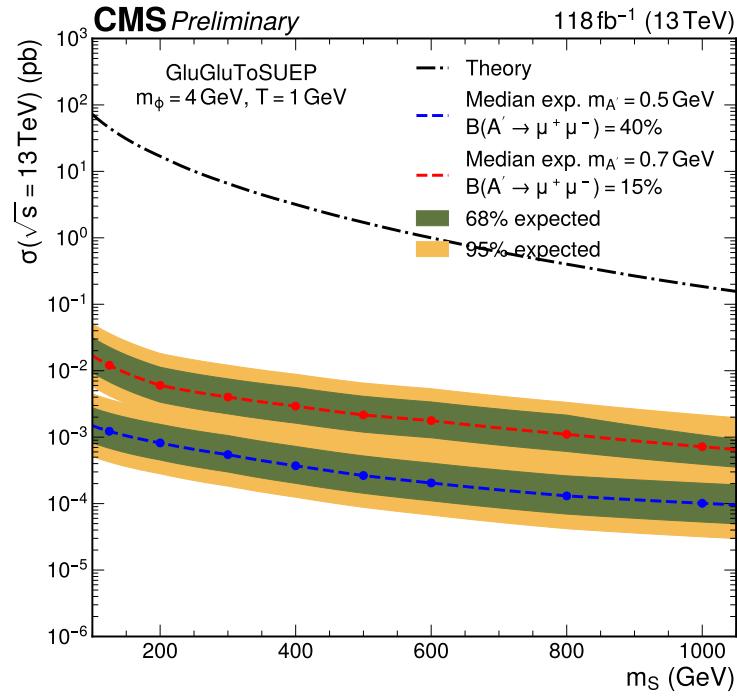


Figure D.3: 1D limit for $m_\phi = 4$ GeV, $T = 1$ GeV (both decay modes) as a function of m_S .

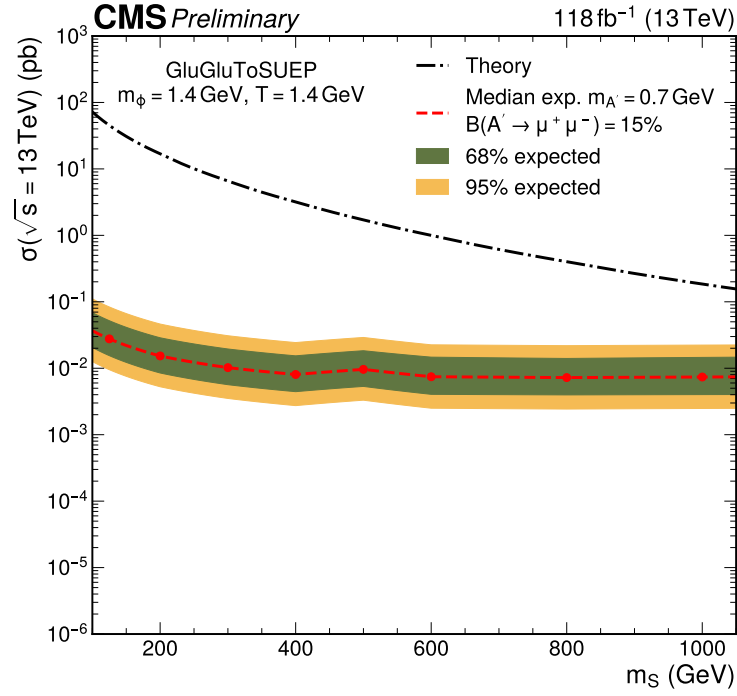


Figure D.4: 1D limit for $m_\phi = 1.4 \text{ GeV}$, $T = 1.4 \text{ GeV}$ (both decay modes) as a function of m_S .

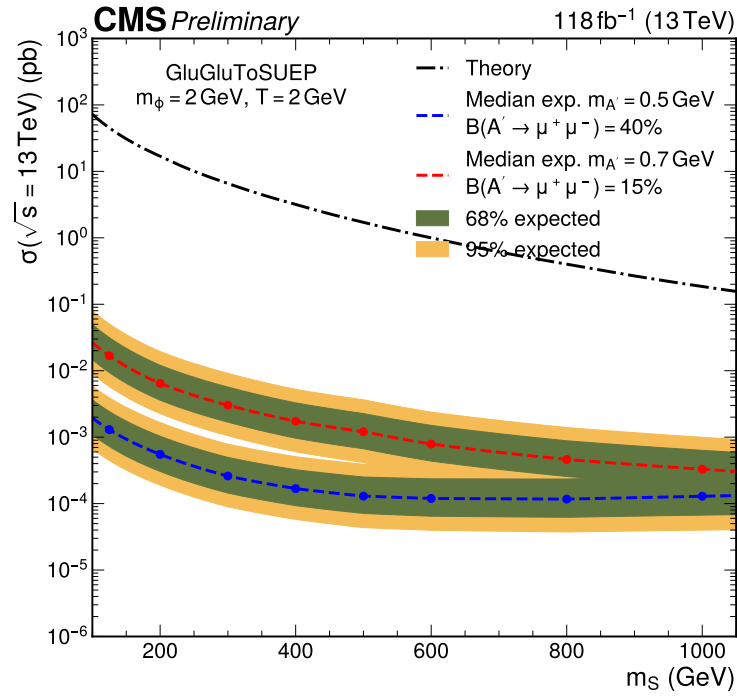


Figure D.5: 1D limit for $m_\phi = 2 \text{ GeV}$, $T = 2 \text{ GeV}$ (both decay modes) as a function of m_S .

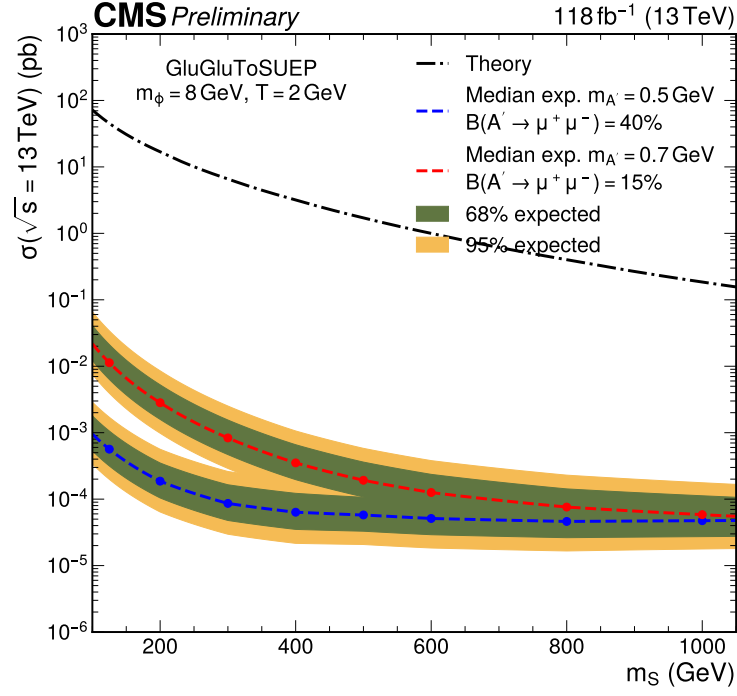


Figure D.6: 1D limit for $m_\phi = 8 \text{ GeV}, T = 2 \text{ GeV}$ (both decay modes) as a function of m_S .

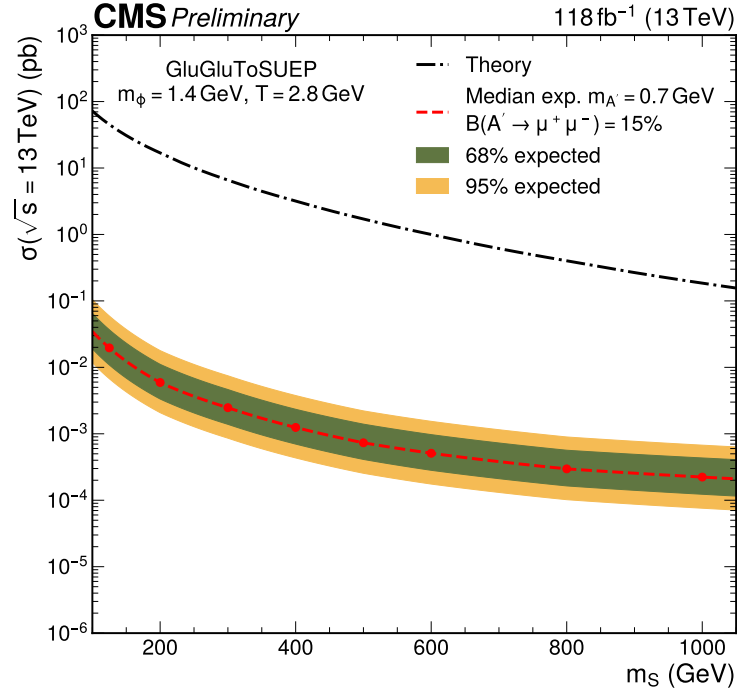


Figure D.7: 1D limit for $m_\phi = 1.4 \text{ GeV}, T = 2.8 \text{ GeV}$ (both decay modes) as a function of m_S .

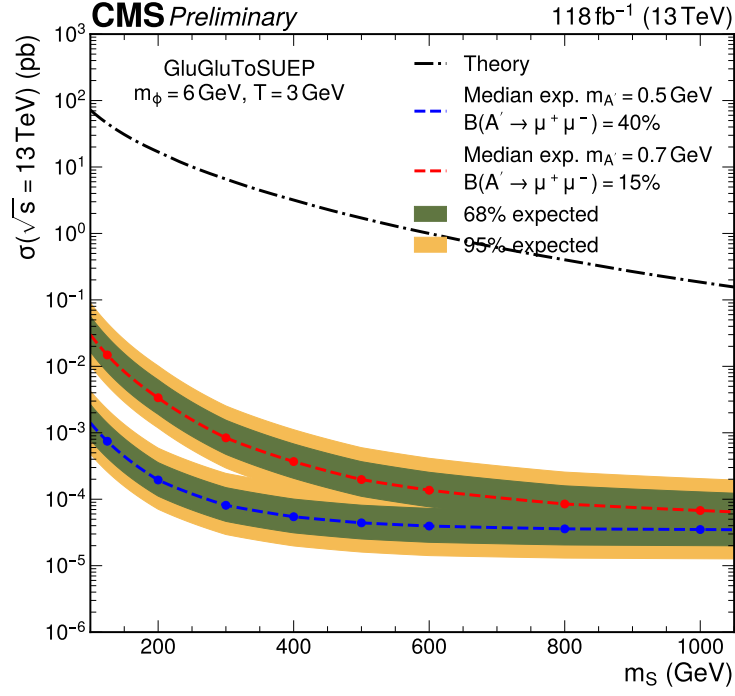


Figure D.8: 1D limit for $m_\phi = 6$ GeV, $T = 3$ GeV (both decay modes) as a function of m_S .

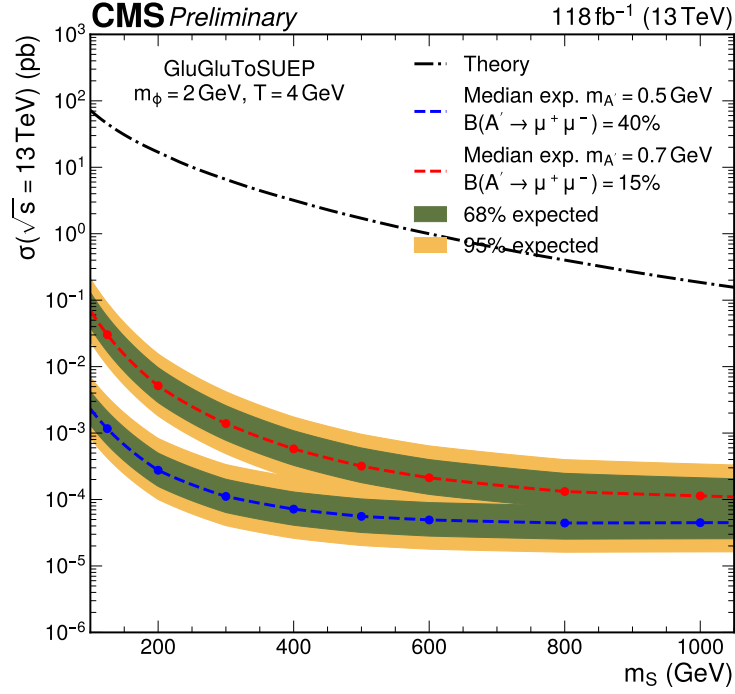


Figure D.9: 1D limit for $m_\phi = 2$ GeV, $T = 4$ GeV (both decay modes) as a function of m_S .

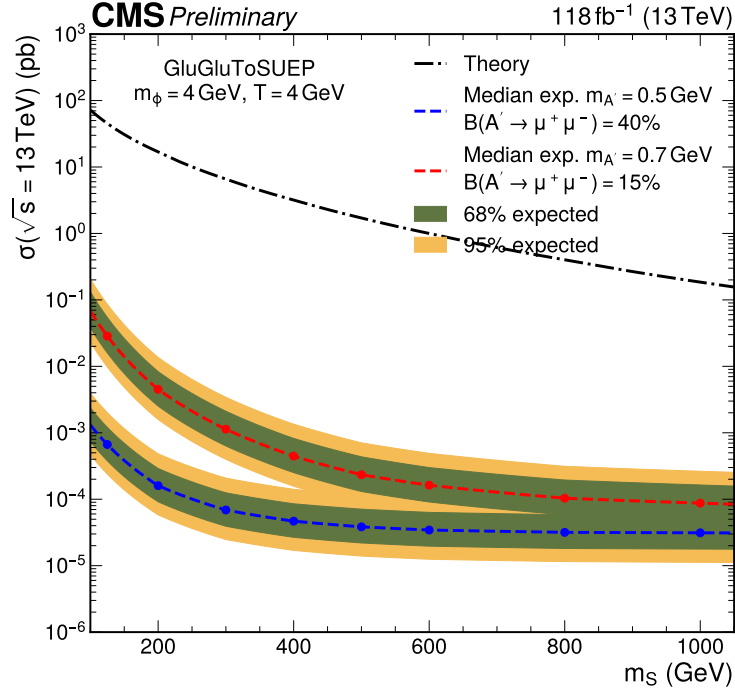


Figure D.10: 1D limit for $m_\phi = 4 \text{ GeV}$, $T = 4 \text{ GeV}$ (both decay modes) as a function of m_S .

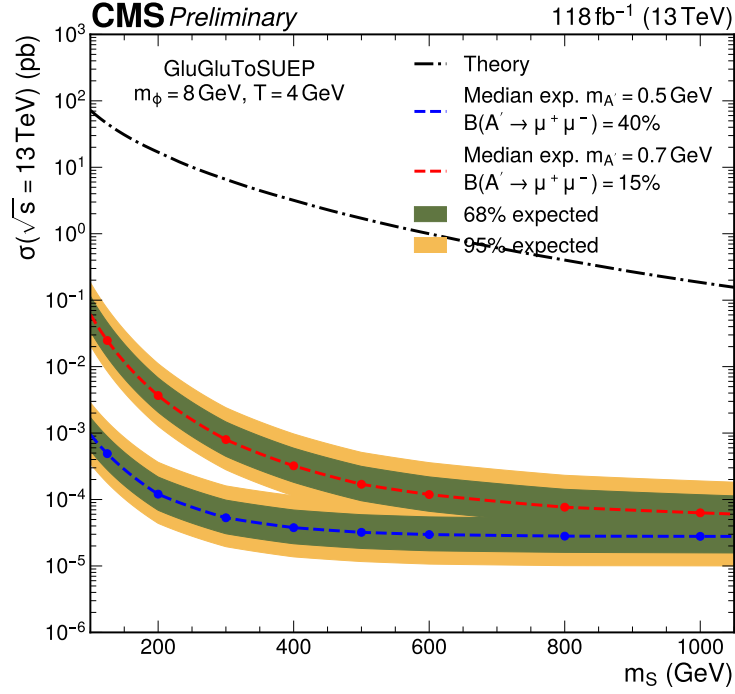


Figure D.11: 1D limit for $m_\phi = 8 \text{ GeV}$, $T = 4 \text{ GeV}$ (both decay modes) as a function of m_S .

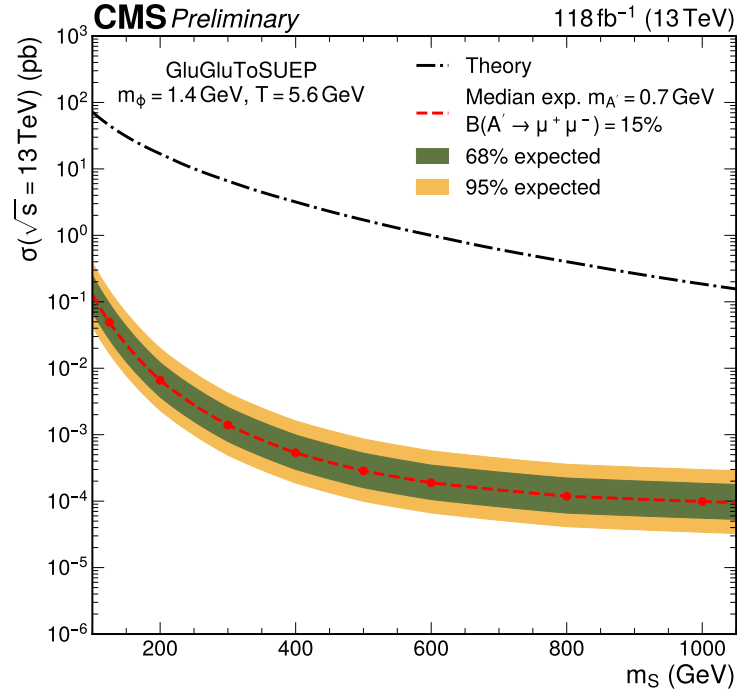


Figure D.12: 1D limit for $m_\phi = 1.4 \text{ GeV}$, $T = 5.6 \text{ GeV}$ (both decay modes) as a function of m_S .

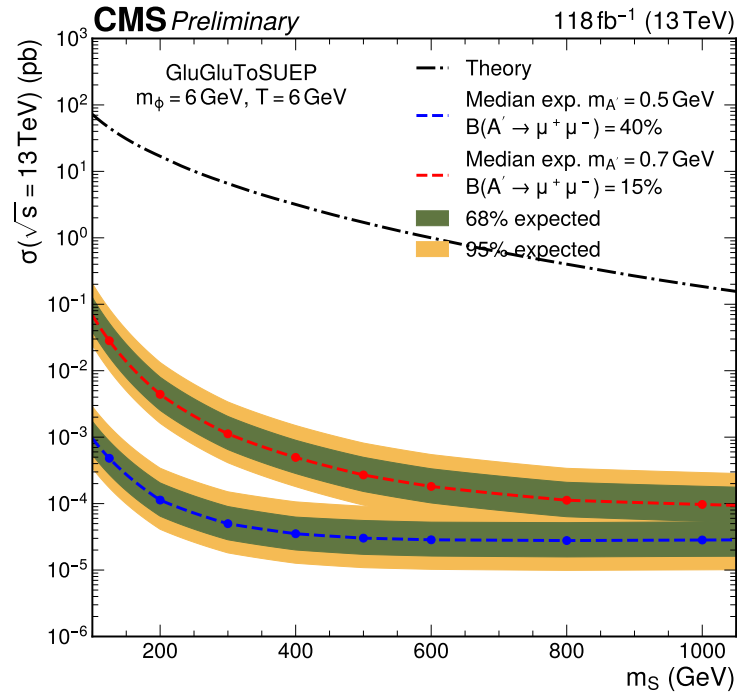


Figure D.13: 1D limit for $m_\phi = 6 \text{ GeV}$, $T = 6 \text{ GeV}$ (both decay modes) as a function of m_S .

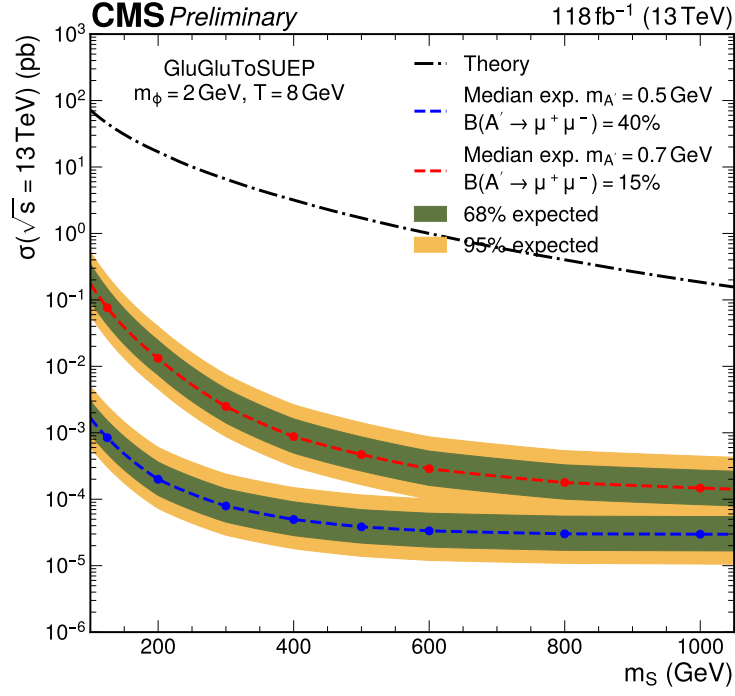


Figure D.14: 1D limit for $m_\phi = 2 \text{ GeV}$, $T = 8 \text{ GeV}$ (both decay modes) as a function of m_S .

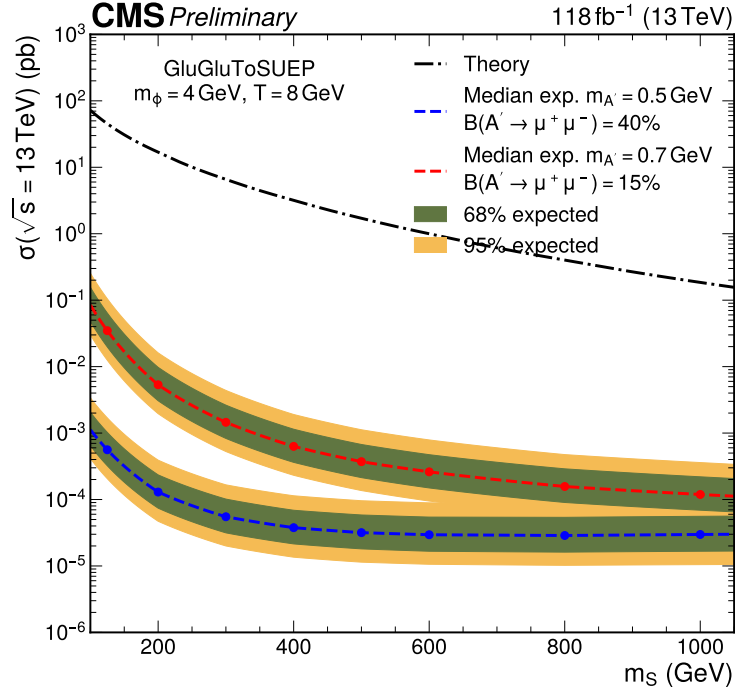


Figure D.15: 1D limit for $m_\phi = 4 \text{ GeV}$, $T = 8 \text{ GeV}$ (both decay modes) as a function of m_S .

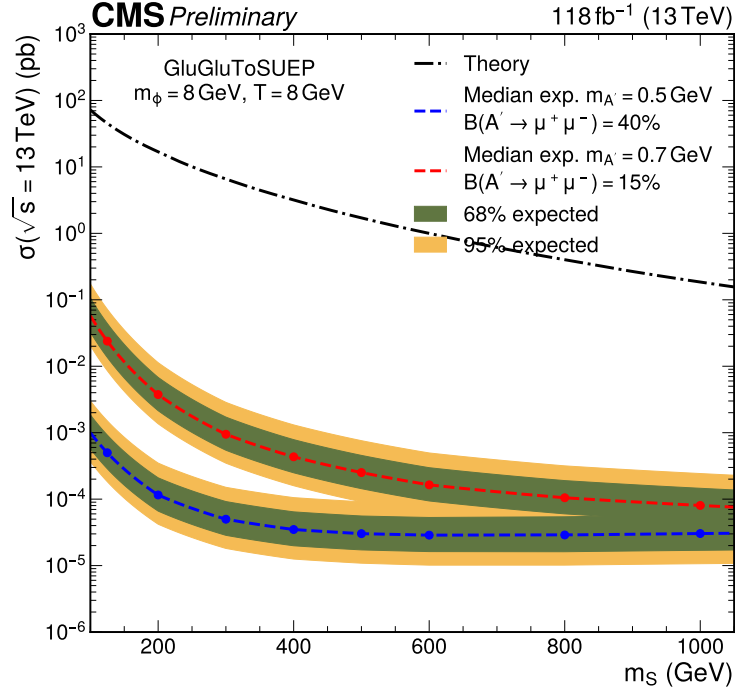


Figure D.16: 1D limit for $m_\phi = 8 \text{ GeV}, T = 8 \text{ GeV}$ (both decay modes) as a function of m_S .

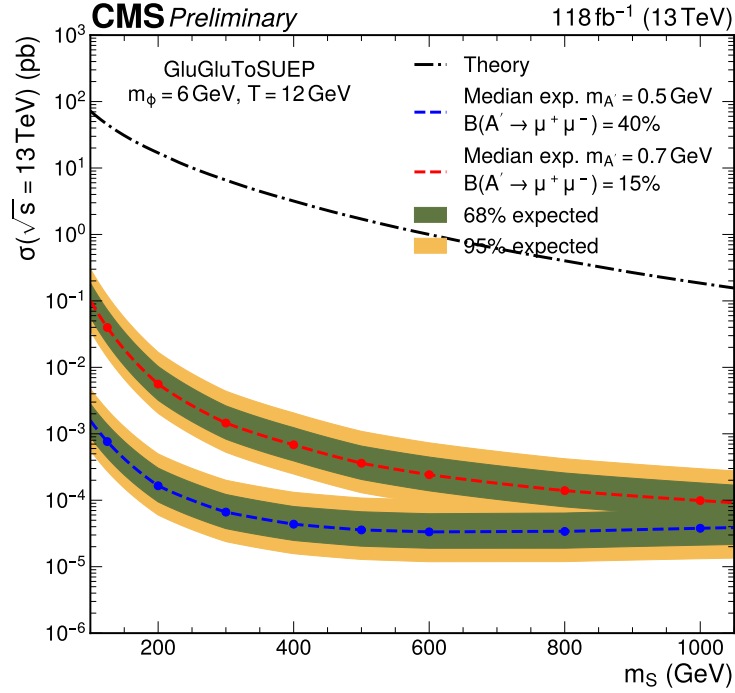


Figure D.17: 1D limit for $m_\phi = 6 \text{ GeV}, T = 12 \text{ GeV}$ (both decay modes) as a function of m_S .

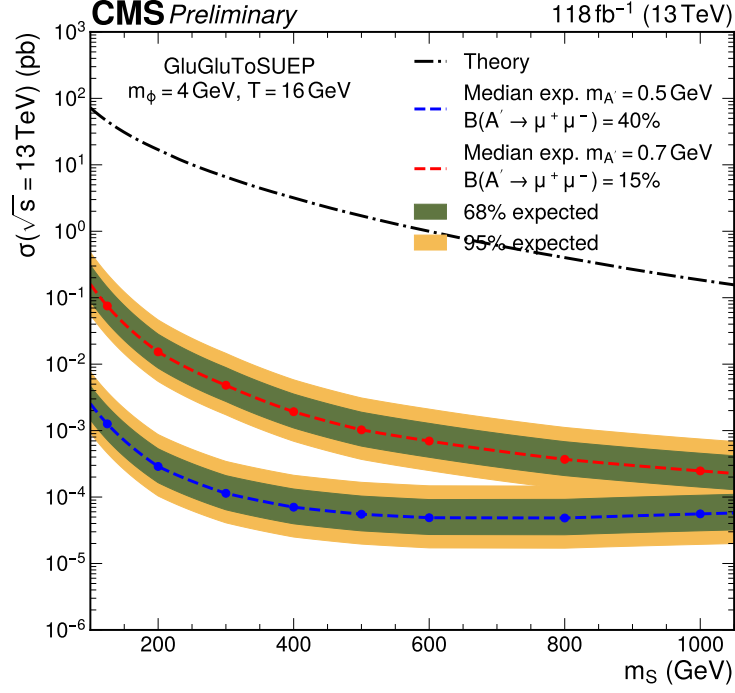


Figure D.18: 1D limit for $m_\phi = 4 \text{ GeV}$, $T = 16 \text{ GeV}$ (both decay modes) as a function of m_S .

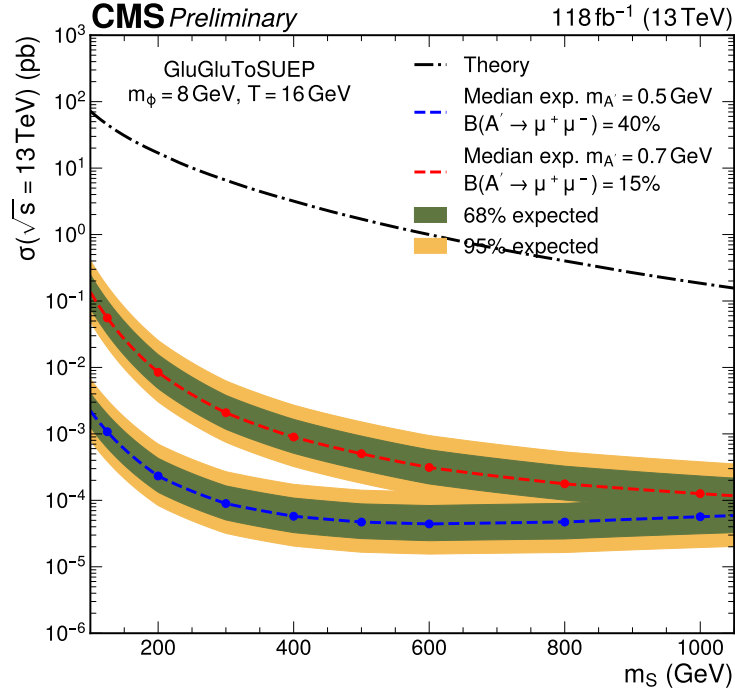


Figure D.19: 1D limit for $m_\phi = 8 \text{ GeV}$, $T = 16 \text{ GeV}$ (both decay modes) as a function of m_S .

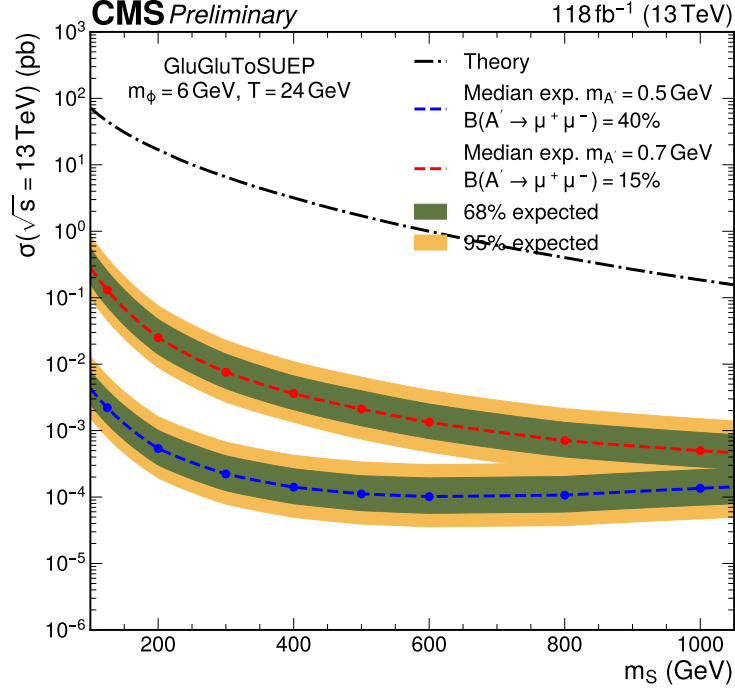


Figure D.20: 1D limit for $m_\phi = 6 \text{ GeV}$, $T = 24 \text{ GeV}$ (both decay modes) as a function of m_S .

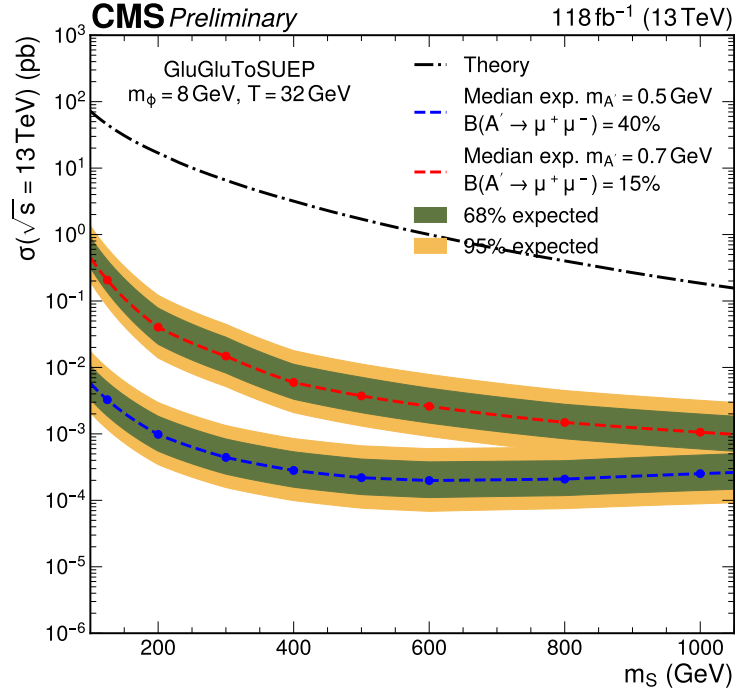


Figure D.21: 1D limit for $m_\phi = 8 \text{ GeV}$, $T = 32 \text{ GeV}$ (both decay modes) as a function of m_S .

Bibliography

- [1] Wikimedia Commons. Standard model of elementary particles, 2019. File: Standard Model of Elementary Particles.svg.
- [2] Janosh Riebesell. Higgs potential tikz.net.
- [3] K. G. Begeman, A. H. Broeils, and R. H. Sanders. Extended rotation curves of spiral galaxies: Dark haloes and modified dynamics. *Mon. Not. Roy. Astron. Soc.*, 249:523, 1991.
- [4] Ewa Lopienska. The CERN accelerator complex, layout in 2022, 2022. General Photo.
- [5] AC Team. Diagram of an LHC dipole magnet, 1999.
- [6] Tai Sakuma and Thomas McCauley. Detector and event visualization with sketchup at the cms experiment. *Journal of Physics: Conference Series*, 513(2):022032, jun 2014.
- [7] Tai Sakuma. Cutaway diagrams of CMS detector, 2019.
- [8] The Tracker Group of the CMS Collaboration. The cms phase-1 pixel detector upgrade, 2020.
- [9] CMS. The Phase-2 Upgrade of the CMS Tracker. Technical report, CERN, Geneva, 2017.
- [10] A. M. Sirunyan et al. Calibration of the CMS hadron calorimeters using proton-proton collision data at $\sqrt{s} = 13\text{TeV}$. *JINST*, 15:P05002, 2020.
- [11] A. M. Sirunyan et al. Performance of the CMS muon detector and muon reconstruction with proton-proton collisions at $\sqrt{s} = 13\text{TeV}$. *JINST*, 13:P06015, 2018.
- [12] M. Paneva on behalf of the CMS Collaboration. Local reconstruction algorithms in the cathode strip chambers of CMS. In *Proc. 23rd International Conference on Computing*

- in High Energy and Nuclear Physics (CHEP 2018): Sofia, Bulgaria, July 9--13, 2018*, 2019. [EPJ Web Conf. 214 (2019) 02014].
- [13] Jesse Heilman. Work on CMS Muon Detector (CSCs) during Long Shutdown 1 (LS1). CMS Collection., 2014.
 - [14] S. Chatrchyan et al. The CMS Experiment at the CERN LHC. *JINST*, 3:S08004, 2008.
 - [15] S. Chatrchyan et al. Calibration of the CMS drift tube chambers and measurement of the drift velocity with cosmic rays. *JINST*, 5:T03016, 2010.
 - [16] K. Bunkowski. *Optimization, synchronization, calibration and diagnostic of the RPC PAC muon trigger system for the CMS detector*. PhD thesis, Warsaw University, 2009. CERN-THESIS-2009-160.
 - [17] E. P. Corrin. *Development of digital readout electronics for the CMS tracker*. PhD thesis, Imperial College London, 2002. CERN-THESIS-2002-074.
 - [18] C. Calabria on behalf of the CMS GEM Collaboration. Large-size triple GEM detectors for the CMS forward muon upgrade. In *Proc. 37th International Conference on High Energy Physics (ICHEP 2014): Valencia, Spain, July 2--9, 2014*, 2016. [Nucl. Part. Phys. Proc. 273--275 (2016) 1042].
 - [19] M. Abbas et al. Benchmarking LHC background particle simulation with the CMS triple-GEM detector. *JINST*, 16:P12026, 2021.
 - [20] Christos Papageorgakis. Oxygen diffusion paper - GitHub repository. <https://github.com/chrispap95/oxygen-diffusion-paper>, 2022.
 - [21] Matthew J. Strassler. Why Unparticle Models with Mass Gaps are Examples of Hidden Valleys. <https://arxiv.org/abs/0801.0629>, 1 2008.
 - [22] Simon Knapen, Simone Pagan Griso, Michele Papucci, and Dean J. Robinson. Triggering Soft Bombs at the LHC. *JHEP*, 08:076, 2017.
 - [23] Philip Ilten, Yotam Soreq, Mike Williams, and Wei Xue. Serendipity in dark photon searches. *JHEP*, 06:004, 2018.

- [24] Jared Barron, David Curtin, Gregor Kasieczka, Tilman Plehn, and Aris Spourdalakis. Unsupervised hadronic SUEP at the LHC. *JHEP*, 12:129, 2021.
- [25] Serguei Chatrchyan et al. Observation of a New Boson at a Mass of 125 GeV with the CMS Experiment at the LHC. *Phys. Lett. B*, 716:30--61, 2012.
- [26] Georges Aad et al. Observation of a new particle in the search for the Standard Model Higgs boson with the ATLAS detector at the LHC. *Phys. Lett. B*, 716:1--29, 2012.
- [27] Takaaki Kajita. Nobel Lecture: Discovery of atmospheric neutrino oscillations. *Rev. Mod. Phys.*, 88(3):030501, 2016.
- [28] Matthew J. Strassler and Kathryn M. Zurek. Echoes of a hidden valley at hadron colliders. *Phys. Lett. B*, 651:374--379, 2007.
- [29] Peter W. Higgs. Broken Symmetries and the Masses of Gauge Bosons. *Phys. Rev. Lett.*, 13:508--509, 1964.
- [30] F. Englert and R. Brout. Broken Symmetry and the Mass of Gauge Vector Mesons. *Phys. Rev. Lett.*, 13:321--323, 1964.
- [31] J. Goldstone. Field Theories with Superconductor Solutions. *Nuovo Cim.*, 19:154--164, 1961.
- [32] S. Navas et al. Review of particle physics. *Phys. Rev. D*, 110(3):030001, 2024.
- [33] Tao Han. Collider phenomenology: Basic knowledge and techniques. In *Theoretical Advanced Study Institute in Elementary Particle Physics: Physics in $D \geq 4$* , pages 407--454, 8 2005.
- [34] Guido Altarelli and G. Parisi. Asymptotic Freedom in Parton Language. *Nucl. Phys. B*, 126:298--318, 1977.
- [35] N. Aghanim et al. Planck 2018 results. VI. Cosmological parameters. *Astron. Astrophys.*, 641:A6, 2020. [Erratum: *Astron. Astrophys.* 652, C4 (2021)].
- [36] Lars Bergström. Nonbaryonic dark matter: Observational evidence and detection methods. *Rept. Prog. Phys.*, 63:793, 2000.
- [37] F. Zwicky. On the Masses of Nebulae and of Clusters of Nebulae. *Astrophys. J.*, 86:217--246, 1937.

- [38] Vera C. Rubin and W. Kent Ford, Jr. Rotation of the Andromeda Nebula from a Spectroscopic Survey of Emission Regions. *Astrophys. J.*, 159:379--403, 1970.
- [39] Douglas Clowe, Anthony Gonzalez, and Maxim Markevitch. Weak lensing mass reconstruction of the interacting cluster 1E0657-558: Direct evidence for the existence of dark matter. *Astrophys. J.*, 604:596--603, 2004.
- [40] R. Adam et al. Planck 2015 results. I. Overview of products and scientific results. *Astron. Astrophys.*, 594:A1, 2016.
- [41] Lyndon Evans and Philip Bryant. LHC Machine. *JINST*, 3:S08001, 2008.
- [42] Maurizio Vretenar, editor. *Linac4 design report*, volume 6/2020 of *CERN Yellow Reports: Monographs*. CERN, Geneva, 9 2020.
- [43] M. Benedikt, P. Collier, V. Mertens, J. Poole, and K. Schindl. LHC Design Report. 3. The LHC injector chain. Technical report, CERN, 12 2004.
- [44] Oliver S. Bruning, P. Collier, P. Lebrun, S. Myers, R. Ostojic, J. Poole, and P. Proudlock. LHC Design Report Vol.1: The LHC Main Ring. Technical report, CERN, 6 2004.
- [45] Werner Herr and B Muratori. Concept of luminosity. Technical report, CERN, 2006.
- [46] Vladimir Shiltsev and Frank Zimmermann. Modern and Future Colliders. *Rev. Mod. Phys.*, 93:015006, 2021.
- [47] B. Muratori and T. Pieloni. Luminosity levelling techniques for the LHC. In *ICFA Mini-Workshop on Beam-Beam Effects in Hadron Colliders*, pages 177--181, 2014.
- [48] Aram Hayrapetyan et al. Development of the CMS detector for the CERN LHC Run 3. *JINST*, 19(05):P05064, 2024.
- [49] P. Tropea, J. Daguin, D. Giakoumi, N. Koss, P. Petagna, H. Postema, D. Schmid, B. Verlaat, and L. Zwalinski. Advancements and plans for the LHC upgrade detector thermal management with CO₂ evaporative cooling. *Nucl. Instrum. Meth. A*, 936:644--645, 2019.
- [50] Aram Hayrapetyan et al. Operation and performance of the CMS silicon strip tracker with proton-proton collisions at the CERN LHC. *arxiv*, 6 2025.

- [51] CMS. *The CMS electromagnetic calorimeter project*. Technical design report. CMS. CERN, Geneva, 1997.
- [52] G. Bayatian et al. The hadron calorimeter. CMS Technical Proposal CERN-LHCC-97-31, CMS-TDR-2, CERN, 1997.
- [53] S. Abdullin et al. Design, performance, and calibration of CMS hadron-barrel calorimeter wedges. *Eur. Phys. J. C*, 55:159, 2008.
- [54] S. Abdullin et al. Design, performance, and calibration of the CMS hadron-outer calorimeter. *Eur. Phys. J. C*, 57:653, 2008.
- [55] S. Abdullin et al. Design, performance, and calibration of CMS forward calorimeter wedges. *Eur. Phys. J. C*, 53:139, 2008.
- [56] CMS HCAL/ECAL Collaborations. The CMS barrel calorimeter response to particle beams from 2 to 350 GeV/c. *Eur. Phys. J. C*, 60:359, 2009. Erratum: 10.1140/epjc/s10052-009-1024-0.
- [57] G. Acquistapace et al. CMS, the magnet project: Technical design report. Technical report, CERN, 5 1997.
- [58] A Hervé, Bertrand Blau, P Brédy, D Campi, P Cannarsa, B Curé, T F Dupont, P Fabbricatore, S Farinon, F Feyzi, P Fazilleau, A Gaddi, H Gerwig, Michela Greco, J P Grillet, V Kaftanov, F Kircher, V Klyukhin, B Levesy, R Loveless, G Maire, R Musenich, Y Pabot, A Payn, G Perinic, P Petiot, F Rondeaux, H Rykaczewski, E Sbrissa, S Sequeira-Lopes-Tavares, Stefano Sgobba, R P Smith, L Veillet, and G Waurick. Status of the construction of the CMS magnet. *IEEE Trans. Appl. Supercond.*, 14(2):542--547, 2004.
- [59] F. Sauli. GEM: A new concept for electron amplification in gas detectors. *Nucl. Instrum. Meth. A*, 386:531, 1997.
- [60] D. Abbaneo et al. Layout and assembly technique of the GEM chambers for the upgrade of the CMS first muon endcap station. *Nucl. Instrum. Meth. A*, 918:67, 2019.
- [61] A. M. Sirunyan et al. Performance of the CMS Level-1 trigger in proton-proton collisions at $\sqrt{s} = 13\text{TeV}$. *JINST*, 15:P10017, 2020.

- [62] D. Acosta et al. CMS technical design report for the Level-1 trigger upgrade. CMS Technical Proposal CERN-LHCC-2013-011, CMS-TDR-012, CERN, 2013.
- [63] A. M. Sirunyan et al. Performance of the CMS muon trigger system in proton-proton collisions at $\sqrt{s} = 13\text{TeV}$. *JINST*, 16:P07001, 2021.
- [64] T. Baweji et al. The new CMS DAQ system for Run 2 of the LHC. *IEEE Trans. Nucl. Sci.*, 62:1099, 2015.
- [65] G. Bauer et al. The new CMS DAQ system for LHC operation after 2014 (DAQ2). In *Proc. 20th International Conference on Computing in High Energy and Nuclear Physics (CHEP 2013): Amsterdam, Netherlands, October 14--18, 2013*, 2014. [J. Phys. Conf. Ser. 513 (2015) 012014].
- [66] G. Bauer et al. The Terabit/s super-fragment builder and trigger throttling system for the Compact Muon Solenoid experiment at CERN. *IEEE Trans. Nucl. Sci.*, 55:190, 2008.
- [67] J. Hegeman et al. The CMS timing and control distribution system. In *Proc. 2015 IEEE Nuclear Science Symposium and Medical Imaging Conference (NSS/MIC 2015): San Diego CA, USA, October 31--November 7, 2015*, 2016.
- [68] G. Bauer et al. The CMS event builder and storage system. In *Proc. 17th International Conference on Computing in High Energy and Nuclear Physics (CHEP2009): Prague, Czech Republic, March 21--27, 2009*, 2010. [J. Phys. Conf. Ser. 219 (2015) 022038].
- [69] E. Ayala et al. The pixel luminosity telescope: a detector for luminosity measurement at CMS using silicon pixel sensors. *Eur. Phys. J. C*, 83:673, 2023.
- [70] A. Kornmayer on behalf of the CMS Collaboration. The CMS pixel luminosity telescope. In *Proc. 13th Pisa Meeting on Advanced Detectors: Frontier Detectors for Frontier Physics (FDFP 2015): La Biodola, Italy, May 24--30, 2015*, 2016. [Nucl. Instrum. Meth. A 824 (2016) 304].
- [71] K. Rose on behalf of the CMS Collaboration. The new pixel luminosity telescope of CMS at the LHC. In *Proc. 2015 IEEE Nuclear Science Symposium and Medical Imaging Conference (NSS/MIC 2015): San Diego CA, USA, October 31--November 7, 2015*, 2016.

- [72] M. Guthoff on behalf of the CMS Collaboration. The new fast beam condition monitor using poly-crystalline diamond sensors for luminosity measurement at CMS. In *Proc. 14th Pisa Meeting on Advanced Detectors: Frontier Detectors for Frontier Physics (Pisameet): La Biodola, Italy, May 27--June 2, 2018*, 2019. [Nucl. Instrum. Meth. A 936 (2019) 717].
- [73] J. Wańczyk on behalf of the CMS Collaboration. Upgraded CMS fast beam condition monitor for LHC Run 3 online luminosity and beam induced background measurements. In *Proc. 11th International Beam Instrumentation Conference (IBIC 2022): Cracow, Poland, September 11--15, 2022*, 2022. [JACoW IBIC2022 (2018) TH2C2].
- [74] J. Mans et al. CMS technical design report for the Phase 1 upgrade of the hadron calorimeter. CMS Technical Proposal CERN-LHCC-2012-015, CMS-TDR-010, CERN, 2012.
- [75] Torbjörn Sjöstrand, Stefan Ask, Jesper R. Christiansen, Richard Corke, Nishita Desai, Philip Ilten, Stephen Mrenna, Stefan Prestel, Christine O. Rasmussen, and Peter Z. Skands. An introduction to PYTHIA 8.2. *Comput. Phys. Commun.*, 191:159--177, 2015.
- [76] Johan Alwall, Michel Herquet, Fabio Maltoni, Olivier Mattelaer, and Tim Stelzer. MadGraph 5 : Going Beyond. *JHEP*, 06:128, 2011.
- [77] Serguei Chatrchyan et al. Description and Performance of Track and Primary-Vertex Reconstruction with the CMS Tracker. *JINST*, 9(10):P10009, 2014.
- [78] A. M. Sirunyan et al. Particle-flow reconstruction and global event description with the CMS detector. *JINST*, 12(10):P10003, 2017.
- [79] C. Papageorgakis, M.Y. Aamir, A. Belloni, T.K. Edberg, S.C. Eno, B. Kronheim, and C. Palmer. Effects of oxygen on the optical properties of phenyl-based scintillators during irradiation and recovery. *Nuclear Instruments and Methods in Physics Research Section A: Accelerators, Spectrometers, Detectors and Associated Equipment*, 1059:168977, 2024.
- [80] S. Bertolucci et al. The CDF Central and Endwall Hadron Calorimeter. *Nucl. Instrum. Meth. A*, 267:301--314, 1988.

- [81] Dmitri Smirnov. Status of the DØ fiber tracker and preshower detectors. *Nucl. Instrum. Meth. A*, 598(1):94--97, 2009. Instrumentation for Colliding Beam Physics.
- [82] D Lincoln. New technologies in the DØ central tracker upgrade. *Nucl. Instrum. Meth. A*, 379(3):424--426, 1996. Proceedings of the Sixth International Conference on Instrumentation for Experiments at e+ e- Colliders.
- [83] Y. Hernandez. The ATLAS tile calorimeter performance at LHC. *Nucl. Instrum. Meth. A*, 718:83--85, 2013. Proceedings of the 12th Pisa Meeting on Advanced Detectors.
- [84] J Mans, J Anderson, B Dahmes, P de Barbaro, J Freeman, T Grassi, E Hazen, J Mans, R Ruchti, I Schimdt, T Shaw, C Tully, J Whitmore, and T Yetkin. CMS Technical Design Report for the Phase 1 Upgrade of the Hadron Calorimeter. Technical report, CERN, 2012.
- [85] Christophe Ochando. HGCal: A High-Granularity Calorimeter for the endcaps of CMS at HL-LHC. *J. Phys.: Conf. Ser.*, 928(1):012025, 2017.
- [86] M. Antonello, M. Caccia, R. Ferrari, G. Gaudio, L. Pezzotti, G. Polesello, E. Proserpio, and R. Santoro. Expected performance of the IDEA dual-readout fully projective fiber calorimeter. *Journal of Instrumentation*, 15(06):C06015, jun 2020.
- [87] Theodor Förster. Zwischenmolekulare energiewanderung und fluoreszenz. *Ann. Phys. (Berl.)*, 437:55, 1947.
- [88] J. B. Birks. *The theory and practice of scintillation counting*. International Series of Monographs on Electronics and Instrumentation, Volume 27. Pergamon Press, The Macmillan Company, New York, 1964.
- [89] W. Adam and et. al. The CMS Phase-1 pixel detector upgrade. *Journal of Instrumentation*, 16(02):P02027, feb 2021.
- [90] CMS Collaboration. Measurements with silicon photomultipliers of dose-rate effects in the radiation damage of plastic scintillator tiles in the CMS hadron endcap calorimeter. *JINST*, 15(06):P06009--P06009, jun 2020.
- [91] CMS. The Phase-2 upgrade of the CMS endcap calorimeter. Technical Report CERN-LHCC-2017-023, CMS, 2017.

- [92] H Jivan, E Sideras-Haddad, R Erasmus, S Liao, M Madhuku, G Peters, K Sekonya, and O Solvyanov. Radiation hardness of plastic scintillators for the tile calorimeter of the ATLAS detector. *J. Phys.: Conf. Series*, 645:012019, 2015.
- [93] R. Pedro and. Optics robustness of the ATLAS tile calorimeter. *Journal of Physics: Conference Series*, 1162:012004, 2019.
- [94] Carl Zorn. Plastic and liquid organic scintillators. In Fabio Sauli, editor, *Instrumentation in High Energy Physics, Advanced Series on Directions in High Energy Physics*, volume 9, page 218. World Scientific, 1992.
- [95] Yu.N. Kharzheev. Radiation hardness of scintillation detectors based on organic plastic scintillators and optical fibers. *Phys. Part. Nucl.*, 50(1):42--76, 2019.
- [96] E. Biagtan, E. Goldberg, R. Stephens, E. Valeroso, and J. Harmon. Gamma dose and dose-rate effects on scintillator light output. *Nucl. Instrum. Meth. B*, 108:125, 1996.
- [97] U. Holm and K. Wick. Radiation stability of plastic scintillators and wave-length shifters. *IEEE Trans. Nucl. Sci.*, 36:579, 1989.
- [98] K. Wick, D. Paul, P. Schröder, V. Stieber, and B. Bicken. Recovery and dose-rate dependence of radiation damage in scintillators, wavelength shifters and light guides. *Nucl. Instrum. Meth. B*, 61:472, 1991.
- [99] B. Bicken, U. Holm, T. Marckmann, K. Wick, and M. Rohde. Recovery and permanent radiation damage of plastic scintillators at different dose rates. *IEEE Trans. Nucl. Sci.*, 38:188, 1991.
- [100] B. Bicken, A. Dannemann, U. Holm, T. Neumann, and K. Wick. Influence of temperature treatment on radiation stability of plastic scintillator and wave-length shifter. *IEEE Trans. Nucl. Sci.*, 39:1212, 1992.
- [101] A. D. Bross and A. Pla-Dalmau. Radiation damage of plastic scintillators. *IEEE Trans. Nucl. Sci.*, 39:1199, 1992.
- [102] N. D. Giokaris, M. Contreras, A. Pla-Dalmau, J. Zimmerman, and K. F. Johnson. Study of dose-rate effects on the radiation damage of polymer-based SCSN23, SCSN81, SCSN81+Y7, SCSN81+Y8 and 3HF scintillators. *Radiat. Phys. Chem.*, 41:315, 1993.

- [103] V. Khachatryan et al. Dose-rate effects in the radiation damage of the plastic scintillators of the CMS hadron endcap calorimeter. *JINST*, 11:T10004, 2016. [Erratum: doi 10.1088/1748-0221/14/08/E08001].
- [104] K. Gillen and M. Celina. Predicting polymer degradation and mechanical property changes for combined radiation-thermal aging environments. *Rubber Chemistry & Technology*, 91:27, 2018.
- [105] C. Papageorgakis, M. Al-Sheikhly, A. Belloni, T.K. Edberg, S.C. Eno, Yongbin Feng, Geng-Yuan Jeng, Abraham Kahn, Yihui Lai, T. McDonnell, Ameer Mohammed, C. Palmer, Ruhi Perez-Gokhale, F. Ricci-Tam, Zishuo Yang, and Yao Yao. Dose rate effects in radiation-induced changes to phenyl-based polymeric scintillators. *Nucl. Instrum. Meth. A*, 1042:167445, 2022.
- [106] Wise, K. Gillen, and R. Clough. Quantitative model for the time development of diffusion-limited oxidation profiles. *Polymer*, 38:1929--1944, 1997.
- [107] K. Gillen and R. Clough. Rigorous experimental confirmation of a theoretical model for diffusion-limited oxidation. *Polymer*, 38:1929, 1992.
- [108] Kenneth T. Gillen, Jonathan Wise, and Roger L. Clough. General solution for the basic autoxidation scheme. *Polymer Degradation and Stability*, 47:149 -- 161, 1995.
- [109] D. Horstmann and U. Holm. Fluorescence quenching of plastic scintillators in oxygen. *Radiation Physics and Chemistry*, 41(1):395--400, 1993.
- [110] Matthieu Hamel. *Plastic scintillators: chemistry and applications*. Springer Cham, July 2021.
- [111] J.W.T. Spinks and R.J. Woods. *An Introduction to radiation chemistry*. Wiley-Interscience, 1990.
- [112] J.W.T. Spinks and Al Pikaev. *Applied Radiation Chemistry: Radiation Processing*. Wiley, 1993.
- [113] Thomas Pöschl, Daniel Greenwald, Martin J. Losekamm, and Stephan Paul. Measurement of ionization quenching in plastic scintillators. *NIM A*, 988:164865, 2021.

- [114] W. Busjan, K. Wick, and T. Zoufal. Shortlived absorption centers in plastic scintillators and their influence on the fluorescence light yield. *Nucl. Instrum. Meth. B*, 152:89, 1999.
- [115] A. V. Cunliffe and A. Davis. Photo-oxidation of thick polymer samples --- Part II: The influence of oxygen diffusion on the natural and artificial weathering of polyolefins. *Polym. Degrad. Stab.*, 4:17, 1982.
- [116] Bojie Wang and Peter R. Ogilby. Activation barriers for oxygen diffusion in polystyrene and polycarbonate glasses: effects of codissolved argon, helium, and nitrogen. *Canadian Journal of Chemistry*, 73(11):1831--1840, 1995.
- [117] K. Gillen, J. Wallace, and R. Clough. Dose-rate dependence of the radiation-induced discoloration of polystyrene. *Radiat. Phys. Chem.*, 41:101, 1993.
- [118] J. L. Bolland. Kinetic studies in the chemistry of rubber and related materials. I. The thermal oxidation of ethyl linoleate. *J. L. Proc. R. Soc. A*, 186:218, 1946.
- [119] S. W. Shalaby and R. L. Clough. Radiation effects on polymers. *Am. Chem. Soc. Symp. Ser.*, 475:457, 1991.
- [120] Aiysha Ashfaq, Marie-Claude Clochard, Xavier Coqueret, Clelia Dispenza, Mark S. Driscoll, Piotr Ulański, and Mohamad Al-Sheikhly. Polymerization reactions and modifications of polymers by ionizing radiation. *Polymers*, 12, 2020.
- [121] James E. Mark, editor. *Physical properties of polymers handbook*. Springer, New York, NY, 2007.
- [122] Chris Maxwell. private communication. Eljen Technology.
- [123] Dorothea Pfeiffer, Georgi Gorine, Hans Reithler, Bartolomej Biskup, Alasdair Day, Adrian Fabich, Joffrey Germa, Roberto Guida, Martin Jaekel, and Federico Ravotti. The radiation field in the gamma irradiation facility GIF++ at CERN. *Nucl. Instrum. Meth. A*, 866:91 -- 103, 2017.
- [124] NIST. NIST ASTAR database. Accessed: 2021-03-29.
- [125] Adolf Fick. Ueber diffusion. *Ann. Phys.*, 170(1):59--86, 1855.

- [126] Adolph Fick. V. On liquid diffusion. *The London, Edinburgh, and Dublin Philosophical Magazine and Journal of Science*, 10(63):30--39, 1855.
- [127] William Henry and Joseph Banks. III. Experiments on the quantity of gases absorbed by water, at different temperatures, and under different pressures. *Philosophical Transactions of the Royal Society of London*, 93:29--274, 1803.
- [128] W R Vieth. *Diffusion in and through polymers: Principles and applications*. Hanser, 1991.
- [129] P. Neogi. *Diffusion in Polymers*. *Plastics Engineering*. Taylor & Francis, 1996.
- [130] S. A. Stern and Joel R. Fried. *Permeability of Polymers to Gases and Vapors*, chapter 61, pages 1033--1047. Springer New York, New York, NY, 2007.
- [131] Tadao Seguchi, Shoji Hashimoto, Waichiro Kawakami, and Isamu Kuriyama. Radiation damage of polymer materials, 1. Technical report, Japan Atomic Energy Research Inst., 1977.
- [132] Tadao Seguchi, Shoji Hashimoto, Kazuo Arakawa, Naohiro Hayakawa, Waichiro Kawakami, and Isamu Kuriyama. Radiation induced oxidative degradation of polymers--I: Oxidation region in polymer films irradiated in oxygen under pressure. *Radiat. Phys. Chem.*, 17:195, 1981.
- [133] J. Crank and G.S. Park. *Diffusion in Polymers*. Academic Press, 1968.
- [134] Pauli Virtanen, Ralf Gommers, Travis E. Oliphant, Matt Haberland, Tyler Reddy, David Cournapeau, Evgeni Burovski, Pearu Peterson, Warren Weckesser, Jonathan Bright, Stéfan J. van der Walt, Matthew Brett, Joshua Wilson, K. Jarrod Millman, Nikolay Mayorov, Andrew R. J. Nelson, Eric Jones, Robert Kern, Eric Larson, C J Carey, Ilhan Polat, Yu Feng, Eric W. Moore, Jake VanderPlas, Denis Laxalde, Josef Perktold, Robert Cimrman, Ian Henriksen, E. A. Quintero, Charles R. Harris, Anne M. Archibald, Antônio H. Ribeiro, Fabian Pedregosa, Paul van Mulbregt, and SciPy 1.0 Contributors. SciPy 1.0: Fundamental Algorithms for Scientific Computing in Python. *Nature Methods*, 17:261--272, 2020. See more at: https://docs.scipy.org/doc/scipy/reference/generated/scipy.integrate.solve_bvp.html.

- [135] G.C. Furneaux, K.J. Ledbury, and A. Davis. Photo-oxidation of thick polymer samples|Part I: The variation of photo-oxidation with depth in naturally and artificially weathered low density polyethylene. *Polymer Degradation and Stability*, 3(6):431--442, 1981.
- [136] O. Cicchetti. Mechanisms of oxidative photodegradation and of uv stabilization of polyolefins. In *Fortschritte der Hochpolymeren-Forschung*, pages 70--112, Berlin, Heidelberg, 1970. Springer Berlin Heidelberg.
- [137] J. L. Bolland. Kinetic studies in the chemistry of rubber and related materials. VI. The benzoyl peroxide-catalysed oxidation of ethyl linoleate. *Trans. Faraday Soc.*, 44:669--677, 1948.
- [138] J. L. Bolland. Kinetics of olefin oxidation. *Q. Rev. Chem. Soc.*, 3:1--21, 1949.
- [139] L. Bateman. Olefin oxidation. *Q. Rev. Chem. Soc.*, 8:147--167, 1954.
- [140] Pierre Van Rysselberghe. Remarks concerning the Clausius-Mossotti law. *The Journal of Physical Chemistry*, 36(4):1152--1155, 1932.
- [141] Helge Kragh. The Lorenz-Lorentz formula: Origin and early history. *Substantia*, 2(2):7--18, Sep. 2018.
- [142] L. Lorenz. Ueber die refractionsconstante. *Ann. Phys.*, 247(9):70--103, 1880.
- [143] H. A. Lorentz. *Concerning the Relation Between the Velocity of Propagation of Light and the Density and Composition of Media*, chapter 1, pages 1--119. Springer Netherlands, Dordrecht, 1936.
- [144] JW Brühl. On the influence of single and so-called multiple bonds of atoms on the light refraction of bodies. *Zs. Phys. Chem.*, 1(1):307--361, 1887.
- [145] JW Brühl. Ueber das pyron. *Ber. Deut. Chem. Gesselsch.*, 24(2):2450--2455, 1891.
- [146] CROW. Polymer data: Free encyclopedia of polymer science and technology. <https://polymerdatabase.com/index.html>, 2022. Accessed: 2022-12-21.

- [147] Eljen Technology. Eljen Technology website. <https://eljentechnology.com/products/plastic-scintillators/ej-200-ej-204-ej-208-ej-212>, 2022. Accessed: 2022-12-21.
- [148] W. Sellmeier. Ueber die durch die aetherschwingungen erregten mitschwingungen der körpertheilchen und deren rückwirkung auf die ersteren, besonders zur erklärang der dispersion und ihrer anomalien. *Annalen der Physik*, 223(11):386--403, 1872.
- [149] Dorothea Pfeiffer, Georgi Gorine, Hans Reithler, Bartolomej Biskup, Alasdair Day, Adrian Fabich, Joffrey Germa, Roberto Guida, Martin Jaekel, and Federico Ravotti. The radiation field in the gamma irradiation facility GIF++ at CERN. *Nuclear Instruments and Methods in Physics Research Section A: Accelerators, Spectrometers, Detectors and Associated Equipment*, 866:91--103, 2017.
- [150] G. Bradski. The OpenCV Library. *Dr. Dobb's Journal of Software Tools*, 2000.
- [151] David J Ketcham, Roger W Lowe, and J William Weber. Image enhancement techniques for cockpit displays. *Hughes Aircraft Co Culver City Ca Display Systems Lab*, 6, 1974.
- [152] Robert Hummel. Image enhancement by histogram transformation. *Computer Graphics and Image Processing*, 6(2):184--195, 1977.
- [153] Abraham. Savitzky and M. J. E. Golay. Smoothing and differentiation of data by simplified least squares procedures. *Analytical Chemistry*, 36(8):1627--1639, 1964.
- [154] Effilia Allun Jaladri and Eko Nursulistiyo. Development of physical practicum tools to determine the refractive index through measurement of real depth and apparent depth. *Journal of Physics: Conference Series*, 1511(1):012077, apr 2020.
- [155] Mikhail N. Polyanskiy. Refractive index database.
- [156] Matthew J. Strassler and Kathryn M. Zurek. Discovering the Higgs through highly-displaced vertices. *Phys. Lett. B*, 661:263--267, 2008.
- [157] Timothy Cohen, Mariangela Lisanti, and Hou Keong Lou. Semivisible Jets: Dark Matter Undercover at the LHC. *Phys. Rev. Lett.*, 115(17):171804, 2015.

- [158] Pedro Schwaller, Daniel Stolarski, and Andreas Weiler. Emerging Jets. *JHEP*, 05:059, 2015.
- [159] Guillaume Albouy et al. Theory, phenomenology, and experimental avenues for dark showers: a Snowmass 2021 report. *Eur. Phys. J. C*, 82(12):1132, 2022.
- [160] K. F. Di Petrillo, J. N. Farr, C. Guo, T. R. Holmes, J. Nelson, and K. Pachal. Optimizing trigger-level track reconstruction for sensitivity to exotic signatures. *JHEP*, 02:034, 2023.
- [161] Cari Cesarotti and Jesse Thaler. A Robust Measure of Event Isotropy at Colliders. *JHEP*, 08:084, 2020.
- [162] Simranjit Singh Chhibra, Nadezda Chernyavskaya, Benedikt Maier, Maurizio Pierini, and Syed Hasan. Autoencoders for real-time SUEP detection. *Eur. Phys. J. Plus*, 139(3):281, 2024.
- [163] Aram Hayrapetyan et al. Search for Soft Unclustered Energy Patterns in Proton-Proton Collisions at 13 TeV. *Phys. Rev. Lett.*, 133(19):191902, 2024.
- [164] Aram Hayrapetyan et al. Dark sector searches with the CMS experiment. <https://arxiv.org/abs/2405.13778>, 5 2024.
- [165] Michael Reid. *Search for Soft Unclustered Energy Patterns In Proton-Proton Collisions with $\sqrt{s} = 13$ TeV Recorded by the Compact Muon Solenoid Detector*. PhD thesis, Cornell U., 2023.
- [166] CMS Collaboration. Search for soft unclustered energy patterns using scouting dataset. Cadi entry EX0-23-001, CMS, 2023.
- [167] SUEP working group. Search for soft unclustered energy patterns. CMS Note 2021/119, CMS, 2021.
- [168] SUEP working group. Search for soft unclustered energy patterns. CMS Note 2023/041, CMS, 2023.
- [169] CMS Collaboration. Search for soft unclustered energy patterns in association with a vector boson. Cadi entry EX0-23-003, CMS, 2023.
- [170] SUEP working group. Search for soft unclustered energy patterns in association with a vector boson with run ii data. CMS Note 2022/102, CMS, 2022.

- [171] CMS Collaboration. Search for sueps produced in association with a vector boson (wh channel). Cadi entry EX0-24-030, CMS, 2024.
- [172] SUEP working group. Search for soft unclustered energy patterns in association with a w boson using run 2 data. CMS Note 2023/183, CMS, 2023.
- [173] Diego M. Hofman and Juan Maldacena. Conformal collider physics: Energy and charge correlations. *JHEP*, 05:012, 2008.
- [174] Joseph Polchinski and Matthew J. Strassler. Deep inelastic scattering and gauge / string duality. *JHEP*, 05:012, 2003.
- [175] Shu Lin and Edward Shuryak. Toward the AdS/CFT gravity dual for high energy collisions. 2. The stress tensor on the boundary. *Phys. Rev. D*, 77:085014, 2008.
- [176] Yoshitaka Hatta and Toshihiro Matsuo. Jet fragmentation and gauge/string duality. *Phys. Lett. B*, 670:150--153, 2008.
- [177] J. Cleymans. The Thermal Model at the Large Hadron Collider. *Acta Phys. Polon. B*, 43:563--570, 2012.
- [178] F. Becattini and G. Passaleva. Statistical hadronization model and transverse momentum spectra of hadrons in high-energy collisions. *Eur. Phys. J. C*, 23:551--583, 2002.
- [179] Yoshitaka Hatta and Toshihiro Matsuo. Thermal hadron spectrum in e+e- annihilation from gauge/string duality. *Phys. Rev. Lett.*, 102:062001, 2009.
- [180] Matt Graham, Christopher Hearty, and Mike Williams. Searches for Dark Photons at Accelerators. *Ann. Rev. Nucl. Part. Sci.*, 71:37--58, 2021.
- [181] SUEP working group. SUEPNano, March 2025. <https://github.com/chrispap95/SUEPNano>.
- [182] A. M. Sirunyan et al. Precision luminosity measurement in proton-proton collisions at $\sqrt{s} = 13\text{TeV}$ in 2015 and 2016 at CMS. *Eur. Phys. J. C*, 81:800, 2021.
- [183] CMS Collaboration. CMS luminosity measurement for the 2018 data-taking period at $\sqrt{s} = 13\text{TeV}$. CMS Physics Analysis Summary CMS-PAS-LUM-18-002, CMS, 2019.

- [184] CMS Collaboration. CMS luminosity measurement for the 2017 data-taking period at $\sqrt{s} = 13$ TeV. CMS Physics Analysis Summary CMS-PAS-LUM-17-004, CMS, 2018.
- [185] LUM POG. Luminosity recommendations for run 2 analyses, September 2022. <https://twiki.cern.ch/twiki/bin/view/CMS/LumiRecommendationsRun2>.
- [186] S. Agostinelli et al. GEANT4 - A Simulation Toolkit. *Nucl. Instrum. Meth. A*, 506:250--303, 2003.
- [187] Carlos Francisco Erice Cid. Bug in ul pt binned dy samples. Generator Tools and MC production cms-talk channel, June 2022. <https://cms-talk.web.cern.ch/t/bug-in-ul-pt-binned-dy-samples/11639>.
- [188] Johan Alwall et al. Comparative study of various algorithms for the merging of parton showers and matrix elements in hadronic collisions. *Eur. Phys. J. C*, 53:473--500, 2008.
- [189] Paolo Nason. A New method for combining NLO QCD with shower Monte Carlo algorithms. *JHEP*, 11:040, 2004.
- [190] Stefano Frixione, Paolo Nason, and Carlo Oleari. Matching NLO QCD computations with Parton Shower simulations: the POWHEG method. *JHEP*, 11:070, 2007.
- [191] Simone Alioli, Paolo Nason, Carlo Oleari, and Emanuele Re. A general framework for implementing NLO calculations in shower Monte Carlo programs: the POWHEG BOX. *JHEP*, 06:043, 2010.
- [192] Stefano Frixione, Paolo Nason, and Giovanni Ridolfi. A Positive-weight next-to-leading-order Monte Carlo for heavy flavour hadroproduction. *JHEP*, 09:126, 2007.
- [193] Albert M Sirunyan et al. Extraction and validation of a new set of CMS PYTHIA8 tunes from underlying-event measurements. *Eur. Phys. J. C*, 80(1):4, 2020.
- [194] Richard D. Ball et al. Parton distributions from high-precision collider data. *Eur. Phys. J. C*, 77(10):663, 2017.
- [195] D J Lange, M Hildreth, V N Ivantchenko, I Osborne, and (for the CMS Collaboration). Upgrades for the CMS simulation. *Journal of Physics: Conference Series*, 608(1):012056, apr 2015.

- [196] Simon Knapen. SUEP generator PYTHIA plugin in gitlab, September 2020. https://gitlab.com/simonknapen/suep_generator.
- [197] SUEP working group. SUEP with muons request, April 2024. https://gitlab.cern.ch/cms-exo-mci/EXO-MCsampleRequests/-/merge_requests/256.
- [198] LHC Higgs working group. BSM Higgs production cross sections at $\sqrt{s} = 13$ tev (update in CERN report4 2016), November 2023. https://twiki.cern.ch/twiki/bin/view/LHCPhysics/CERNYellowReportPageBSMA13TeV#gluon_gluon_Fusion_Process.
- [199] PVT main. Utilities for accessing pileup information for data, February 2024. <https://twiki.cern.ch/twiki/bin/viewauth/CMS/PileupJSONFileforData>.
- [200] Albert M Sirunyan et al. Measurement of the inelastic proton-proton cross section at $\sqrt{s} = 13$ TeV. *JHEP*, 07:161, 2018.
- [201] Laurent Thomas. Reweighting recipe to emulate level 1 ecal and muon prefiring, October 2021. <https://twiki.cern.ch/twiki/bin/viewauth/CMS/L1PrefiringWeightRecipe>.
- [202] MUO POG. Muon recommendations for analysis, March 2025. <https://muon-wiki.docs.cern.ch/guidelines/corrections/>.
- [203] MUO POG. Tnp overview for muon official recommendations, April 2023. <https://twiki.cern.ch/twiki/bin/view/CMS/SWGuideMuonTnPOverview>.
- [204] MUO POG. Muon correction recommendations, March 2025. <https://muon-wiki.docs.cern.ch/guidelines/recommendations/>.
- [205] MUO POG. Muon efficiencies, April 2022. <https://gitlab.cern.ch/cms-muonPOG/muonefficiencies/-/blob/master/Run2/UL/>.
- [206] CMS Collaboration. Miniaod analysis documentation, March 2019. <https://twiki.cern.ch/twiki/bin/view/CMSPublic/WorkBookMiniAOD2017>.
- [207] Aram Hayrapetyan et al. The CMS Statistical Analysis and Combination Tool: Combine. *Comput. Softw. Big Sci.*, 8(1):19, 2024.

- [208] CMS Collaboration. Nanoaodv9 reference - muon, March 2025. https://cms-nanoaod-integration.web.cern.ch/autoDoc/NanoAODv9/2018UL/doc_TTToSemiLeptonic_TuneCP5_13TeV-powheg-pythia8_RunIISummer20UL18NanoAODv9-106X_upgrade2018_realistic_v16_L1v1-v1.html#Muon.
- [209] Matteo Cacciari, Gavin P. Salam, and Gregory Soyez. FastJet User Manual. *Eur. Phys. J. C*, 72:1896, 2012.
- [210] Matteo Cacciari, Gavin P. Salam, and Gregory Soyez. The anti- k_t jet clustering algorithm. *JHEP*, 04:063, 2008.
- [211] F. James and M. Roos. Minuit: A System for Function Minimization and Analysis of the Parameter Errors and Correlations. *Comput. Phys. Commun.*, 10:343--367, 1975.
- [212] Hans Dembinski and Piti Ongmongkolkul et al. scikit-hep/iminuit, Dec 2020. <https://doi.org/10.5281/zenodo.3949207>.
- [213] Baldenegro, Cristian and Cunqueiro, Cristian and Nguyen, Matthew. Measurement of the primary Lund jet plane density in proton-proton collisions at $\sqrt{s}=13$ tev. CMS Note 2022/001, CERN, 2022.
- [214] Valentina Mariani. Pion efficiency with D^* in UL. https://indico.cern.ch/event/1128089/contributions/4739089/attachments/2390750/4086870/DS_efficiency_UL_1402.pdf.
- [215] M. Cacciari, S. Frixione, M. L. Mangano, P. Nason, and G. Ridolfi. The t anti- t cross-section at 1.8-TeV and 1.96-TeV: A Study of the systematics due to parton densities and scale dependence. *JHEP*, 04:068, 2004.
- [216] Stefano Catani, Daniel de Florian, Massimiliano Grazzini, and Paolo Nason. Soft gluon resummation for Higgs boson production at hadron colliders. *JHEP*, 07:028, 2003.
- [217] PYTHIA, March 2025. <https://pythia.org/latest-manual/Variations.html>.
- [218] R Barlow and C Beeston. Fitting using finite Monte Carlo samples. *Comput. Phys. Commun.*, 77:219--228. 16 p, 1993.
- [219] J. S. Conway. Incorporating Nuisance Parameters in Likelihoods for Multisource Spectra. In *PHYSTAT 2011*, pages 115--120, 2011.

- [220] Higgs combine team. Higgs combine tool manual, September 2022. <https://cms-analysis.github.io/HiggsAnalysis-CombinedLimit/>.
- [221] Glen Cowan, Kyle Cranmer, Eilam Gross, and Ofer Vitells. Asymptotic formulae for likelihood-based tests of new physics. *Eur. Phys. J. C*, 71:1554, 2011. [Erratum: *Eur.Phys.J.C* 73, 2501 (2013)].